Neural network integration from multimodal imaging in epilepsy and healthy controls

Dissertation

for the award of the degree *"Doctor rerum naturalium"*

of the Georg-August-Universität Göttingen

within the doctoral program *Theoretical and Computational Neurosciences*

of the Georg-August University School of Science (GAUSS)

submitted by Daniel van de Velden

from Dinslaken, Deutschland

Göttingen, 2022

Thesis Committee

Prof. Dr. Niels K. Focke
Clinic for Neurology, University Medical Center Göttingen

Dr. Andreas Neef
Institute for Dynamics of Biological Networks, Neurophysics Laboratory, Göttingen Campus

Prof. Dr. Florentin Wörgötter
Third Institute of Physics, Biophysics, Georg-August-University Göttingen

Members of the Examination Board

Referee: Prof. Dr. Niels K. Focke
Clinic for Neurology, University Medical Center Göttingen

2nd Referee: Dr. Andreas Neef
Institute for Dynamics of Biological Networks, Neurophysics Laboratory, Göttingen Campus

Further members of the Examination Board

Prof. Dr. Melanie Wilke
Dept. of Cognitive Neurology, University Medical Center Göttingen

Prof. Dr. Alexander Ecker
Neural Data Science, Institute of Computer Sciences, Georg-August-University Göttingen

Prof. Dr. Alexander Gail
Sensorimotor Group, German Primate Center

Prof. Dr. Fred Wolf
Dept. of Physics of Biological Systems, Göttingen Campus Institute for Dynamics of Biological Networks

Date of oral examination: 27.01.2023, 10:45am

Widmung

„Für meine geliebte Familie.

Die Familie, in die ich geboren wurde und die Familie, die ich mir im Laufe meines Lebens ausgesucht habe.“

Dedication

“For my beloved family.

The family I was born into and the family I have chosen throughout my life.”

Danksagung

Auch wenn mein Name unter dem Titel dieses Werkes steht, bin ich nicht allein für seinen Erfolg verantwortlich. Ich habe zwar die Arbeit erbracht, aber ich hätte das alles nicht ohne die Hilfe und Unterstützung vieler Menschen tun können. Mein Dank gilt meinem Doktorvater Niels K. Focke. Seine aufmerksame und erfahrene Führung hat es mir ermöglicht eigenständig an jeglichen Aufgaben zu wachsen, meine Fähigkeiten zu verbessern, neue Dinge zu lernen, andere Dinge zu hinterfragen, sowie meine Stärken zu. Weiterhin danke ich meinen Arbeitsgruppenmitgliedern, deren Gespräche und Diskussionen, fachlich oder nicht, ich immer genossen habe. Auch sie halfen mir zu wachsen und haben meine Dissertationszeit zu etwas Besonderem gemacht. Daher „vielen Dank“: Christina, Ev-Christin, David, Marysol und Barbara.
Weiterhin möchte ich meinen sehr guten Freunden danken: Markus, Julian, Tobias, Melissa, Julian, Ronja, Vanessa, Albert, Julia, Dominik, David. Seither haben sie mein Leben und auch meine Promotionszeit durch ihre außergewöhnliche Freundlichkeit, Lebensfreude und Hilfe bereichert.
Weiterhin geht mein Dank an meine Familie. Seit meiner Geburt habt ihr mich geliebt und geformt. Ohne euch wäre ich nicht die Person, die ich heute bin.
Schließlich möchte ich meiner geliebten Frau meine größte Dankbarkeit aussprechen. Ihr unausdrückbares Maß an Unterstützung, Geduld und Liebe waren unabdingbare Größen ohne die ich nicht so weit gekommen wäre.

Acknowledgements

Even though my name is under the title of this work, I am not solely responsible for its success. I may have done the work, but I could not have done it all without the help and support of many people. My thanks go to my doctoral advisor, Niels K. Focke. His thoughtful and experienced guidance has enabled me to grow independently on any task, to improve my skills, to learn new things, to question other things, as well as to complement my strengths. Furthermore, I thank my working group members whose conversations and discussions, professional or not, I always enjoyed. They also helped me grow and made my dissertation time special. Therefore, "thank you", Christina, Ev-Christin, David, Marysol, and Barbara.
Furthermore, I would like to thank my very good friends: Markus, Julian, Tobias, Melissa, Julian, Ronja, Vanessa, Albert, Julia, Dominik, David. From the beginning, they have enriched my life and also my doctoral period with their extraordinary kindness, joie de vivre and help.
Furthermore, my thanks go to my family. Since my birth, you have loved, supported, and shaped me. Without you I would not be the person I am today.
Finally, I would like to express my deepest gratitude to my beloved wife. Her inexpressible level of support, patience, and love have been indispensable factors without which I would not have come this far.

Abstract

Different imaging modalities can be used to probe distinct aspects of the brain, such as cerebral anatomy (MRI), tissue diffusion directions (DTI), metabolic activity (PET), neurovascular activity (fMRI), or electrophysiological activity (EEG/MEG). The imaging modalities differ not only in terms of the aspect they represent, but also in their spatial resolution and in their temporal resolution. The medical imaging of the brain with each modality separately obtains valuable information. However, the joint use of neuroimaging techniques (measured in parallel or sequential) offers the possibility to combine the information from multiple modalities to obtain a broader picture of the human brain.

Epilepsy is characterized by a permanent predisposition of the brain leading to an epileptic seizure, a transient occurrence of abnormally synchronous neuronal brain activity. The two most common epilepsy syndromes are focal epilepsy, defined by a focal origin of the epileptic seizures, and idiopathic generalized epilepsy (IGE), in which epileptic seizure activity rapidly involves both cerebral hemispheres of the brain. Epilepsy is characterized as a network disease of the brain. Changes in brain networks have been detected in patients with IGE at rest, i.e., in the absence of seizures, or discharges, and under the situation by patients completing a set specific task. Brain network changes in patients with focal epilepsy are also known and identified with respect to diagnosis and treatment options. Though it has not been established whether measuring multiple imaging modalities in parallel (EEG-fMRI) provides data of sufficient quality in the modalities to detect, for example, group differences between two cohorts or constant components in a group of subjects.

This dissertation aimed at the examination and integration of brain networks from different parallel and sequential measured medical imaging modalities in cohorts of patients with epilepsy and healthy controls.

In the first main chapter, the impact of inside MR-scanner measurement condition on high-density electroencephalography (hd-EEG) was investigated to assess whether known statistical group differences of EEG power and phase-based functional connectivity could be replicated in patients with IGE compared to healthy controls during a parallel acquisition of fMRI. We observed that the analysis of phased-based functional connectivity (imaginary part of coherency) of EEG data is suitable for parallel measured hd-EEG-fMRI, and that group differences in a comparison of patients with IGE against controls remain identifiable. Moreover, between thalamus and the occipital cortical brain, spatial congruence of group

differences in seed-based functional connectivity (IGE>controls) was found between the two modalities measured in parallel, hd-EEG and fMRI.

In the second main chapter, the influence of different inverse methods for electric source imaging (ESI), as well as different stages of interictal epileptic discharges (IEDs) on the spatial identification of the epileptogenic zone in patients with focal epilepsy was investigated. Furthermore, the spatial relationship of the [18F]fluorodeoxyglucose-positron emission tomography (^{18}FDG-PET) hypometabolism found in patients with focal epilepsy and the different stages of IEDs (IED-onset, -rise, and -peak) were investigated. The second main chapter provides observations for the spatial least distance of ESI at the time when IEDs reach their maximum amplitude and the epileptogenic zone. In addition to that, the inverse method 'standardized low resolution brain electromagnetic tomography' (sLORETA) was observed to provide best results in identifying the epileptogenic zone.

In the third main chapter, the presence of metabolic, vascular, and neuronal resting-state networks, spatially stable across a cohort of healthy subjects and patients with focal epilepsy, were investigated in a fully simultaneous hd-EEG/fMRI/^{18}FDG-PET dataset. The possibility of identifying known resting-state functional networks from simultaneous hd-EEG/fMRI/^{18}FDG-PET data using group independent component analysis in each modality was demonstrated. Differences in the spatial expression of these networks were observed among modalities and could reflect differences between modalities in regard of signal origin, as well as spatial and temporal resolution.

Overall, this dissertation provides results from the integration of networks from different imaging modalities, from a parallel or sequential measurement setting.

Identifying relevant group differences between IGE and controls from an hd-EEG with parallel measured fMRI linked our knowledge of network changes in IGE across modalities. Furthermore, it encourages future EEG-fMRI epilepsy studies to subject both imaging modalities to same analyses and consideration of their results for conclusions.

Further work in this dissertation promotes careful choice of parameters in ESI in pre-surgical assessment in patients with focal epilepsy. Furthermore, it helps to elucidate the relationship between electric source imaging of interictal epileptic discharges and ^{18}FDG-PET in preoperative diagnosis and provides an impetus to investigate this relationship in future work.

Finally, we utilized the benefit of temporal synchrony of the fully simultaneous measurement of three modalities (hd-EEG/fMRI/^{18}FDG-PET) to demonstrate the presence and spatial

concordance of functional resting-state networks in three modalities and provide evidence for the rich potential of this measurement set-up.

Across projects, this dissertation demonstrates that integrating imaging data from multiple modalities can provide broader insight into the objects of study in neuroscience and, more broadly, neurological disease (exemplified here by epilepsy).

Table of contents

1. INTRODUCTION

This dissertation examines the integration of neural brain networks from the medical imaging modalities electroencephalography (EEG), functional magnetic resonance imaging (fMRI) and [18F] fluorodeoxyglucose positron emission tomography (^{18}FDG-PET) in epilepsy patients and healthy controls. The first chapter of this thesis provides the reader with an overview of the disease of epilepsy in humans, and of three imaging modalities (EEG, fMRI, and ^{18}FDG-PET), which reveal different aspects of brain activity/function, of their simultaneous application and the obtained results. It furthermore introduces the concept of brain networks and describes the methods with which they were inferred from brain imaging data.

1.1. EPILEPSY

Epilepsy is a disease, which, since the 1980s, has been steadily characterized and defined in more detail by the International League Against Epilepsy (ILAE) task force based on worldwide research results (League & Epilepsy, 1985). Epilepsy is now characterized as a network disease (Blumenfeld, 2014; Fisher et al., 2005). The term epilepsy does not describe a single disease but is the umbrella term for a variety of brain disorders that can have different causes (Fisher et al., 2005). Affected individuals suffer from recurrent, transient, and temporally unpredictable episodes of abnormally excessive or synchronous neuronal activity in the brain, which are, and cause disturbances of normal brain function (Fisher et al., 2005, 2017). Epileptic seizures occur due to abnormally excessive or synchronous neuronal activity within different parts of the brain (Fisher et al., 2017). The manifestations of this neuronal activity vary from a momentary lapse of attention to prolonged/persistent muscle spasms (Panebianco et al., 2016). Ten percent of the population experience a seizure in their lifetime, but not all develop epilepsy (Devinsky et al., 2018).

EPIDEMIOLOGY AND MORTALITY

Around 46 million people worldwide are affected by epilepsy (Beghi et al., 2019; Ngugi et al., 2010). In 2015, epilepsy was ranked as one of the top three diseases contributing to the global burden of neurological diseases (Vos et al., 2016) making it a relevant cause of disability and mortality worldwide. The onset of epilepsy can occur at any age, but the prevalence increases with age into early adult and late adulthood (Fiest et al., 2017). The incidence of epilepsy is bimodally distributed over age with the first peak during infancy and early childhood and the

second one in adults over 50 years of age (Fiest et al., 2017; Singh & Trevick, 2016). Thereafter, the prevalence of epilepsy decreases with age (Fiest et al., 2017).

Epilepsy carries a definite risk of death. This can be a more or less direct result of an epileptic seizure e.g., sudden unexpected death, which occurs approximately in 1 in 1000 adults with epilepsy (Sveinsson et al., 2017). Complications of a status epilepticus can lead to unexpected death, such as pulmonary aspiration with consequent pneumonia, or by accidents brought about by the seizure, i.e., drowning, head injuries, burns and motor vehicle accidents (Devinsky et al., 2015). Epilepsy can also be indirectly linked to mortality, as a cause of suicide and due to adverse effects of antiseizure or other psychiatric drugs (Devinsky et al., 2015). In addition to indirect effect of seizures, obesity and cardiovascular illness are associated with epilepsy (Devinsky et al., 2015). An estimate of mortality shows that in high-income countries the age-specific mortality rate, or most commonly expressed as standardized mortality rate, is 2.3 (per 1,000 people with epilepsy) for individuals with epilepsy and 2.6 (per 1,000 people with epilepsy) in low- and middle-income countries, with the highest mortality rates in the younger age groups (Levira et al., 2017; Thurman et al., 2017). Aside from premature death, epilepsy has other influences on the lives of those affected. Around 50% of people with epilepsy have coexisting physical or psychiatric conditions, as well as intellectual disabilities and these people are also commonly associated with neurodegenerative diseases (WHO, 2019; Yuen et al., 2018).

DIAGNOSTIC PROCESS

When an individual presents with seizures, several essential steps need to be performed by the examining physician to make an accurate diagnosis. In the beginning, the clinician must determine that the seizure was indeed an epileptic seizure, as differential diagnoses of epilepsy imitators are also possible. Those imitators include paroxysmal movement disorders, migraine associated syncope, parasomnias, and behavioral, psychological, and psychiatric disorders (for a full list of epilepsy imitators see: https://www.epilepsydiagnosis.org/epilepsy-imitators.html). Differentiating epilepsy from epilepsy imitators can be a difficult task, since the patient's own reports of the seizure are usually inaccurate or unavailable, so that the diagnosis relies on reports from witnesses to the seizures, which are also error-prone. Once

these imitators have been ruled out as the cause of the seizure, the clinician starts with the epilepsy classification by classifying the seizure type (Scheffer et al., 2017).

In many cases, the diagnostic process ends with the decision that the seizure was, indeed, epileptic, as there is no further data or even access to further diagnostic tools such as EEG, video EEG or other imaging techniques. For other patients, there is simply too little information to be able to make a more detailed diagnosis (Scheffer et al., 2017). For example, the presentation of a patient with only a single occurrence of a seizure offers little potential for the diagnosis of epilepsy, let alone its further classification based on the current International League Against Epilepsy guidelines, a diagnosis of epilepsy may be made if any of the following conditions are met (Fisher et al., 2014): First, at least two unprovoked (or reflex) seizures occurring more than 24 hours apart. Second, one unprovoked (or reflex) seizure, plus a probability of further seizures equal to the risk of another seizure (at least 60%) occurring after two unprovoked seizures within the next 10 years. Third a diagnosis of an epilepsy syndrome.

SEIZURE TYPE CLASSIFICATION

Classifying the epilepsy seizure type is important for several reasons: (i) the classification serves as a worldwide communication framework for clinical usage, (ii) the classification aids in determining the appropriate therapy for the patient, (iii) specific seizure types can be related to syndromes or etiologies, (iv) classification allows a more focused approach for research studies, and (v) the classification enables the patients to effectively described their diseases (Scheffer et al., 2017). Once the clinician has ruled out all differential diagnoses and is certain that the seizure was of epileptic nature, and a routine EEG was performed, the first stage of epilepsy classification can be initiated with the search for the origin of the abnormal neuronal activity that led to the ictal event. If the origin of the seizures cannot be determined, the seizure is classified as 'unknown' (Fisher et al., 2017). Otherwise, the seizure is classified as ‘focal’ or ‘generalized’ in origin. A focal seizure implies that the onset of the seizure has its origin in the network of one hemisphere. Whereas 'generalized' seizures are considered to rapidly involve bilaterally distributed brain networks (Fisher et al., 2017).

EPILEPSY TYPE CLASSIFICATION

With adequate information, the clinician is able to perform the second level of epilepsy classification, which is to determine the epilepsy type. During the recording of routine EEG (~20min) data in the clinic or in research, a seizure only occurs in a minority of the patients. The evaluation of the EEG recordings with the patient in a wake state with eyes closed is the main tool for diagnosing the epilepsy type. In this state, which is also called interictal state ("between seizures") in epilepsy patients, typical epileptiform EEG discharges can occur. Namely, interictal epileptic discharges (IED), which take the form of spike patterns in the EEG recordings, distinguishable from the normal background activity. Multiple different IED patterns are observed in epilepsy patients (Pond, 2019). Current epilepsy type classifications are: 'focal epilepsy', 'generalized epilepsy', 'combined generalized & focal epilepsy', and 'unknown epilepsy' (Fisher et al., 2017). Focal epilepsies include disorders with single or multiple focal events, and additionally those with seizures affecting only one hemisphere. Interictal EEG recordings typically show focal IEDs. Focal aware seizures, focal impaired awareness seizures, focal motor seizures, focal non-motor seizures, and focal to bilateral tonic–clonic seizures are the range of seizure types that are associated with focal epilepsy (Scheffer et al., 2017). Generalized epilepsy shows generalized spike-wave discharges (GSWD), which are a distinct IED pattern only present in generalized epilepsy. GSWD show up as spike complex in most EEG channels simultaneously during measurement. This EEG feature is essential for the diagnosis of generalized epilepsy. Seizure types like absence, myoclonic, atonic, tonic, and tonic–clonic seizures are the possible manifestations of a seizure for patients with generalized epilepsy (Fisher et al., 2017). Less commonly, patients have both focal and generalized seizures and may even show both focal IEDs and GSWD in interictal EEG recordings. However, the presence of epileptiform activity is not required for the diagnosis of 'combined generalized & focal epilepsy' (Fisher et al., 2017). When the clinician is unable to determine the type of epilepsy due to insufficient information or unclear indications, the patient is diagnosed with 'unknown epilepsy' (Scheffer et al., 2017).

EPILEPSY SYNDROME CLASSIFICATION

Once the clinician has been able to determine the particular type of epilepsy in the patient, combined analyses such as seizure type, EEG and other imaging techniques can ideally be used

to identify a syndrome that underlies the epilepsy disorder. The syndromes are often associated with certain characteristics such as seizure trigger, prognosis, and occurrence at a certain age (Commission on Classification and Terminology of the International League Against Epilepsy, 1981, 1989). For further information, the ILAE has created a website, which has been designed as a teaching tool. It provides the individual parameters of diagnoses, videos of the individual seizure types and EEG characteristics of established syndromes (www.epilepsydiagnosis.org). In the present dissertation, patients with focal and a subgroup of generalized epilepsy, called idiopathic generalized epilepsy (IGE) were studied. Therefore, the reader will be informed in more detail about the two epilepsy types in the two following sections.

1.2. Focal epilepsy

The following section provides the reader with information on focal epilepsy, as the analysis of this is a focus of this dissertation. Around 60% of all diagnosed epilepsies in adults are focal epilepsy (Freitag et al., 2001; Semah et al., 1998).

As a rule, focal epilepsy is further subdivided into two subgroups, based on the localization results of the electrophysiological examinations, namely mesiotemporal and neocortical epilepsy. In adults the common focal epilepsy is temporal lobe epilepsy (Téllez-Zenteno & Hernández-Ronquillo, 2012). In the following, the etiology of focal epilepsy and the treatment and outcome of focal epilepsy therapy is presented.

Etiology

Focal epilepsy usually results from abnormal structural changes in the brain. It is most common to perform magnetic resonance imaging (MRI) to identify such changes, although they cannot always be detected (Cendes et al., 2016). In approximately 25% of all focal epilepsy cases neuroimaging studies are inconclusive and the cause of the focal epilepsy remains unknown (Jobst et al., 2000).

In the rest of the focal epilepsy cases a variety of structural abnormalities can be the origin of the disease. In adults with temporal lobe epilepsy the most common structural brain abnormality is hippocampal sclerosis (HS, alias “mesial temporal sclerosis”) (Blümcke, 2009; Blümcke et al., 2013). HS is characterized by a segmental loss of pyramidal cells in any area of the hippocampal formation, which is accompanied with astrogliosis leading to a hardening

and thickening of the brain tissue (Blümcke et al., 2013). Based on the localization and spread of brain tissue hardening the hippocampal sclerosis can be determined by a classification system from the ILAE (Blümcke et al., 2013): (i) HS ILAE type 1 shows serious neuronal cell loss and gliosis predominantly involving CA1 (>80% cell loss) and CA4. However, all other regions of the hippocampus are also affected by neuronal cell loss. (ii) For HS ILAE type 2 only the CA1 shows neuronal cell loss and gliosis, whereas the regions CA2, CA3 and CA4 remain unaffected. (iii) The HS ILAE type 3 is defined by a neuronal cell loss of >50% in the CA4 regions, with all other regions being unaffected. For the regional definition of CA1-4 the ILAE adopted the terminology of Duvernoy (Duvernoy et al., 2005). In general, affected focal epilepsy patients show bilateral HS pathology, although one side is more severely affected than the other (Sadler, 2006). The cell loss, described by the term hippocampal sclerosis, may lead to a reorganization of the neuronal networks, which could promote epileptogenesis (Sloviter, 1994), although the pathogenesis is not fully understood. Besides HS, other structural causes for focal epilepsy are known. In later life, vascular malformations, and neoplasms (Avila & Graber, 2010) are the most frequent causes. In infants and early childhood, perinatal injuries are generally the cause of focal epilepsy. Focal epilepsy often occurs at the age between one and 26 years (mean: 7 years) due to cortical dysplasia (Sisodiya et al., 2009; Tassi, 2002; Whiting & Duchowny, 1999). In early adulthood post-traumatic focal epilepsy due to head injuries are most frequent (Emanuelson & Uvebrant, 2009). Without any specific age incidence strokes (Hauser et al., 1993) and central nervous system infections can also lead to focal epilepsy. Apart from structural brain abnormalities, there are also epilepsy syndromes in which the focal epilepsy originates mainly in the frontal or temporal lobes. Most of these syndromes are genetic manifestations, like autosomal dominant nocturnal frontal lobe epilepsy (Andermann et al., 2005; Cho et al., 2008; De Marco et al., 2007; Hayman et al., 1997; Parrino et al., 2012; Scheffer, 2000), autosomal dominant lateral temporal epilepsy (Andermann et al., 2005; Dazzo et al., 2018; Fanciulli et al., 2012; Kalachikov et al., 2002; Kawamata et al., 2010; Michelucci et al., 2000; Striano et al., 2008; Tessa et al., 2007; Winawer et al., 2002), and some of the familial temporal lobe epilepsies (Andermann et al., 2005; Andrade-Valença et al., 2008; Angelicheva et al., 2009; Michelucci et al., 2000; Striano et al., 2011).

Treatment And Outcome

The diagnosis of focal epilepsy is made on clinical grounds, as described in section 1.1. The aim of therapy is the elimination or, at least, reduction of seizures, with minimally adverse treatment effects, aimed at improving the physical and psychological condition in order to increase the quality of life (Devinsky et al., 2018).

The primary approach to epilepsy therapy is the administration of anti-seizure medications (ASMs). The choice of the initial ASMs must be tailored to the individual patient, based on the patient's epilepsy syndrome and seizures, as well as the patient's age and possible interactions with other medications or other existing medical conditions (Glauser et al., 2013). Most people diagnosed with epilepsy have a good prognosis, and their seizures can be controlled with medication. However, 20–30 % will develop drug-resistant epilepsy (Kwan & Brodie, 2000; Vos et al., 2016). In these patients with drug-refractory epilepsy, surgery can be an important treatment option with a significantly better outcome with regard to seizure frequency and quality of life compared to continued drug therapy (Engel, 2018; Wiebe et al., 2001). The aim of epilepsy surgery is to resect the epileptogenic zone to prevent further seizures, while sparing non-epileptic tissue with its important neuropsychological and neurological function (Vakharia et al., 2018). An accurate spatial identification of the epileptogenic zone is vital for the resection surgery to be successful. The presurgical work-up typically starts with a non-invasive evaluation ("phase 1"), encompassing MR imaging (MRI), video scalp electroencephalography (EEG), and detailed neuropsychological assessment (Baumgartner et al., 2019; Rosenow, 2001). In many cases ^{18}F-fluorodesoxyglucose positron emission tomography (^{18}FDG-PET) or ictal single photon emission computed tomography (SPECT) are additionally used. Some epilepsy centers also apply high-density EEG (hd-EEG) with electric source imaging (ESI) or, magnetencephalography (MEG) with magnetic source imaging (Ryvlin et al., 2014) of the IED events to identify the epileptogenic zone.

The overall results of epilepsy surgery are very favorable: seizure frequency decreases while quality of life is improved (Engel, 2018). Another study showed that patients with drug-resistant epilepsy who underwent resection surgery experienced an alleviation of their anxiety, depression, and other behavioral comorbidities, while patients who did not have surgery experienced deterioration in these aspects (Ramos-Perdigués et al., 2016). Reducing the frequency of seizures also lowered the likelihood of sudden unexpected death in epilepsy

(SUDEP) (Sperling et al., 2016). Taken together with the fact that a study on temporal lobe resection reported a mortality rate of 1.4% (after temporal lobectomy of registered cases in a national database), shows that surgical treatment of epilepsy is an option that should be considered (Kerezoudis et al., 2018).

1.3. Idiopathic generalized epilepsy

Approximately 15-20% of all epilepsy patients are diagnosed with genetic generalized epilepsy (GGE) (Jallon & Latour, 2005). Recently, the classification of genetic generalized epilepsies was updated and is now subdivided into two major epilepsy syndrome groups (Hirsch et al., 2022). One syndrome group is the idiopathic generalized epilepsy (IGE) that comprises four subsyndromes: childhood absence epilepsy (CAE), juvenile absence epilepsy (JAE), juvenile myoclonic epilepsy (JME) and epilepsy with generalized tonic-clonic seizures alone (GTCA). Those epilepsy syndromes are well defined in terms of their usual age of onset, their development, frequency, and duration of seizures, as well as interictal epileptiform and ictal EEG representation (Hirsch et al., 2022). Patients that do not fit the criteria of those four IGEs are now classified as patients with IGE without a specific epilepsy syndrome.

Etiology

Idiopathic generalized epilepsy is now presumed to have an underlying genetic basis, a finding that has emerged from decades of clinical genetic research. The inheritance of IGEs is complex, and they can arise with or without the influence of the environment (Hirsch et al., 2022). However, even though clinical genetic evidence is available, the identification of the involved genes is a slow process, mainly because of the polygenic basis of IGE, in which the presence of multiple alleles, each with low to moderate risk, is required for the disease to be expressed (Hirsch et al., 2022). The first genome-wide association study in 2009 brought new insights to the field, and in 2018 the ILAE Consortium for Complex Epilepsies conducted a genome-wide mega-analysis on >15,000 patients with epilepsy and approximately 30,000 healthy controls and were able to identify 16 loci significantly associated with IGE, of which eleven were novel findings (International League Against Epilepsy Consortium on Complex Epilepsies, 2018).

Treatment And Outcome

The diagnosis process of IGE is made on clinical grounds, as described in section 1.1. As with focal epilepsy, pharmacological treatment is the initial treatment approach. The anti-seizure medication is tailored to the specific IGE type, sex, as well as comorbidities. Similar to the ASMs used in other forms of epilepsy, pharmacological mechanisms of ASMs used in IGE include blockade of voltage-gated sodium and calcium channels, enhancement of GABA transmission, inhibition of glutamate transmission, or synaptic vesicle modulation (Devinsky et al., 2018).

In addition to medication, other important cornerstones for successful treatment of patients with IGE are training in self-management of the disease, avoidance of seizure triggers, education, and psychological intervention. Also, in IGE, patients can develop drug resistance and again experience seizures, which is the case in about 12-36% of all adult patients with IGE (Cerulli Irelli et al., 2020; Kwan & Brodie, 2000). Multiple seizure types, seizure onset in childhood, occurrence of status epilepticus, and psychiatric comorbidities worsen the prospects of successful treatment (Gesche et al., 2017, 2020). In order to provide a clear delineation of treatment options it is important to note that, unlike in focal epilepsies, resection surgery is not an option for IGEs. Since the seizures have no focal origin and rapidly spread into bilateral brain networks, no area can be identified for resection.

1.4. Modalities in brain imaging

In the main chapter of this dissertation, we will focus on the use of EEG, fMRI and ^{18}FDG-PET to study brain activity and synchronization in healthy controls, focal epilepsy patients and IGE patients, as well as the possibilities of integrating multiple modalities in these cohorts. In the following, the reader will be introduced to the individual modalities, their processing, and the methods applied to them to extract information about brain networks from each modality.

1.4.1. Electroencephalography (EEG)

The EEG is directly measuring the electrical potentials in the brain via sensors on the scalp. Electrical potentials in the human brain are generated by active neurons. When neurons act in large groups and act synchronously with their neighboring neurons, they form an electrical, oscillatory potential, which can be picked up by the EEG sensors. Tens of thousands of synaptic

potentials, each generated due to another neuron, lead to electric currents which cause electrical potentials that can be measured on the human scalp.

The outer layer of the human brain, the grey-matter or neocortex, contains pyramidal neurons in the cortex, which are oriented vertically to the cortex surface and parallel to each other. Excitation of postsynaptic neurons leads to intracellular and extracellular current flows that generate an electric field along the major axis of the neurons that can be measured externally. The measurement of these cortical activities is carried out over time and results in a temporally resolved voltage time series in each EEG sensor. Each sensor (or channel) records a different time series at a specific location on the scalp. The EEG with its high sampling frequency allows measurement of signals with high temporal resolution in the millisecond range. This makes it the ideal technique to detect and investigate brain oscillations in terms of their amplitude, which represents the strength of the brain activity, and the signal frequency and phase shifts between those oscillations, which resemble communication and information exchange in the human brain (Lopes da Silva, 2013; Womelsdorf et al., 2007). Even though the time series at sensor level are only a projection of the actual electrical brain activity, analyses can be performed at sensor level. However, with sensor-level analyses, one must be aware of the limitations in interpreting the results, e.g., in terms of functional connectivity (Lai et al., 2018). In order to determine time-resolved activity within the brain, one can reconstruct the neuronal sources from the measured sensor data.

EEG SOURCE RECONSTRUCTION

Reconstruction of cerebral activity in time and space in EEG/MEG measurements is difficult and is related to the so-called inverse problem, or neural source imaging problem. The recordings of these modalities are used to reconstruct the origin of the electromagnetic fields, i.e., the cerebral current sources (Hämäläinen et al., 1993). Five problems arise when reconstructing the source origins:

i. The current flow in the brain can only be estimated due to imperfect knowledge of the geometric and physical properties of the head and brain (Pascarella & Sorrentino, 2011).
ii. The changes in the electromagnetic fields are not known for the entire continuous surface of the brain, but only for discrete measurement points.

iii. The sources of electromagnetic field changes measured by the sensors are not limited to the inside of the brain. Therefore, the measurement consists of a superposition of neuronal activity, other biological sources, and ambient noise.

iv. The simultaneous neural activity of two or more sources in the brain leads to a measured electromagnetic field that is a superposition of these two individual fields (Dammers & Ioannides, 2000).

v. Due to the infinite number of source variations that can generate the same measurement signal in a sensor, there is no unique solution to the inverse problem (Von Helmholtz, 1853).

There are a variety of approaches for solving the inverse problem, from dipole methods (Mosher et al., 1992; Schimpf et al., 2002) to distributed source analysis, including methods based on minimum-norm estimators (Hämäläinen & Ilmoniemi, 1994; Pascual-Marqui et al., 1994), and inverse methods with spatial filters, so-called beamformers (Gross et al., 2001; Van Veen et al., 1997) and others (Michel et al., 2004). These inverse methods all have different constraints in estimating neuronal activity from the measured data. However, the physical basis for the generation of electromagnetic fields in all inverse methods are Maxwell's equations.

The reconstruction of brain sources from measured EEG/MEG data is called the inverse problem and to solve this problem an accurate forward model is required (Grech et al., 2008). The forward model comprises several a priori information, which remain constant during the entire measurement. An important part of the forward model is the so-called 'head model', which provides information of the geometry of the subject's head. This information is usually obtained from a volumetric reconstruction of the subject's individual MRI that was obtained near to the time to the EEG/MEG measurement. The spatial sensor configuration in relation to the subject's head is passed to the forward model and is referred to as the 'sensor model'. Furthermore, each forward model requires a 'source model' that defines the positions at which the brain activity is to be reconstructed at each time point of the measurement (Hansen et al., 2010; Michel et al., 2004). Source models can be roughly divided into two types: surface models, which limit the reconstructions of brain activity to the cortical surface, and volume models, which reconstruct brain activity for a defined three-dimensional grid within the brain. Those combined model information led to the solution of the forward problem as a vector

field, the so-called lead field $\mathcal{L}$, which describes the spatial sensitivity of each sensor by means of the direction and amplitude of a source current at a specific location of the source model. Each sensor i is obtained with a unique lead field L_i and a sensitivity based on the sensor configuration. This results in a lead field matrix $\mathcal{L}$. The lead field matrix $\mathcal{L}$ is calculated once for each measurement, since it depends on properties, which are constant during the measurement (e.g., subject's head, sensor configuration, electric conductivity). The sensors are represented as a matrix M containing the data accumulated over time with dimensions $n_r \times n_t$. n_r is the number of sensors and n_t is the number of time points recorded. The source activation matrix S in the dimension of $n_s \times n_t$, where n_s is the number of sources defined in the source model. The relation between source distribution S and the measured data M can be written as:

$$M = \mathcal{L}S + N$$

where an additional noise matrix N with the dimensions of $n_r \times n_t$ is added to the sensors and $\mathcal{L}$ is the leadfield. An estimate of the sources in the brain can be written as:

$$\hat{S} = GM = G(\mathcal{L}S + N) = G\mathcal{L}S + GN = RS + GN$$

where $\hat{S}$ represents the reconstructed sources for the measurement data matrix M. The variable R describing the relationship between true and estimated sources and G is the inverse operator matrix.

The purpose of any inverse method is to reconstruct the source distribution $\hat{S}$ from the known data matrix M using the known inverse operator G. With the formulation of the inverse operator the different inverse methods start to differ.

The common expression for the minimum norm estimation (MNE) inverse method is written as (Dale & Sereno, 1993):

$$G_{MNE} = \mathcal{L}^T(\mathcal{L}\mathcal{L}^T + \lambda \mathrm{C})^{-1}$$

, in which λ is introduced as a regularization parameter for the noise covariance matrix denoted as C. That results in resolution matrix for MNE as follows:

$$\hat{S}_{MNE} = G_{MNE}M = \mathcal{L}^T(\mathcal{L}\mathcal{L}^T + \lambda \mathrm{C})^{-1}M$$

By introducing a depth-weighting matrix D to G_{MNE} the inverse operator becomes more sensible to deeper sources (Lin et al., 2006). This weighted minimum norm estimation (wMNE) is written as:

$$G_{wMNE} = \mathrm{D}\mathcal{L}^T(\mathcal{L}\mathcal{L}^T + \lambda \mathrm{C})^{-1}$$

Another source estimation method is the so called Standardized low resolution brain electromagnetic tomography (sLORETA) (Pascual-Marqui, 2002). It is a method whose estimation of the source distribution is based on the standardized source distribution. It uses the estimate of the source distribution given by the minimum norm estimate G_{MNE} and standardizes it by $W_{sLORETA}$, which is the diagonal of the MNE resolution matrix $\hat{S}_{MNE}$.

$$W_{sLORETA} = \sqrt{Diag(\hat{S}_{MNE})}^{-1}$$

That given the sLORETA is written as:

$$G_{sLORETA} = W_{sLORETA}\, G_{MNE}$$

Thus, source reconstruction using sLORETA yields an estimate of the standardized source activity distribution.

Yet another approach of estimating the source activity distribution $\hat{S}$ from the measurement data matrix M are spatial filters or virtual sensors, also called beamformers. One example of beamformer beamformers used in neuroscience is the linearly constrained minimum variance (LCMV) beamformer (Van Veen et al., 1997). It assumes that a spatial filter for a source should respond only to the activity of that source:

$$G\,\mathcal{L} = 1$$

Other activities in the brain are suppressed at the same time. In contrast to the minimum-norm method, sources are not modeled here using the leadfield matrix $\mathcal{L}$, but it is assumed that the activities at other locations are captured by the covariance matrix of the data C_D. This suppressing effect for the source i is mathematically formulated as:

$$G_i\, C_D\, G_i^T \rightarrow minimal$$

This results for the linearly constrained minimum variance beamformer in:

$$G_i^{LCMV} = \mathcal{L}_i^T C_D^{-1} / (\mathcal{L}_i^T C_D^{-1} \mathcal{L}_i)$$

, where C_D is the signal covariance matrix. Different variations of beamformer approaches are present that optimize for dipolar source pairs (Brookes et al., 2007), or time- and frequency-dependent beamformer methods (Dalal et al., 2011; Gross et al., 2001; Woolrich et al., 2013).

At this point it must be said that no ideal inverse method could be identified. They all are differently influenced by their current application scenario, a priori constraints and assumptions, as well as physiological restrictions (Michel et al., 2004). For example, noise signals are treated differently in the methods (see standardization in sLORETA by G_{MNE}), or the assumption for the inverse method differs from others (see beamformer approaches and their assumption of influence from other sources while reconstructing another source). Studying reconstructed neuronal activity oscillations allows us to gain new insights into how the brain functions and communicates in different states, such as at rest or during tasks. Furthermore, it allows us to identify pathological changes in the brain in diseases such as epilepsy versus healthy control groups (Cendes et al., 2016; Chavez et al., 2010; Chowdhury et al., 2014; Elshahabi et al., 2015; Middlebrooks et al., 2017).

1.4.2. Functional Magnetic Resonance Imaging (fMRI)

fMRI is a functional neuroimaging technique, which is capable of measuring brain activity based on the changes in blood oxygenation and blood flow, which are affected by neural activity. Brain regions with higher activity consume more oxygen, which leads to an increased blood flow in order to fulfill this higher oxygen demand (Belliveau et al., 1991; Kwong et al., 1992; Ogawa et al., 1990). In 1990 Ogawa et al., discovered the blood oxygenation level dependent (BOLD) contrast in rats. A decreased intensity of the vascular signal in gradient-echo (GE) images for deoxygenated blood was observed, with an increase in intensity as the flow of freshly oxygenated blood increased (Ogawa et al., 1990). This BOLD mechanism was then used to image functional brain activity in humans (Kwong et al., 1992; Ogawa et al., 1990). Imaging with fMRI results in a higher spatial resolution on the neuronal activity than EEG source reconstructions, but with a medium temporal resolution in the dimension of seconds and is also completely non-invasive (Logothetis et al., 2001). Measurement results of the fMRI is usually provided as three-dimensional voxels with a resolution of 1 to 4 millimeters (Huettel et al., 2004). However, one must be aware that fMRI measures a surrogate of neuronal activity and, in particular, that the coupling of neuronal activity and blood flow is not clear (Attwell & Iadecola, 2002; Drew, 2019).

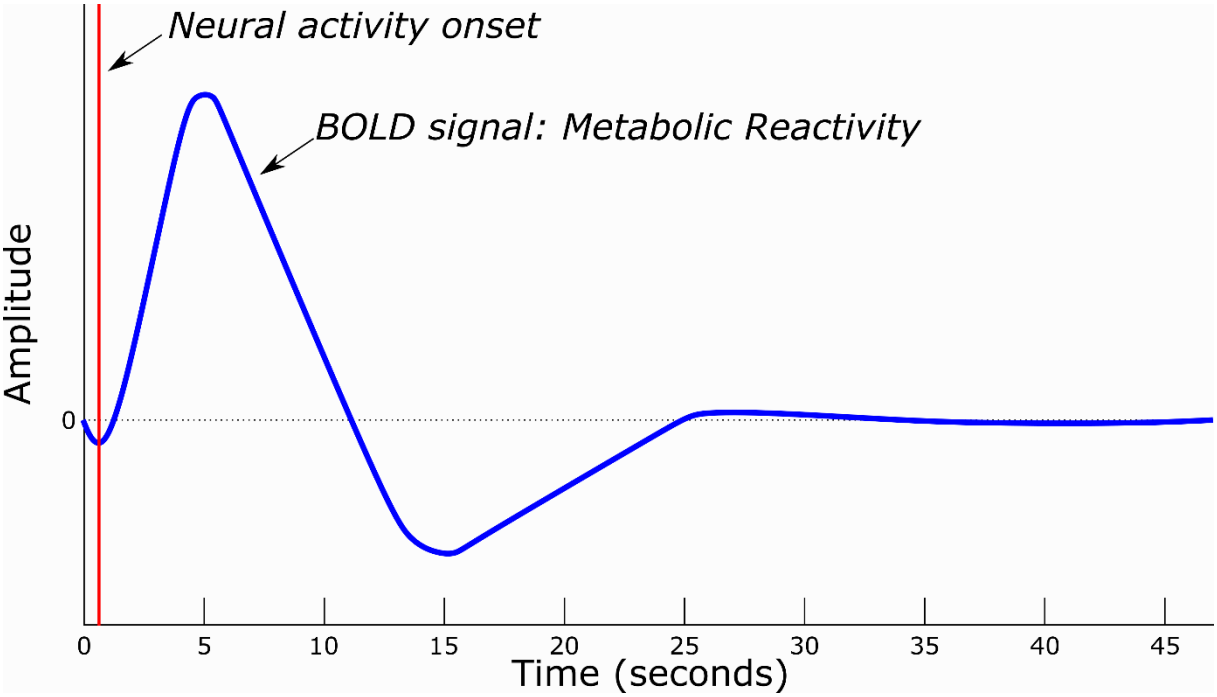

Figure 1.1: Schematic hemodynamic response function following the onset of a short neural activity.
A negative initial dip, a strong positive BOLD response, and a subsequent negative undershoot.

The possibility to obtain blood oxygenation level dependent functional imaging has led to an increased use of MRI in neuroscience (Ogawa et al., 1990; Kwong et al., 1992), and fMRI is nowadays one of the most important and frequently used neuroimaging modalities. However, fMRI as an imaging technique is not commonly used in everyday clinical practice. There it is applied to localize functional brain areas in patients using various stimuli or tasks that elicit specific neuronal responses, which are then measured with a "task-based" fMRI. The effective mapping of such brain areas with task-based fMRI are in good agreement with the gold standard methods, e.g., cortical stimulation during awake craniotomy (Ghinda et al., 2018). Nevertheless, scanning a patient performing an active task in the MR scanner has some disadvantages, i.e., cooperation of the patient, reduced data quality due to possible increased movement of the patient, among others. Therefore, many studies have investigated whether resting-state fMRI, in which the subject does nothing and thinks of nothing specific has the potential for clinical applications (Detre, 2006; Eickhoff & Grefkes, 2020; Lee et al., 2013; Matthews et al., 2006; Takamura & Hanakawa, 2017).

Reportedly, resting-state fMRI can provide biomarkers of neurological and psychiatric diseases, such as Alzheimer, schizophrenia, autism, and depression (D. Zhang & Raichle, 2010). Furthermore, fMRI offers us the opportunity to study the functioning and organization of the

human brain. In the past and in ongoing research, fMRI imaging has been used to gain new insights into brain regions at rest and their connections, for example, regions of the brain that are connected to: speech, movement, sensing, and hearing (Lee et al., 2013).

1.4.3. Positron Emissions Tomography (PET)

Positron emission tomography is an imaging modality that quantifies the distribution of a defined substance in a field of view (FOV). The substance is a radioactively labelled tracer that is injected into a vein of the person under study and metabolized in the body. Different applications require different radiotracers that all have characteristic decay properties such as half-life, decay type(s) and decay energy. Upon decay they emit alpha, beta particles and/or gamma radiation. The principle of visualizing the tracer distribution is based on the simultaneous detection by opposing pairs of detectors of two gamma ray photons with 511keV, which are emitted by the tracer decay with a radiation angle of exactly 180° to each other. Over the period of the measurement, all detected events in the individual detectors are added up and saved in a histogram format accumulating events per location. In order to reconstruct the origin and subsequently the distribution of the tracer, image reconstruction algorithms are applied (Fukuchi et al., 2017; Nolte et al., 2020; Tong et al., 2010). Multiple image reconstruction algorithms exist and can be roughly divided in analytical and iterative methods (for detailed information see: (Tong et al., 2010)). The resulting two-dimensional images, each on a defined axis for the FOV, are stacked to form a three-dimensional image volume (Fukuchi et al., 2017; Nolte et al., 2020; Tong et al., 2010). Due to the fact that the gamma photon pairs pass through different types of tissue on their way from the origin to the detectors, and in most cases one or both are either absorbed or scattered, correction methods are needed in order to achieve quantitative image information (detailed information: (Tong et al., 2010)). Since the first working prototype PET-CT scanner in 1998 (Beyer et al., 2000), this hybrid imaging modality is now established in the clinic and is commonly used for PET imaging (Nolte et al., 2020; Townsend et al., 2003, 2004). Under these circumstances, computer tomography, which is a three-dimensional x-ray scan, is usually performed before each PET measurement. This CT scan is coregistered to the PET images and provides attenuation factors for the different tissues, allowing an anatomically precise attenuation correction (Humm et al., 2003; Nolte et al., 2020). A new, more unusual approach is the

coregistration of the PET image to an MRI image to perform the attenuation correction. Unlike CT, MRI provides high soft tissue contrast. Moreover, many different contrasts can be used with MRI. Among other things, information on diffusion (diffusion weighted imaging) or brain activity (fMRI) can be obtained (Lopci & Fanti, 2020). Briefly, image data acquired with MRI is divided into different sections (i.e., tissue types) and each of these sections is assigned an attenuation constant, similar to a CT images. In general, attenuation correction methods can be divided into three classes of approaches: Segmentation-based, Atlas-based, and PET-based. Many methods for attenuation correction in PET/MR scanners have been developed and the performance of these methods is steadily advancing (Izquierdo-Garcia & Catana, 2016).

PET imaging has been a great asset in oncology, as many tracers allow spatial detection and assessment of all cancers (Lopci & Fanti, 2020). It has also been proven to be very useful in non-oncology applications, as it can be used in the diagnosis and assessment of a wide range of diseases (Jiménez-Bonilla & Banzo, 2018).

For metabolic brain imaging, the common radiotracer [18F]-2-fluoro-2-deoxy-D-glucose, or more simply fluorodeoxyglucose, or ^{18}FDG for short, is used. ^{18}FDG-PET is used to visualize glucose metabolism in the body. The glucose metabolism reflects the neuronal energy consumption. Regions with increased neuronal activity show higher ^{18}FDG accumulation, due to the consumption of glucose in neuronal activity processes. ^{18}FDG-PET brain imaging provides acceptable spatial resolution in the millimeter range (4-10 mm) (Sokoloff, 2008; Tulay et al., 2019).

Dynamic ^{18}FDG-PET imaging can be performed to provide information on the change in glucose metabolism over time. Therefore, a sequence of contiguous acquisitions can be performed, or the data can be acquired in the so-called list mode, which stores the detection times for all event counts for the corresponding location. This leads to a four-dimensional dataset. Analogous to the image reconstruction of the static ^{18}FDG-PET images, the tracer distribution can be reconstructed for each measured time frame, which shows the change in glucose metabolism over time in temporal resolution of in a the second to minute range.

Recently, a high-temporal resolution ^{18}FDG-PET approach with constant infusion, so-called functional PET or fPET was introduced which provides a temporal resolution of under 60 seconds or less (Jamadar et al., 2020).

1.4.4. Parallel multimodal imaging

The information obtained from the different imaging modalities is used complementarily. As in the example of the PET-CT, where the CT contributes to the processing of the data obtained by PET (see Chapter 1.4.3), or the anatomical information derived from an MRI scan that contributes to the creation of the forward model for EEG source estimation (see Chapter 1.4.1). Besides the single successive execution of different imaging modalities (non-parallel multimodal imaging), parallel multimodal imaging has shown potential in clinical practice (e.g., PET-CT scanner) and is a current object of research.

The potential of multimodal integration of various brain imaging modalities is enormous. Since different imaging techniques map activity in the brain due to different signal origins (e.g., ^{18}FDG-PET: metabolic, BOLD-fMRI: vascular, and EEG: electrophysiological). In addition, these techniques differ in terms of spatial and temporal detection of activity in the brain.

Furthermore, the simple fact that a parallel imaging machine (e.g., PET-CT machine, and PET-MR machine) offers a simplified measurement workflow and reduces measurement time as well as saving space for the equipment itself, the possibility of simultaneous multimodal brain imaging provides completely new ways and opportunities to investigate important aspects and clarify fundamental questions in neuroscience. Especially with regard to a completely simultaneous measurement of the functional processes of the brain, which allows a temporal correlation that would not be possible with separate measurements.

Parallel PET-fMRI

To promote information gain and a broader understanding of the brain, hybridization for parallel imaging of the two important functional neuroimaging techniques, PET, and fMRI, was also pursued (Judenhofer et al., 2008; Schlemmer et al., 2008). The ability of time-resolved ^{18}FDG-PET to image metabolic processes with limited temporal resolution and fMRI with the temporal resolution of seconds and high spatial resolution to image vascular changes complement each other. After demonstrating the feasibility of parallel combined PET-fMRI studies of the rat brain at rest or under task-related conditions (Wehrl et al., 2013), studies in which time-resolved PET and fMRI measurements of the human brain were performed in parallel have been published.

Studies provided evidence that local neuronal activity derived from metabolic activity determines BOLD functional connectivity at rest in humans (Riedl et al., 2014). Further, established fMRI metrices such as regional homogeneity and fractional amplitude of low frequency fluctuations were observed to have a strong relationship to glucose metabolic activity derived from ^{18}FDG-PET in human at rest (Aiello et al., 2015; Nugent, Martinez, et al., 2015). In addition, a resting-state study analyzing data from parallel PET and fMRI measurements found matching resting-state networks across both modalities (Di et al., 2012; Savio et al., 2017). Recently, an animal study utilizing parallel PET-fMRI showed resting-state networks with high spatial concordance across both modalities in Lewis rats at rest (resting-state networks) (Ionescu et al., 2021).

The application of PET-fMRI also provided insights in the linkage of metabolic and functional activity, functional connectivity into neurological diseases, such as Alzheimer (Marchitelli et al., 2018; Sun et al., 2021; Zhang et al., 2022), depression (Su et al., 2018). Furthermore, medication effects in Parkinson were studied with static ^{18}FDG-PET and fMRI measured sequentially (Aljuaid et al., 2019), and resting-state functional connectivity from time-resolved ^{18}FDG-PET and fMRI measured sequentially (Ruppert et al., 2021) and simultaneously (Zang et al., 2022) in Parkinson. Also, variations of resting-state networks in appearance, space and time were observed in individuals with disorders of consciousness (Schnakers et al., 2018).

Also, in the field of epilepsy research, studies conducted using multimodal parallel PET-fMRI imaging have observed higher cross modality coupling (fMRI: fractional amplitude of low frequency fluctuation and ^{18}FDG-PET: standardized uptake value ratio) in patients with medial temporal lobe epilepsy (J. Wang et al., 2020).

Parallel EEG-fMRI

EEG and functional MRI provide non-invasive measurements of brain activity at different spatial and temporal resolutions, and simultaneous recording of these modalities can maximize the respective strengths of the two methods while balancing their weaknesses in terms of spatial and temporal resolutions. Therefore, studies on realizing multimodal EEG-fMRI imaging were performed in the 1990s and it was shown that parallel EEG-fMRI measurement was technically feasible and safe for subjects (Hill et al., 1995; Ives et al., 1993; Lemieux et al., 1997; Warach et al., 1996).

Nevertheless, in all parallel EEG-fMRI studies the EEG data is contaminated with unavoidable artifacts. The strongest is the gradient artifact (GA) that is caused by the sequentially switched magnetic gradients during the MR imaging process, resulting in steep signal peaks with large amplitudes, whose magnitudes are larger than the biophysiological EEG amplitudes (Allen et al., 2000; Felblinger et al., 1999). The other artifact is the ballistocardiographic artifact (BCG) which is the movement of the electrodes in the static magnetic field of the MR scanner caused by the motion of the blood being pumped through the aorta (Allen et al., 1998; Bonmassar et al., 2002). Over the years, correction of these artifacts has improved with more reliable hardware and software solutions, leading to numerous studies that take advantage of EEG-fMRI imaging (Warbrick, 2022). A common approach for dealing with MR-related artifacts in simulatively measured EEG data is average artifact subtraction followed by removal of residuals to remove GA. In addition, BCG artifacts are removed using an optimal basis set (OBS) algorithm (Niazy et al., 2005). The goal of correcting BCG artifacts led to several studies that improved our understanding of the origin and properties of BCGs and their influence on EEG data in parallel fMRI recordings (Debener et al., 2008; Mantini et al., 2007; Masterton et al., 2007; Vasios et al., 2006). Thus EEG-informed fMRI analyses were shown to be a valuable type of analysis for event-related potential (ERP) studies when the study paradigm of these studies, which triggers ERPs, elicits responses in both modalities (Warbrick et al., 2013). Furthermore, studies investigating epilepsy also made early use of multimodal EEG-fMRI imaging which provided insights into the disease (Bénar et al., 2003; Krakow et al., 2001; Lemieux et al., 2001).

Parallel EEG/fMRI/^{18}FDG-PET

As these problems have been overcome in the past, there have been many multimodality studies that have made important contributions to our understanding of the brain. The combined fully parallel EEG/fMRI/^{18}FDG-PET measurements allow simultaneous monitoring of brain activity on slow (^{18}FDG-PET), medium (fMRI), and fast (EEG) time scales and have the capacity to complement each other in various dimensions (e.g., function, temporal, spatial, anatomic, and clinical utility etc.) (Shah et al., 2013). It is possible to obtain a better understanding of brain function by combining the results of each modality with each other, and thus brain function can be viewed simultaneously in metabolic, vascular, and

electrophysiological dimensions. For example, short temporal events in the range of milliseconds, such as an interictal epileptic discharge in individuals with focal epilepsy, can only be identified in high temporal resolution EEG. Recording these events by means of fully parallel EEG/fMRI/^{18}FDG-PET measurements thus allow the investigation of such rapid events in all aspects of simultaneous trimodal measurement due to the identification of such by EEG. Fully simultaneous EEG/fMRI/^{18}FDG-PET trimodal neuroimaging is an unusual measurement and has so far only been employed in research and this only at a few institutes (e.g., Research Center Juelich, University Hospital Tuebingen, Klinikum rechts der Isar in Munich). Furthermore, only few studies have been published presenting results based on fully parallel measured data from EEG/fMRI/^{18}FDG-PET.

The utility of simultaneously recorded trimodal data (EEG/fMRI/^{18}FDG-PET) has been investigated in recent years since 2015 with the intention of developing an "advanced metabolic imaging scanner" for in vivo human measurements (Shah, 2015). The attenuation effect of the EEG cap on the gamma ray photons emitted by radio tracer in EEG/fMRI/^{18}FDG-PET measurement was evaluated in terms of the imaging quality of each modality and was found to be inconsequential (Rajkumar et al., 2017). Further early evaluations of the trimodal imaging approach showed strong correlation of the fMRI BOLD signal and the glucose consumption rate in default mode areas, which is in line with previous reports in the literature (Shah et al., 2017). The authors further expressed that they see great potential in the use of simultaneous EEG/fMRI/^{18}FDG-PET measurements, such as simplifying the collection of data at only one time point when urgent pharmacological intervention is indicated (Shah et al., 2017). A recent study, using parallel measured EEG/fMRI/^{18}FDG-PET data, demonstrated a link between neuronal excitation and inhibition by showing a significantly higher distribution of glutamate and γ-aminobutyric acid (GABA) and their receptors in regions of the default-mode and somatomotor networks compared to non-resting-state network regions (Rajkumar et al., 2021). The combined EEG/fMRI/^{18}FDG-PET measurement of a cohort of 20 patients suffering from disorders of consciousness evaluated EEG band power, fMRI network connectivity, and ^{18}FDG-PET metabolic activity as markers for preserved consciousness and ^{18}FDG-PET and EEG were considered to be a suitable tool for evaluating their level of consciousness (Golkowski et al., 2017). It was further evaluated as a cost-effective imaging tool for investigating neuronal networks in the human brain as well as in the search of biomarkers for schizophrenia (Del

Guerra et al., 2018). Further knowledge of the cross-modal relations in multiple dimensions will increase our understanding by putting the findings of each modality in a more multifaceted context (Presigny & De Vico Fallani, 2022).

1.5. Human brain networks - Conceptualization and identification

In the main chapters of this dissertation, group differences, spatial relationships, and cross modal linkage of brain networks are reported. The following section describes the concept of brain networks and methodological approaches for their identification and characterization.

The term "network" describes a system with multiple underlying similar organizational units that are interconnected and enable communication exchange and/or interaction with each other. In neuroscience, the modern way of looking at the brain as a system of networks means that brain networks represent individual organized parts of the brain that are structurally and/or functionally interconnected and interacting (Bassett & Sporns, 2017). The description/definition of a brain network is also dependent on the perspective of the observer, and also on the underlying data (modality) on which the definition is based (Bartolomei et al., 2017). Brain networks can be roughly categorized as structural or functional networks.

Structural or anatomical networks can be identified by analyzing anatomical/morphological and histological similarities in different areas of the brain (Yao et al., 2015), and these structural network identifications form the basis of many anatomical brain atlases (Desikan et al., 2006; Destrieux et al., 2010; Fischl et al., 2002). Functional brain networks are defined as multiple separate brain regions and functional connections between multiple brain regions (Yao et al., 2015). To identify different functional networks in the brain, functional data that maps the dynamic processes (electrophysiological, vascular, metabolic, etc.) in the brain is analyzed.

One of the most widely used approaches to identify brain networks in functional data is seed-based connectivity (SBC) analysis, which identifies co-oscillations in time-resolved functional brain data and thus categorizes them as brain networks (Friston et al., 1993). The advantages of this approach are the freedom to designate any point in the brain as a region of interest (ROI) and the convenience of interpreting the results of the analysis. Temporal linkage between the time course of the ROI and other timecourses can be established using various connectivity methods. Functional connectivity describes the statistical relationship between

two time courses. It can be calculated in the time domain, for example by multivariate autoregressive modelling (Hytti et al., 2006) or, as used in this work, Pearson correlation metric (Greenblatt et al., 2012). Other connectivity metrics quantify the linkage of time courses for different frequencies, which requires a transformation into the frequency domain. Connectivity metrics calculated in the frequency domain include phase lag index, coherence, or imaginary part of coherence, etc. (Greenblatt et al., 2012). The choice of connectivity method is highly application-specific, with all methods having their own advantages and disadvantages. Throughout time many fMRI studies utilized seed-based Pearson correlation analysis in order to identify specific regions (e.g., motor cortex) from resting-state fMRI data (Biswal et al., 1995; Xiong et al., 1999).

A more mathematically sophisticated approach to identifying correlated regions is the independent component analysis (ICA) (Jutten & Herault, 1991). This method decomposes the given data into multiple components by maximizing their individual statistical independence in one dimension (usually space). This analysis results in a set of spatial maps of correlated regions, one map for each independent component in the data. It allows the simultaneous identification of multiple functional networks with one analysis, based solely on the underlying data. The advantage of this approach is that it does not require any a priori regional information, although one should be able to monitor the resulting set of components for artifact or noise components. This analysis approach was adapted to be applied on a group level in order to identify independent components that are consistent over a group of subjects (Beckmann & Smith, 2005; Calhoun et al., 2001). The application of group-independent component analysis to resting-state fMRI data led to the identification of independent resting-state networks (Damoiseaux et al., 2006; Smith et al., 2009).

The so-called resting-state condition is a common term for one type of measurement in research. The resting-state mode is defined by the circumstances that the brain is not exposed to any specific stimuli, does not have to cope with any specific task, and that the person is not thinking about anything in particular. These resting-state networks were found to exhibit sustained spontaneous brain activity even in a task-free situation, similar to a default condition of the brain work. Such resting-state networks are e.g., the visual (Hampson et al., 2004; Stern, 2002), somatomotor (Biswal et al., 1995), and default mode network (Raichle et al., 2001). Since these resting networks show a clear spatial delimitation functional brain

atlases were constructed, such as the so-called Yeo7/17 atlas (Yeo et al., 2011). This functional brain atlas was constructed based on resting-state functional connectivity data of 1000 subjects and identified different connectivity profiles of neighboring regions indicate that they participate in distributed networks (Yeo et al., 2011). For future functional characterization an atlas of at least seven resting-state functional networks was created, that are: visual, somatomotor, dorsal attention, ventral attention, limbic, frontoparietal, and default mode network (DMN) (Yeo et al., 2011). The same study also provides a functional brain atlas of further spatial division, separating the previously mentioned brain networks in sub areas, and adding the resting-state brain network called temporo-parietal network to the atlas.

Spatially coherent resting-state network patterns have also been found in MEG studies, overlapping spatially with established fMRI-based resting-state networks that show up in multiple frequency bands (Brookes et al., 2011, 2012).

1.6. Epilepsy as a brain network disorder

As described in the previous chapter, the brain is a system of interacting networks that are the origin of our behavior. Yet, a malfunction of parts of these networks leads to pathological conditions, such as epilepsy (Blumenfeld, 2014; Fisher et al., 2005).

Understanding epilepsy from a network perspective thus represents a shift toward an integrative view of brain structural and functional alterations that encompasses multiple spatial and temporal scales (Bassett & Sporns, 2017). This includes the study of comorbidities of epilepsy, such as cognitive or behavioral problems, as well as multimodal imaging of patients' brain activity and connectivity while performing tasks and during rest. In particular, the resting-state condition has found a wide application in the search for biological markers of disease (Fox & Raichle, 2007).

Given the multifactorial nature of the epilepsy disorder, the integration of multiple levels of information, derived from one or multiple imaging techniques is highly promising for the study, localization, and delimitation of epilepsy. Therefore, examining the whole brain using, e.g., non-invasive neural imaging methods is an important part of the picture to unravel the global network machinery in generalized and focal epilepsy.

1.6.1. Brain networks in focal epilepsy

Even when a suspected lesion has been detected, the modern concept of epileptogenic networks in focal epilepsy comprises several network zones, such as the epileptogenic zone network, propagation network, as well as non-involved networks (Bartolomei et al., 2017). It proposes a hierarchical organization with regard to epileptogenicity in the brain of a patient with focal epilepsy and is solely based on stereo EEG (sEEG) recordings, which is a method of placing intracerebral electrodes in regions of interest (Bartolomei et al., 2017).

Thus, for use in the preoperative assessment of patients with focal epilepsy, six cortical zones are defined (Rosenow, 2001), whose spatial definition comes from different modalities and is characterized by different features (Figure 1.2). The symptomatogenic zone is the area of the cortex that is activated when ictal discharges occur and produces the ictal symptoms. The irritative zone is defined as the area of the brain that produces the interictal epileptic discharges (IEDs). The seizure onset zone is defined as the area of the brain from which the clinical seizures actually originate. The epileptogenic zone, on the other hand, describes the area that is mandatory for the initiation of epileptic seizures. The functional deficit zone is the region in the brain that shows pathological functional changes in the interictal phase, such as the ^{18}FDG-PET hypometabolism (please see below). The epileptogenic zone is a theoretical concept and defined as the region in the brain that is mandatory for the development of epileptic seizures (Rosenow, 2001). These zones are not spatially clearly delineated from each other but can overlap (see Figure 1.2). For promising epilepsy surgery, the most accurate possible identification of the individual zones is of great importance, since the goal of resective epilepsy surgery is the complete resection of the epileptogenic zone, as well as the areas that are responsible for the development of clinical seizures, while sparing uninvolved brain regions (Baumgartner et al., 2019; Ryvlin et al., 2014).

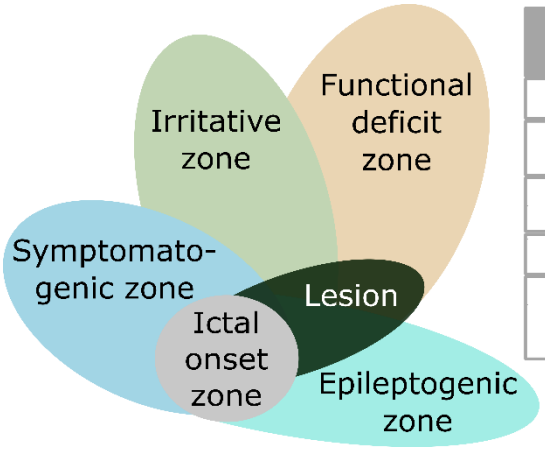

Zone	Useable modalities to characterize it
Irritative zone	EEG, MEG, EEG-fMRI
Seizure-onset zone	EEG, ictal SPECT lesser, fMRI and MEG
Symptomatogenic zone	The initial symptomatology of the seizure is used
Epileptogenic lesion	MRI
Functional deficit zone	Neurological/neuropsychological examination, and interictal SPECT and PET

Figure 1.2: Simplified illustration of the conceptualization of the epileptogenic zones in patients with focal epilepsy and modalities to identify those *(Edited from (Jehi, 2018) and used with permission)*

In patients with focal epilepsy the interictal epileptic discharges produced in the irritative zone (Engel, 1984; Lozano et al., 2009; Pillai & Sperling, 2006; Tatum et al., 2018) show distinct temporal characteristics and development, and can be divided into typical phases (Kane et al., 2017). The first phase of the interictal epileptic discharges is called IED-Onset, which marks the beginning of the interictal epileptic discharge event. The phase when the interictal epileptic discharge reaches its maximum amplitude is called IED-Peak. When half the maximum amplitude is reached one defines the IED-Rise phase. The IED-Peak is followed by one or multiple slow afterwaves (Figure 1.3). With respect to the accuracy of electric source imaging in the presurgical evaluation of focal epilepsy patients it is important to consider the propagation of interictal epileptic discharges as an important influencing variable for interictal epileptic discharge source localization (Lantz et al., 2003; Zumsteg et al., 2006).

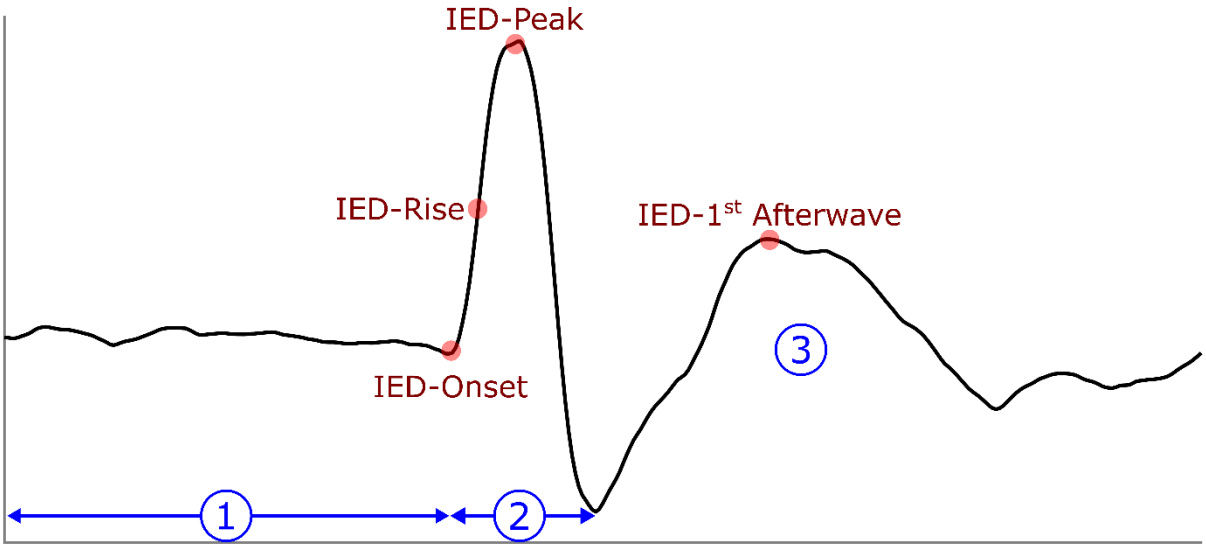

Figure 1.3: Sketch of an interictal epileptic discharge based on averaging multiple interictal epileptic discharges from averaged EEG sensors.
Simplified normal course of EEG sensor activity (1), disrupted by an interictal epileptic discharge (2), followed by a slow wave form that superimposes the normal EEG sensor activity (3).

^{18}FDG-PET REGIONAL CEREBRAL GLUCOSE METABOLISM IN PATIENTS WITH FOCAL EPILEPSY

In the course of the pre-surgical evaluation of a patient with focal epilepsy, the evaluation of interictal ^{18}FDG-PET data has an established role in the spatial identification of the epileptogenic foci (Sarikaya, 2015). In the focal epilepsy patient's interictal state, shares of the epileptogenic network are often represented as a regional decrease of cerebral glucose metabolism (rCGM). Hypometabolism is only present in one to two thirds of focal epilepsy patients and when present, it often extends beyond the genuine epileptogenic area (Alavi et al., 2011). Extensions into the frontal lobe can be often found in temporal lobe epilepsy patients (la Fougère et al., 2009), and the presence of such hypometabolic extensions are associated with an unfavorable post-surgical outcome (Lagarde et al., 2020). Extratemporal hypometabolism was a predictor of poor postoperative seizure outcome, while localized temporal hypometabolism predicted good outcome (Jaisani et al., 2020).

However, the pathophysiological origin of this hypometabolism is not fully understood, and many reasons have been hypothesized regarding its underlying mechanism (Taussig et al., 2021). First, there could be neuronal loss in the functional deficit zone, or the existence of hypometabolic macro- or microscopic lesions (Knowlton et al., 2001; O'Brien et al., 1997). Second, reduced synaptic activity is conceivable, but also deafferentation with a reduction in the number of synapses, as well as an underlying post-ictal metabolic depression (Mauguière

& Ryvlin, 2004). Third, it could be a breakdown of inhibitory mechanisms due to an advanced stage of the disease (Koutroumanidis et al., 2000).

To gain more insight into this topic, studies investigated the spatial characteristics of ^{18}FDG-PET hypometabolism and ictal events derived from EEG data in mesiotemporal lobe epilepsy (MTLE). It is assumed, that the region of ^{18}FDG-PET hypometabolism mainly reflects patterns of ictal EEG, and multiple studies reported results that support this assumption. One study observed high frequency oscillations in stereo EEG in hypometabolic areas in ^{18}FDG-PET. The authors further hypothesized that a pathophysiologic mechanism common to epileptogenesis was involved (Lamarche et al., 2016). Further studies on MTLE patients found concordance between ^{18}FDG-PET hypometabolism topography and EEG patterns of ictal onset at sensor level, which indicates that neural brain networks are spatially related during ictal events and glucose metabolic changes (Chassoux, 2004).

1.6.2. Brain networks in generalized epilepsy

The marked difference between patients with generalized epilepsy and those with focal epileptic discharges is the short transient episodes of synchronous bilateral discharges without a focal origin present in patients with generalized epilepsy (Leutmezer et al., 2002). Interictal EEG measurements are commonly used to identify such generalized spike-wave discharges (GSWD), which can be seen in a large number of channels with a high amplitude and a frequency of 2-3 Hz (Sazgar & Young, 2019).

As the status of GSWD in the dynamics of epileptic networks has not been fully elucidated, it has become a topic of great interest in many studies. Parallel EEG-fMRI measurements of the patients are mostly used for this purpose, since the occurrence of GSWD can be determined in the highly temporally resolved EEG, and the location of the origin as well as its integration into the brain networks before, during and after these events can be investigated in the spatially highly resolved fMRI (Aghakhani et al., 2004; Benuzzi et al., 2012; Gotman et al., 2005; Hamandi et al., 2006; Klamer et al., 2018; Szaflarski et al., 2013; Tangwiriyasakul et al., 2018). This showed bilaterally increased BOLD amplitude in frontal and parietal cortical areas ten seconds before the GSWD event, and specifically in the occipital-medial default mode network (DMN) region, which is anatomically described as the precuneus posterior cingulate region (Aghakhani et al., 2004; Benuzzi et al., 2012; Hamandi et al., 2006). In addition, there were

BOLD increments in thalamus, cerebellum, and anterior cingulate gyrus at GSWD onset with decreases in BOLD amplitude in default mode network regions after the GWSD (Benuzzi et al., 2012; Gotman et al., 2005).

Further neural imaging studies reinforced the position of thalamocortical and cortico-cortical networks as a central element in patients with IGE (Bernhardt et al., 2009; Blumenfeld et al., 2003; Klamer et al., 2018; Larivière et al., 2020; Moeller et al., 2008; Tangwiriyasakul et al., 2018). The changes in the brain networks of patients with IGE before and after GSWD suggested permanent changes in the interictal periods in the resting-state condition.

Many fMRI studies investigated the possible resting-state network alterations in patients with IGE and found connectivity changes in the DMN networks (Parsons et al., 2020), and additionally in the frontal lobe regions (McGill et al., 2012), as well as cerebellar areas (Kay et al., 2014). In contrast to fMRI studies that examined GSWD or resting-state data in patients with IGE, the number of studies that used EEG data to gain insights is much smaller, although in most studies EEG was measured simultaneously with the fMRI in order to temporally mark the GWSD events for further fMRI data analysis (Aghakhani et al., 2004; Benuzzi et al., 2012; Gotman et al., 2005; Hamandi et al., 2006; Klamer et al., 2018; Szaflarski et al., 2013; Tangwiriyasakul et al., 2018).

Unlike fMRI, the EEG and/or MEG measures the neuronal signal directly with a higher temporal resolution (Lopes da Silva, 2013) and also focuses on the origin and characterization of GSWD in the brain network of patients with IGE (Holmes et al., 2004; Westmijse et al., 2009). Resting-state network alterations were derived from sensor-level EEG/MEG studies and rich connectivity with modular structure was observed and further, differences in brain network topography have been observed in patients with IGE (Chowdhury et al., 2014).

Alterations in resting-state MEG and EEG were also recently found in source-level connectivity and power in patients with IGE (Elshahabi et al., 2015; Li Hegner et al., 2018; Stier et al., 2021, 2022); all with a consistent finding of increased connectivity in the theta frequency band in the frontotemporal and central regions of the brain.

2. AIM OF THE DISSERTATION

Multimodal imaging has shown great potential for the clinical practice and is current body of investigation in neuroscience research. The functions of the brain can be mapped under different aspects - neuronal, vascular, metabolic, and anatomical. Given the multifactorial nature of epilepsy, which is defined in modern terms as a network disease (Blumenfeld, 2014; Fisher et al., 2005), the integration of multiple levels of information from multiple imaging modalities can increase the understanding of the disease. The study of interictal epileptic discharges, as well as the resting-state condition during interictal periods in different imaging modalities, has revealed distinct changes in the large-scale brain networks in patients with epilepsy. However, it is not entirely clear to what extent the identified brain network changes in one modality such as EEG are reflected or complemented in another imaging modality, e.g., fMRI. Furthermore, it was not known whether resting-state brain networks, whose identification from fMRI data is an established method, are reflected in other common brain imaging modalities and to what extent they are spatially or temporally related. In addition, the relationship of brain network components from the epileptogenic networks in focal epilepsy patients from different brain imaging modalities such as interictal epileptic discharges and ^{18}FDG-PET hypometabolism is unclear. Clarification of the relationship of brain network components from different brain imaging modalities should provide a better understanding of the informativeness of each imaging modality on its own, which in turn would provide a better understanding of epilepsy itself and, hopefully in the long term, enable a better treatment of the disease.

Therefore, in the first part of this dissertation project, we investigated whether known relevant group differences in power and/or connectivity between patients with idiopathic generalized epilepsy and healthy controls, which are known from previous EEG/MEG studies, also emerged from EEG data measured in parallel with fMRI. Furthermore, we analyzed to what extent group differences were congruent across imaging modalities (Chapter 4.1). This not only served to clarify the validation of the information content from EEG data during a parallel fMRI after data cleaning but will also serve to increase the understanding of the multimodal evaluation of the analysis results for further neuroscientific studies.

In the second part of this dissertation project (Chapter 4.2), I discuss the influence of different source reconstruction methods and different time phases of interictal epileptic discharges in

patients with focal epilepsy in terms of their accuracy for localizing the epileptogenic zone. Furthermore, I investigated the spatial relationship of these interictal epileptic discharges and the ^{18}FDG-PET hypometabolism detected in the patients.

Building on the results of the first part of this dissertation project, I investigated in the final part of my work whether known functional resting-state networks can be extracted from the data of fully simultaneous hd-EEG/fMRI/^{18}FDG-PET measurements in a mixed cohort (Chapter 4.3). These results may provide the encouragement for further multimodal imaging studies (e.g., hd-EEG/fMRI/^{18}FDG-PET) for general studies of brain networks in humans, as well as the study of epilepsy and other neuronal diseases.

In summary, I addressed the subsequent overarching questions in this dissertation:

- *Is it possible to extract relevant group differences in patients with idiopathic generalized epilepsy from the hd-EEG of a parallel hd-EEG-fMRI measurement after MR artifact cleaning?*
- *What is the linkage of the ^{18}FDG-PET hypometabolism found in patients with focal epilepsy and the interictal epileptic discharges occurring in these patients?*
- *Are known resting-state brain networks expressed in all modalities of a simultaneous hd-EEG/fMRI/^{18}FDG-PET measurement and what is their spatial linkage?*

3. Materials and Data

3.1. Multimodal imaging in idiopathic generalized epilepsy

For the purpose of investigation, the influence of MR artefacts in a parallel EEG-fMRI measurement on the statistically significant group differences in idiopathic generalized epilepsy patients compared to controls, as well as the cross-modal linkage of significant group differences we utilized the cohort data used in Stier et al. (Stier et al., 2022).

In this project a patient sample with mixed IGE syndromes and a cohort of healthy controls was recruited through the Department of Neurology, University Hospital of Tübingen, Germany. Exclusion criteria for participation were neurologic or psychiatric disorders, cardiac or respiratory diseases, and medication intake.

In the course of this project, among others, all subjects underwent eyes-closed resting-state hd-EEG (30min) measurements in supine position. Furthermore, simultaneous fMRI-EEG measurements (30min) in resting-state condition and anatomical and diffusion tensor imaging (T1 weighted/T2-FLAIR/DTI) was conducted.

My contributions:

I have developed the data analysis procedure for this project, which includes the data processing, as well as first and second level analysis.

Chapter 4.1 of this dissertation contains the results of this data analysis, based on hd-EEG data with parallel and non-parallel fMRI, as well as anatomical MRI data.

3.2. Impact of inverse methods and spike phases on interictal hd-EEG source reconstruction and its relation to ^{18}FDG-PET hypometabolism

The study of influencing factors on high-density electric source imaging (hd-ESI) and multimodal spatial coupling in presurgical workflow is based on retrospective data of patients with focal epilepsy, who underwent successful epileptic surgery.

From the clinical database of the Department of Neurology at the University Medical Center Göttingen, patients were identified for whom the following data sets were available: presurgical monitoring hd-EEG (≥60 min), high-resolution pre- and post-surgical anatomical MRIs, and static ^{18}FDG-PET data sets. All patients underwent their first epilepsy surgery with good outcome (Engel I) (Engel, 1993; Wieser et al., 2001).

From 21 patient's hd-EEG data an experienced clinician identified interictal epileptic discharges visually. Additionally automated detection of interictal epileptic discharges via the usage of a set of neural networks from a commercial EEG analysis software called Persyst (Persyst, San Diego, USA; non-clinical use, version 14, Rev. C) was applied.

My contributions:

I formulated the hypothesis and developed the analysis workflow accordingly. I have developed my own analysis functions for this project, based on existing literature. I processed the data and applied statistical evaluation on the processed results.

Chapter 4.2 of this dissertation contains the results of this data analysis, based on interictal epileptic discharges from hd-EEG data, pre-and post-surgical anatomic MRI, as well as metabolic ^{18}FDG-PET data.

The results of a second project can be found in chapter 7.1. Therein hd-EEG, pre- and postoperative anatomical MRI were used to evaluate the feasibility of hd-ESI under the influence of the number of spikes and under the application of automatic spike detection by the commercial software Persyst.

3.3. IDENTIFICATION AND CROSS-MODAL SPATIAL RELATIONSHIP OF HUMAN RESTING-STATE NETWORKS IN SIMULTANEOUSLY MEASURED HD-EEG/FMRI/^{18}FDG-PET IMAGING

In order to investigate temporal and spatial relationship of resting-state brain networks across multiple modalities, we recruited a cohort of patient with lesional and non-lesional focal epilepsy, as well as a group of healthy control subjects through the Department of Neurology, University Hospital of Tübingen, Germany.

Control individuals with neurologic or psychiatric disorders, cardiac or respiratory diseases, and medication intake were excluded.

All subjects underwent eyes-closed resting-state hd-EEG/fMRI/^{18}FDG-PET measurement (30min) in supine position. Furthermore, we collected anatomical and diffusion tensor imaging (T1 weighted/T2-FLAIR/DTI) data for each subject.

On a second appointment all subjects underwent the same measurement of a fully simultaneously hd-EEG/fMRI/^{18}FDG-PET measurement (30min) in supine position under a motor-task (finger tapping) paradigm. Furthermore, we collected anatomical and diffusion tensor imaging (T1 weighted/T2-FLAIR/DTI) data for each subject.

My contributions:

I assisted in recruitment decisions, as well as advised on data acquisition settings. I was also the leading role in data transfer, curation, and documentation at the University Medical Center Göttingen. I have designed and performed the data analysis workflow for each modality in this project, which includes the data processing, as well as first and second level analysis.

Chapter 4.3 of this dissertation contains the results of this data analysis, based on anatomical MRI, as well as fully simultaneously measured hd-EEG/fMRI/^{18}FDG-PET data at the resting-state condition.

4. ORIGINAL ARTICLES

I have summarized my research contributions to this dissertation in the following three main articles:

Comparison of resting-state EEG network analyses with and without parallel MRI in genetic generalized epilepsy

Authors: **Daniel van de Velden**[1]; Christina Stier[1,2]; Raviteja Kotikalapudi[2,3]; Ev-Christin Heide[1]; David Garnica Agudelo[1]; Niels K. Focke[1,2]

[1] *Clinic for Neurology, University Medical Center Göttingen, 37075 Göttingen, Germany*
[2] *Department of Neurology and Epileptology, Hertie Institute of Clinical Brain Research, University Medical Center Tübingen, University of Tübingen, 72076 Tübingen, Germany*
[3] *Clinic for Neurology, University Medical Center Essen/University Duisburg-Essen, 45147 Essen, Germany*

NKF and DvdV designed and conceptualized the study; CS and RK acquired data; DvdV analyzed the data and performed statistical analyses and visualization; DvdV and NKF interpreted the results; NKF supervised the project; DvdV drafted the manuscript; NKF, CS, RK, EH, and DG revised the manuscript for intellectual content.

Published in *Brain Topography*, 2023.

Impact of inverse methods and spike phases on interictal hd-EEG source reconstruction and its relation to ^{18}FDG-PET

Authors: **Daniel van de Velden**[1]; Ev-Christin Heide[1]; Caroline Bouter[2]; Jan A. Bucerius[2]; Christian Riedel[3]; Niels K. Focke[1]

[1] *University Medical Center Göttingen, Clinic for Neurology, 37075 Göttingen, Germany*
[2] *University Medical Center Göttingen, Department of Nuclear Medicine, 37075 Göttingen, Germany*
[3] *University Medical Center Göttingen, Institute for Diagnostic and Interventional Neuroradiology, 37075 Göttingen, Germany*

NKF, EH, and DvdV designed and conceptualized the study; EH reviewed clinical data and provided DvdV with EEG data for analysis; DvdV analyzed the data and performed statistical analyses and visualization; DvdV and NKF interpreted the results; NKF supervised the project; DvdV drafted the manuscript; NKF, EH, CR, CB and JAB revised the manuscript for intellectual content.

Published in *Clinical Neurophysiology*, 2023.

Identification and cross-modal relationship of functional resting-state networks in simultaneously measured hd-EEG/fMRI/^{18}FDG-PET imaging

Authors: **Daniel van de Velden[1];** Ev-Christin Heide[1]; Pascal Martin[2]; Benjamin Bender[3]; Sebastian von Beschwitz[4]; Adham Elshahabi[5]; Tudor Ionescu[6]; Bernd Pichler[6]; Christian la Fougère[4*]; Niels K. Focke[1,2*]

[1] *Clinic for Neurology, University Medical Center Göttingen, 37075 Göttingen, Germany*
[2] *Department of Neurology and Epileptology, Hertie Institute of Clinical Brain Research, University Medical Center Tübingen, University of Tübingen, 72076 Tübingen, Germany*
[3] *Department of Diagnostic and Interventional Neuroradiology, University Hospital Tübingen, 72076 Tübingen, Germany*
[4] *Department of Nuclear Medicine and Clinical Molecular Imaging, University Hospital Tübingen, 72076 Tübingen, Germany*
[5] *Department of Neurology, University Hospital Zurich, 8091 Zurich, Switzerland*
[6] *Department of Preclinical Imaging and Radiopharmacy, Werner Siemens Imaging Center, University Hospital Tübingen, 72076 Tübingen, Germany*

ClF and NKF designed and conceptualized the study; TI acquired data; DvdV analyzed the data and performed statistical analyses and visualization; DvdV interpreted the results; NKF supervised the project; DvdV drafted the manuscript.

In preparation for submission.

4.1. COMPARISON OF RESTING-STATE EEG NETWORK ANALYSES WITH AND WITHOUT PARALLEL MRI IN GENETIC GENERALIZED EPILEPSY

At this point, it is important to mention that a cohort of patients with idiopathic generalized epilepsy (IGE) was analyzed in this study. At the time of the analysis, the terminology genetic generalized epilepsy (GGE) was still used to refer to the syndrome of the included patients. The terminology genetic generalized epilepsy for this cohort is used only in this main article of the dissertation.

Brain Topography (2023) 36:750–765
https://doi.org/10.1007/s10548-023-00977-6

RESEARCH

Comparison of Resting-State EEG Network Analyses With and Without Parallel MRI in Genetic Generalized Epilepsy

Daniel van de Velden[1] · Christina Stier[1,2] · Raviteja Kotikalapudi[2,3] · Ev-Christin Heide[1] · David Garnica-Agudelo[1] · Niels K. Focke[1,2]

Received: 20 July 2022 / Accepted: 12 June 2023 / Published online: 24 June 2023

Abstract

Genetic generalized epilepsy (GGE) is conceptualized as a brain disorder involving distributed bilateral networks. To study these networks, simultaneous EEG-fMRI measurements can be used. However, inside-MRI EEG suffers from strong MR-related artifacts; it is not established whether EEG-based metrics in EEG-fMRI resting-state measurements are suitable for the analysis of group differences at source-level. We evaluated the impact of the inside-MR measurement condition on statistical group comparisons of EEG on source-level power and functional connectivity in patients with GGE versus healthy controls. We studied the cross-modal spatial relation of statistical group differences in seed-based FC derived from EEG and parallel fMRI. We found a significant increase in power and a frequency-specific change in functional connectivity for the inside MR-scanner compared to the outside MR-scanner condition. For power, we found reduced group difference between GGE and controls both in terms of statistical significance as well as effect size. Group differences for ImCoh remained similar both in terms of statistical significance as well as effect size. We found increased seed-based FC for GGE patients from the thalamus to the precuneus cortex region in fMRI, and in the theta band of simultaneous EEG. Our findings suggest that the analysis of EEG functional connectivity based on ImCoh is suitable for MR-EEG, and that relative group difference in a comparison of patients with GGE against controls are preserved. Spatial correspondence of seed-based FC group differences between the two modalities was found for the thalamus.

Keywords Hd-EEG · fMRI · Resting-state · Genetic generalized epilepsy · Brain network connectivity · Thalamus

Abbreviations

ASM	Antiseizure medication
BCG	Ballistocardiogram
BEM	Boundary element model
DMN	Default mode network
ECG	Electrocardiogram
FC	Functional connectivity
fMRI	Functional magnetic resonance imaging
GA	Gradient artifact
GGE	Genetic generalized epilepsy
GSWD	Generalized spike-wave discharges
HC	Healthy controls
hd-EEG	High density electroencephalography
ICA	Independent component analysis
ICC	Intracalcarine cortex
ImCoh	Imaginary part of coherency
MNI	Montreal Neurological Institute
MR(I)	Magnetic resonance (imaging)
OBS	Optimal basis set
ROI	Region of interest
PALM	Permutation Analysis of Linear Models
PCC	Precuneus cortex
rsFC	Resting-state functional connectivity

Handling Editor: Christian-G. Bénar.

✉ Daniel van de Velden
daniel.velden@med.uni-goettingen.de

✉ Niels K. Focke
niels.focke@med.uni-goettingen.de

[1] Clinic for Neurology, University Medical Center Göttingen, 37075 Göttingen, Germany

[2] Department of Neurology and Epileptology, Hertie Institute of Clinical Brain Research, University Medical Center Tübingen, University of Tübingen, 72076 Tübingen, Germany

[3] Clinic for Neurology, University Medical Center Essen/University Duisburg-Essen, 45147 Essen, Germany

sbFC Seed-based functional connectivity
SUMA Surface-based mapping, part of toolbox "Analysis of Functional NeuroImages

Introduction

Electroencephalography (EEG) and functional magnetic resonance imaging (fMRI) are typical modalities for imaging the human brain and its network functions. Both methods can be used either individually or combined as parallel EEG-fMRI and are of particular importance for the investigation of epilepsy and seizures. Approximately 50 million people worldwide suffer from epilepsy, and 15–30% of all diagnosed epilepsy cases are classified as genetic generalized epilepsy (GGE) (Beghi et al. 2019; Jallon and Latour 2005). GGE is regarded as a genetically caused epilepsy syndrome involving distributed bilateral networks. One approach to reaching a better and more detailed understanding of the pathophysiology in patients with GGE is the investigation of alterations in their brain networks with neuroimaging techniques.

There are two commonly used approaches in studying GGE cohorts: (i) analysis of task-based data, usually focusing on the occurrence of (generalized) spike wave discharges (GSWD) in epilepsy patients, (ii) and the analysis of resting-state.

In the first type of studies, EEG is used primarily to define the occurrence of GSWD, and their coupled perfusion changes appearing in fMRI are then analyzed. This approach allows one to assess the potential generators of GSWD, i.e. EEG patterns that are typical for generalized epilepsies in the interictal state. Multiple studies using EEG to define the timing of GSWD found a deactivation of the DMN regions in patients with GGE, with an activation in the thalamus (Aghakhani et al. 2004; Benuzzi et al. 2012; Gotman et al. 2005; Hamandi et al. 2006; Szaflarski et al. 2013). Those event-based studies focused on determining the development of the epileptic activity and the participating brain regions. Klamer et al. analyzed the BOLD time courses in patients with GGE in a time span before and after GSWD and found a similar deactivation of the DMN and activation of the thalamus region during the GSWD. They further applied dynamic causal modelling to calculate directed/effective connectivity results. They were able to show that two regions of the DMN, i.e. the precuneus cortex (PCC) and medial prefrontal cortex are key regions behind these connectivity changes (Klamer et al. 2018). Another study found a core network structure, consisting of the thalamus, and parietal cortex, among others in children with absence seizures that is involved in the GSWD activity (Carney et al. 2012, 2010; Masterton et al. 2012). A recent study provided evidence that there is a spatially specific power change and a change in FC between brain regions before GSWD (Tangwiriyasakul et al. 2018).

The other common approach is to study the functional brain state at rest, i.e. without external stimulus and (often) without knowledge of the occurrence of GSWD. Such studies allow insights into the default state of the brain since, in most patients, GSWD are relatively rare und brief events. Hence, functional connectivity (FC) analysis on resting-state data of patients with GGE allows to study persistent brain network alterations within the default mode and other networks. From such analyses, frontal and parietal brain regions were found to have a significant decrease in seed-based FC in patients with GGE.

McGill et al. found decreased seed-based FC from PCC and medial prefrontal cortex to the prefrontal region in patients with GGE (McGill et al. 2012). In another study, seed-based FC was applied on resting-state fMRI and showed a significant increase in FC in posterior DMN regions for the thalamus seed (Ji et al. 2015).

In contrast to fMRI, which typically probes vascular changes, EEG and/or MEG can investigate the neuronal signal directly. Similar to fMRI studies, early EEG/MEG studies focused on the analysis of the GSWD to localize the origin and characterize these GSWD (Holmes et al. 2004; Westmijse et al. 2009Miao et al. 2014).

Recently, increases in resting-state MEG and EEG source-level connectivity and power were found in patients with GGE compared to healthy controls (HC). FC was mainly increased in frontal, central, and inferior parietal regions of the brain, whereas power was increased in central, temporo-parietal regions and subcortical structures (Elshahabi et al. 2015; Li Hegner et al. 2018). In a further study, hd-EEG (high-density EEG) and MEG were used to analyze differences between patients with GGE and healthy controls and confirmed previously found regions with increased FC (Stier et al. 2021). Using hd-EEG, the largest FC increases were found in the theta frequency band in frontotemporal and central regions (Stier et al. 2022).

Currently, it is not established if EEG metrics based on inside MR-scanner EEG, such as power or functional connectivity, can be used for group differences at source-level. One limiting factor is the presence of strong artifacts contaminating the EEG measurements. At first, the rapid changes of the MR scanner gradients and the currents/potentials induced by them are by orders of magnitude stronger than the brain's voltage fields and completely dominate the EEG signal (Hoffmann et al. 2000; Anami et al. 2003; Garreffa et al. 2003). Secondly, the ballistocardiogram (BCG), which is generated by pulse-related movement of the EEG electrodes and cables in the strong magnetic field in the MR scanner, is also a source of strong artifact in within scanner EEG (Allen et al. 1998). Different tools were developed to remove the gradient artifact (GA) and BCG artifacts from

the EEG sensor data. A common approach is average artifact subtraction followed by removal of the residuals and BCG artifacts using an optimal basis set algorithm (OBS) (Niazy et al. 2005). The aim of correcting BCG artifacts led to several studies that improved our understanding of the origin and properties of BCGs and their influence on EEG data in parallel fMRI recordings (Debener et al. 2008; Mantini et al. 2007; Masterton et al. 2007; Mullinger et al. 2008; Vasios et al. 2006). Furthermore, it is known from the literature that beamformer source reconstruction methods are able to attenuate BCG artifacts in EEG-fMRI data (Brookes et al. 2008; Uji et al. 2021). A previous study on focal epilepsy patients showed that simultaneous electrical source imaging and fMRI analysis to be a robust approach of combining both modalities (Vulliemoz et al. 2009).

It is not established whether metrics such as power and FC at the source level of resting-state EEG in a parallel measurement of MRI are useful to detect known group differences in patients with GGE. Hence, one goal of this study was to clarify if simultaneous hd-EEG can still be used for source-reconstructed power and connectivity analysis for patients with GGE and if, despite the extensive data cleaning, the results are comparable to outside-MR scanner EEG. Therefore, we did an hd-EEG source-level connectivity and power analysis in patients with GGE versus healthy controls measured both inside (with parallel fMRI) as well as outside the MR scanner. We hypothesize that it is possible to reproduce the previously reported group difference of increased connectivity and power in patients with GGE observed in our previous works in the same cohort from EEG data measured with a parallel fMRI (Stier et al. 2021, 2022). In addition, we wanted to investigate whether seed-based multimodal connectivity analysis is suitable for simultaneous EEG and fMRI.

Methods

Participants

This study used the same subjects were used as in our previous work on outside-MR EEG (Stier et al. 2022), which included 28 patients diagnosed with GGE based on the International League Against Epilepsy classification (Scheffer et al. 2017). Furthermore, 50 healthy controls (HC) were recruited. HC had never experienced any seizures, were free of any neurological and psychiatric diseases, and were not taking any medication. Of these, a total of 15 patients with GGE and 16 HC had simultaneous hd-EEG-fMRI and outside-MR scanner hd-EEG available and were included in the present study (Table 1). Four of the 15 patients were diagnosed with juvenile absence epilepsy, three patients with childhood absence epilepsy, two patients with juvenile myoclonic epilepsy, three patients with isolated generalized tonic–clonic seizures, and three patients with GGE that could not be further classified. Except for one patient, all other patients were on antiseizure medication (ASM; mean number of drugs: 1.26, range: 0–2).

Table 1 Study population

	Patients with GGE	Healthy controls
Total (N)	15	16
Female n (%)	9 (60%)	7 (43.75%)
Age range	19–50	19–57
Mean (m)	32.5	31.77
Standard deviation (sd)	10.6	12.0

The measurements took place at the Universitätsklinikum in Tübingen. The local Ethics Committee of the Medical Faculty of the University of Tübingen gave approval for this study (ethical reference number: 646/2011BO1). The study was performed in concordance with the principles of the Declaration of Helsinki. All subjects gave informed consent before study participation.

EEG and fMRI Data Acquisition

Hd-EEG acquisition was done using a 256-channel EEG system (Electrical Geodesics, Inc., Eugene, OR, USA) with a sampling rate of 1 kHz. The measurement was performed twice: first, outside the MR scanner room in supine position with eyes closed for 30 min ('outside') in a magnetically shielded room distant to the MR-scanner room. A second measurement was performed as a simultaneous hd-EEG-fMRI data acquisition within a 3 T scanner. Ten datasets were acquired using a Siemens MAGNETOM Trio, and 21 measurements were performed using a Siemens Prisma (Siemens AG, Erlangen, Germany). The measurement time varied across subjects; we acquired 10 min of data for five subjects, 15 min of data for 22 subjects, and four subjects were measured for 30 min. Also, a 3D T1-weighted 3D-MPRAGE sequence was acquired as high-resolution anatomical reference (TR: 2.3 s, TE: 3.03 ms, flip angle = 8°, voxel size: $1 \times 1 \times 1$ mm). All functional MR data was acquired with a gradient-echo planar T2*-weighted sequence covering the entire brain (TR: 2 s, TE: 31 ms, voxel size: $3 \times 3 \times 4.2$ mm, anterior–posterior (AP) phase encoding). To correct the functional MR images for distortions we also acquired 15 volumes with reversed phase-encoding (posterior–anterior) for each subject.

Hd-EEG Processing

All preprocessing and further analysis steps on hd-EEG data were performed using Fieldtrip (https://www.fieldtript

oolbox.org/, version 20191127) running in Matlab (version 9.5.0.1298439 (R2018b) Update 7, Mathworks Inc.). The resting-state outside scanner hd-EEG data was filtered with a Butterworth band-pass filter with 1 Hz high pass and 70 Hz low pass. Also, a 50 Hz band stop filter was applied to account for line noise as well as its 100 Hz and 150 Hz harmonics. After that the data was downsampled to 250 Hz. We divided the continuous data in trials of 2-s lengths each. The data was visually inspected and noisy trials and/or trials artifacts contaminated by eye movements, blinks, cardiac, and muscle activity were rejected. Afterwards, we performed an independent component analysis to identify and remove components evincing electrocardiogram and blink/eye movement artifacts. In the patient group, any trial showing GSWD were manually marked by an experienced clinician and also removed together with the trials immediately before and after the GSWD trial.

The inside-MR scanner hd-EEG data was superimposed with the gradient artifact (GA) as well as the ballistocardiogram artifact. To remove those artifacts, we used algorithms implemented in the manufacturer's software (Geodesic EGI tools, version: 5.4.2 (r29917)). In order to remove the GA, an average artifact subtraction method was applied. This method constructs an average GA template in each EEG channel and subtracts this template at the TR-trigger events from the raw EEG signal. The algorithm from Niazy et al. was used to detect and reject the BCG artifacts (Niazy et al. 2005). This algorithm applies a principal component analysis on the EEG sensor data time-locked to the detected cardiac events in the data. Principal components describing the BCG artifacts were chosen based on their amount of explained variance. This leads to the construction of an optimal basis set of the BCG artifact. Such OBS were used for adaptive artifact removal (Niazy et al. 2005). Further EEG data processing was performed in MATLAB identical to the outside-MRI EEG data, except for the separation of the continuous resting-state hd-EEG data in trials. Trials (2 s each) were synchronized by the MR-scanners TR trigger event, in order to achieve full correspondence between fMRI volumes and EEG trials.

Forward Modelling and Source Analysis

For each subject, an individual cortical surface based on their anatomical MR image was reconstructed using FreeSurfer (https://surfer.nmr.mgh.harvard.edu, version 6.0.0) and subjected to SUMA (https://afni.nimh.nih.gov). The SUMA toolbox reduced the cortical surface of each subject to a fixed number of vertices (ld: 10, resulting in 2004 cortical vertices) based on the 'fsaverage' template (FreeSurfer). Furthermore, six subcortical nuclei (bilateral amygdala, hippocampus, thalamus, caudate, putamen and pallidum) were surface reconstructed using a total of 334 vertices from the fsaverage template. Those standardized subcortical vertices are transformed back to the individual anatomical space by using the inverted DARTEL transformation (DARTEL; SPM12; https://www.fil.ion.ucl.ac.uk/spm/software/spm12). This led to a total of 2338 vertices for each subject, with each vertex characterized to resemble a point-for-point anatomical correspondence for cortical and subcortical regions across all subjects. In the last step, each subject's individual surface map was aligned to the CTF sensor space with the anatomical landmarks of fiducial positions (left/right preauricular point, nasion). For the subsequent source reconstruction, an individual boundary element model (BEM) with three layers of different conductivity (scalp: 0.33 *S/m*, skull: 0.004 *S/m*, brain: 0.33 *S/m*) was constructed using the 'dipoli' method implemented in Fieldtrip. The sensor time series were separated into common EEG frequency bands, namely delta 0–4 Hz (δ), theta 4–8 Hz (θ), alpha 8–12 Hz (α), beta1 12–20 Hz (β1), beta2 21–29 Hz (β2) and gamma 32–48 Hz (γ). Next, source projection was performed using dynamic imaging of coherent sources (DICS), a beamformer method, with λ regularization of 5% for each frequency band separately (Gross et al. 2001). This approach was shown to be able to attenuate residual gradient and BCG artifacts that remained after averaged artifact subtraction methods (Brookes et al. 2008; Uji et al. 2021). The DICS method calculated a set of adaptive spatial filters, and the sensor level time courses were reconstructed in each vertex for each frequency band. Power estimation was calculated at each source vertex and for each frequency band. The source reconstruction was done separately for both conditions (inside and outside MR). For each subject, we randomly chose 200 wake-only trials, i.e. 400 s of data, to make all analyses comparable and to account for differences in the length of the measurement.

EEG Functional Connectivity

For the electrophysiological data, FC analysis was performed by calculating the imaginary part of coherency (ImCoh) among all source-space time series and was calculated as noted below (Nolte et al. 2004):

$$Coherency_{xy}(f) = \frac{S_{xy}(f)}{\sqrt{S_{xx}(f) \cdot S_{yy}(f)}} \quad (1)$$

$$ImCoh_{xy}(f) = Imag\left\{Coherency_{xy}(f)\right\} \quad (2)$$

where $S_{xy}(f)$ is the cross spectral density of the time series x and y at the frequency f. Further $S_{xx}(f)$ and $S_{yy}(f)$ are the power spectral densities of time series x and y. We took the absolute imaginary part of coherency $\left|ImCoh_{xy}(f)\right|$ as a measure for FC for each vertex. For each vertex in source space,

we averaged all links (i.e. connectivity to all other vertices) as vertex-based connectivity (in the terminology of graph theory also called node strength). In addition, we calculated the global ImCoh as well as the global power values by averaging the vertex-based values for each subject in both inside-scanner as well as outside-scanner condition. We further calculated the relative difference (Δ%) of global power/FC group between the inside- and outside-MR scanner condition's group average in GGE and HC.

fMRI Data Preprocessing

First, a correction of the data for slice-timing differences (SPM12, version 7487) was performed, followed by a head movement estimation using the Linear Image Registration Tool (FSL version 6.0.3, MCFLIRT) (Jenkinson 2002) as well as a distortion correction using the reversed phase-encoded scan (FSL, topup) (Andersson et al. 2003). The further processing steps were then performed using the CONN toolbox (http://www.nitrc.org/projects/conn, RRID:SCR_009550) (Whitfield-Gabrieli and Nieto-Castanon 2012). Outlier identification was done with the Artifact Detection Tools (ART) implemented in CONN and was set to 'conservative' settings. Thus, scans were marked as outliers if the observed global BOLD signal change was > 3 standard deviations and/or the amount of head movement was greater than 0.5 mm. In addition, in patients with GSWD, the corresponding fMRI volume and the following nine volumes (= 18 s) were marked as outliers in the fMRI data. A spatial co-registration of the averaged functional MR dataset to the anatomical T1 reference of each subject was performed. The anatomical T1 was segmented into tissue classes using the unified segmentation in SPM12 resulting in six tissue classes (grey-matter, white-matter, skull, scalp, cerebrospinal fluid and others) and a non-linear transformation of each individual T1 scan to the MNI152 T1 reference. This transformation matrix was used to spatially normalize all fMRI volumes and the segmentation masks to the MNI152 space. The grey matter class was further parcellated into different atlas regions according to the Harvard–Oxford Cortical Atlas, and network regions were created by grouping atlas nodes. The fMRI data was further smoothed using a Gaussian kernel of 8 mm full-width at half maximum. To further control for spurious effects of head motion, and cardiac and respiratory rhythms, each subject's data was corrected by partial regression in CONN removing the following confounds: six motion parameters (three rotation and three translation parameters, based on the MCFLIRT rigid body transformation), subject-specific confounding factors that modeled nuisance signals within the white matter and CSF segmentation masks, each with three PCA parameters that were used as temporal covariates. No global signal regression was applied, to avoid the introduction of spurious connectivity (Murphy et al. 2009; Weissenbacher et al. 2009). Finally, the BOLD time series was band-pass filtered with 0.008–0.09 Hz.

Seed-Based Functional Connectivity Analysis of EEG and fMRI

A seed-based functional connectivity (sbFC) analysis was performed in both modalities, choosing seed-regions from the grey matter parcelling based on the atlases included in the CONN-toolbox. Seed regions were chosen based on a priori information from previous studies that reported differences in GGE versus HC comparisons. Namely, one network seed at the medial prefrontal cortex, the left and right lateral–parietal default mode network (DMN-LP L/R), and an atlas seed at the precuneus cortex (PCC) (Luo et al. 2011; McGill et al. 2012). Also the intracalcarine cortex (left and right) was used as an atlas seed in both hemispheres, since they are located close to the PCC region and are also associated with the default mode network. Lastly, the left and right thalamus atlas regions were added to the list of seeds of interest, given their known involvement in GSWD-associated as well as resting-state network changes in GGE (Gotman et al. 2005; Hamandi et al. 2006; Ji et al. 2015; McGill et al. 2014; Wang et al. 2011). Seed-based FC (Pearson correlation) in fMRI was performed in MNI voxel space between each seed region and every other voxel in the brain, defined using the default standard 'brainmask' in CONN, which includes both cortical and subcortical voxels. Additionally, the subject-specific seed-based functional connectivity maps were transformed and resampled from 3D MNI space to the surface vertices (SUMA and subcortical surface) to allow direct spatial comparison to the hd-EEG sbFC maps.

Similar to fMRI, a seed-based FC in hd-EEG was calculated using the imaginary part of coherency (Nolte et al. 2004). To this end, all surface vertices were labeled according to the CONN atlas via the individual spatial transformation matrix generated by SPM. We grouped vertices with identical region labels and chose the same regions as seeds as we did for the fMRI seed-based analysis to calculate sbFC on EEG data for each subject.

Permutation Analysis of Linear Models

The non-parametric statistics toolbox 'Permutation Analysis of Linear Models' (PALM) was used to calculate group differences between patients with GGE and healthy controls for power and FC in the EEG as well as seed-based FC in both modalities (https://fsl.fmrib.ox.ac.uk/fsl/fslwiki/PALM, version: alpha103) (Winkler et al. 2014).

Briefly, using PALM, general linear models were run for each vertex and one at the global level, with additional

covariates of subject age and gender. A comparison was made using a one-tailed t-contrast for the groups on a vertex-, and voxel-level, as well as at the global level, separately for each frequency band. This was determined based on the results of our previous studies (Stier et al. 2022). The resulting p-values were generated based on an estimate of the empirical distribution of t-statistics under the null hypothesis by 20,000 random permutations of the subjects. In the vertex-, and voxel-based analysis, we corrected for multiple comparisons at the cluster level using a threshold-free cluster enhancement with default parameters set by PALM (height = 2, and extend = 1) (Smith and Nichols 2009). In order to evaluate the hypothesis that the same pattern can be found for inside-MR scanner EEG data, we performed the same comparison (GGE versus healthy controls) for both conditions (outside MR, inside MR). Furthermore, we tested the differences in global power and FC depending on the measurement condition, and an interaction with the group assignment (patients with GGE and controls) using a 2-way ANOVA (2-groups, and 2-levels per subject) in PALM and applied false discovery rate (FDR) (Benjamini and Hochberg 1995) correction across frequency bands. We also applied FDR correction for the $-log_{10}$ p-values from the group differences in global power and functional connectivity across frequency bands. We also reported both uncorrected values and $-log_{10}$ p-values that survived FDR correction. Statistically significant group differences on fMRI seed-based FC were derived from the sbFC maps in 3D MNI space, as well as from the sbFC resampled on the surface vertices of each subject. Statistical comparisons were carried out with 20,000 random permutations. For each permutation, a general linear model was estimated including sex and age (and for fMRI data, the number of scan volumes) as covariates of no interest. To correct for multiple comparisons across space, familywise error correction (FWE) was applied to p values of all vertex- and voxel-based tests, represented as $-log_{10}$ p. Statistical significance level was defined for values > 1.3 (corresponding to $p < 0.05$ [corrected]). Additionally, effect sizes (Cohen's d) was calculated for each statistical test, defining effect sizes of $d = 0.2$ as small, $d = 0.5$ medium and $d = 0.8$ as a large effect size (Cohen 1992). In order to quantify the spatial similarity between EEG group difference maps ($-log_{10}$ p-value maps without a threshold) of inside and outside MR-scanner for vertex-based power and functional connectivity we calculated Pearson correlation with corresponding p-values, which were FDR corrected across frequency bands.

Cross-Modal Spatial Relation

We compared the group differences (GGE > HC) for each seed-based functional connectivity map from fMRI data. Only seeds that showed a suprathreshold group difference ($p_{FWE} < 0.05$) were considered further for cross-modal spatial correlation analysis. In addition, we only considered EEG frequency bands that showed a statistical significant group difference ($p_{FWE} < 0.05$) in vertex-based functional connectivity for further analysis.

Pearson correlation coefficients were used to estimate the spatial concordance between EEG and fMRI group difference maps. To control for chance findings, we generated surrogate datasets by shuffling the EEG sensors of inside-MR hd-EEG data of each subject. This was done 50 times yielding 50 different surrogate datasets for each subject. Identical to the analysis of the real data, the surrogate datasets underwent source analysis and the results were used to calculate a seed-based FC map for each statistically significant fMRI seed-based FC analyses in each in frequency band that showed statistical significance in the group comparisons of vertex-based FC. After that, a group comparison was calculated via PALM. This was done for 500 surrogate permutations; in each permutation, surrogate data was chosen randomly for every subject from the 50 available surrogate datasets. This resulted in 500 FWE-corrected $-log_{10}$ p-value maps for each frequency band that showed statistical significance in the group comparisons of vertex-based FC and each statistically significant fMRI seed-based FC analyses. The cross-modal correlation to the fMRI $-log_{10}$ p-value map was then also performed for all $-log_{10}$ p-value maps based on surrogate datasets. Only cross-modal correlation values of the real data that surpassed the 95th percentile of the surrogate data were considered significant. The resulting p-values were multiple comparison corrected using false discovery rate (Benjamini and Hochberg 1995).

Results

A statistical group comparison of HC and patients with GGE showed no significant differences for age or sex between the groups (age: $p = 0.456$ [t-test]; sex: $p = 0.37$ [χ^2 test]). On average 31% of the trials (133 ± 48) for the inside MR-scanner condition and 29% (283 ± 138) for the outside MR-scanner condition we rejected due to artifacts in the data. In total five trials with GSWD were identified and rejected in four different patients in the inside MR-scanner condition. For the outside MR-scanner condition five trials with GSWDs in five different patient) were marked and also rejected.

Global Power

For global power, significant group differences (GGE > HC) were found in each frequency band for the outside-MR scanner condition ($-log_{10}$ $p > 1.3$), as expected from previous work. For the inside-MR condition, an overall increase of global power was observed for both groups (HC and

GGE) in all frequency bands. The relative differences (Δ%) between the group means from outside to inside condition were increased in both groups and all frequency bands (Δ%(delta) = HC: 40%, GGE: 28%; Δ%(theta) = HC: 49%, GGE: 32%; Δ%(alpha) = HC: 37%, GGE: 24%; Δ%(beta1) = HC: 55%, GGE: 32%, Δ%(beta2) = HC: 49%, GGE: 34%; and Δ%(gamma) = HC: 80%, GGE: 53%) (Appendix: Table 3). The difference of global power between conditions (inside > outside) was highly significant ($p_{FDR} \leq 0.001$, $d > 1.2$) in all frequency bands. However, the interaction of inside–outside condition and group difference was not significant after error correction ($p_{FDR} > 0.05$, $d < 0.25$) (Appendix: Table 2). The group differences between HC and GGE were not statistically significant in any frequency band for the inside-MR condition (Fig. 1). Equally, the effect sizes were smaller in the inside- (d: 0.13–0.43) compared with the outside- (d: 0.75–0.96) MR condition.

Global Functional Connectivity

The change in the group means for FC varied across frequencies, and no common pattern was evident. The relative difference (Δ%) between the GGE and HC group means of global FC was different in all frequency bands from outside to inside condition (Δ%(delta) = HC: 25%, GGE: 18%; Δ%(theta) = HC: 18%, GGE: 22%; Δ%(alpha) = HC: − 8%, GGE: 1%; Δ%(beta1) = HC: 7%, GGE: 13%, Δ%(beta2) = HC: 6%, GGE: 17%; and Δ%(gamma) = HC: − 1%, GGE: 10%) (Appendix: Table 4). The difference of global FC between conditions (inside > outside) was highly significant for two frequency bands (delta: $p_{FDR} < 0.001$, $d \approx 1.0$; theta: $p_{FDR} < 0.01$, $d \approx 0.73$). No significant interaction effect was observed ($p_{FDR} > 0.05$, $d < 0.05$) (Appendix: Table 2). Statistically significant group differences (GGE > HC) were only found in theta for both conditions (outside-MR condition $-log_{10}\, p = 1.56$; inside-MR scanner condition $-log_{10}\, p = 1.56$). For both conditions, a medium to large effect size (outside: $d = 0.734$; inside $d = 0.827$) was found in theta. As opposed to power, we even found an increase in $-log_{10}\, p$-values and statistical effect sizes (d) from outside- to inside-MR scanner group differences in all frequency bands, except for the delta band (Fig. 2).

Vertex-Based Analysis of Power

The statistical group analysis of vertex-based power in the outside-MR scanner condition showed a widespread significant increase for patients with GGE in all frequency bands ($-log_{10}\, p > 2$) (Fig. 3A). An occipital/precuneus and lateral–parietal focus of power increase in patients with GGE was found in all frequency bands with the highest significance in the delta and gamma bands ($-log_{10}\, p > 3$). In addition, the medial frontal regions showed greater power in patients with GGE in all frequency bands, except beta2.

The topographies of the significant increase of power in patients with GGE in each frequency band are similar to the

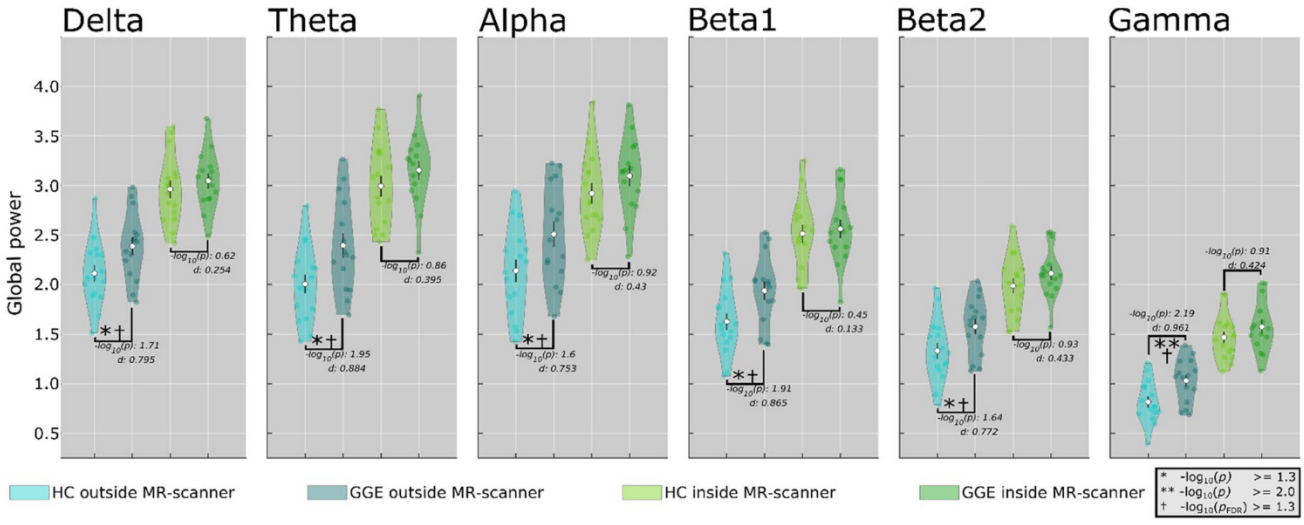

Fig. 1 Global power depicts in violin plots. Distribution of global power for patients with GGE and HC in the inside- (green colors) and outside-MR scanner condition (blue colors) for each frequency band. Violin plots show subject-specific data points, the density of the group data, group means, and standard error of the means for global power in each frequency band. Asterisks mark statistically significant differences between groups (GGE > HC) (*$-log_{10}\, p >= 1.3$), and † mark statistically significant differences that survived FDR correction (*$-log_{10}\, p_{FDR} >= 1.3$). Note that significant group differences and large effect sizes were found for all frequency bands for the outside condition only (GGE > HC), and all survived multiple comparison correction via FDR. The significant group differences and effect sizes for the inside condition are smaller compared with the outside condition in all frequency bands

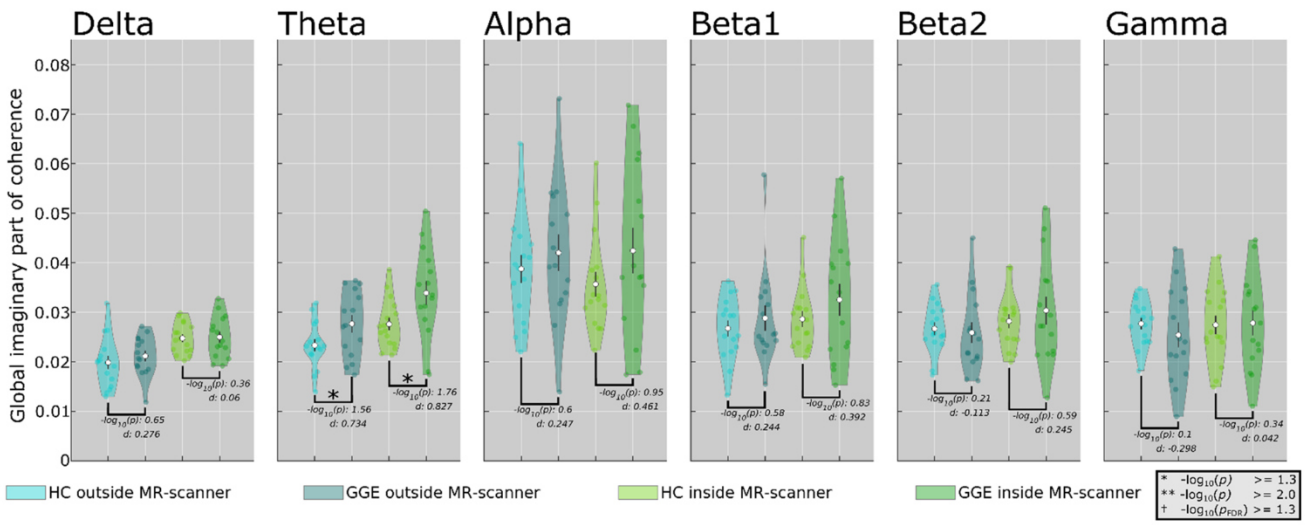

Fig. 2 Global imaginary part of coherency depicted in violin plots. Distribution of global functional connectivity (ImCoh) for patients with GGE and HC in the inside- (green colors) and outside-MR scanner condition (blue colors) for each frequency band. Violin plots show subject-specific data points, the density of the group data, group means, and standard error of mean for global connectivity in each frequency band. Asterisks mark statistically significant differences between groups (GGE > HC) (*$-log_{10}\, p >= 1.3$). Note that significant group differences ($-log_{10}\, p$) were found for the theta (*$-log_{10}\, p > 1.3$) band only (GGE > HC) for both conditions. However, this difference would not surpass FDR correction for multiple comparisons. The effect size values for the inside condition were higher compared with the outside condition in all frequency bands, but delta

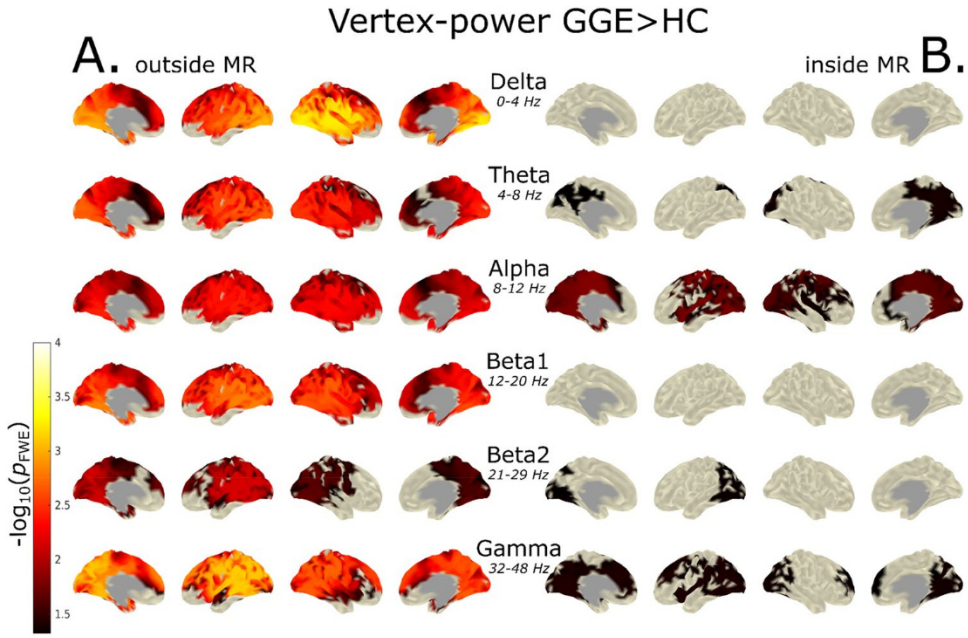

Fig. 3 Vertex-power group analysis (GGE > HC) of inside- and outside-MR scanner conditions. Group contrast between patients with GGE and heathy controls (GGE > HC) of vertex-based power in each frequency band calculated using PALM. In row **A** the statistical contrast of the outside-MR data based on vertex power is shown and row **B** illustrates the inside-MR scanner condition. Note that the $-log_{10}\, p$-values in the inside-scanner condition were smaller than in the outside condition but they still surpassed the statistical significance threshold of $-log_{10}\, p > 1.3$ and attained significance in fewer but identical regions. Note that the $-log_{10}\, p$-values in the inside scanner condition are smaller in comparison to the outside condition, but show high spatial similarity ($r > 0.85$, $p_{FDR} < 0.001$) between measurement conditions

results of our previous work. A decrease in $-log_{10}\ p$ values was evident in all frequency bands.

Contrary to this, we found a strong reduction in the group differences (GGE > HC) for the inside-scanner condition ($-log_{10}\ p \approx 1.3–2.0$) in all frequency bands (Fig. 3B). After correction for multiple comparisons the group differences in the delta and beta1 frequency bands did not surpass the significance threshold. The greatest group difference was found in the alpha band ($-log_{10}\ p \approx 2$), while the other frequency bands showed smaller, but statistically significant group differences ($-log_{10}\ p \approx 1.3–1.5$). An occipital/precuneus and lateral–parietal focus of power increase in patients with GGE was found in most frequency bands.

Although both significance, as well as effect size decreased for the inside condition and reached significance in fewer but identical regions, the increased power in patients with GGE in the posterior regions of the brain was consistent. Further, the group difference maps of inside and outside MR-scanner for vertex-based power showed high spatial similarity in all frequency bands ($r > 0.85$, $p_{FDR} < 0.001$).

Vertex-Based Functional Connectivity Analysis

In the outside- as well as inside-MR scanner condition, the group comparison (GGE > HC) surpass the cutoff of $-log_{10}\ p > 1.3$ after statistical correction only in the theta frequency band. Hence, to better visualize the effect of the inside-MR scanner measurement condition in all frequency bands, we compared the group differences between the conditions on the basis of effect sizes (Cohen's *d*) (Fig. 4A, B).

The group difference effect sizes (*d*) of vertex-based functional connectivity for GGE > HC in the outside condition were largest in the theta band ($d > 1$), located in the right lateral parietal cortex (DMN lateral–parietal right) region and in the PCC in both hemispheres (Fig. 4). We also found large effect sizes ($d > 1$) in the left superior temporal region. In the delta frequency band, large effect sizes ($d > 1$) were found in the fronto-parietal region, with stronger effects in the right hemisphere. In alpha and beta1 medium to large effect sizes (d: 0.75 to > 1) were found in the medial prefrontal cortex region. A similar distribution was detected in beta2, but with medium effect sizes ($d \approx 0.5$), which were smaller for gamma ($d \approx 0.35$). The topography of the effect size is similar to the results of our previous work of the same cohort with corresponding group differences in delta, theta and alpha.

For the inside-MR condition, we found the largest effect sizes in the theta band ($d > 1$) with a focus on the PCC region, and the same effect size pattern ($d \approx 0.8–1.0$) in the left region of the hemisphere. In beta1 medium effect sizes ($d \approx 0.3–0.4$) with an effect size cluster at the right lateral–parietal region with large effect sizes ($d \approx 0.85–1.0$) were found. In beta2 a similar distribution was found, but with considerably smaller effect sizes than in beta1 ($d \approx 0.4–0.55$), and even smaller in gamma ($d \approx 0.3–0.4$).

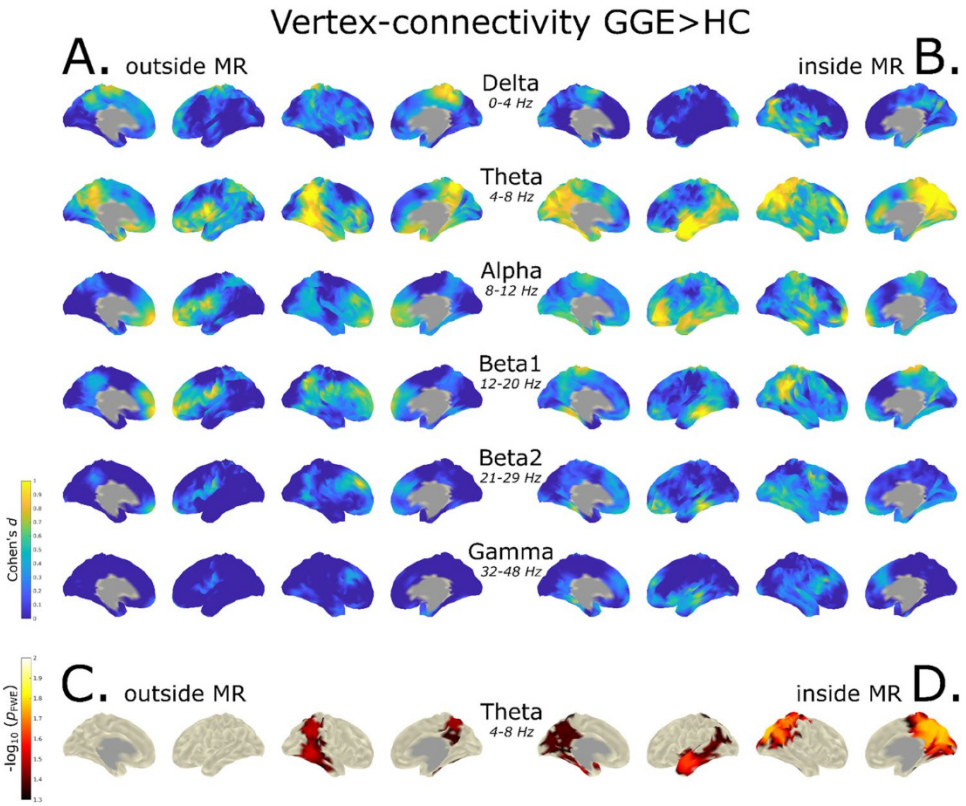

Fig. 4 Vertex-connectivity group analysis (GGE > HC) of inside- and outside-MR scanner conditions. Standardized effect sizes (Cohen's *d*) for group differences (GGE > HC) for the outside- (**A**) and inside-MR condition (**B**). In addition, the significantly different vertices ($p < 0.05$, FWE corrected) are shown for the outside- (**C**) and inside-MR condition (**D**). Note that the strongest effects were found in the theta band, and the group differences were only significant in this frequency band after FWE-correction. Interestingly the significance was higher ($-log_{10}\ p \approx 1.8$) and the effect size stronger ($d > 1$) for the inside-MR scanner condition. High spatial similarity was found for the statistical group difference $-log_{10}$ *p*-value maps for theta ($r = 0.55$, $p_{FDR} < 0.001$)

Across conditions, we found the largest effect sizes ($d > 0.95$) and coherent distributions in the PCC region in the theta band. Effect sizes showed an increase and a wider spatial extension compared with the outside-scanner results. In addition, the right lateral parietal region had large effect sizes in both conditions. However, in the inside-MR scanner condition the focus was found to be more posterior and superior. The large fronto-temporal cluster seen on the effect size maps of the left hemisphere for the outside-MR scanner condition was only located in the left temporal lobe in the inside-MR scanner results. Between conditions a minor increase in effect sizes was visible in all frequency bands, except for delta.

Statistical significance was only found in the theta band after FWE-correction in both conditions with greater group differences for GGE > HC (Fig. 4C, D). Inside and outside MR $-log_{10}\,p$ maps showed relevant spatial similarity ($r = 0.55$, $p < 0.001$) between both conditions in the theta band, but no relevant spatial similarity was observed in the other frequency bands.

For the outside-MR scanner condition statistically significant FC increases were found in patients with GGE in the right lateral–parietal to temporal cortex ($-log_{10}\,p \approx 1.5$–1.6) and the right PCC region ($-log_{10}\,p \approx 1.55$) (Fig. 4C). The inside-MR scanner condition showed FC increases in patients with GGE in the left temporal lobe ($-log_{10}\,p \approx 1.6$) and PCC region in both hemispheres (left: $-log_{10}\,p > 1.4$; right: $-log_{10}\,p > 1.75$) and (Fig. 4D).

fMRI Seed-Based Functional Connectivity

We found a statistically significant increased sbFC in patients with GGE for the thalamus seed regions and posterior cingulate/precuneus areas, both for a voxel as well as surface-based approach (Fig. 5). This group difference was slightly stronger for the left thalamus seed region but both seeds surpassed the FWE-corrected cutoff of $-log_{10}\,p > 1.3$.

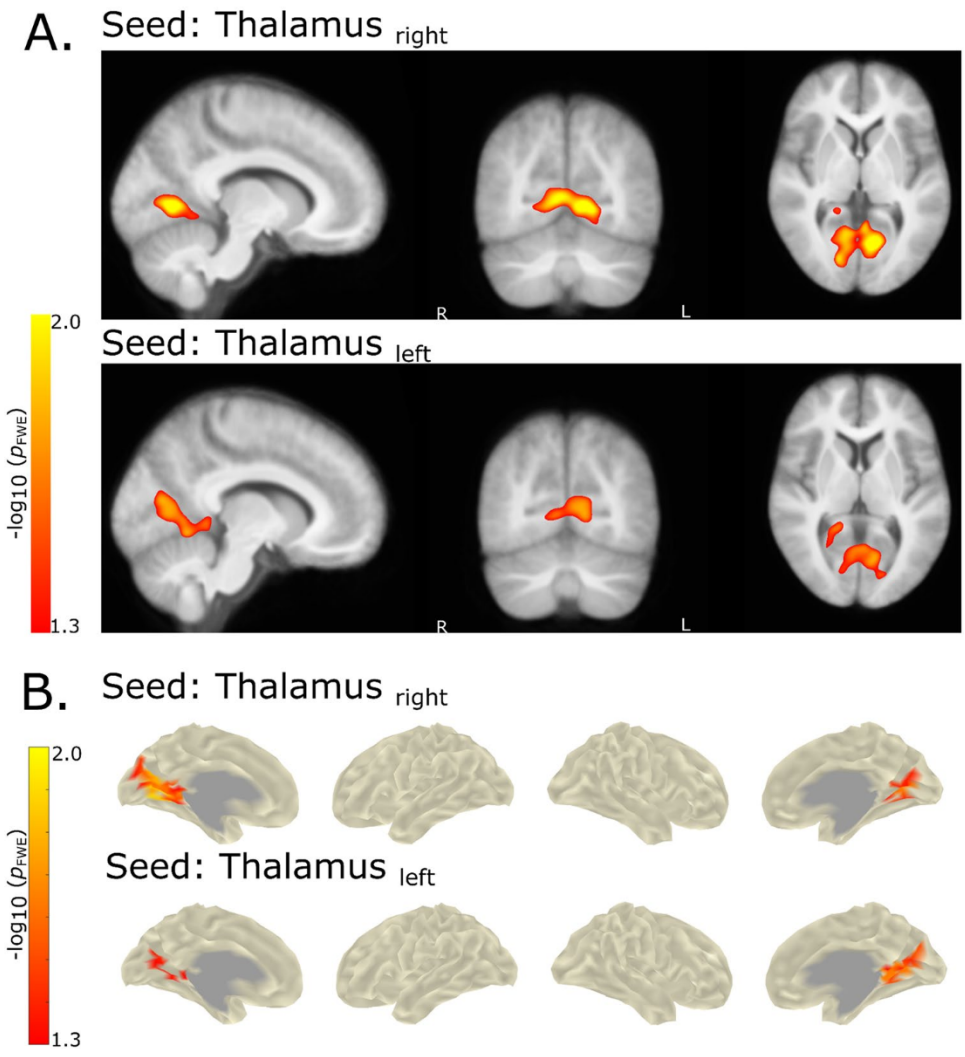

Fig. 5 Group differences (GGE > HC) of seed-based FC derived from fMRI data. Statistically significant increases of seed-based FC for GGE > HC for thalamus seed regions. **A** Based on voxel correlation maps derived from CONN and **B** derived from transformed and resampled correlation maps on surface vertices. Note that both approaches show nearly identical increases in sbFC for GGE > HC from thalamus seed regions to regions of the PCC. Moreover, no decreases, but only increases in sbFC were found in patients with GGE

No other seed regions showed a statistically significant increase or decrease in patients with GGE versus controls.

Spatial Relation of fMRI and EEG Seed-Based Functional Connectivity

Further, we aimed to link the fMRI and EEG seed-based FC group differences. Figure 6 shows the side-by-side surface plot of fMRI (based on correlation) as well as EEG seed-based FC (based on ImCoh) group differences. The topography was similar, however, the group differences were more extended for EEG. A spatial correlation was calculated between EEG and fMRI (left ≈ 0.39; right ≈ 0.4). These correlation values were significantly higher (left: $p_{FDR} = 0.024$; right: $p_{FDR} = 0.024$) than the correlation values derived from the surrogate EEG data, indicating that these correlations are stronger than what could be expected by chance.

Group differences of sbFC from the right thalamus seed region did not surpass the statistical threshold of $-log_{10}\, p > 1.3$ but showed a stronger spatial correlation across modalities than the left thalamus seed region. The topographies of increased sbFC in patients with GGE in the occipital, lateral–parietal and temporal regions resemble the increase in vertex-based FC in the theta band.

Discussion

We analyzed resting-state EEG data of patients with GGE and healthy controls under two measurement conditions: inside (with simultaneous fMRI) and outside the MR scanner. We showed that the analysis of power is strongly affected by the within-MR conditions, whereas imaginary part of coherency was less influenced. Moreover, seed-based FC analysis was suitable for simultaneous EEG-fMRI revealing a consistent multi-modal functional connectivity increase for GGE between thalamus and posterior cingulate cortex, indicating that the thalamo-cortical loops may play a role in the increased resting-state connectivity observed in GGE.

Compared to our previous work, we observed a similarly significant power increase in patients with GGE in all frequency bands in the outside-MR scanner condition. Further, we were able to reproduce the statistically significant group difference for outside-MR scanner global FC in the theta band but with slightly lower effect size and statistical significance. In addition, we found lower statistical significance at vertex-level in frequency bands delta and alpha compared with previous results. The observed lower statistical significance is likely due to a smaller number of subjects available in the present study than in the previous analysis (GGE: + 8

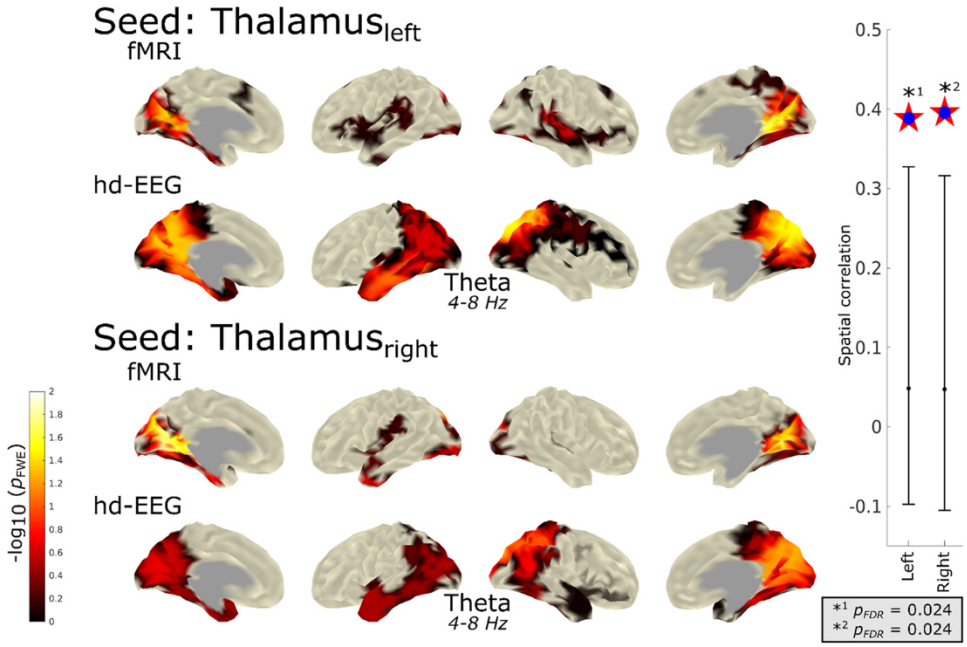

Fig. 6 Cross-modal spatial correlation of sbFC group contrasts results of GGE > HC in fMRI and EEG. This figure shows the spatial topography of seed-based functional connectivity for left and right thalamus seed regions for fMRI and EEG. On the right, the distribution of the observed spatial correlation versus the surrogate data is shown including error bars representing the 95th percentiles. It is evident that the overserved correlation between EEG and fMRI was significantly higher than surrogate data (left: $p_{FDR} = 0.024$; right: $p_{FDR} = 0.024$). Note: for better visualization of the full topography of the maps, no cutoff was used. Values below 0.05 are shown as transparent. Statistical significance of spatial correlation was assessed via the comparison to surrogate data

subjects, HC: + 16 subjects) (Stier et al. 2022). It is also likely that the altered topological representation of group differences in patients with GGE in this study is related to the cohort differences of the two analyses.

Furthermore, to allow for synchrony with the fMRI TR we used 2-s trials for both conditions. It has been shown that the length of EEG data trials is affecting the estimation of some FC metrics (Brookes et al. 2011), which may have an impact on the group-level results in this study. Yet, previous work has shown that 5–6 min of data is sufficient for a reliable analysis of FC at rest (Marquetand et al. 2019; Rolle et al. 2022). In this study, we used more than 6.5 min to compensate for the shortening of the trial duration. Besides technical reasons, it is also plausible that the different measurement environment influenced the subject's physiological state. The confined surroundings in an MR scanner with its loud noise may lead to a different mental state in the subjects.

A highly significant increased global power was observed in all groups and frequency bands for the inside-MR condition, accompanied by a reduced GGE-control group differences. However, the interaction of these two factors was not significant after error correction.

Although common GA and BCG artifact removal methods were applied, residual noise could alter the power spectral density of the sensor timeseries (Allen et al. 1998). Since the signal-interaction of different artifact sources (including subject motion) is complex, a complete artifact removal is hardly possible (Jansen et al. 2012). Therefore, it is most likely that noise residuals remain embedded in the data. The increase in signal amplitude (Allen et al. 1998) and spectral power in the artifact-corrected parallel EEG-fMRI data was observed at a similar extent in previous work (Abreu et al. 2016; Debener et al. 2007; LeVan et al. 2013; Masterton et al. 2007; McIntosh et al. 2021; van der Meer et al. 2016). Consequently, global and vertex-based results derived from EEG power for inside-MR scanner must be interpreted with caution, despite the topographic similarity of group differences (GGE > HC) at vertex-level.

Higher signal power is associated with increased phase-based FC metrics (Daffertshofer and van Wijk 2011; Moon et al. 2015). Therefore, the power increase seen at global- as well as at vertex-level could have influenced the FC calculation and have resulted in higher FC values. Even though the imaginary part of coherence is based solely on phase-shifted connectivity, it is still amplitude biased, e.g. via leakage of applied inverse methods (Sekihara et al. 2011). This fact, in combination with noisier data, might also lead to a poorer estimation of phases, and therefore lead to deviations in the topological representation of FC values in the inside-MR scanner condition. However, temporally synchronized artifacts in the data should have less effect on this metric, since the imaginary part of coherence is focused on phase-shifted connectivity (Nolte et al. 2004), which could explain why we found largely similar results for the statistically significant difference between GGE and HC in theta for the inside- and outside-MR conditions. This is supported by the finding of existing peaks in the Fourier spectrogram in the theta band for inside and outside MR-scanner data sets, as well as MR-artifact uncorrected data sets. Despite the theta frequency band spatial correlation between inside and outside MR-scanner condition was found to be rather small (see Supplementary Fig. 8). From a previous study, it is known that compared to power, ImCoh is a relatively unstable metric in repeated measurements. This means that the results for ImCoh of a measurement cannot be an exact representation of the results of a previous measurement, even for the same cohort (Marquetand et al. 2019).

Our findings for the seed-based fMRI connectivity are in line with an earlier study, that found increased FC from the thalamus to posterior cingulate cortex regions in resting-state fMRI data (Ji et al. 2015). In contrast to other studies, we did not observe decreased seed-based FC in other DMN brain regions in patients with GGE (Luo et al. 2011; McGill et al. 2012). Various factors can be responsible for the differing results, e.g. the composition of our cohort with mixed GGE syndromes, and also technical features. Other studies used different spherical seed radiuses from 6 to 10 mm (Luo et al. 2011; McGill et al. 2012) and/or 26-neighborhood voxels around the seed position (Luo et al. 2011), while we used an atlas-based definition for seed regions. Further, McGill et al. (2012) applied global signal regression on their resting-state fMRI data before doing FC analysis, as the global signal in functional MRI time courses was often considered a nuisance effect. In our analysis the global signal regression was omitted, because this step might introduce spurious connectivity into the data and there is an ongoing debate in the field if this should be included or not (Murphy et al. 2009, 2013; Weissenbacher et al. 2009; Saad et al. 2012; Murphy and Fox 2017; Liu et al. 2017; Aquino et al. 2020).

Concerning the EEG seed-based connectivity, we provided evidence of an increased connectivity between thalamus and posterior cingulate cortex region in GGE patient's theta band derived from EEG with a parallel fMRI measurement. Multiple previous studies described FC increases (review: Faiman et al. 2021), in particular in the theta band in patients with GGE using outside-MR scanner EEG/MEG data (Clemens et al. 2011; Douw et al. 2010; Elshahabi et al. 2015; Li Hegner et al. 2018; Routley et al. 2020; Stier et al. 2021, 2022). In this work, we observed a strong similarity between vertex-based sbFC and FC results in the theta band, indicating that thalamo-cortical loops may play a role in the generation of this increased FC at rest. However, for our analysis we cannot identify the underlying causes of this network alteration in GGE patients' theta band. Nevertheless, in addition to the already known involvement of the thalamus

in the development and propagation of GSWD as reported in MEG studies (Westmijse et al. 2009; Miao et al. 2014), our results indicate a stronger continuous involvement of the thalamus in resting-state/default mode brain networks in patients with GGE in the theta band. Future studies are required to investigate the thalamo-cortical connectivity in patients with GGE in more detail.

Previously, the FC increase in GGE between thalamus and posterior cingulate cortex was only shown in an fMRI study (Ji et al. 2015). Our work demonstrates that this network alteration in GGE can be extracted from both modalities. Further, the spatial cross-modal coherence of thalamocortical network alterations in GGE at rest indicates that these changes are expressed at both levels: neuronal electrical activity and vascular changes.

Limitations

Due to the small sample size and a mixed cohort of patients with GGE, we were unable to identify GGE sub-syndrome specific effects or detect their influence on the analysis. Further, although we utilized well-established techniques to remove the GA and BCG artifacts in the EEG data (Niazy et al. 2005) more elaborated methods may lead to different results. For example, artifact correction using carbon-wire loops during EEG-fMRI acquisition might have improved the artifact rejection and thus led to less noisy EEG data (van der Meer et al. 2016). In addition, other approaches of removing MR artefacts may give different results, e.g. using the online method proposed by Masterton et al. (2007). In addition, we cannot evaluate the impact of our equipment on our measurements because no alternative compatible equipment was available for direct comparison. Finally, we used measurement time for parallel EEG-fMRI of 10–30 min. Longer measurement times may lead to different and/or more stable results. However, similar fMRI studies used 6–8 min of data for their analysis (Ji et al. 2015; Luo et al. 2011; McGill et al. 2012; Wang et al. 2011), which is similar to the data amount used in this works analysis.

Conclusion

Overall, we showed that EEG resting-state network analysis is suitable for inside-MR data. After conventional EEG artifact cleaning, the power estimates inside the MR scanner were significantly increased. Nevertheless, similar spatial topography and general direction of group differences remained. Phase-lagged coherence (ImCoh) was less affected by the inside-MR condition and yielded group difference significances comparable to those of the outside-MR scenario. Moreover, with seed-based FC we found increased connectivity from the thalamus to the precuneus cortex for GGE in fMRI and EEG theta band. This indicates that both modalities probe directly related processes and networks.

Supplementary Information The online version contains supplementary material available at https://doi.org/10.1007/s10548-023-00977-6.

Author Contributions The concept and design of the study was created by NKF. Data collection was carried out by CS and RK.The analysis of the data was performed by DV.The first draft of the manuscript was written by DV. All authors revised the manuscript and all authors read and approved the final manuscript.

Funding Open Access funding enabled and organized by Projekt DEAL. Authors C.S., R.K., and N.K.F. were supported by Deutsche Forschungsgemeinschaft Grant FO 750/5-1. Authors D.v.d.V., and N.K.F. were supported by the Deutsche Forschungsgemeinschaft Grant FO 750/7-1. Author D.G. was supported by the Deutscher Akademischer Austauschdienst Funding-ID 2019/20 (57440921).

Data Availability The data that support the findings of this study are available from the corresponding author upon reasonable request.

Declarations

Conflict of Interest N.K.F. has received honoraria from Arvelle, Bial, Eisai, and EGI-Phillips, all unrelated to the current work. None of the other authors has any conflict of interest to disclose. We confirm that we have read the Journal's position on issues involved in ethical publication and affirm that this report is consistent with those guidelines.

Ethics Approval The local Ethics Committee of the Medical Faculty of the University of Tübingen (ethical reference number: 646/2011BO1) gave approval for this study. The study was performed in concordance with the principles of the Declaration of Helsinki. All subjects gave informed consent before study participation.

References

Abreu R, Leite M, Jorge J, Grouiller F, van der Zwaag W, Leal A, Figueiredo P (2016) Ballistocardiogram artifact correction taking into account physiological signal preservation in simultaneous EEG-fMRI. Neuroimage 135:45–63. https://doi.org/10.1016/j.neuroimage.2016.03.034

Aghakhani Y, Bagshaw AP, Bénar CG, Hawco C, Andermann F, Dubeau F & Gotman J (2004) fMRI activation during spike and wave discharges in idiopathic generalized epilepsy. Brain 127(5):1127–1144. https://doi.org/10.1093/brain/awh136

Allen PJ, Polizzi G, Krakow K, Fish DR, Lemieux L (1998) Identification of EEG events in the MR scanner: the problem of pulse artifact and a method for its subtraction. Neuroimage 8(3):229–239. https://doi.org/10.1006/nimg.1998.0361

Anami K, Mori T, Tanaka F, Kawagoe Y, Okamoto J, Yarita M, Ohnishi T, Yumoto M, Matsuda H, & Saitoh O (2003) Stepping stone sampling for retrieving artifact-free electroencephalogram during functional magnetic resonance imaging. NeuroImage 19(2):281–295. https://doi.org/10.1016/S1053-8119(03)00048-X

Andersson JLR, Skare S, Ashburner J (2003) How to correct susceptibility distortions in spin-echo echo-planar images: application to diffusion tensor imaging. Neuroimage 20(2):870–888. https://doi.org/10.1016/S1053-8119(03)00336-7

Aquino KM, Fulcher BD, Parkes L, Sabaroedin K, Fornito A (2020) Identifying and removing widespread signal deflections from fMRI data: rethinking the global signal regression problem. Neuroimage 212:116614. https://doi.org/10.1016/j.neuroimage.2020.116614

Beghi E, Giussani G, Nichols E, Abd-Allah F, Abdela J, Abdelalim A et al (2019) Global, regional, and national burden of epilepsy, 1990–2016: a systematic analysis for the Global Burden of Disease Study 2016. Lancet Neurol 18(4):357–375. https://doi.org/10.1016/S1474-4422(18)30454-X

Benjamini Y, Hochberg Y (1995) Controlling the false discovery rate: a practical and powerful approach to multiple testing. J R Stat Soc Ser B Methodol 57(1):289–300. http://www.jstor.org/stable/2346101

Benuzzi F, Mirandola L, Pugnaghi M, Farinelli V, Tassinari CA, Capovilla G et al (2012) Increased cortical BOLD signal anticipates generalized spike and wave discharges in adolescents and adults with idiopathic generalized epilepsies. Epilepsia 53(4):622–630. https://doi.org/10.1111/j.1528-1167.2011.03385.x

Brookes MJ, Mullinger KJ, Stevenson CM, Morris PG, Bowtell R (2008) Simultaneous EEG source localisation and artifact rejection during concurrent fMRI by means of spatial filtering. Neuroimage 40(3):1090–1104. https://doi.org/10.1016/j.neuroimage.2007.12.030

Brookes MJ, Hale JR, Zumer JM, Stevenson CM, Francis ST, Barnes GR et al (2011) Measuring functional connectivity using MEG: Methodology and comparison with fcMRI. Neuroimage 56(3):1082–1104. https://doi.org/10.1016/j.neuroimage.2011.02.054

Carney PW, Masterton RAJ, Harvey AS, Scheffer IE, Berkovic SF, Jackson GD (2010) The core network in absence epilepsy: differences in cortical and thalamic BOLD response. Neurology 75(10):904–911. https://doi.org/10.1212/WNL.0b013e3181f11c06

Carney PW, Masterton RAJ, Flanagan D, Berkovic SF, Jackson GD (2012) The frontal lobe in absence epilepsy: EEG-fMRI findings. Neurology 78(15):1157–1165. https://doi.org/10.1212/WNL.0b013e31824f801d

Clemens B, Puskás S, Bessenyei M, Emri M, Spisák T, Koselák M et al (2011) EEG functional connectivity of the intrahemispheric cortico-cortical network of idiopathic generalized epilepsy. Epilepsy Res 96(1–2):11–23. https://doi.org/10.1016/j.eplepsyres.2011.04.011

Cohen J (1992) A power primer. Psychol Bull 112(1):155–159. https://doi.org/10.1016/j.jorganchem.2011.01.025

Daffertshofer A, van Wijk BCM (2011) On the influence of amplitude on the connectivity between phases. Front Neuroinform 5(July):1–12. https://doi.org/10.3389/fninf.2011.00006

Debener S, Mullinger KJ, Niazy RK, Bowtell RW (2008) Properties of the ballistocardiogram artefact as revealed by EEG recordings at 1.5, 3 and 7 T static magnetic field strength. Int J Psychophysiol 67(3):189–199. https://doi.org/10.1016/j.ijpsycho.2007.05.015

Debener S, Mullinger KJ, Niazy RK, & Bowtell RW (2008) Properties of the ballistocardiogram artefact as revealed by EEG recordings at 1.5, 3 and 7 T static magnetic field strength. J. Psychophysiol 67(3):189–199. https://doi.org/10.1016/j.ijpsycho.2007.05.015

Douw L, van Dellen E, de Groot M, Heimans JJ, Klein M, Stam CJ, Reijneveld JC (2010) Epilepsy is related to theta band brain connectivity and network topology in brain tumor patients. BMC Neurosci. https://doi.org/10.1186/1471-2202-11-103

Elshahabi A, Klamer S, Sahib AK, Lerche H, Braun C, Focke NK (2015) Magnetoencephalography reveals a widespread increase in network connectivity in idiopathic/genetic generalized epilepsy. PLoS One 10(9):1–16. https://doi.org/10.1371/journal.pone.0138119

Faiman I, Smith S, Hodsoll J, Young AH, Shotbolt P (2021) Resting-state EEG for the diagnosis of idiopathic epilepsy and psychogenic nonepileptic seizures: a systematic review. Epilepsy Behav 121:108047. https://doi.org/10.1016/j.yebeh.2021.108047

Garreffa G, Carni M, Gualniera G, Ricci GB, Bozzao L, De Carli D et al (2003) Real-time MR artifacts filtering during continuous EEG/fMRI acquisition. Magn Reson Imaging 21(10):1175–1189. https://doi.org/10.1016/j.mri.2003.08.019

Gotman J, Grova C, Bagshaw A, Kobayashi E, Aghakhani Y, Dubeau F (2005) Generalized epileptic discharges show thalamocortical activation and suspension of the default state of the brain. Proc Natl Acad Sci 102(42):15236–15240. https://doi.org/10.1073/pnas.0504935102

Gross J, Kujala J, Hämäläinen M, Timmermann L, Schnitzler A, Salmelin R (2001) Dynamic imaging of coherent sources: studying neural interactions in the human brain. Proc Natl Acad Sci 98(2):694–699. https://doi.org/10.1073/PNAS.98.2.694

Hamandi K, Salek-Haddadi A, Laufs H, Liston A, Friston K, Fish DR et al (2006) EEG–fMRI of idiopathic and secondarily generalized epilepsies. Neuroimage 31(4):1700–1710. https://doi.org/10.1016/j.neuroimage.2006.02.016

Hoffmann A, Jäger L, Werhahn KJ, Jaschke M, Noachtar S, & Reiser M (2000) Electroencephalography during functional echo-planar imaging: Detection of epileptic spikes using post-processing methods. Magn Reson Med 44(5):791–798. https://doi.org/10.1002/1522-2594

Holmes MD, Brown M, Tucker DM (2004) Are "generalized" seizures truly generalized? Evidence of localized mesial frontal and frontopolar discharges in absence. Epilepsia 45(12):1568–1579. https://doi.org/10.1111/j.0013-9580.2004.23204.x

Jallon P, Latour P (2005) Epidemiology of idiopathic generalized epilepsies. Epilepsia 46(s9):10–14. https://doi.org/10.1111/j.1528-1167.2005.00309.x

Jansen M, White TP, Mullinger KJ, Liddle EB, Gowland PA, Francis ST et al (2012) Motion-related artefacts in EEG predict neuronally plausible patterns of activation in fMRI data. Neuroimage 59(1):261–270. https://doi.org/10.1016/j.neuroimage.2011.06.094

Jenkinson M (2002) Improved optimization for the robust and accurate linear registration and motion correction of brain images. Neuroimage 17(2):825–841. https://doi.org/10.1016/S1053-8119(02)91132-8

Ji G-J, Zhang Z, Xu Q, Wang Z, Wang J, Jiao Q et al (2015) Identifying corticothalamic network epicenters in patients with idiopathic generalized epilepsy. Am J Neuroradiol 36(8):1494–1500. https://doi.org/10.3174/ajnr.A4308

Klamer S, Ethofer T, Torner F, Sahib AK, Elshahabi A, Marquetand J et al (2018) Unravelling the brain networks driving spike-wave discharges in genetic generalized epilepsy-common patterns and individual differences. Epilepsia Open 3(4):485–494. https://doi.org/10.1002/epi4.12252

LeVan P, Maclaren J, Herbst M, Sostheim R, Zaitsev M, Hennig J (2013) Ballistocardiographic artifact removal from simultaneous

EEG-fMRI using an optical motion-tracking system. Neuroimage 75:1–11. https://doi.org/10.1016/j.neuroimage.2013.02.039

Li Hegner Y, Marquetand J, Elshahabi A, Klamer S, Lerche H, Braun C, Focke NK (2018) Increased functional MEG connectivity as a hallmark of MRI-negative focal and generalized epilepsy. Brain Topogr 31(5):863–874. https://doi.org/10.1007/s10548-018-0649-4

Liu TT, Nalci A, Falahpour M (2017) The global signal in fMRI: nuisance or information? Neuroimage 150:213–229. https://doi.org/10.1016/j.neuroimage.2017.02.036

Luo C, Li Q, Lai Y, Xia Y, Qin Y, Liao W et al (2011) Altered functional connectivity in default mode network in absence epilepsy: a resting-state fMRI study. Human Brain Mapp 32(3):438–449. https://doi.org/10.1002/hbm.21034

Mantini D, Perrucci MG, Del Gratta C, Romani GL, Corbetta M (2007) Electrophysiological signatures of resting state networks in the human brain. Proc Natl Acad Sci 104(32):13170–13175. https://doi.org/10.1073/pnas.0700668104

Marquetand J, Vannoni S, Carboni M, Li Hegner Y, Stier C, Braun C, Focke NK (2019) Reliability of magnetoencephalography and high-density electroencephalography resting-state functional connectivity metrics. Brain Connect 9(7):539–553. https://doi.org/10.1089/brain.2019.0662

Masterton RAJ, Abbott DF, Fleming SW, Jackson GD (2007) Measurement and reduction of motion and ballistocardiogram artefacts from simultaneous EEG and fMRI recordings. Neuroimage 37(1):202–211. https://doi.org/10.1016/j.neuroimage.2007.02.060

Masterton RA, Carney PW, Jackson GD (2012) Cortical and thalamic resting-state functional connectivity is altered in childhood absence epilepsy. Epilepsy Res 99(3):327–334. https://doi.org/10.1016/j.eplepsyres.2011.12.014

McGill ML, Devinsky O, Kelly C, Milham M, Castellanos FX, Quinn BT et al (2012) Default mode network abnormalities in idiopathic generalized epilepsy. Epilepsy Behav 23(3):353–359. https://doi.org/10.1016/j.yebeh.2012.01.013

McGill ML, Devinsky O, Wang X, Quinn BT, Pardoe H, Carlson C et al (2014) Functional neuroimaging abnormalities in idiopathic generalized epilepsy. NeuroImage Clin 6:455–462. https://doi.org/10.1016/j.nicl.2014.10.008

McIntosh JR, Yao J, Hong L, Faller J & Sajda P (2021) Ballistocardiogram Artifact reduction in simultaneous EEG-fMRI using deep learning. IEEE Trans. Biomed. Eng, 68(1):78–89. https://doi.org/10.1109/TBME.2020.3004548

Miao A, Tang L, Xiang J, Guan Q, Ge H, Liu H, Wu T, Chen Q, Yang L, Lu X, Hu Z & Wang X (2014) Dynamic magnetic source imaging of absence seizure initialization and propagation: A magnetoencephalography study. Epilepsy Res 108(3):468–480. https://doi.org/10.1016/j.eplepsyres.2014.01.006

Moon JY, Lee UC, Blain-Moraes S, Mashour GA (2015) General relationship of global topology, local dynamics, and directionality in large-scale brain networks. PLoS Comput Biol 11(4):1–21. https://doi.org/10.1371/journal.pcbi.1004225

Mullinger K, Debener S, Coxon R, Bowtell R (2008) Effects of simultaneous EEG recording on MRI data quality at 1.5, 3 and 7 tesla. Int J Psychophysiol 67(3):178–188. https://doi.org/10.1016/j.ijpsycho.2007.06.008

Murphy K, Fox MD (2017) Towards a consensus regarding global signal regression for resting state functional connectivity MRI. Neuroimage 154:169–173. https://doi.org/10.1016/j.neuroimage.2016.11.052

Murphy K, Birn RM, Handwerker DA, Jones TB, Bandettini PA (2009) The impact of global signal regression on resting state correlations: are anti-correlated networks introduced? Neuroimage 44(3):893–905. https://doi.org/10.1016/j.neuroimage.2008.09.036

Murphy K, Birn RM, Bandettini PA (2013) Resting-state fMRI confounds and cleanup. Neuroimage 80:349–359. https://doi.org/10.1016/j.neuroimage.2013.04.001

Niazy RK, Beckmann CF, Iannetti GD, Brady JM, Smith SM (2005) Removal of FMRI environment artifacts from EEG data using optimal basis sets. Neuroimage 28(3):720–737. https://doi.org/10.1016/j.neuroimage.2005.06.067

Nolte G, Bai O, Wheaton L, Mari Z, Vorbach S, Hallett M (2004) Identifying true brain interaction from EEG data using the imaginary part of coherency. Clin Neurophysiol 115(10):2292–2307. https://doi.org/10.1016/j.clinph.2004.04.029

Rolle CE, Narayan M, Wu W, Toll R, Johnson N, Caudle T et al (2022) Functional connectivity using high density EEG shows competitive reliability and agreement across test/retest sessions. J Neurosci Methods 367:109424. https://doi.org/10.1016/j.jneumeth.2021.109424

Routley B, Shaw A, Muthukumaraswamy SD, Singh KD, & Hamandi K (2020) Juvenile myoclonic epilepsy shows increased posterior theta, and reduced sensorimotor beta resting connectivity. Epilepsy Res 163:106324. https://doi.org/10.1016/j.eplepsyres.2020.106324

Saad ZS, Gotts SJ, Murphy K, Chen G, Jo HJ, Martin A, Cox RW (2012) Trouble at rest: how correlation patterns and group differences become distorted after global signal regression. Brain Connect 2(1):25–32. https://doi.org/10.1089/brain.2012.0080

Scheffer IE, Berkovic S, Capovilla G, Connolly MB, French J, Guilhoto L et al (2017) ILAE classification of the epilepsies: position paper of the ILAE Commission for Classification and Terminology. Epilepsia 58(4):512–521. https://doi.org/10.1111/epi.13709

Sekihara K, Owen JP, Trisno S, Nagarajan SS (2011) Removal of spurious coherence in MEG source-space coherence analysis. IEEE Trans Biomed Eng. https://doi.org/10.1109/TBME.2011.2162514

Smith S, Nichols T (2009) Threshold-free cluster enhancement: addressing problems of smoothing, threshold dependence and localisation in cluster inference. Neuroimage 44(1):83–98. https://doi.org/10.1016/j.neuroimage.2008.03.061

Stier C, Elshahabi A, Li Hegner Y, Kotikalapudi R, Marquetand J, Braun C et al (2021) Heritability of magnetoencephalography phenotypes among patients with genetic generalized epilepsy and their siblings. Neurology 97(2):e166–e177. https://doi.org/10.1212/WNL.0000000000012144

Stier C, Loose M, Kotikalapudi R, Elshahabi A, Li Hegner Y, Marquetand J et al (2022) Combined electrophysiological and morphological phenotypes in patients with genetic generalized epilepsy and their healthy siblings. Epilepsia 63(7):1643–1657. https://doi.org/10.1111/epi.17258

Szaflarski JP, Kay B, Gotman J, Privitera MD, Holland SK (2013) The relationship between the localization of the generalized spike and wave discharge generators and the response to valproate. Epilepsia 54(3):471–480. https://doi.org/10.1111/epi.12062

Tangwiriyasakul C, Perani S, Centeno M, Yaakub SN, Abela E, Carmichael DW, Richardson MP (2018) Dynamic brain network states in human generalized spike-wave discharges. Brain 141(10):2981–2994. https://doi.org/10.1093/brain/awy223

Uji M, Cross N, Pomares FB, Perrault AA, Jegou A, Nguyen A et al (2021) Data-driven beamforming technique to attenuate ballistocardiogram artefacts in electroencephalography–functional magnetic resonance imaging without detecting cardiac pulses in electrocardiography recordings. Hum Brain Mapp 42(12):3993–4021. https://doi.org/10.1002/hbm.25535

van der Meer JN, Pampel A, Van Someren EJW, Ramautar JR, van der Werf YD, Gomez-Herrero G et al (2016) Carbon-wire loop based artifact correction outperforms post-processing EEG/fMRI corrections—a validation of a real-time simultaneous EEG/fMRI correction method. Neuroimage 125:880–894. https://doi.org/10.1016/j.neuroimage.2015.10.064

Vasios CE, Angelone LM, Purdon PL, Ahveninen J, Belliveau JW, Bonmassar G (2006) EEG/(f)MRI measurements at 7 Tesla using a new

EEG cap (“InkCap”). Neuroimage 33(4):1082–1092. https://doi.org/10.1016/j.neuroimage.2006.07.038

Vulliemoz S, Thornton R, Rodionov R, Carmichael DW, Guye M, Lhatoo S et al (2009) The spatio-temporal mapping of epileptic networks: combination of EEG–fMRI and EEG source imaging. Neuroimage 46(3):834–843. https://doi.org/10.1016/j.neuroimage.2009.01.070

Wang Z, Lu G, Zhang Z, Zhong Y, Jiao Q, Zhang Z et al (2011) Altered resting state networks in epileptic patients with generalized tonic–clonic seizures. Brain Res 1374:134–141. https://doi.org/10.1016/j.brainres.2010.12.034

Weissenbacher A, Kasess C, Gerstl F, Lanzenberger R, Moser E, Windischberger C (2009) Correlations and anticorrelations in resting-state functional connectivity MRI: a quantitative comparison of preprocessing strategies. Neuroimage 47(4):1408–1416. https://doi.org/10.1016/j.neuroimage.2009.05.005

Westmijse I, Ossenblok P, Gunning B, van Luijtelaar G (2009) Onset and propagation of spike and slow wave discharges in human absence epilepsy: a MEG study. Epilepsia 50(12):2538–2548. https://doi.org/10.1111/j.1528-1167.2009.02162.x

Whitfield-Gabrieli S, Nieto-Castanon A (2012) Conn: a functional connectivity toolbox for correlated and anticorrelated brain networks. Brain Connect 2(3):125–141. https://doi.org/10.1089/brain.2012.0073

Winkler AM, Ridgway GR, Webster MA, Smith SM, Nichols TE (2014) Permutation inference for the general linear model. Neuroimage 92:381–397. https://doi.org/10.1016/j.neuroimage.2014.01.060

4.2. EFFECTS OF INVERSE METHODS AND SPIKE PHASES ON INTERICTAL HIGH-DENSITY EEG SOURCE RECONSTRUCTION

Clinical Neurophysiology 156 (2023) 4–13

Contents lists available at ScienceDirect

Clinical Neurophysiology

journal homepage: www.elsevier.com/locate/clinph

Effects of inverse methods and spike phases on interictal high-density EEG source reconstruction

Daniel van de Velden [a,1,*], Ev-Christin Heide [a,1], Caroline Bouter [b], Jan Bucerius [b], Christian H. Riedel [c], Niels K. Focke [a,*]

[a] University Medical Center Göttingen, Clinic for Neurology, 37075 Göttingen, Germany
[b] University Medical Center Göttingen, Department of Nuclear Medicine, 37075 Göttingen, Germany
[c] University Medical Center Göttingen, Institute for Diagnostic and Interventional Neuroradiology, 37075 Göttingen, Germany

HIGHLIGHTS

- Accuracy of 3 inverse methods (LCMV, sLORETA, wMNE) and of spike phases for high-density electric source imaging were evaluated.
- The beamformer method LCMV was as accurate as sLORETA; half-rise and peak phase best localized the sources.
- The clinical hypothesis-based cluster of PET hypometabolism was more accurate than the cluster with the smallest *p*-value.

ARTICLE INFO

Article history:
Accepted 24 August 2023
Available online

Keywords:
EEG
Interictal electrical source imaging
^{18}FDG-PET hypometabolism
Inverse methods
Focal epilepsy

ABSTRACT

Objective: To determine the effect of inverse methods and timepoints of interictal epileptic discharges (IEDs) used for high-density electric source imaging (hd-ESI) in pharmacoresistant focal epilepsies.
Methods: We retrospectively evaluated the hd-ESI and [18F]fluorodeoxyglucose positron emission tomography (^{18}FDG-PET) of 21 operated patients with pharmacoresistant focal epilepsy (Engel I). Volumetric hd-ESI was performed with three different inverse methods such as the inverse solution linearly constrained minimum variance (LCMV, a beamformer method), standardized low resolution electromagnetic tomography (sLORETA) and weighted minimum-norm estimation (wMNE) and at different IED phases. Hd-ESI accuracy was determined by volumetric overlap and distance between hd-ESI source maximum, as well as ^{18}FDG-PET hypometabolic region relative to the resection zone (RZ).
Results: In our cohort, the shortest distances and greatest volumetric overlaps to the RZ were found in the half-rise and peak-phase for all inverse methods. The distance to the RZ was not different between the centroid of the clinical hypothesis-based cluster and the source maximum in peak-phase. However, the distance of the hypothesis-based cluster was significantly shorter compared to the cluster selected by the smallest *p*-value.
Conclusions: Hd-ESI provides the greatest accuracy in determining the RZ at the IED half-rise and peak-phase for all applied inverse methods, whereby sLORETA and LCMV were equally accurate.
Significance: Our results offer guidance in selecting inverse methods and IED phases for hd-ESI, compare the performance of hd-ESI and ^{18}FDG-PET and encourage future studies in investigating the relationship between interictal ESI and ^{18}FDG-PET hypometabolism.

Abbreviations: AH, Amygdalohippocampectomy; ASM, Anti-seizure medication; ATR, Anterior temporal resection; BEM, Boundary element model; cluster$_{HPT}$, clinical hypothesis-based cluster; cluster$_{mSIG}$, statistically most significant cluster; CSF, Cerebrospinal fluid; CT, Computed tomography; DARTEL, Diffeomorphic anatomical registration using exponentiated Lie algebra; DSC, Dice similarity coefficient; EZ, Epileptogenic zone; ESI, Electric source imaging; FCD, Focal cortical dysplasia; FDG-PET, Fluorodeoxyglucose-positron emission tomography; FDR, False discovery rate; GG, Ganglioglioma; Hd-ESI, High-density electric source imaging; Hd-EEG, High-density electroencephalography; IED, Interictal epileptic discharge; LAURA, Local autoregressive average; LCMV, Linearly constrained minimum variance; LiTT, Laser interstitial thermal therapy; ICA, Independent component analysis; MRI, Magnetic resonance imaging; (E)TLE, (Extra) temporal lobe epilepsy; RZ, Resection zone; (s)LORETA, (Standardized) low resolution electromagnetic tomography; SNR, Signal-to-noise ratio; SOZ, Seizure onset zone; SV, Scoring value; (w)MNE, (Weighted) minimum-norm estimation.

* Corresponding authors.
E-mail addresses: daniel.velden@med.uni-goettingen.de (D. van de Velden), niels.focke@med.uni-goettingen.de (N.K. Focke).
[1] These authors contributed equally to this work.

https://doi.org/10.1016/j.clinph.2023.08.020
1388-2457/

1. Introduction

One third of all cases of epilepsy are pharmacoresistant, i.e. they do not respond to two tolerated, appropriately chosen and applied anti-seizure medication (ASM) (Kwan et al., 2009). For these patients, epilepsy surgery is an important treatment option, as it offers significantly better outcomes in terms of seizure frequency and quality of life than continued ASM treatment (Engel, 2018; Wiebe et al., 2001). In a study by (Sperling et al., 2016), surgically treated patients had a significantly lower mortality rate than those without surgery (n = 1110 patients). The aim of epilepsy surgery is to resect the epileptogenic zone (EZ) and thereby achieve freedom from seizures while sparing tissue with important neuropsychological and neurological functions (Vakharia et al., 2018).

Therefore, a detailed presurgical evaluation is necessary. The presurgical work-up starts with a noninvasive evaluation, which includes high-resolution magnetic resonance imaging (MRI), video scalp electroencephalography (EEG), and detailed neuropsychological assessment. An adjunctive method of characterizing the EZ is to use electromagnetic imaging techniques like high-density EEG (hd-EEG) or magnetencephalography with subsequent electric/-magnetic source imaging (ESI/MSI) (Ryvlin et al., 2014). This method provides a spatial reconstruction of the generators of interictal epileptic discharges (IEDs), usually phrased "irritative zone", indicating that this is not identical to the EZ (Guo et al., 2022; Lagarde et al., 2020), but often closely related (Duez et al., 2019; Jehi, 2018). Electric source imaging (ESI) is an estimation of the source distribution in the brain based on the electric activity recorded at the scalp.

An estimation of the underlying sources can be determined using various inverse methods. The classical dipole fitting method models a small number (often a single dipole) of focal sources as current dipoles. In contrast, distributed imaging methods such as the depth weighted minimum-norm estimation (wMNE) (Hämäläinen and Ilmoniemi, 1994), and the standardized low resolution electromagnetic tomography (sLORETA) (Pascual-Marqui, 2002) estimate currents across the whole source space, typically the cortical surface. In contrast to LORETA (Pascual-Marqui et al., 1994), sLORETA's localization interference is based on images of standardized current density (Pascual-Marqui, 2002). As opposed to dipole modeling and distributed source imaging, beamformer methods like linear constrained minimum variance (LCMV) take an adaptive spatial-filtering approach, independently scanning each location in a predefined region of interest within the source space (Van Veen et al., 1997). However, these methods differ in their algorithmic approach to source reconstruction and their estimated brain activities consequently also differ to a certain extent. A recent study compared the spatial accuracy of six different inverse methods for EEG source reconstruction of IEDs at a single timepoint, the IED half-rise phase (Carboni et al., 2022). LORETA and local autoregressive average (LAURA) were shown to be more noise-robust inverse methods with more accurate results for interictal EEG source localization. However, a dipole fitting method and beamformer method were not assessed in the study.

However, propagation of IEDs is known to be an important influencing variable for IED source localization (Lantz et al., 2003; Mălîia et al., 2016; Zumsteg et al., 2006). In a previous study, the distances between the source maxima of different timepoints of high-density electric source imaging (hd-ESI) and the resected brain area were compared. It was found that timepoints earlier than 50% of the IED's half-rise phase gave less accurate results (Vorderwülbecke et al., 2020). We therefore studied the combined effect of different EEG inverse methods and of different IED phases on the accuracy to map irritative and epileptogenic zones in presurgical evaluation.

Moreover, in many epilepsy centers [18F]fluorodeoxyglucose-positron emission tomography (^{18}FDG-PET) is additionally used to identify epileptogenic foci. ^{18}FDG-PET detects the rate of cerebral glucose metabolism, which is mainly determined by neuronal activity (Sokoloff, 2008). Given the rather low temporal resolution of static ^{18}FDG-PET, images are usually obtained in the interictal phase. Interictal regional glucose hypometabolism is related to the functional deficit zone in focal epilepsy patients (Rosenow and Lüders, 2001). This metabolic alteration has an established role in noninvasive characterization of epileptogenic foci in focal epilepsy patients (la Fougère et al., 2009). In addition to its diagnostic usefulness, it was shown that ^{18}FDG-PET hypometabolism is a predictive variable for the surgical outcome (Vinton et al., 2007). Hypometabolism in the temporal lobe is associated with better postoperative seizure control while extensions of the ^{18}FDG-PET hypometabolism to extratemporal areas, as can be often found in temporal lobe epilepsy patients (TLE) (la Fougère et al., 2009), were reported to be associated with an unfavorable post-surgical outcome (Lagarde et al., 2020).

This study evaluated the effect of inverse methods and of different IED phases of patient's source reconstructed interictal events/spikes, on the distance to and the volumetric overlap with the resected zone. In addition, the distance between the region of ^{18}FDG-PET hypometabolism and the RZ was compared to the distance between hd-ESI and the RZ.

2. Methods

Patient cohort: We studied patients selected from the database of the Department of Neurology at the University Hospital of Göttingen, Germany. All patients had been admitted to our epilepsy monitoring unit for preoperative noninvasive epilepsy evaluation between 1st September 2017 and 1st February 2021. We defined the following inclusion criteria: (I) a diagnosis of pharmacoresistant focal epilepsy, (II) a presurgical evaluation with 256-channel, long-term ($\geq$2h) hd-EEG recording, and high-resolution 3 T MRI following an epilepsy specific protocol, (III) $\geq$10 IEDs in hd-EEG recording, (IV) subsequent initial resective brain surgery with good Engel outcome (I) and (V) a post-surgical brain MRI. Our exclusion criteria were (I) multifocal epilepsy and (II) prior epilepsy surgery. The presurgical evaluation also included a neurological and neuropsychological examination, a long-term low-density video-EEG recording ($\geq$7 days), hd-EEG, high-resolution 3 T MRI with an epilepsy specific protocol and ^{18}FDG-PET/computed tomography as clinically indicated (CT; except for two patients). Post-surgical outcome was classified using the Engel Outcome Scale (Engel, 1998). The results are classified as Class I: free of disabling seizures with (IA) completely seizure-free since surgery, (IB) non disabling simple partial seizures only since surgery, (IC) some disabling seizures after surgery, but free of disabling seizures for at least 2 years, (ID) generalized convulsions with ASM withdrawal only, Class II: rare disabling seizures, Class III: worthwhile improvement and Class IV: no worthwhile improvement. The local Ethics Committee of the University Medical Center of Göttingen gave its approval for this study (ethics number 3/7/22).

MRI acquisition and pre-processing: For each patient, an individual presurgical high resolution T1 or MPRAGE 3-T MRI of the entire head was performed (Magnetom Prisma, Siemens Medical Systems). 3D structural T1 weighted images (repetition time = 1900 ms, echo time = 2.26 ms, field of view = 256 $\times$ 256 $\times$ 256 voxel, flip angle = 9°, and voxel size = 1 $\times$ 1 $\times$ 1 mm) were added. A T1 image was required for the post-surgical MRI. All anatomical T1 images were segmented into common tissue classes (grey matter and

white matter, and cerebrospinal fluid (CSF), etc.) and reconstructed using Freesurfer (version 6.0.0; https://surfer.nmr.mgh.harvard.edu/). Furthermore, each patient's anatomical T1 image was normalized to standard Montreal Neurological Institute space using the non-linear normalization approach of the toolbox for "Diffeomorphic Anatomical Registration using Exponentiated Lie algebra" (DARTEL; SPM12; https://www.fil.ion.ucl.ac.uk/spm/software/spm12/). The deformation field applied for normalization was saved for further usage.

Definition of resection zone (RZ): The post-surgical T1 was coregistered with the presurgical T1 via SPM12, using a normalized mutual information cost function. As the resected volume was mainly filled with CSF after surgery, we determined the differences between the preoperative and postoperative CSF tissue class by subtracting the postoperative T1 CSF tissue class from the preoperative T1 CSF tissue class. A semi-automated smoothing and correction process was then applied. In the first step, misidentified scattered voxels, e.g. in the subarachnoid space, were filtered (kernel: 3 × 3 × 3 mm). This was followed by applying a filter (4 × 4 × 4 mm) to adjust for residual spatial differences at the edges of the resected volume. According to the preoperative and postoperative MRI, the RZ masks were visually reviewed and manually corrected as needed. Finally, a three-dimensional filter (9 × 9 × 9 mm) was applied to the edited masks, followed by a re-binarization with threshold 0.3 to remove sharp edges from manual editing. Since we only included patients with a good postoperative outcome (Engel I), one can assume that the RZ contained the EZ or at least the clinically relevant areas of early ictal spread (Mălîia et al., 2016).

^{18}FDG-PET acquisition and processing: ^{18}FDG-PET computed tomography scans were acquired prior to surgical resection using a Philips Vereos PET/CT scanner (Philips Medical Systems, Cleveland, Ohio, USA) using a 128 × 128 matrix and a slice thickness of 2 mm in 19 out of 21 patients. There were two patients without PET data since it was not clinically indicated (fully concordant data, unifocal epilepsy), therefore those patients were excluded from any ^{18}FDG-PET data-based analysis in this study. One additional patient was excluded due to endoscopic third ventriculostomy for obstructive hydrocephalus and gross anatomical differences of enlarged ventricles. ^{18}F-FDG was injected intravenously (207.8 ± 10.25 MBq), and images were acquired 60 min after the tracer injection with a 10-min scan duration. All patients had fasted at least 6 h prior to the tracer injection, and blood sugar levels were measured in order to exclude hyperglycemia. All patients rested for 20 min in a quiet and dimly lit room prior to and for 10 min after tracer injection. Images were reconstructed using an ordered subset-expectation maximization algorithm with three reconstruction iterations and 15 subsets. A low-dose CT scan was used for attenuation correction. Further image processing was performed using the SPM12 toolbox (SPM12, version 7487; https://www.fil.ion.ucl.ac.uk/spm/software/spm12). Individual ^{18}FDG-PET image volumes were coregistrated to the anatomical T1 image. The same non-linear deformation field applied to the anatomical image data was used for the ^{18}FDG-PET data images to spatially normalize them into standard Montreal Neurological Institute space with voxel sizes of 1.5 × 1.5 × 1.5 mm. Finally, smoothing with an 8 × 8 × 8 mm kernel was applied.

Definition of ^{18}FDG-PET hypometabolism: The spatial definition of hypometabolism in each patient was done with a semi-automatized algorithm at voxel level using the SPM12 software. Each patient was statistically compared to the group of 38 healthy subjects (two-sided, two-sample t-test). The control group consisted of ten healthy subjects from our local database (ethical reference number: 295/2015BO1) and twenty-eight subjects from the CERMEP-IDB-MRXFDG database (Mérida et al., 2021). Each image was then intensity normalized by dividing each in-brain voxel by the global average of all in-brain voxels to correct for patient - and scanner variations in brain metabolism. Images were masked for voxels inside the brain. All ^{18}FDG-PET control and patient data scans were processed identically (Mayoral et al., 2016). Each patient was compared to the control group in a general linear model, and significant decreases at a threshold of $p < 0.01$ (family-wise error corrected) were marked (Mayoral et al., 2016; Person et al., 2010). These suprathreshold voxels were clustered in groups with a three-dimensional 26 neighborhood connection. Those maps showing ^{18}FDG-PET hypometabolism were transformed back to the individual subject-specific space and resampled to T1 resolution 1 × 1 × 1 mm. Resulting clusters with less than 2 voxels (=2 mm^3) were rejected.

Finally, the results were visually reviewed by an experienced clinician (E.-C. Heide, aware of clinical information) based on the plausibility of the position and the underlying tissue types. Clusters in brainstem, cerebellum, corpus callosum and in ventricles were removed.

Most patients showed multiple regions of hypometabolism. For each patient, the ^{18}FDG-PET hypometabolism cluster which was clinically most plausible based on the hypothesis of the epileptogenic focus was chosen for all further analysis. It was referred to as hypothesis-based cluster (cluster$_{HPT}$; cluster$_{HPT}$ size: 7435.6 ± 8882.5 mm^3). In addition to that, the ^{18}FDG-PET hypometabolism cluster encompassing the smallest *p*-value in a single voxel (strongest statistical difference to healthy controls, "peak voxel") compared to the control group was chosen and further referred to as most significant cluster (cluster$_{mSIG}$; cluster$_{mSIG}$: 4566.5 ± 9587.2 mm^3).

hd-EEG acquisition and pre-processing: hd-EEG acquisition with a 256-channel EEG system was performed on the video-EEG monitoring unit using a GES400 system (Electrical Geodesics, Inc., now Magstim EGI, Eugene, Oregon, USA) with a sampling rate of 250 or 1000 Hz. In patients with fewer than 10 IED per hour in the preceding low-density EEG, a long-term hd-EEG (≥03:00 h) was performed, whereas in patients with more than 10 IED per hour a short-term hd-EEG (≥01:45–03:00 h) was deemed clinically sufficient. The hd-EEG data was 70 Hz low pass and 0.3 Hz high pass, and 50 Hz notch filtered to account for line noise and further reviewed by one EEG experienced clinician (E.-C. Heide, aware of clinical information), and all spikes (<70 ms) and sharp waves (70–120 ms) were marked on the IEDs' peaks. IEDs were classified and grouped at lobar resolution, based on their morphology and topography. If more than one IED population was found, the one with the largest amount of IEDs was selected for processing (mean: 87 ± 101 IEDs). After filtering, epochs containing the visually detected IEDs (±2 s) were clipped.

The preprocessing and further analysis steps were performed using Fieldtrip (https://www.fieldtriptoolbox.org/, version: fieldtrip-20191127) running in Matlab (version 9.0, R2018b, Mathworks Inc.). All selected IED trials were down sampled to 250 Hz. This was followed by a visual inspection and rejection of noisy trials and/or trial artifacts contaminated by eye movements, blinks, cardiac, and muscle activity. We then performed an independent component analysis (ICA) to identify and remove components reflecting electrocardiogram and ocular artifacts. The IED trials were then visually checked and temporally aligned to the peak of the IED. Finally, all IED trials were averaged.

hd-EEG forward modelling and source analysis: In addition to the measured EEG activity and the inverse method, a forward model is needed for hd-ESI. The forward model is based on the head model, the source model and the electrode model. For the head model, the anatomical T1 of each patient was used. An individual boundary element model (BEM) with three layers of different conductivity (scalp: 0.33 S/m, skull: 0.004 S/m, brain: 0.33 S/m) was constructed

using the 'dipoli' method implemented in Fieldtrip. A 5 mm volumetric grid was constructed in the SPM12 CAT12 template (CAT12; Christian Gaser 2018, https://www.neuro.uni-jena.de/cat/) and those standardized volumetric grid points were transformed back to the individual anatomical space using the inverted DARTEL deformation field (DARTEL; SPM12; https://www.fil.ion.ucl.ac.uk/spm/software/spm12/). These volumetric grid points were further used to define the positions in space in the source model for each patient's forward model. For the sensor model, the sensors were spatially aligned to the anatomical T1 using anatomical landmarks of fiducial positions (left/right preauricular point, nasion, inion) and further projected on to the scalp of the BEM. The averaged sensor data of each patient's main IED population was projected to each volumetric grid point using the following inverse methods:

wMNE: MNE estimates and optimizes a distribution of sources in the brain based on the assumption that the measured data in the sensors come from a brain source distribution with minimum power (Hämäläinen and Ilmoniemi, 1994). To compensate for the lower gain of deeper sources the wMNE including a weighting matrix was introduced and used (Pascual-Marqui, 1999).

sLORETA: For single source localization, the regularized sLORETA gives the best solution in terms of both localization error and ghost sources. It is an noise-normalized adaption of the MNE method. The source reconstruction is standardized by the variance of the estimated sources (Pascual-Marqui, 2002).

In addition to the distributed linear inverse solutions wMNE and sLORETA we also used a beamformer approach for source reconstruction.

LCMV: Beamformer approaches design a set of spatial filters to reconstruct sources in the brain. One well-known time-domain beamformer approach is the LCMV method (Van Veen et al., 1997). This approach estimates the brain activity at each position in the brain, while surpressing the influence from other locations.

Since the dipole fitting method is a common source model in clinical applications, we also calculated a dipole fit. For this purpose, a single dipole fit was calculated in MATLAB using the Fieldtrip toolbox (number of dipoles = 1, initial grid search, non-linear fitting) for each time bin of the averaged IED timecourses (Sarvas, 1987).

All inverse methods used here include a regularization parameter λ in their source estimation procedure. This was chosen to be the same for all inverse methods in this study and was calculated as:

$$\lambda = 1/SNR$$

where *SNR* was defined as the quotient of the amplitude at the spike peak of the IED and the standard deviation of the baseline (−2 s to −0.2 s) of the averaged spike epoch. For each patient's dataset, the regularization parameter was calculated individually (mean λ: 0.0 051 ± 0.005). Following the source reconstruction, the electrophysiological current distribution of all volumetric points were interpolated in the anatomical 3D MRI space. A brain mask was applied to get an 1 × 1 × 1 mm 3D image of source activity for each timepoint in the averaged trial. Furthermore, 95th percentile ($95\%_{tile}$) of the activities of all sources inside the brain was applied as threshold to the source activity in 3D space. This threshold was chosen empirically. We further determined the three different time phases of the epileptic spike discharge: (1) IED onset-phase: Defined by the first timebin surpassing the mean value of the baseline (−2 s to −0. 2 s), plus two times the standard deviation of baseline. (2) IED peak-phase: Defined by the timebin with maximum amplitude. (3) IED half-rise -phase: Defined by the timebin when half of the maximum is reached. The defined timepoints of the IED phases were checked and approved by an experienced clinician.

hd-EEG and ^{18}FDG-PET analysis: In order to evaluate the spatial accuracy of the three different inverse methods, the Euclidean distance between the voxel with the maximum amplitude of each patient's source reconstruction and the RZ was calculated in subject-specific MRI datasets and spaces. If the maximum amplitude was inside the RZ, the distance was taken as 0 mm. As an additional reference, the nearest Euclidean distance between the centroid of the ^{18}FDG-PET hypometabolism region and the RZ in subject-specific ^{18}FDG-PET datasets and spaces was measured. Furthermore, distances were classified and assigned to ordinal scoring values (SV) as: 0 mm = 1 SV, <10 mm = 2 SV, <20 mm = 3 SV, and >20 mm = 4 SV.

In addition to distance evaluation, we also evaluated source reconstructions and hypometabolism in terms of volumetric overlap with the RZ. Therefore, the Dice similarity coefficient (DSC) (Zou et al., 2004) was calculated as noted below

$$DSC = \frac{2 \cdot |X \cap Y|}{|X| + |Y|}$$

where |X| and |Y| represent the binarized entirety of two volumes. The DSCs were classified and assigned to ordinal SVs as follows: 0 = 4 SV, <0.2 = 3 SV, <0.4 = 2 SV, and > 0.4 = 1 SV. All measures of spatial concordance were calculated for each inverse method's reconstruction in each of the different IED phases.

Statistics: Statistical analyses were performed in Matlab. A sign test (one-sided) was used to compare the spatial measures (Euclidean distance, DSC) across inverse methods in each IED phase, as well as for each inverse method across IED phases. We applied a one-sided test as we hypothesized that rising-phase and peak-phase have a better accuracy compared to the onset-phase based on literature (Brodbeck et al., 2011; Lantz et al., 2003; van Mierlo et al., 2017). In contrast, we applied a two-sided sign test for the comparison between the PET hypometabolism cluster and the ESI peak-phase as a plausible hypothesis could not be defined. Data was passed to statistical analysis as SVs for each metric. We corrected the resulting *p*-values for multiple comparison via false discovery rate (FDR) and *p*-values smaller than 0.05 were considered statistically significant. In Addition, standardized effect sizes (Cohen's *d*) were calculated for each statistical test, defining effect sizes as $d > 0.5$ as moderate, and $d > 0.8$ as large effect size (Cohen, 1992). The study was exploratory.

The following is an overview of the workflow in Fig. 1.

3. Results

Twenty-one patients in the time period described above met our inclusion criteria and none had to be excluded (for details see Table 1). Five of the 21 patients were diagnosed with extratemporal lobe epilepsy (ETLE) due to low-grade developmental epilepsy-associated brain tumors (LEAT), focal cortical dysplasia (FCD), or cavernomas, whereas the remaining 16 patients had TLE, mostly with hippocampal sclerosis as underlying cause. An overview of the clinical data is given in Table 1. ^{18}FDG-PET was not performed in two patients since it was not clinically indicated (fully concordant data, unifocal epilepsy), and these patients were excluded from any ^{18}FDG-PET data-based analysis. One additional patient was excluded from any ^{18}FDG-PET data-based analysis due to internal hydrocephalus including endoscopic third ventriculostomy and grossly abnormal ventricles.

Euclidean distance: The proportion of patients with an ESI showing zero distance to the RZ was highest in the IEDs peak-phase for all inverse methods, and the most accurate results were found for sLORETA and LCMV (Fig. 2, and Table 2). The lowest rate of zero distance was found at the IED onset for all inverse methods.

In detail, sLORETA gave a significantly shorter distance than wMNE in all IED phases (sLORETA < wMNE: $p_{FDR} < 0.05$, $d > 0.5$). Similarly, LCMV showed significantly smaller distances to the RZ than wMNE at IED onset and half-rise (LCMV < wMNE: $p < 0.05$, $d > 0.5$). There was no significant difference between sLORETA and LCMV in any IED phase.

When comparing the different IED phases of each inverse method, the mean distance increased from onset to peak-phase. wMNE showed significantly smaller distances in the peak-phase than in the onset-phase (Peak < $Onset_{wMNE}$: $p = 0.02$, $d > 0.5$). Likewise, a tendency to smaller distances in the peak-phase compared with the onset was observed with LCMV (Peak < $Onset_{LCMV}$: $p_{FDR} = 0.09$ and sLORETA (Peak < $Onset_{sLORETA}$: $p_{FDR} = 0.14$). There was no significant difference in the distance between half-rise and peak-phase in any inverse method.

In addition, the dipole fitting method showed much larger distances at our IED timepoints (full data not shown) (Onset: 44.6 ± 25.4 mm; Half-rise: 31.3 ± 21.6 mm; Peak: 27.9 ± 21.6 mm) than the results from our distributed source model approaches.

The ^{18}FDG-PET hypometabolism $cluster_{HPT}$ showed a similar proportion of zero mm distance to RZ compared with ESI in the IED peak-phase ($cluster_{HPT}$: 44%). However, $cluster_{mSIG}$ showed significantly smaller distances to the RZ than ESI of sLORETA in the IED peak-phase ($p_{FDR} = 0.045$, $d = 0.96$) and than $cluster_{HPT}$ ($p_{FDR} = 0.02$, $d = 1.37$). Furthermore, $cluster_{mSIG}$ showed smaller distances to the RZ than ESI of LCMV in the IED peak-phase at trend level ($p_{FDR} = 0.077$, $d = 0.86$).

Volumetric overlap with the RZ: ESI in the IED onset-phase showed the lowest proportion of patients with DSC > 0.4 for all inverse methods (Fig. 3, and Table 3). In the IED half-rise phase, volumetric overlap increased for all inverse methods. The highest proportion of patients with DSC > 0.4 was found in the IED peak-phase.

When comparing the inverse methods, sLORETA showed greater volumetric overlap than the other inverse methods in all IED phases. The comparison was significantly different only at the onset (sLORETA > LCMV: $p_{FDR} < 0.05$, $d > 0.5$; sLORETA > wMNE: $p_{FDR} < 0.05$, $d > 0.5$).

Regarding the IED phases of one inverse method, LCMV and wMNE showed significantly greater volumetric overlap in the peak-phase compared with the onset-phase (Peak > $Onset_{LCMV}$: $p_{FDR} < 0.05$, $d > 0.5$; Peak > $Onset_{wMNE}$: $p_{FDR} < 0.05$, $d > 0.5$). There was no significant difference between the IED phases of sLORETA.

There was no significant difference in the volumetric overlap between ^{18}FDG-PET hypometabolism $cluster_{HPT}$ and ESI in the peak-phase ($cluster_{HPT}$: 32%). $Cluster_{mSIG}$ showed significantly lower volumetric overlap to the RZ than ESI in the peak-phase (wMNE: $p_{FDR} = 0.045$, $d = 1.0$; sLORETA: $p_{FDR} = 0.025$, $d = 1.3$; LCMV: $p_{FDR} = 0.043$, $d = 1.2$) and than $cluster_{HPT}$ ($p_{FDR} = 0.002$, $d = 0.97$).

4. Discussion

In this study we evaluated the effect of inverse methods and of different IED phases on hd-ESI and relate hd-ESI to the resection zone and FDG-PET hypometabolism. We showed that among the three inverse methods LCMV, wMNE, and sLORETA, the best concordance to the RZ was achieved with the distributed method sLORETA and the beamforming method LCMV in the half-rise and the IED peak-phase. Moreover, the concordance of the clinical hypothesis-based hypometabolic PET cluster was significantly higher compared to the cluster with the shortest *p*-value. Hd-ESI concordance was not significantly different from the hypothesis-based FDG-PET hypometabolic cluster. However, the most significant FDG-PET was clearly less concordant with the RZ than hd-ESI.

Hd-ESI – IED's timepoint: In our cohort, there was a significant difference for wMNE between onset and peak, and a tendency for sLORETA and LCMV, with smaller distances in peak-phase. However, the difference not significant between half-rise and peak. A previous study provided evidence that the most accurate results were obtained in the IED half-rise phase utilizing the inverse method of LAURA (Vorderwülbecke et al., 2020). In line with Vorderwülbecke et al. (2020), other studies found half-rise to be an optimal compromise between little propagation at onset and high signal-to-noise ratio (SNR) in peak-phase (Brodbeck et al., 2011; Lantz et al., 2003). In contrast, a study by van Mierlo et al. (2017) found the most accurate results in peak-phase. This was most probably due to the best SNR in peak-phase and less propagation within the IED (van Mierlo et al., 2017).

The SNR and the propagation increase together from IED onset-to peak-phase (Aydin et al., 2015). A previous study investigated the frequency of occurrence of propagation within IED events in patients being evaluated for epilepsy surgery (Mălîia et al., 2016). They observed that in half of the patient's propagation occurred during the IED events (Mălîia et al., 2016). However, this propagation remained within the resected area in most of the cases. These results are concordant with a previous, smaller study (Lantz et al., 2003). Our data showed that not more than three patients among all inverse methods had a propagation of their maximum more than 10 mm from onset to peak compared with to the RZ (LCMV: 5%, sLORETA: 0%, wMNE: 10%; see Supplementary Fig. 1). This small number of patients with a greater propagation may explain the good performance in the peak-phase in our cohort. If more propagation is expected, earlier timepoints than half-rise might be preferable (Plummer et al., 2019). These aspects should be taken into account when choosing the optimal timepoint for hd-ESI in a patient.

Hd-ESI - Inverse methods: In our cohort, sLORETA showed a better spatial concordance with only small differences between the different IED phases compared with wMNE. This observation was probably due to the underlying calculation of sLORETA, which includes smoothing by dividing the estimated sources by their variance (Pascual-Marqui, 2002). This results in the attenuation of strong changes in the source distribution of the reconstructed IEDs between different IED phases. In addition, the small amount of patients with propagation could account for the small differences between the IED phases.

Moreover, our findings showed a significantly smaller distance for LCMV (except for peak-phase) compared with wMNE. LCMV gave slightly higher distances to the RZ than sLORETA that were without significant difference. Therefore, suppressing other sources while estimating the brain activty at one position is beneficial for the identificaction of the IED source.

In literature, there are only a few studies on the comparison of inverse methods regarding hd-ESI in presurgical evaluation (Carboni et al., 2022; Heers et al., 2016; Pascarella et al., 2023). LCMV estimates the activity of a source at a given location, while simultaneously suppressing the contribution from all other sources and from noise (Jaiswal et al., 2020). As this approach differs from the distributed inverse solution, a comparison with LCMV is particularly interesting. We are aware of only one recent study by Pascarella et al. 2023 comparing LCMV beamformers and nine other source imaging methods in evoked potentials by electrical stimulation of intracranial EEG (Pascarella et al., 2023). In their analysis, dipole methods provided better ESI results than distributed methods. However, in this study, ESI was based on a very focal stimulation of single electrode contacts and not on IEDs generated by a, usually more distributed, biological source. Additionally, the input parameters in our study were different. A recent study by Carboni et al. in 2022 compared six distributed inverse methods for interictal hd-ESI. It revealed a better spatial concor-

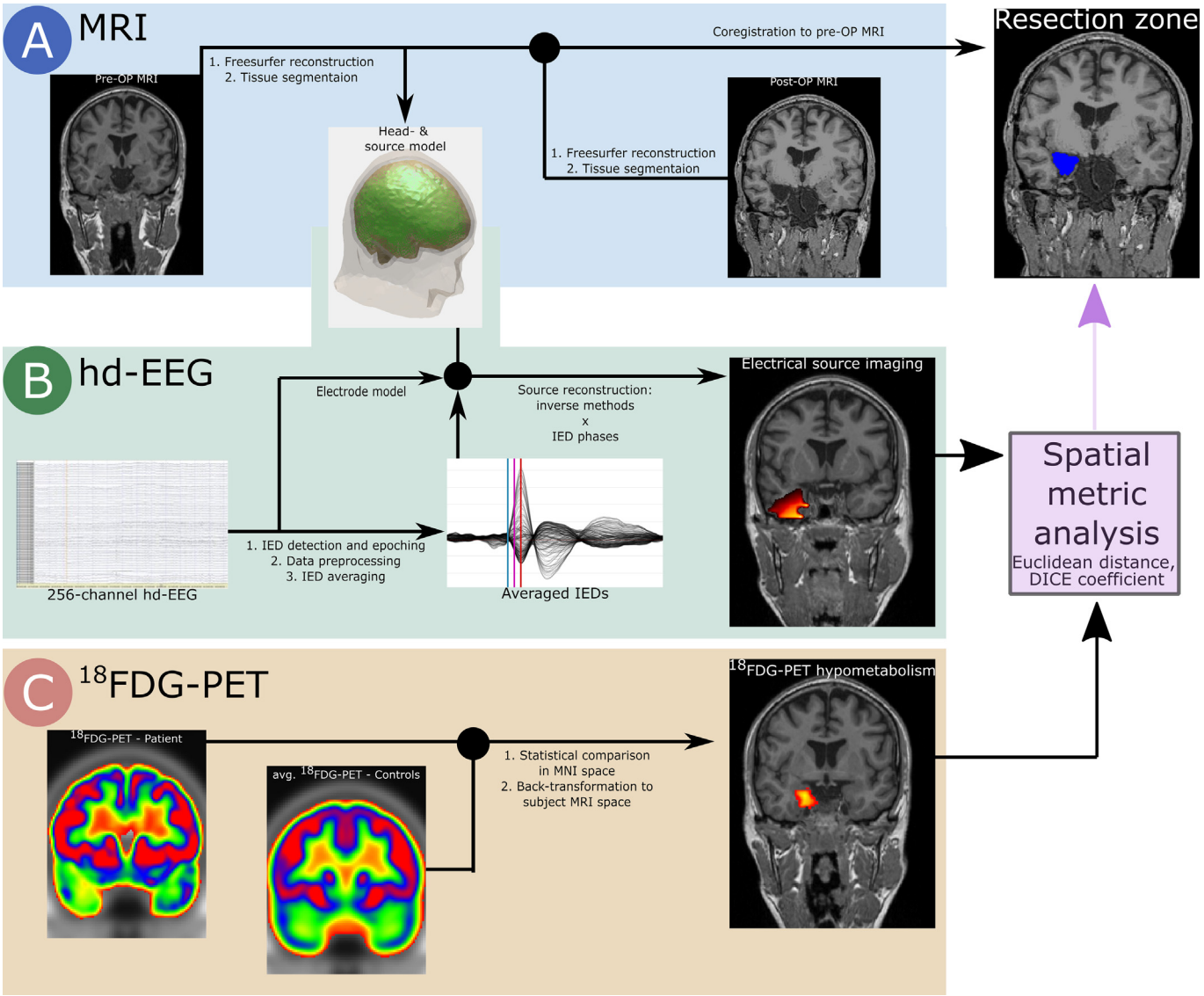

Fig. 1. Workflow of the data processing including: (A) the MRI data for identifying the resection zone (RZ), (B) the high-density EEG (hd-EEG) trial data for reconstructing the sources of the interictal epileptic discharges (IED) in the brain, (C) and the fluorodeoxyglucose-positron emission tomography (^{18}FDG-PET) data for extracting the regions of hypometabolism. *Following the processing of the MRI, hd-EEG and PET data, the hd-EEG electric source imaging (ESI) of each IED phase and ^{18}FDG-PET hypometabolism were used to calculate the spatial metrics (Euclidean distance, Dice similarity coefficient) for each patient in reference to the RZ.*

dance of LORETA and LAURA compared with other distributed inverse methods such as sLORETA and wMNE (Carboni et al., 2022). However, no statistical comparison was made between the distances calculated by wMNE and sLORETA. In line with our results, sLORETA showed a higher proportion of patients with zero mm distances to the RZ than wMNE. We did not include the inverse methods LORETA and LAURA, but the distances of sLORETA in the peak-phase gave results in our cohort that were similar to the distances with these two recommended inverse methods. Furthermore, Carboni et al. reported a better volumetric overlap with the RZ of wMNE than did sLORETA, which is most likely due to a different definition of volumetric overlap than used in our study. Carboni et al. used an approach based on locating the source maximum with respect to an atlas and an ordinal scoring (inside resection, sub lobar, lobar, lateralization, or contralateral), whereas we quantified the volumetric overlap via a similarity statistic metric (DSC). Therefore, a direct comparison of their volumetric overlap measurements with those of our study was not possible. Additional reasons for study differences were the different software packages used, cohort-specific differences, the amount and spike heterogeneity of IED trials, and analysis approaches (e.g., rejection of cheek electrodes, source-space limited to grey-matter, and fixed regularization λ for all patients).

In line with our findings, previous studies evaluating distributed EEG source modeling methods in benign focal epilepsy demonstrated greater consistency in interictal source reconstruction for sLORETA versus MNE and LORETA (Plummer et al., 2010b). However, the analysis was performed on the cortex surface sources, which differs from the recent study of Carboni et al. in 2022 (Carboni et al., 2022) and our analysis. This highlights the need for standardization of evaluation procedures for electromagnetic imaging analysis.

^{18}FDG-PET hypometabolism: We found that the ^{18}FDG-PET hypometabolism showed similar distances to the RZ as the ESI for all inverse methods in the IED peak-phase when the selection is based on a clinical hypothesis and not on the cluster with the most significant *p*-value. This is in line with previous studies, which reported a good performance of ^{18}FDG-PET hypometabolism in defining the EZ in patients with epilepsy due to malformations of cortical development (Lagarde et al., 2020). Furthermore,

Table 1
Study population.

		All patients	Patients with ^{18}FDG-PET
Group Size		21	18
Sex	Female	8 (38.1%)	8 (44.4%)
	Male	13 (61.9%)	10 (55.6%)
Time from epilepsy onset to surgery *(years)* *Average [standard deviation]*		14.0 [12.8]	15.7 [13.3]
Age at surgery *(years)* *Average [standard deviation]*		39.2 [10.0]	39.8 [11.1]
Structural MRI	Lesional	14 (66.7%)	11 (61.1%)
	Non-lesional	7 (33.3%)	7 (38.9%)
Hd-EEG spike trials *Average [standard deviation]*		72 [51.0]	62 [49.9]
Location of seizure onset zone	Temporal	16 (76.2%)	14 (77.8%)
	Extratemporal	5 (23.8%)	4 (22.2%)
Hemisphere of seizure onset zone	Left	12 (57.1%)	10 (55.6%)
	Right	9 (42.9%)	8 (44.4%)
Surgery	AH + ATR	11 (52.4%)	10 (55.6%)
	AH	2 (9.5%)	1 (5.6%)
	LiTT	1 (4.8%)	1 (5.6%)
	Other	7 (33.3%)	6 (33.3%)
Histology	Hippocampal sclerosis	7 (31.8%)	7 (38.9%)
	Ganglioglioma	3 (13.6%)	2 (11.1%)
	Focal cortical dysplasia	2 (9.1%)	1 (5.6%)
	Cavernoma	3 (13.6%)	3 (16.7%)
	Normal cortex / Gliosis	6 (27.3%)	5 (27.8%)
Surgical outcome at last follow-up $\geq$ *12 months; Engel Classification*	IA	15 (71.4%)	14 (77.8%)
	IB	1 (4.8%)	1 (5.6%)
	ID	5 (23.8%)	3 (16.7%)
Post-op follow-up (months) *Average [standard deviation]*		20.3 [8.0]	19.2 [7.1]

Abbreviations: AH = amygdalohippocampectomy; ATR = anterior temporal resection; Hd-EEG = high-density EEG; LiTT = laser interstitial thermal therapy.

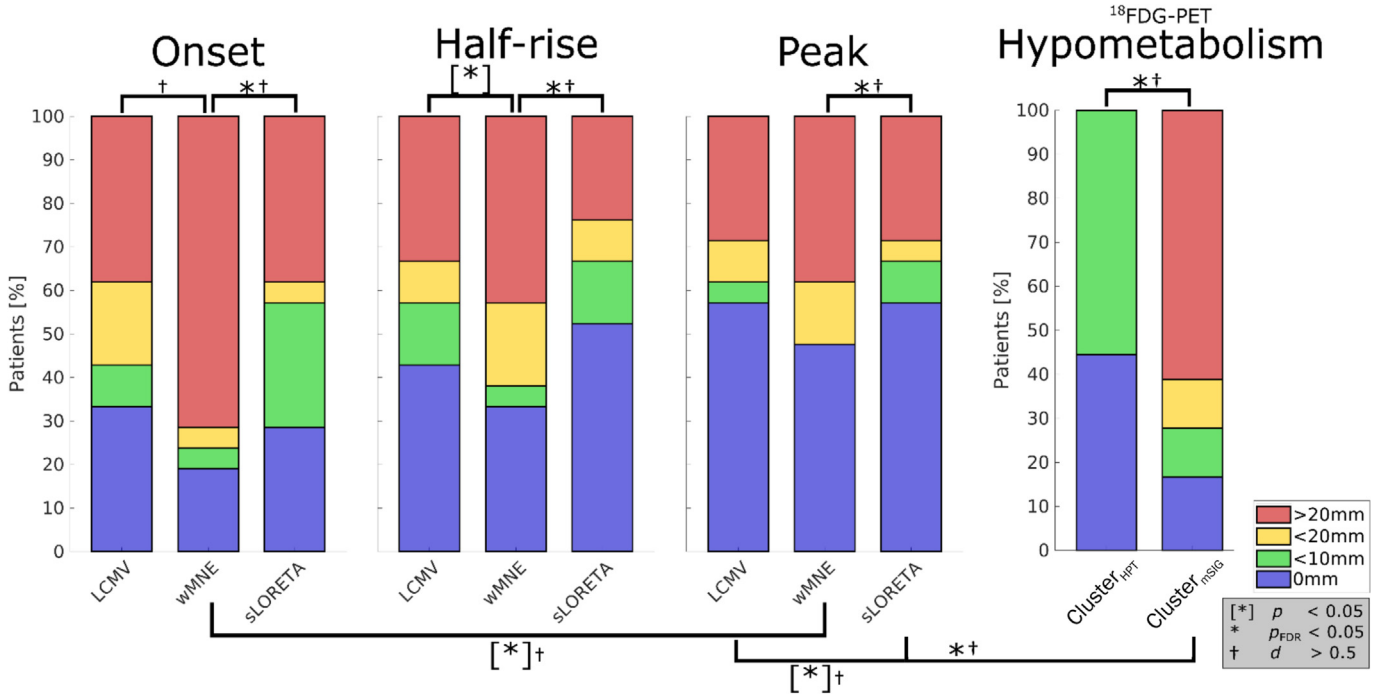

Fig. 2. Euclidean distance between high-density EEG source reconstruction (hd-ESI) of interictal epileptic discharges (IED), as well as fluorodeoxyglucose-positron emission tomography (^{18}FDG-PET) hypometabolism regions, and the resection zone (RZ). *Euclidean distance from the maximum amplitude of hd-ESI (linearly constrained minimum variance (LCMV), standardized low resolution electromagnetic tomography (sLORETA), weighted minimum-norm estimation (wMNE)) to the RZ in each IED phase and the distance of the hypometabolic regions to the RZ. Asterisks in brackets mark statistically uncorrected and significant differences between inverse methods ([*] $p < 0.05$), whereas asterisks without brackets mark statistically corrected and significant differences (false discovery rate (FDR)-corrected) between inverse methods (* $p_{FDR} < 0.05$), and † mark Cohen's d effect sizes greater than 0.5. Note: The smallest distances between RZ and ESI were found in the half-rise and peak-phase with sLORETA and LCMV. Distances between RZ and the clinical hypothesis-based cluster (cluster$_{HPT}$) were similar to ESI in the IED peak-phase. Similarly, cluster$_{HPT}$ had significant smaller distances to the RZ than the cluster with the most significant p-value (cluster$_{mSIG}$; pFDR = 0.02, d = 1.37).*

Table 2
Mean Euclidean distance between high-density EEG (hd-EEG) source reconstruction of interictal epileptic discharges (IED) and the resection zone (RZ), as well as percentage of the patients' electric source imaging showing zero distance to the RZ.

[mm]	Onset	Half-rise	Peak
LCMV	27.5	22.1	19.6
wMNE	42.6	26.1	24.7
sLORETA	27.2	20.3	18.0
Electric source imaging with zero distance to the resection zone [%]			
LCMV	33%	43%	57%
wMNE	19%	33%	48%
sLORETA	29%	52%	57%

Abbreviations: LCMV = linearly constrained minimum variance; sLORETA = standardized low resolution electromagnetic tomography; wMNE = weighted minimum-norm estimation.

another study reported similar accuracy (sensitivity and specificity) of electromagnetic source imaging (using sLORETA) and ^{18}FDG-PET to intracranial measurements (Duez et al., 2019). The poor volumetric overlap of the ^{18}FDG-PET hypometabolism region and the RZ fits the concept of "cortical zones" in patients with epilepsy, in which the ^{18}FDG-PET hypometabolism region did overlap, but did not spatially coincide with the EZ (Jehi, 2018; Rosenow and Lüders, 2001). The similar Euclidean distances of ESI and ^{18}FDG-PET hypometabolism region to the RZ show that there is an equal spatial proximity of hd-ESI and ^{18}FDG-PET hypometabolism region to the RZ. This is consistent with findings of previous studies, which reported about the proximately located the area of ^{18}FDG-PET hypometabolism to IED and seizure onset zone (SOZ) (Alkonyi et al., 2009; Grouiller et al., 2015; Jeong et al., 2017; Juhász et al., 2000; Juhász and John, 2020). In a previous patient study (n = 6), electrical source activity (inverse method: LORETA) in half-rise and peak-phase was associated with an area of hypometabolism in most patients (Storti et al., 2014). Similarly, in another study the dipole location matched the ^{18}FDG-PET hypometabolic area in all patients (Pozo, 2000). When comparing the clinical hypothesis-based hypometabolism cluster to the cluster with the smallest p-value, the clinical hypothesis-based cluster was significantly more accurate in detecting the RZ. In direct comparison to ESI in the peak-phase, the clinical hypothesis-based cluster was similar accurate. This highlights the importance of combining multi-modal information when interpreting additional modalities like ^{18}FDG-PET in the presurgical workup.

4.1. Limitations

Since we chose to use Fieldtrip, a common Matlab-based toolbox for EEG/MEG processing, we were limited in the choice of inverse methods we could evaluate. Other inverse methods include dynamic statistical parametric mapping (Dale et al., 2000), Classical LORETA Analysis Recursively Applied (CLARA) (Iordanov et al., 2014), and LAURA (Menendez et al., 2001). Nevertheless, our study results are in line with similar previous studies (Carboni et al., 2022; Plummer et al., 2010a) and therefore provide a context for the different inverse methods and the choice of different timing of IEDs. Furthermore, the scoring/selection of IED trials was done by one clinician, hence, a certain amount of subjectivity / operator bias cannot be ruled out. Finally, the RZ, used as a surrogate for the EZ, is not an ideal spatial reference for comparison with ESI, as the IED source reconstructions represent the irritative zone. This irritative zone is often closely located to the EZ and the SOZ (Brodbeck

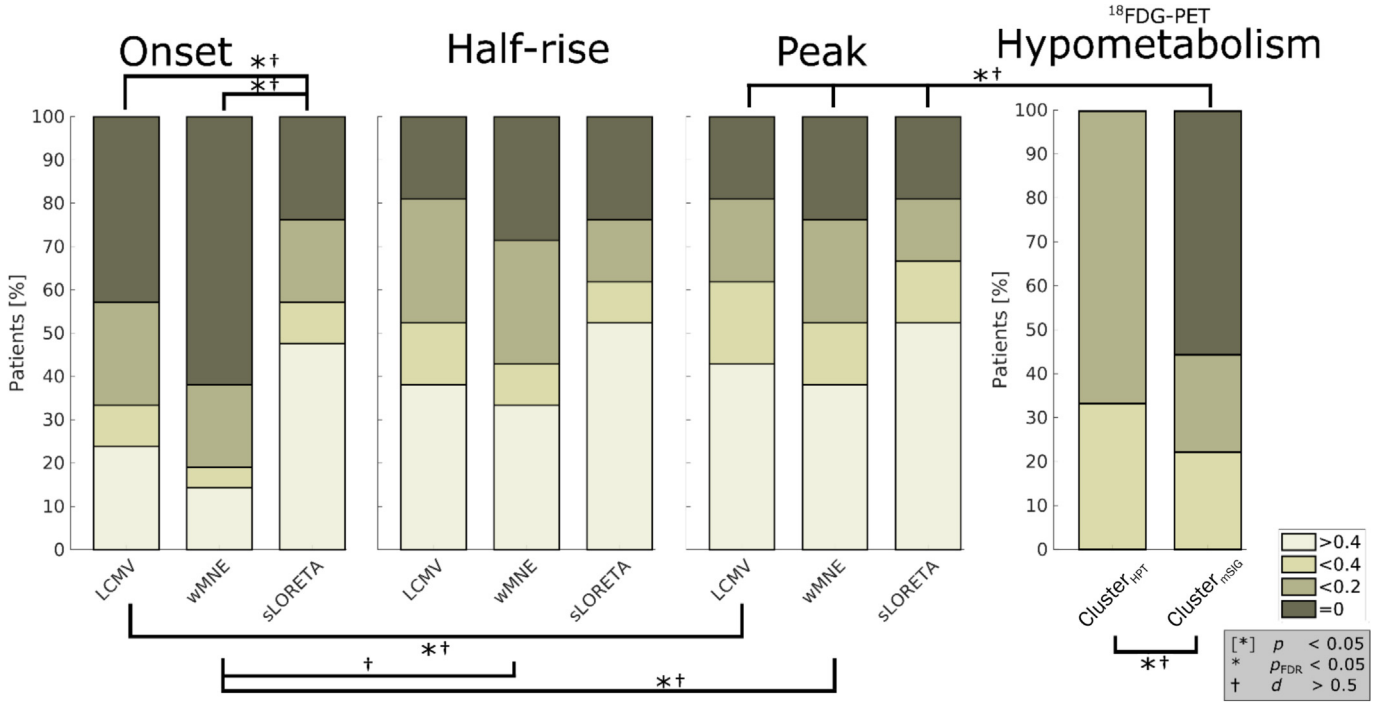

Fig. 3. Volumetric overlap estimated by Dice similarity coefficient (DSC) of resection zone (RZ) and interictal epileptic discharge (IED) electric source imaging (ESI), as well as fluorodeoxyglucose-positron emission tomography (^{18}FDG-PET) hypometabolism. *Volumetric overlap of ESI (linearly constrained minimum variance (LCMV), standardized low resolution electromagnetic tomography (sLORETA), weighted minimum-norm estimation (wMNE)) and the RZ in each IED time phase and the volumetric overlap of the hypometabolic regions to the RZ. Asterisks in brackets mark statistically uncorrected and significant differences without brackets mark statistically corrected and significant differences (false discovery rate (FDR)-corrected) between inverse methods (* p_{FDR} < 0.05), and † mark Cohen's d effect sizes greater than 0.5. Note: The greatest volumetric overlap of RZ and ESI was found in the peak-phase, with statistical significance compared with the onset-phase for LCMV and wMNE. All in all, sLORETA showed the greatest volumetric overlap in all IED phases, with statically significance compared with other inverse methods in the IED onset-phase (sLORETA > LCMV: p_{FDR} < 0.05, d > 0.5; sLORETA > wMNE: $p_{FDR} < 0.05, d > 0.5$). Volumetric overlap between RZ and cluster$_{HPT}$ was not significantly different compared to the one of peak-phase in all inverse methods.*

Table 3
Mean volumetric overlap estimated by Dice similarity coefficient (DSC) of high-density EEG (hd-EEG) source reconstruction of interictal epileptic discharges (IED) and the resection zone (RZ), as well as percentage of the patients' electric source imaging and RZ showing DSC > 0.4.

[DSC]	Onset	Half-rise	Peak
LCMV	0.195	0.265	0.294
wMNE	0.077	0.211	0.291
sLORETA	0.308	0.325	0.361
Electric source imaging and the resection zone with DSC > 0.4 [%]			
LCMV	33%	43%	57%
wMNE	19%	33%	48%
sLORETA	29%	52%	57%

Abbreviations: LCMV = linearly constrained minimum variance; sLORETA = standardized low resolution electromagnetic tomography; wMNE = weighted minimum-norm estimation.

et al., 2011; Duez et al., 2019). The threshold for ESI was empirically chosen from a selection of $90\%_{tile}$, $95\%_{tile}$, and $97.5\%_{tile}$ thresholds. Because the choice of this threshold influences the spatial dispersion of the ESI included in the volumetric concordance analysis, we also performed the volumetric concordance analysis for the other thresholds. However, the main conclusions remained the same when a different threshold was applied (see Supplementary Fig. 2). As only patients with good postoperative outcome were included in the study, they might have had less propagation. This could have influenced the choice of the IED timepoint. Nevertheless, the results are in line with another cohort described by Vorderwülbecke et al. in 2020 (Vorderwülbecke et al., 2020). Moreover, the selection of the ^{18}FDG-PET hypometabolism $cluster_{HPT}$ biases the specificity. However, in the presurgical evaluation the estimation of the EZ is based on the accordance of different modalities such as MRI, hd-ESI, ^{18}FDG-PET. Often, ^{18}FDG-PET is used to confirm or reject the assumed location of the EZ. Therefore, we chose the cluster based on the clinically most plausible EZ location. Additionally, analyzing the hd-ESI of the other spike groups would be an interesting question for further studies.

5. Conclusion

Overall, we showed that for the inverse methods studied here, the IED half-rise and peak-phase showed the best concordance with the RZ. Furthermore, sLORETA and LCMV were the inverse methods with the shortest distances to the RZ in our study. Moreover, we provide evidence of similar accuracy of ^{18}FDG-PET hypometabolism compared with hd-ESI in presurgical evaluation and guide clinicians to choose the clinical hypothesis-based hypometabolism cluster instead of the one with the smallest *p*-value in the presurgical workup.

Funding information

Deutsche Forschungsgemeinschaft, Grant/ Award Number: FO750/7-1.

Conflict of interest disclosure

N.K. Focke received honoraria from Arvelle/Angelini, Bial, Esai and Jazz, all unrelated to the present work. Jan Bucerius, C. Bouter, E. Heide, C. H. Riedel and D. van de Velden report no disclosures.

Appendix A. Supplementary data

Supplementary data to this article can be found online at https://doi.org/10.1016/j.clinph.2023.08.020.

References

Alkonyi B, Juhász C, Muzik O, Asano E, Saporta A, Shah A, et al. Quantitative brain surface mapping of an electrophysiologic/metabolic mismatch in human neocortical epilepsy. Epilepsy Res 2009;87(1):77–87. https://doi.org/10.1016/j.eplepsyres.2009.08.002.

Aydin Ü, Vorwerk J, Dümpelmann M, Küpper P, Kugel H, Heers M, et al. Combined EEG/MEG can outperform single modality EEG or MEG source reconstruction in presurgical epilepsy diagnosis. PLoS One 2015;10(3):e0118753. https://doi.org/10.1371/journal.pone.0118753.

Brodbeck V, Spinelli L, Lascano AM, Wissmeier M, Vargas MI, Vulliemoz S, et al. Electroencephalographic source imaging: a prospective study of 152 operated epileptic patients. Brain 2011;134(10):2887–97. https://doi.org/10.1093/brain/awr243.

Carboni M, Brunet D, Seeber M, Michel CM, Vulliemoz S, Vorderwülbecke BJ. Linear distributed inverse solutions for interictal EEG source localisation. Clin Neurophysiol 2022;133:58–67. https://doi.org/10.1016/j.clinph.2021.10.008.

Cohen J. A power primer. *Psychol Bull* 1992;112(1):155–9. https://doi.org/10.1016/j.jorganchem.2011.01.025.

Dale AM, Liu AK, Fischl BR, Buckner RL, Belliveau JW, Lewine JD, et al. Dynamic statistical parametric mapping: Combining fMRI and MEG for high-resolution imaging of cortical activity. Neuron 2000;26(1):55–67. https://doi.org/10.1016/S0896-6273(00)81138-1.

Duez L, Tankisi H, Hansen PO, Sidenius P, Sabers A, Pinborg LH, et al. Electromagnetic source imaging in presurgical workup of patients with epilepsy: a prospective study. Neurology 2019;92(6):e576–86. https://doi.org/10.1212/WNL.0000000000006877.

Engel J. Classifications of the international league against epilepsy: time for reappraisal. Epilepsia 1998;39(9):1014–7. https://doi.org/10.1111/j.1528-1157.1998.tb01453.x.

Engel J. The current place of epilepsy surgery. Curr Opin Neurol 2018;31(2):192–7. https://doi.org/10.1097/WCO.0000000000000528.

Grouiller F, Delattre BMAA, Pittau F, Heinzer S, Lazeyras F, Spinelli L, et al. All-in-one interictal presurgical imaging in patients with epilepsy: single-session EEG/PET/(f)MRI. Eur J Nucl Med Mol Imaging 2015;42(7):1133–43. https://doi.org/10.1007/s00259-015-3045-2.

Guo K, Wang J, Cui B, Wang Y, Hou Y, Zhao G, et al. [18F]FDG PET/MRI and magnetoencephalography may improve presurgical localization of temporal lobe epilepsy. Eur Radiol 2022;32(5):3024–34. https://doi.org/10.1007/s00330-021-08336-4.

Hämäläinen MS, Ilmoniemi RJ. Interpreting magnetic fields of the brain: minimum norm estimates. Med Biol Eng Compu 1994;32(1):35–42. https://doi.org/10.1007/BF02512476.

Heers M, Chowdhury RA, Hedrich T, Dubeau F, Hall JA, Lina JM, et al. Localization accuracy of distributed inverse solutions for electric and magnetic source imaging of interictal epileptic discharges in patients with focal epilepsy. Brain Topogr 2016;29(1):162–81. https://doi.org/10.1007/s10548-014-0423-1.

Iordanov T, Hoechstetter K, Berg P, Paul-Jordanov I, Scherg M. CLARA: classical LORETA analysis recursively applied. 20th Annual Meeting of Organization of Human Brain Mapping (OHBM) 2014:8–12.

Jaiswal A, Nenonen J, Stenroos M, Gramfort A, Dalal SS, Westner BU, et al. Comparison of beamformer implementations for MEG source localization. Neuroimage 2020;216. 116797. https://doi.org/10.1016/j.neuroimage.2020.116797.

Jehi L. The epileptogenic zone: concept and definition. Epilepsy Curr 2018;18(1):12–6. https://doi.org/10.5698/1535-7597.18.1.12.

Jeong J-W, Asano E, Pilli VK, Nakai Y, Chugani HT, Juh Asz C, et al. Objective 3D surface evaluation of intracranial electrophysiologic correlates of cerebral glucose metabolic abnormalities in children with focal epilepsy. Hum Brain Mapp 2017;38:3098–112. https://doi.org/10.1002/hbm.23577.

Juhász C, Chugani DC, Muzik O, Watson C, Shah J, Shah A, et al. Is epileptogenic cortex truly hypometabolic on interictal positron emission tomography? Ann Neurol 2000;48(1):88–96. https://doi.org/10.1002/1531-8249(200007)48:1<88::AID-ANA13>3.0.CO;2-3.

Juhász C, John F. Utility of MRI, PET, and ictal SPECT in presurgical evaluation of non-lesional pediatric epilepsy. Seizure 2020;77:15–28. https://doi.org/10.1016/j.seizure.2019.05.008.

Kwan P, Arzimanoglou A, Berg AT, Brodie MJ, Allen Hauser W, Mathern G, et al. Definition of drug resistant epilepsy: consensus proposal by the ad hoc Task Force of the ILAE Commission on Therapeutic Strategies. Epilepsia 2009;51(6):1069–77. https://doi.org/10.1111/j.1528-1167.2009.02397.x.

La Fougère C, Rominger A, Förster S, Geisler J, Bartenstein P. PET and SPECT in epilepsy: a critical review. Epilepsy Behav 2009;15(1):50–5. https://doi.org/10.1016/j.yebeh.2009.02.025.

Lagarde S, Boucekine M, McGonigal A, Carron R, Scavarda D, Trebuchon A, et al. Relationship between PET metabolism and SEEG epileptogenicity in focal lesional epilepsy. Eur J Nucl Med Mol Imaging 2020;47(13):3130–42. https://doi.org/10.1007/s00259-020-04791-1.

Lantz G, Spinelli L, Seeck M, de Peralta Menendez RG, Sottas CC, Michel CM. Propagation of interictal epileptiform activity can lead to erroneous source localizations: a 128-channel EEG mapping study. Clin Neurophysiol 2003;20 (5):311–9. https://doi.org/10.1097/00004691-200309000-00003.

Mălîia MD, Meritam P, Scherg M, Fabricius M, Rubboli G, Mîndruţă I, et al. Epileptiform discharge propagation: analyzing spikes from the onset to the peak. Clin Neurophysiol 2016;127(4):2127–33. https://doi.org/10.1016/j.clinph.2015.12.021.

Mayoral M, Marti-Fuster B, Carreño M, Carrasco JL, Bargalló N, Donaire A, et al. Seizure-onset zone localization by statistical parametric mapping in visually normal (18) F-FDG PET studies. Epilepsia 2016;57(8):1236–44. https://doi.org/10.1111/epi.13427.

Menendez RGDP, Andino SG, Lantz G, Michel CM, Landis T. Noninvasive localization of electromagnetic epileptic activity. I. Method descriptions and simulations. Brain Topogr 2001;14(2):131–7. https://doi.org/10.1023/A:1012944913650.

Mérida I, Jung J, Bouvard S, Le Bars D, Lancelot S, Lavenne F, et al. CERMEP-IDB-MRXFDG: a database of 37 normal adult human brain [18F]FDG PET, T1 and FLAIR MRI, and CT images available for research. EJNMMI Res 2021;11(1):91. https://doi.org/10.1186/s13550-021-00830-6.

Pascarella A, Mikulan E, Sciacchitano F, Sarasso S, Rubino A, Sartori I, et al. An in–vivo validation of ESI methods with focal sources. Neuroimage 2023;277. 120219. https://doi.org/10.1016/j.neuroimage.2023.120219.

Pascual-Marqui RD. Review on solving the inverse problem in EEG source analysis. Int J Bioelectromagn 1999;1(2):75–86. http://www.brainmaster.com/software/pubs/brain/loreta/TechnicalDetails.pdf.

Pascual-Marqui RD. Standardized low-resolution brain electromagnetic tomography (sLORETA): technical details. Method Find Exp Clin 2002;24 Suppl D(1):5–12. http://www.nature.com/articles/s41598-019-42984-3.

Person C, Koessler L, Louis-Dorr V, Wolf D, Maillard L, Marie PY. Analysis of the relationship between interictal electrical source imaging and PET hypometabolism. Annu Int Conf IEEE Eng Med Biol Soc 2010;2010:3723–6. https://doi.org/10.1109/IEMBS.2010.5627512.

Plummer C, Wagner M, Fuchs M, Harvey AS, Cook MJ. Dipole versus distributed EEG source localization for single versus averaged spikes in focal epilepsy. Clin Neurophysiol 2010a;27(3):141–62. https://doi.org/10.1097/WNP.0b013e3181dd5004.

Plummer C, Wagner M, Fuchs M, Vogrin S, Litewka L, Farish S, et al. Clinical utility of distributed source modelling of interictal scalp EEG in focal epilepsy. Clin Neurophysiol 2010b;121(10):1726–39. https://doi.org/10.1016/j.clinph.2010.04.002.

Plummer C, Vogrin SJ, Woods WP, Murphy MA, Cook MJ, Liley DTJ. Interictal and ictal source localization for epilepsy surgery using high-density EEG with MEG: a prospective long-term study. Brain 2019;142(4):932–51.

Pozo M. Correlation between FDG PET data and EEG dipole modeling. Clin Positron Imaging 2000;3(4):173. https://doi.org/10.1016/S1095-0397(00)00085-6.

Rosenow F, Lüders H. Presurgical evaluation of epilepsy. Brain 2001;124 (9):1683–700. https://doi.org/10.1093/brain/124.9.1683.

Ryvlin P, Cross JH, Rheims S. Epilepsy surgery in children and adults. Lancet Neurol 2014;13(11):1114–26. https://doi.org/10.1016/S1474-4422(14)70156-5.

Sarvas J. Basic mathematical and electromagnetic concepts of the biomagnetic inverse problem. Phys Med Biol 1987;32(1):11.

Sokoloff L. The physiological and biochemical bases of functional brain imaging. Cogn Neurodyn 2008;2(1):1–5. https://doi.org/10.1007/s11571-007-9033-x.

Storti SF, Boscolo Galazzo I, Del Felice A, Pizzini FB, Arcaro C, Formaggio E, et al. Combining ESI, ASL and PET for quantitative assessment of drug-resistant focal epilepsy. Neuroimage 2014;102(P1):49–59. https://doi.org/10.1016/j.neuroimage.2013.06.028.

Vakharia VN, Duncan JS, Witt J-A, Elger CE, Staba R, Engel J. Getting the best outcomes from epilepsy surgery. Ann Neurol 2018;83(4):676–90. https://doi.org/10.1002/ana.25205.

Van Mierlo P, Strobbe G, Keereman V, Birot G, Gadeyne S, Gschwind M, et al. Automated long-term EEG analysis to localize the epileptogenic zone. Epilepsia Open 2017;2(3):322–33.

Van Veen BD, Van Drongelen W, Yuchtman M, Suzuki A. Localization of brain electrical activity via linearly constrained minimum variance spatial filtering. IEEE Trans Biomed Eng 1997;44(9):867–80. https://doi.org/10.1109/10.623056.

Vinton AB, Carne R, Hicks RJ, Desmond PM, Kilpatrick C, Kaye AH, et al. The extent of resection of FDG-PET hypometabolism relates to outcome of temporal lobectomy. Brain 2007;130(2):548–60. https://doi.org/10.1093/brain/awl232.

Vorderwülbecke BJ, Carboni M, Tourbier S, Brunet D, Seeber M, Spinelli L, et al. High-density electric source imaging of interictal epileptic discharges: How many electrodes and which time point? Clin Neurophysiol 2020;131 (12):2795–803. https://doi.org/10.1016/j.clinph.2020.09.018.

Wiebe S, Blume WT, Girvin JP, Eliasziw M. A randomized, controlled trial of surgery for temporal-lobe epilepsy. N Engl J Med 2001;345(5):311–8. https://doi.org/10.1056/NEJM200108023450501.

Zou KH, Warfield SK, Bharatha A, Tempany CMC, Kaus MR, Haker SJ, et al. Statistical validation of image segmentation quality based on a spatial overlap index. Acad Radiol 2004;11(2):178–89. https://doi.org/10.1016/S1076-6332(03)00671-8.

Zumsteg D, Friedman A, Wieser H, Wennberg R. Propagation of interictal discharges in temporal lobe epilepsy: Correlation of spatiotemporal mapping with intracranial foramen ovale electrode recordings. Clin Neurophysiol 2006;117 (12):2615–26. https://doi.org/10.1016/j.clinph.2006.07.319.

4.3. IDENTIFICATION AND CROSS-MODAL RELATIONSHIP OF FUNCTIONAL RESTING-STATE NETWORKS IN SIMULTANEOUSLY MEASURED HD-EEG/FMRI/^{18}FDG-PET IMAGING

People involved in this study:

Daniel van de Velden[1]; Ev-Christin Heide[1]; Pascal Martin[2]; Benjamin Bender[3]; Sebastian von Beschwitz[4]; Adham Elshahabi[5]; Tudor Ionescu[6]; Bernd Pichler[6]; Christian la Fougère[4*]; Niels K. Focke[1,2*]

[1] Clinic for Neurology, University Medical Center Göttingen, 37075 Göttingen, Germany
[2] Department of Neurology and Epileptology, Hertie Institute of Clinical Brain Research, University Medical Center Tübingen, University of Tübingen, 72076 Tübingen, Germany
[3] Department of Diagnostic and Interventional Neuroradiology, University Hospital Tübingen, 72076 Tübingen, Germany
[4] Department of Nuclear Medicine and Clinical Molecular Imaging, University Hospital Tübingen, 72076 Tübingen, Germany
[5] Department of Neurology, University Hospital Zurich, 8091 Zurich, Switzerland
[6] Department of Preclinical Imaging and Radiopharmacy, Werner Siemens Imaging Center, University Hospital Tübingen, 72076 Tübingen, Germany

ABSTRACT

Introduction: The human brain is 'active' even in the absence of a specific task in the so-called 'resting state'. Data-driven methods can be used to identity spatially and temporarily distinct functional networks resting-state networks (RSN). Such studies are typically based on functional MRI, which has a blood oxygen level-dependent (BOLD) contrast that is an indirect measure of neuronal activity but also by means of EEG and [^{18}F]FDG-PET . Here, we investigated the presence and spatial relationship of metabolic, vascular, and neuronal networks in a cohort of healthy subjects and patients with focal epilepsy in a fully simultaneous hd-EEG/fMRI/[^{18}F]FDG-PET dataset.

Methods: Group independent component analysis (group-ICA) on the fMRI [^{18}F]FDG -PET data and on hd-EEG data was applied to extract RSN from each modality. Derived fMRI and [^{18}F]FDG -PET components were spatially correlated to the Yeo7 resting-state network atlas. Hd-EEG components were spatially correlated to the identified fMRI components.

Results: Established RSN were identified from fMRI data (r: 0.25-0.58, , $p_{FDR} < 0.001$). Similarly, [^{18}F]FDG -PET showed group-ICA components that were spatially correlated for all RSN of the Yeo7 atlas (r: 0.14-0.51, , $p_{FDR} < 0.001$). Most of the brain networks derived from fMRI data were also identified in hd-EEG data via group-ICA (r: 0.32-0.61, , $p_{FDR} < 0.05$).

Conclusion: Our findings suggest that the identification of known functional RSN from simultaneous hd-EEG/fMRI/[^{18}F]FDG -PET data via group-ICA is feasible in each modality. Group-ICA components from [^{18}F]FDG -PET and fMRI showed more spatial similarity than from hd-EEG and fMRI. The differences between the spatial expression and FC of components among modalities likely reflect the different signal origin and spatial and temporal resolution.

INTRODUCTION

Electroencephalography (EEG) and functional magnetic resonance imaging (fMRI) are typical modalities for imaging the human brain and its network functions. They can be used to probe the functional state of the brain at rest, i.e., without external stimulus. In the last two decades, data-driven processing methods have identified spatially and temporally differentiated functional networks of the human brain that are "active" even in the absence of a specific task in the so-called "resting state" (rs).

Most of the resting-state network (RSN) studies utilize fMRI, which typically is based on blood-oxygen-dependent (BOLD) contrast, i.e., minimal MRI signal fluctuations caused by hemodynamic changes through neurovascular coupling. A whole set of RSN with characteristic spatial profiles was subsequently described for fMRI, which are remarkably stable both within and between subjects (Damoiseaux et al., 2006; De Luca et al., 2006). The most common approach to extract these RSN is based on decomposing the observed whole-brain signal fluctuations into spatially and temporally separated sources using data-driven methods such as independent component analysis (ICA). This analysis method has the advantage that it does not require any a-priori information or spatial seeds. In 2011 a large analysis based on 1,000 rs-fMRI datasets revealed most stable estimations of either 7 or 17 human brain networks (Yeo et al., 2011). By applying ICA (and similar methods) 'visual', 'sensorimotor' and 'auditory' networks were identified, which showed spatially similar profiles to networks found in task-based fMRI studies. Furthermore, more complex 'attention' networks were commonly found , comprising areas associated with working memory and executive functions. Finally, and very consistently between studies, a 'default mode' network was identified (Fox et al., 2005; Raichle et al., 2001). Interestingly, most of the brain's aerobic glucose consumption at rest is accounted for by the default mode ,attention and cognitive control networks (Vaishnavi et al., 2010).

Due to the limited temporal resolution of fMRI and the indirect measurement of neural activity via the BOLD signal, some groups have attempted to validate RSN with neurophysiological imaging techniques such as electroencephalography (EEG) and magnetoencephalography (MEG). Both modalities have very high temporal resolution, which can extend into the kHz range. Most studies have used the classic EEG frequency bands of 1-3 (delta), 4-7 (theta), 8-13 (alpha), 14-30 (beta) and >30 Hz (gamma), sometimes with further

subdivisions to investigate brain networks. The group of Brookes et al. developed an approach based on a source-reconstructed MEG signal and performing a temporal ICA decomposition, similar to the usual method used in fMRI studies. They were able to detect spatially coherent RSN patterns from MEG data for the majority of fMRI-based resting state networks (acquired separately), including the DMN, sensorimotor, visual, and attentional networks evident across multiple frequency bands (Brookes et al., 2011, 2012). Follow-up single-modality studies using EEG/MEG provided via ICA spatially distinct electrophysiological RSN in multiple frequency bands with good overlap to fMRI networks on source-level (Aoki et al., 2015; Ramkumar et al., 2014; Sockeel et al., 2016).

Over the past decade, several simultaneous EEG-fMRI studies have been conducted to elaborate a link between the known resting state networks from fMRI and electrophysiological networks at rest. Using parallel recordings of EEG and (BOLD-) fMRI, topographic patterns of fMRI activations/deactivations were shown e.g., for alpha-band sensor power (Laufs et al., 2003, 2006). Similarly, RSN fMRI time courses were linked to EEG power but showed a complex interaction of RSN fluctuations and the classical EEG frequency bands, each of which correlated relatively weakly (Mantini et al., 2007). These results suggest that there does not appear to be a direct relationship between historically selected EEG frequency bands and RSN activity. More recent studies have shown that global field potential or global field power (quasi stationary EEG topographic maps, called microstates) on a 100-millisecond time scale can map BOLD fMRI activation patterns on sensor level and are spatially consistent with known resting state networks, such as default mode, sensorimotor and auditory networks (Britz et al., 2010; Musso et al., 2010). A single modality EEG study using EEG microstates on source-level demonstrated spatial correspondence to known fMRI resting state networks (Custo et al., 2017). In 2016, a study using parallel EEG-fMRI calculated hemodynamic response function convolved EEG microstates across all frequencies on source-level. Whereupon an independent component analysis for source level EEG microstates and fMRI to identify stable components across their cohort in both modalities followed (Yuan et al., 2016). They found spatially and temporally specific electrophysiological correlates for the fMRI resting state networks (Yuan et al., 2016). However, in most previously mentioned studies, the EEG analyses were performed at the sensor level, and when source reconstruction was performed, the high time-resolution EEG data were down sampled.

Simultaneous EEG-fMRI studies also observed distinct functional connectivity patterns between different brain networks that reliably occur across time and subjects on sensor-level (Allen et al., 2018). Simultaneous EEG-fMRI studies demonstrated the existance of temporal or spectral EEG patterns stable across resting-state on sensor level (Hunyadi et al., 2019; Labounek et al., 2019), which were similar to EEG resting state networks expressed as scalp potentials in an earlier study (Hiltunen et al., 2014). A simultaneous EEG-fMRI study revealed that shares of resting-state connectivity are expressed across EEG and fMRI (Wirsich et al., 2020). An EEG-fMRI study with a measurement time of 34 minutes found temporal correlation patterns between BOLD fMRI and sensor level EEG power on group level with large inter-subject variability (Meyer et al., 2013)

Moreover, as another indirect marker of neuronal activity, positron emission tomography (PET) imaging using the glucose analogue [^{18}F]-fluoro deoxyglucose ([^{18}F]FDG-) allows imaging and quantification of regional cerebral glucose metabolism (rCGM). It has been shown that group ICA can be used to extract unique RSN from single-frame static [^{18}F]FDG -PET images that are spatially similar to those derived from fMRI data (Di et al., 2012; Savio et al., 2017). Using simultaneous PET/MR in rats, the application of a group ICA on dynamic [^{18}F]FDG-PET data identified brain networks not only from BOLD-fMRI but also from rCGM data (Wehrl et al., 2013). The amplitude of signal fluctuations in RS-fMRI as well as measures of functional connectivity derived from graph theory have been shown to be related to changes in rCGM (Aiello et al., 2015; Tomasi et al., 2013). In summary, the available evidence indicates that vascular BOLD-fMRI RSN fluctuations are linked to neuronal processes, as measured by EEG and MEG as well as rCGM, as measured by [^{18}F]FDG-PET. This attenuates initial doubts, if slow-timescale fMRI- RSN fluctuations are neuronal.

In this study we wanted to test if the characteristic RSN can be identified from a simultaneous hd-EEG, fMRI and [^{18}F]FDG-PET in a cohort of healthy subjects and epilepsy patients. The overarching goal of this study is to provide the basis for the development of a multimodal analysis approaches that can be used in further studies , e.g., for the identification of biomarkers of neuronal diseases.

METHODS

Participants: This study included 29 subjects (mean age: 34.9, age range: 22–49 years, male 35%). 14 subjects were healthy controls, and 15 subjects were diagnosed with non-lesional focal epilepsy based on the International League Against Epilepsy classification (Scheffer et al., 2017). All patients were on antiseizure medication. Healthy controls had never experienced any seizures, were free of any neurological and psychiatric diseases, and were not taking any medication. The study (register number: DRKS00014276) was approved by the local ethic committee (295/2015BO1) and performed in concordance with the principles of the Declaration of Helsinki. All subjects gave informed consent before study participation. The measurements took place at the Universitätsklinikum in Tübingen.

Table 4.3.1: Study population

	Patients with focal epilepsy	*Healthy controls*
Total (N)	15	14
Female n (%)	9 (60.0 %)	10 (71.4 %)
Age mean (m); standard deviation (sd)	m: 36.1; sd: 6.7	m: 34.4; sd: 9.2
Age range	26 - 47	25 - 49
Antiseizure medication	m: 1.8; sd: 0.8	-
range	range: 1 - 3	
Temporal epilepsy	10	-
Extra-temporal epilepsy	5	

Simultaneous EEG, fMRI and PET data acquisition: Before the measurement, all subjects fasted at least 12 h. PET and MRI data very simultaneously assessed on a state of the art 3 T PET/MR scanner (Biograph mMR; Siemens Healthineers, Erlangen, Germany) in supine position with eyes closed. 61 minutes long data sampling was started after intravenous injection of 184.1 ± 8.2 MBq [^{18}F]FDG. MRI comprised a T1-weighted 3D-MPRAGE (magnetization prepared rapid gradient echo) sequence was acquired as high-resolution anatomical reference (TR: 1900 ms, TE 2.49 ms, flip angle: 9°, voxel size: 1 × 1 × 1 mm). In addition, functional MR data were acquired with a gradient-echo planar T2*-weighted sequence covering the entire brain

(TR: 2.5 s, TE: 32 ms, voxel size: 3.5 × 3.5 × 3.5 mm, anterior-posterior (AP) phase encoding). To correct the functional MR images for distortions 15 volumes with reversed phase-encoding (posterior-anterior) were also acquired for each subject. Simultaneous Hd-EEG acquisition was done using a 256-channel EEG system (Electrical Geodesics, Inc., Eugene, OR, U.S.A.) with a sampling rate of 1 kHz. The simultaneous hd-EEG-fMRI-[^{18}F]FDG PET measurements were performed during the first 30 min.

Hd-EEG processing: To remove MR gradient as well as ballistocardiogram artifacts we applied the algorithms implemented in the manufacturer's software (Geodesic EGI tools, version: 5.4.2 (r29917)). The gradient artifact was removed via an average artifact subtraction method. This method constructs an average gradient artifact template for each EEG sensor channel and applies a template subtraction at the TR-trigger events from the raw EEG sensor signal. To detect and reject ballistocardiogram artifacts we used the algorithm from Niazy et al. (Niazy et al., 2005). Principal component analysis is applied to the EEG sensor data, temporally linked to the detected cardiac events in the data. Components describing the BCG artifacts were selected based on their contribution to the explained variance. Together, these construct the optimal basis set (OBS) of BCG artifacts. Such OBS have been used for adaptive artifact removal (Niazy et al., 2005).

Further preprocessing and analysis steps on simultaneous hd-EEG data were performed using the Fieldtrip toolbox (https://www.fieldtriptoolbox.org/, version 20191127) running in Matlab (version 9.5.0.1298439 (R2018b) Update 7, Mathworks Inc.). At first, we applied a Butterworth band-pass filter with 1 Hz high pass and 70 Hz low pass on the simultaneous resting-state hd-EEG data. Additionally, to account for line noise, a 50 Hz band stop filter was applied as well as for its 100 Hz and 150 Hz harmonics. For computational proposes we then downsampled the data to 250 Hz. The continuous hd-EEG data was divided in trials of 2.5 seconds lengths each synchronized by the MR-scanner's TR trigger event, resulting in 720 trials for each dataset. We visually inspected each trial and rejected noisy trials and/or trials artifacts contaminated by eye movements, blinks, cardiac, and muscle activity. Afterwards, an independent component analysis (ICA) was applied on the sensor-level data to identify and also reject components that representing residual electrocardiogram and blink/eye movement artifacts. An experienced clinician (E.-C. Heide) further identified and marked any

trial in the patient group data showing interictal discharges (IEDs). Those trials were also rejected together with the trials immediately before and after the IEDs trial.

Forward modelling and source analysis: An individual cortical surface based on their anatomical MR image was reconstructed for each subject using FreeSurfer (https://surfer.nmr.mgh.harvard.edu, version 6.0.0) and subjected to SUMA (https://afni.nimh.nih.gov). By using the SUMA toolbox, the cortical surface of each subject was reduced to a fixed number of vertices (ld: 10, resulting in 2004 cortical vertices) based on the 'fsaverage' template (FreeSurfer). Additionally, the surface of six subcortical nuclei (bilateral amygdala, hippocampus, thalamus, caudate, putamen and pallidum) were reconstructed using a total of 334 vertices from the fsaverage template. By using the inverted DARTEL transformation (DARTEL; SPM12; https://www.fil.ion.ucl.ac.uk/spm/software/spm12) we transformed those standardized subcortical vertices back to the individual anatomical space, resulting in a total of 2338 vertices for each subject, with each vertex characterized to correspond to an anatomical point-by-point correspondence for cortical and subcortical regions across all subjects. Lastly, we aligned each subject's individual surface map to a CTF space by using anatomical landmarks of fiducial positions (left/right preauricular point, nasion). With regard to the source reconstruction, an individual boundary element model (BEM) with three layers of different conductivity (scalp: 0.33 S/m, skull: 0.004 S/m, brain: 0.33 S/m) was constructed using the 'dipoli' method implemented in Fieldtrip. The hd-EEG sensor time series were band-pass filtered into the common EEG frequency bands (delta 0-4 Hz, theta 4-8 Hz, alpha 8-12 Hz, beta1 12-20 Hz, beta2 21-29 Hz, and gamma 32-48 Hz). Source reconstruction was performed by applying dynamic imaging of coherent sources (DICS), a beamformer method, (λ regularization: 5%) for each frequency band separately (Gross et al., 2001). It was shown that beamformer methods are able to attenuate residual gradient and BCG artifacts (Brookes et al., 2008; Uji et al., 2021). A set of adaptive spatial filters is calculated by the DICS method, and the hd-EEG sensor level time courses were reconstructed in each source space vertex for each frequency band. To retain a continuous time series for the further processing, rejected trials were replaced with a subject-specific average trial from all non-rejected trials. Finally, a Hilbert-transformation was applied to provide the instantaneous integrated power of each hd-EEG trial and each frequency band.

fMRI data preprocessing: First, a slice-time correction was applied to the fMRI data (SPM12, version 7487), followed by an estimation of head movement using the Linear Image Registration Tool (FSL version 6.0.3, MCFLIRT) (Jenkinson, 2002) as well as a distortion correction utilizing the reversed phase-encoded scan (FSL, topup) (Andersson, Skare, & Ashburner, 2003). Further processing and analysis steps were performed using the CONN toolbox (www.nitrc.org/projects/conn, RRID:SCR_009550) (Whitfield-Gabrieli & Nieto-Castanon, 2012). The Artifact Detection Tools (ART) implemented in CONN identified outlier scans ('conservative' settings), if the observed global BOLD signal change was >3 standard deviations and/or the amount of head movement was greater than 0.5 mm. In addition, in patients with spike discharges, the corresponding fMRI volume and the following nine volumes (=18 seconds) were marked as outliers in the fMRI data and rejected from the further analysis. Spatial alignment of the mean functional MR dataset to the anatomical T1 reference of each subject was done. Spatial segmentation of the anatomical T1 into tissue classes using the unified segmentation in SPM12 resulting in six tissue classes (grey-matter, white-matter, skull, scalp, cerebrospinal fluid, and others) and a non-linear transformation of each individual T1 scan to the MNI152 T1 reference was done. This transformation matrix was also applied to all fMRI volumes and the segmentation masks to spatially normalize those to the MNI152 space. Furthermore, the fMRI data was smoothed using a Gaussian kernel of 8 mm full width at half maximum. To further control for spurious effects of head motion, and cardiac and respiratory rhythms, each subject's data was corrected by partial regression in CONN removing the following confounds: six motion parameters (three rotation and three translation parameters, based on the MCFLIRT rigid body transformation), subject-specific confounding factors that modelled nuisance signals within the segmentation masks of white matter (three PCA parameters) and cerebrospinal fluid (three PCA parameters). Finally, the BOLD time series was band-pass filtered at 0.008-0.09 Hz.

PET data preprocessing: Dynamic PET data (61 frames à 60 s) were reconstructed using a 3D Ordinary Poisson ordered-subset expectation-maximization (OP-OSEM) algorithm (3 iterations, 21 subsets, 344 matrix size and post-smoothing by a 4-mm Gaussian filter). PET data were corrected for decay, scatter and randoms as well as for attenuation by means of a MR-based attenuation correction (AC). based on an ultra-short echo-time (UTE) sequence with the following imaging sequence parameters: TR: 4.64 ms, TE: 2.46 ms, flip angle: 10°, slice

thickness: 1.5625 mm, field of view: 300 mm x 300 mm, and matrix size: 192 x 192. Further processing steps were performed using the SPM toolbox (SPM12, version 7487). A spatial co-registration of the averaged dynamic [^{18}F]FDG-PET dataset to the anatomical T1 reference of each subject was performed. This transformation matrix was used to spatially normalize all [^{18}F]FDG PET volumes to the MNI152 space. Finally, the [^{18}F]FDG -PET data was smoothed using a Gaussian kernel of 8 mm full-width at half maximum.

Group ICA analysis: We applied group spatial ICA on all subjects on the full-time length of pre-processed fMRI and ^{18}FDG-PET datasets as implemented in the toolbox GIFT (v4.0c, http://icatb.sourceforge.net) (Calhoun et al., 2001) using the FastICA algorithm (Hyvärinen & Oja, 1997). Additionally, the software package ICASSO was used to improve the robustness of the ICA results (Himberg, Hyvärinen, & Esposito, 2004). Briefly, ICASSO repeatedly performs group-ICA and calculates a similarity measure between the independent components from each run and identifies clusters for ICs that originate from the same underlying independent source. The resulting estimates for the ICs are those that show the highest similarity to the other estimates in the respective clusters. In this work the ICASSO is performed with 10 re-runs each with random initial conditions (Himberg et al., 2004). For the ^{18}FDG-PET data, the group ICA was set to extract 20 components based on previous studies (Di et al., 2012). For the fMRI data, we empirically chose to extract 40, guided by the estimated mean number of 43 components based on the in the GIFT toolbox implemented minimum description length criterion estimation (Akaike, 1974; Calhoun et al., 2001). The beta weights of the resulting independent components were z-transformed and visually inspected to reject noise/artifact components. All remaining non-thresholded component were spatially correlated to the Yeo7 functional network atlas (Yeo et al., 2011) to assign them to one of the following atlas brain networks: visual-, somatomotor-, dorsal attention-, ventral attention, limbic-, frontoparietal-, and default mode network. Thus, the components derived from fMRI and ^{18}FDG-PET were identified as components that represent one whole or discernible parts of a of an established functional resting state network. Additionally, the resulting independent components identified from fMRI data were transformed and resampled from 3D MNI space to the surface vertices (SUMA and subcortical surface).

In order to extract IC from the hd-EEG data, we utilized the toolbox EEGIFT, which is related to the GIFT toolbox (Eichele et al., 2011). The analysis workflow is identical to the group-ICA

analysis performed with GIFT, but it applies group-level ICA analysis not in the spatial but in the temporal domain (Nugent et al., 2017; Nugent et al., 2015). In temporal group-ICA, temporally independent ICs are identified from the data by maximizing the statistical independence of time courses (Bridwell, Wu, Eichele, & Calhoun, 2013; Eichele, Calhoun, & Debener, 2009; Huster, Plis, & Calhoun, 2015; Wu, Eichele, & Calhoun, 2010). Because the mean number of components estimated by the in the EEGIFT toolbox implemented minimum description length criterion estimation was extremely high we followed an empirical approach of determining the amount of group independent components to extract. We further performed temporal group-ICA on the EEG datasets with 80 components to be identified (henceforth referred to as group-ICA_{80}). We further identified five additional different amounts of components from the data from 50 to 100 ICs (group-ICA_{50}, group-ICA_{60}, group-ICA_{70}, group-ICA_{90}, and group-ICA_{100}). To obtain the most robust components, we used the ICASSO technique (ten re-runs) as in the group-ICA application on fMRI and ^{18}FDG-PET data. The beta weights of the resulting independent components of each frequency band were z-transformed. To identify the components derived from hd-EEG data as functional resting state networks, we attempted to spatially correlate all hd-EEG components with the components identified from fMRI data, which were identified as established resting state networks according to the Yeo7 atlas for functional networks.

In order to control for chance findings and to estimate the significance of spatial resting-state hd-EEG ICs correlates to brain networks, we generated surrogate datasets by shuffling the EEG sensors of hd-EEG data of each subject. This was done ten times yielding ten different surrogate datasets for each subject. For the surrogate data sets, an identical analysis was performed as for the real data including the source reconstruction and ICA. For each frequency band and each number of group-independent components, 50 permutations of temporal group-ICA analysis were performed. In each permutation, a randomized surrogate hd-EEG data set was used for each subject. Each permutation yielding 80 group-ICA_{80} components (analogously, the number of resulting components varies for the other group ICA approaches: group-ICA_{50} to group-ICA_{100}). The cross-modal correlation to the fMRI components was then also performed for 400 components (group-ICA_{80}) based on surrogate datasets. Only cross-modal spatial correlation values of the real data component that surpassed the 99.9th percentile of the surrogate data components were considered significant ($p < 0.001$). The

resulting p-values were further corrected for multiple comparisons using false discovery rate and a cutoff of $p_{FDR} < 0.05$ (Benjamini & Hochberg, 1995).

Results

Among the 40 fMRI components, twenty-two were identified as brain network related components. Of the 20 [^{18}F]FDG-PET components, 13 showed spatial correlation with the Yeo7 resting state networks. In both modalities, at least one component was assigned for each functional brain network atlas (fMRI, r: 0.25-0.58, $p < 0.001$; ^{18}FDG-PET, r: 0.14-0.51, $p < 0.001$). For visualization purposes, a threshold value of 7 was applied to the ICA component maps for fMRI and [^{18}F]FDG-PET. We decided empirically that for group ICA applied on our hd-EEG data the extraction of 80 group components provided the most presentable results compared to the other approaches of component amounts (Appendix C table 1; Appendix C figure 2). For visualization purposes, the hd- EEG group ICA components were treated with a threshold value of 2.

Visual network: For fMRI, three components with significant spatial correlation (r: 0.49-0.58, $p_{FDR} < 0.001$) to the visual functional network atlas were identified, each comprising the occipital ($fMRI_{\#10}$), medial ($fMRI_{\#17}$), and lateral ($fMRI_{\#22}$) parts of the visual network (Figure 4.3.1). From the [^{18}F]FDG-PET data one component was identified ($PET_{\#18}$) with a spatial correlation of 0.45, distributed spatially across the medial parts of the visual network. For the hd-EEG data, we found one component that reached statistical significance against the surrogate permutation results. The component was found in the beta1 ($EEG_{\#30}$) frequency band and represented the medial visual network ($fMRI_{\#17}$) with significant spatial correlation (r: 0.52, $p_{FDR} < 0.001$) (Figure 4.3.1).

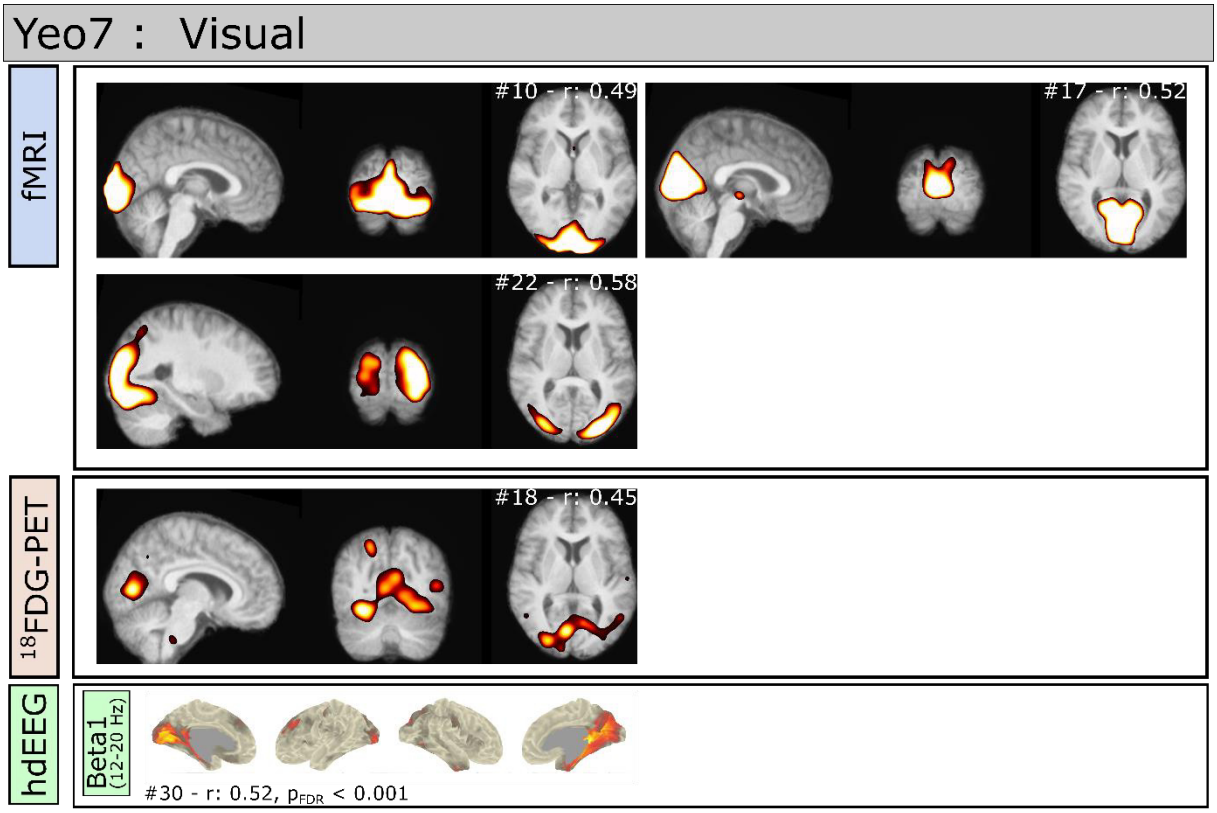

Figure 4.3.1: ***: Visual network components from fMRI, [18]FDG-PET, and hd-EEG.***
Three components from fMRI data and one component from [18]FDG-PET data were identified that showed spatial correlation with the visual network atlas. For hd-EEG, one component was found in the beta1 frequency band. Only significantly correlated ($p_{FDR} < 0.05$) hd-EEG components are shown.

Somatomotor network From fMRI data three components corresponding to the somatomotor network were identified. All three with significant spatial correlations (r: 0.40-0.59, $p_{FDR} < 0.001$) to the Yeo7 reference network (Figure 4.3.2), each comprising a different part of the Yeo7 somatomotor functional network, namely the central-superior ($fMRI_{\#16}$), superior-lateral ($fMRI_{\#13}$), and lateral ($fMRI_{\#08}$) parts were identified. For ^{18}FDG-PET, one component ($PET_{\#20}$) showed spatial correlation (r: 0.23, $p_{FDR} < 0.001$) to the somatomotor functional network. The ^{18}FDG-PET component represented the superior-lateral part of the somatomotor network. From the identified components of the hd-EEG data, only one component exceeded the statistical significance threshold from the surrogate permutations. This component in beta1 showed significant spatial correlations ($EEG_{\#20}$, r: 0.60, $p_{FDR} < 0.001$) to the component derived from fMRI data comprising the central-superior network area ($fMRI_{\#16}$).

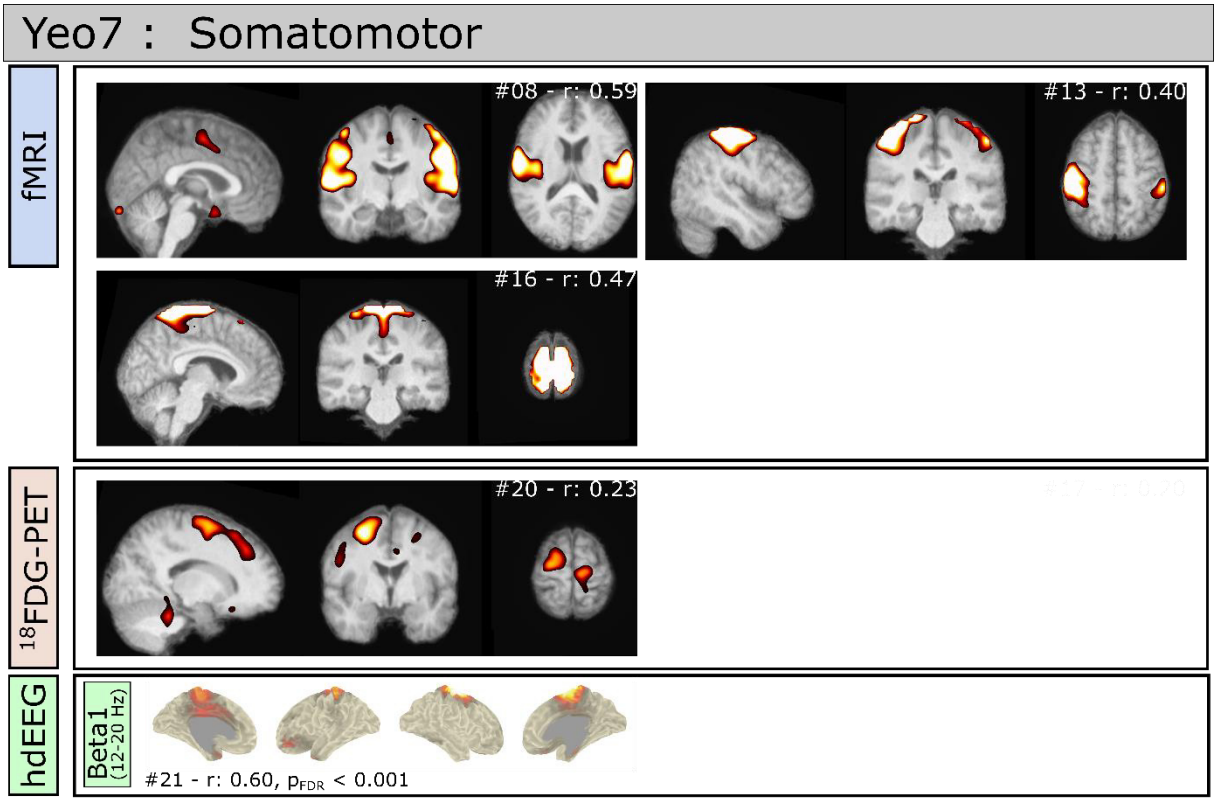

Figure 4.3.2 : Somatomotor network components from fMRI, ^{18}FDG-PET, and hd-EEG.
Three components from fMRI data and one component from ^{18}FDG-PET data were identified that showed spatial correlation with the somatomotor network. One component was identified from hd-EEG in the beta1 frequency band, which showed spatial correlation to the fMRI components of the visual network. Note that component fMRI$_{\#16}$, ^{18}FDG-PET$_{\#16}$, and the three components from the hd-EEG analysis (Beta1: EEG$_{\#21}$) represent the same sub-network of the somatomotor network. Further, only significantly correlated hd-EEG components are shown.

Dorsal Attention network: From fMRI data one component was identified (fMRI$_{\#33}$) with spatial correlation of 0.44 ($p_{FDR} < 0.001$) to the dorsal attention network from the Yeo7 atlas (Figure 4.3.3). Also, from ^{18}FDG-PET data one component (PET$_{\#16}$) was identified, spatially correlated (r: 0.25, $p_{FDR} < 0.001$) with the right hemispheric part of the dorsal attention network of the Yeo7 atlas. For hd-EEG, group-ICA$_{80}$ did not identify any component that showed spatial correlation with dorsal attentional components of the fMRI data exceeded the threshold set by the surrogate data. However, group-ICA$_{100}$ yielded one component spatially related to the dorsal attention network component derived from fMRI data (Appendix C figure 2).

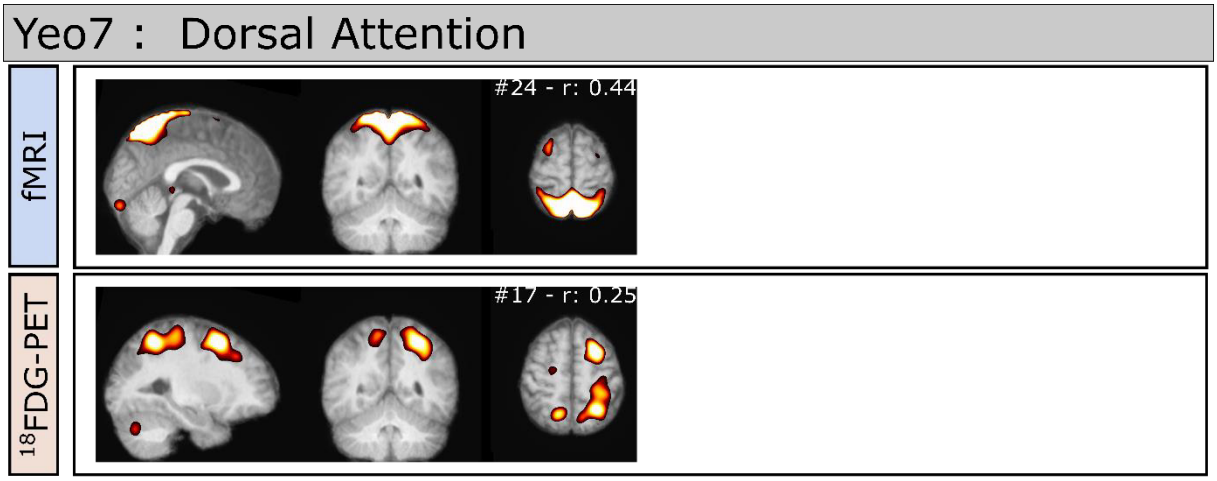

Figure 4.3.3 : Dorsal attention networks components from fMRI and ^{18}FDG-PET.
One component from fMRI data and one component from ^{18}FDG-PET data were identified that showed spatial correlation with the dorsal attention network atlas. No component was identified from hd-EEG data that surpassed the significance threshold set by surrogate data. Note that component fMRI$_{\#24}$, and ^{18}FDG-PET$_{\#17}$ spatially overlap and represent the same share of the dorsal attention network.

Ventral attention network: For fMRI data, one component (fMRI$_{\#28}$) with significant spatial correlation (r: 0.48, $p_{FDR} < 0.001$) was identified, mapping the ventral attention network from the Yeo7 atlas (Figure 4.3.4). Furthermore, from ^{18}FDG-PET data one component showed spatial correlation of 0.24 ($p_{FDR} < 0.001$) to the ventral attention network. The components identified by fMRI and ^{18}FDG-PET showed no spatial overlap. No hd-EEG components derived from group-ICA$_{80}$ showed spatial significant correlation with the ventral attentional components identified in the fMRI data.

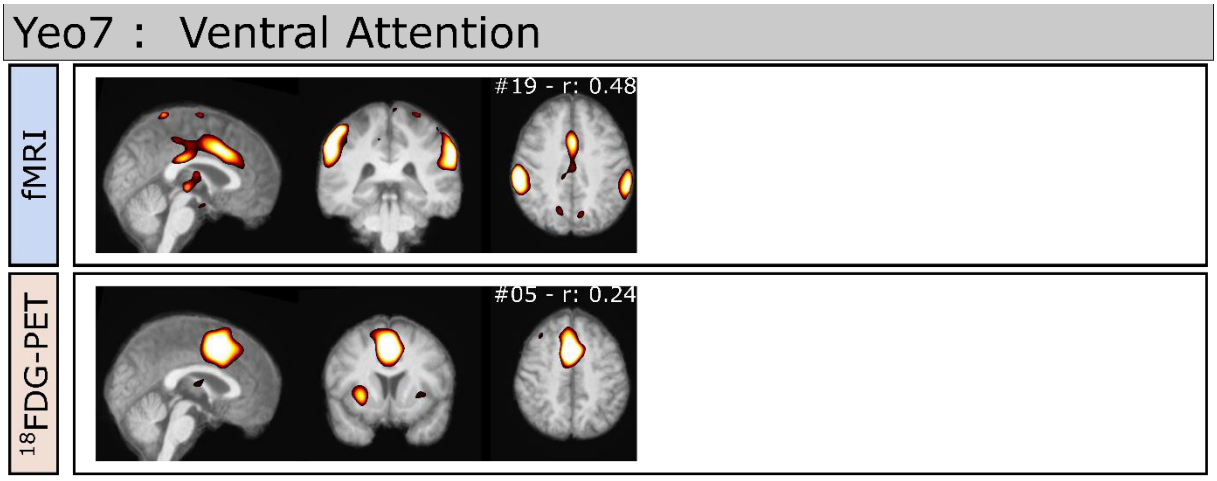

Figure 4.3.4: Ventral attention networks components from fMRI and ^{18}FDG-PET.
One component from fMRI data and one component from ^{18}FDG-PET data were identified that showed spatial correlation with the ventral attention network atlas. No component from hd-EEG surpassed the threshold set by surrogate data. Note that the depicted components fMRI$_{\#19}$ and ^{18}FDG-PET$_{\#24}$ spatially overlap in the midline part of the ventral attention network.

Limbic network: For fMRI, two components were identified with spatial correlation ($fMRI_{\#09}$, r: 0.42, $p_{FDR} < 0.001$; $fMRI_{\#29}$, r: 0.36, $p_{FDR} < 0.001$) to the limbic functional network atlas (Figure 4.3.5). The frontal part of the limbic network atlas is visible in $fMRI_{\#09}$, and $fMRI_{\#29}$. From ^{18}FDG-PET data, three components were identified with spatial correlation to the limbic functional network. One component ($PET_{\#04}$, r: 0.14, $p_{FDR} < 0.001$) represents the frontal portion of the limbic network. The other two components ($PET_{\#07}$, r: 0.19, $p_{FDR} < 0.001$; $PET_{\#19}$, r: 0.23, $p_{FDR} < 0.001$) each comprised a hemispheric part of the temporo-frontal portion of the limbic network atlas. For hd-EEG no components were found via group-ICA_{80} that reached statistical significance against the surrogate permutation results for the limbic network. With 60 and 70 independent components (group-ICA_{60}/group-ICA_{70}) we found for each analysis one component spatially related to the limbic network and exceeding the statistical significance threshold from the surrogate permutations (Appendix C figure 2).

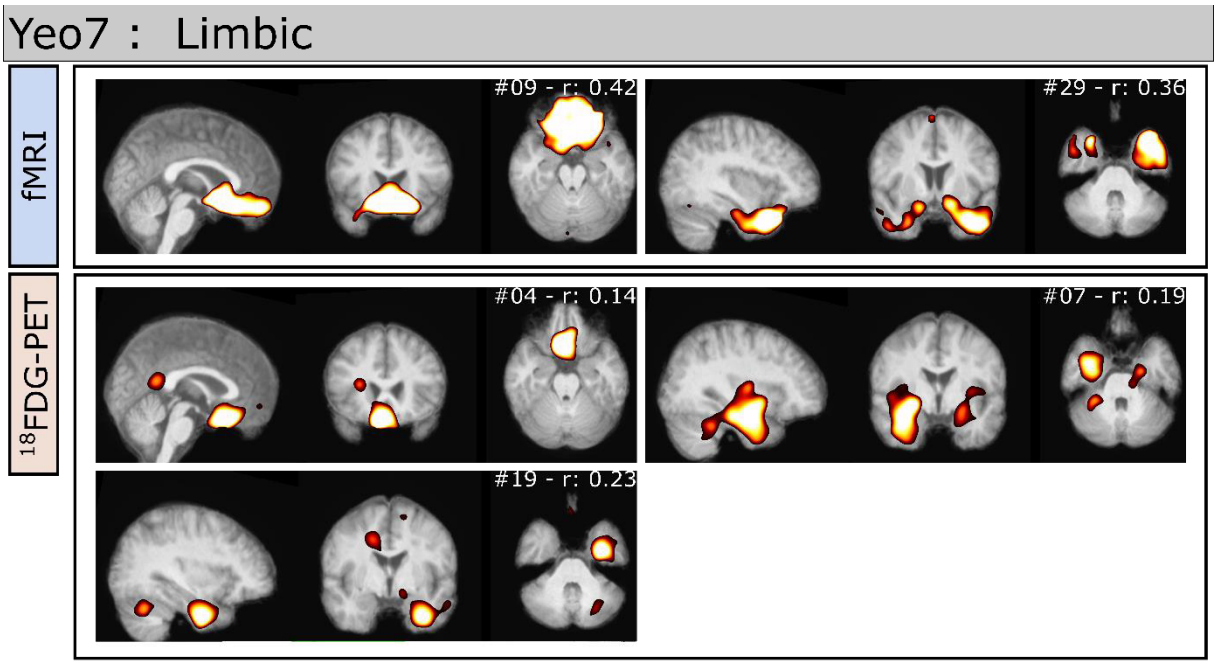

Figure 4.3.5: Limbic network components from fMRI and ^{18}FDG-PET.
Two components from fMRI data and three components from ^{18}FDG-PET data were identified that showed spatial correlation with the limbic network atlas. No component was identified from hd-EEG that surpassed the threshold set by surrogate data. Note that component $fMRI_{\#29}$ is represented as two components in the ^{18}FDG-PET data ($^{18}FDG\text{-}PET_{\#07}$, $^{18}FDG\text{-}PET_{\#19}$).

Frontoparietal network: From fMRI data, five components were identified with spatial correlations ($fMRI_{\#14}$, r: 0.38, $p_{FDR} < 0.001$; $fMRI_{\#15}$, r: 0.39, $p_{FDR} < 0.001$; $fMRI_{\#23}$, r: 0.38, $p_{FDR} < 0.001$; $fMRI_{\#30}$, r: 0.25, $p_{FDR} < 0.001$; $fMRI_{\#40}$ r: 0.43, $p_{FDR} < 0.001$) to the frontoparietal network

atlas (Figure 4.3.6). Each component comprised a different share of the network. For ^{18}FDG-PET, one component was identified with spatial correlation (r: 0.24, $p_{FDR} < 0.001$) to the right hemispheric share of the frontoparietal network from the Yeo7 network atlas.

From hd-EEG data, two components were identified from hd-EEG in the frequency bands alpha, and gamma to the identified fMRI components of the frontoparietal network. The component found in the alpha frequency band ($EEG_{\#62}$) showed significant spatial correlation (r: 0.41, $p_{FDR} < 0.001$) to the fMRI component ($fMRI_{\#23}$) comprising the bilateral fronto-parietal share of the functional network. The other component ($EEG_{\#42}$) found in the gamma frequency band represented the fronto-medial share of the frontoparietal network ($fMRI_{\#40}$) with significant spatial correlation (r: 0.41, $p_{FDR} < 0.05$).

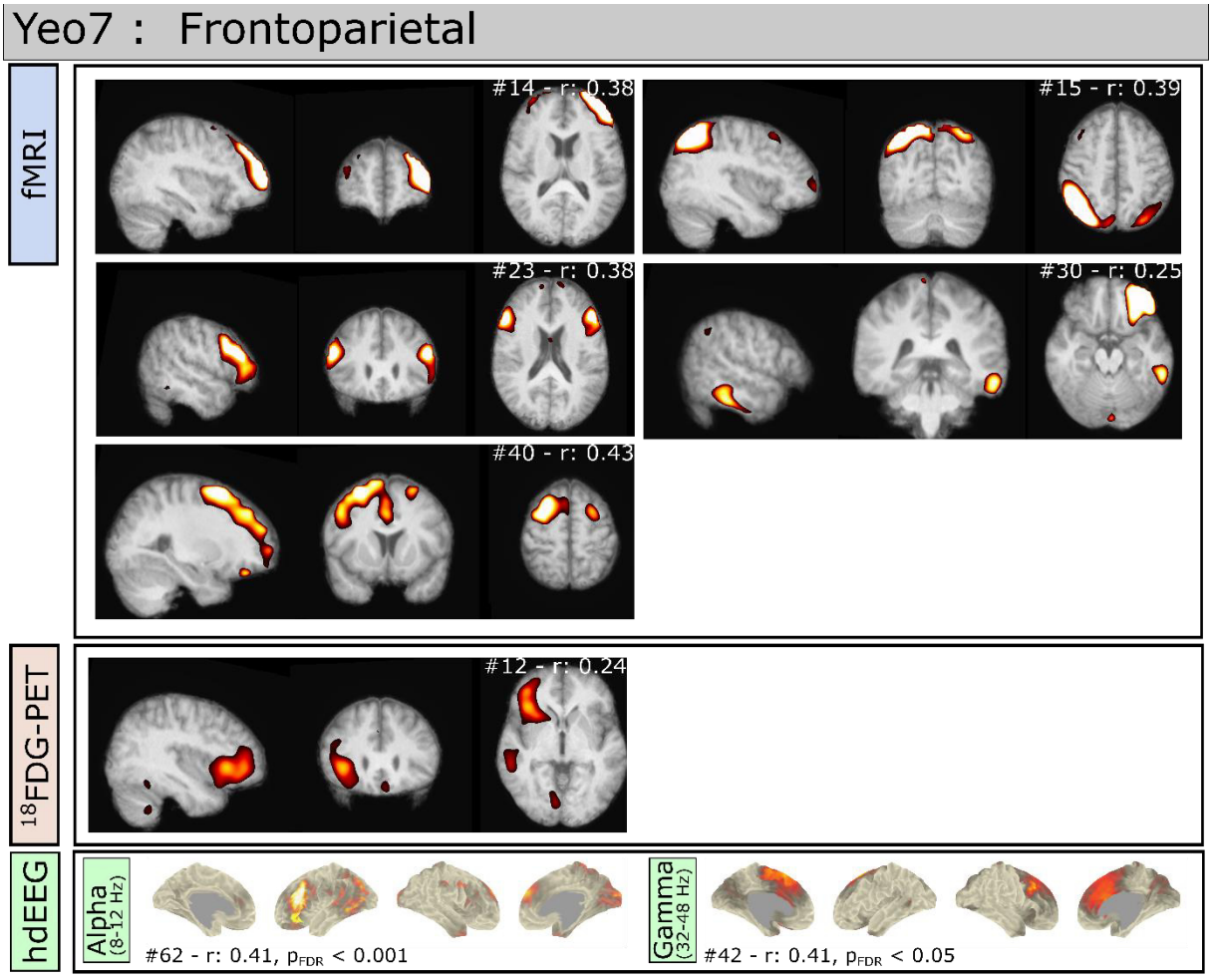

Figure 4.3.6: Frontoparietal network components from fMRI, ^{18}FDG-PET, and hd-EEG.
Five components from fMRI data and one component from ^{18}FDG-PET data were identified that showed spatial correlation with the frontoparietal network atlas. Two components were identified from hd-EEG data from the alpha and gamma frequency bands which showed spatial correlation with the fMRI components of the frontoparietal network. Only significantly correlated ($p_{FDR} < 0.05$) hd-EEG components are shown.

Default mode network: From fMRI data, five components with spatial correlation ($fMRI_{\#11}$, r: 0.25, $p_{FDR} < 0.001$; $fMRI_{\#28}$, r: 0.52, $p_{FDR} < 0.001$; $fMRI_{\#31}$, r: 0.34, $p_{FDR} < 0.001$; $fMRI_{\#33}$, r: 0.37, $p_{FDR} < 0.001$; $fMRI_{\#36}$, r: 0.30, $p_{FDR} < 0.001$) to the default mode network (DMN) were identified (Figure 4.3.7). Each component mapped different spatial shares of the DMN. For ^{18}FDG-PET, two components with spatial correlation ($PET_{\#02}$, r: 0.28, $p_{FDR} < 0.001$; $PET_{\#15}$, r: 0.28, $p_{FDR} < 0.001$) to the DMN of the Yeo7 network atlas was found. For hd-EEG data, we found four components that reached statistical significance against the surrogate permutation results. One component ($EEG_{\#09}$) was found in the delta frequency band with spatial correlation (r: 0.54, $p_{FDR} < 0.05$) to the fMRI component ($fMRI_{\#28}$) representing the frontal share of the default mode network. One hd-EEG component each was found in the alpha ($EEG_{\#70}$), and beta2 ($EEG_{\#62}$), and gamma ($EEG_{\#55}$) frequency band spatially correlating (r: 0.38-0.44, $p_{FDR} < 0.05$) with the fMRI ($fMRI_{\#33}$) component imaging the medial-occipital share of the DMN.

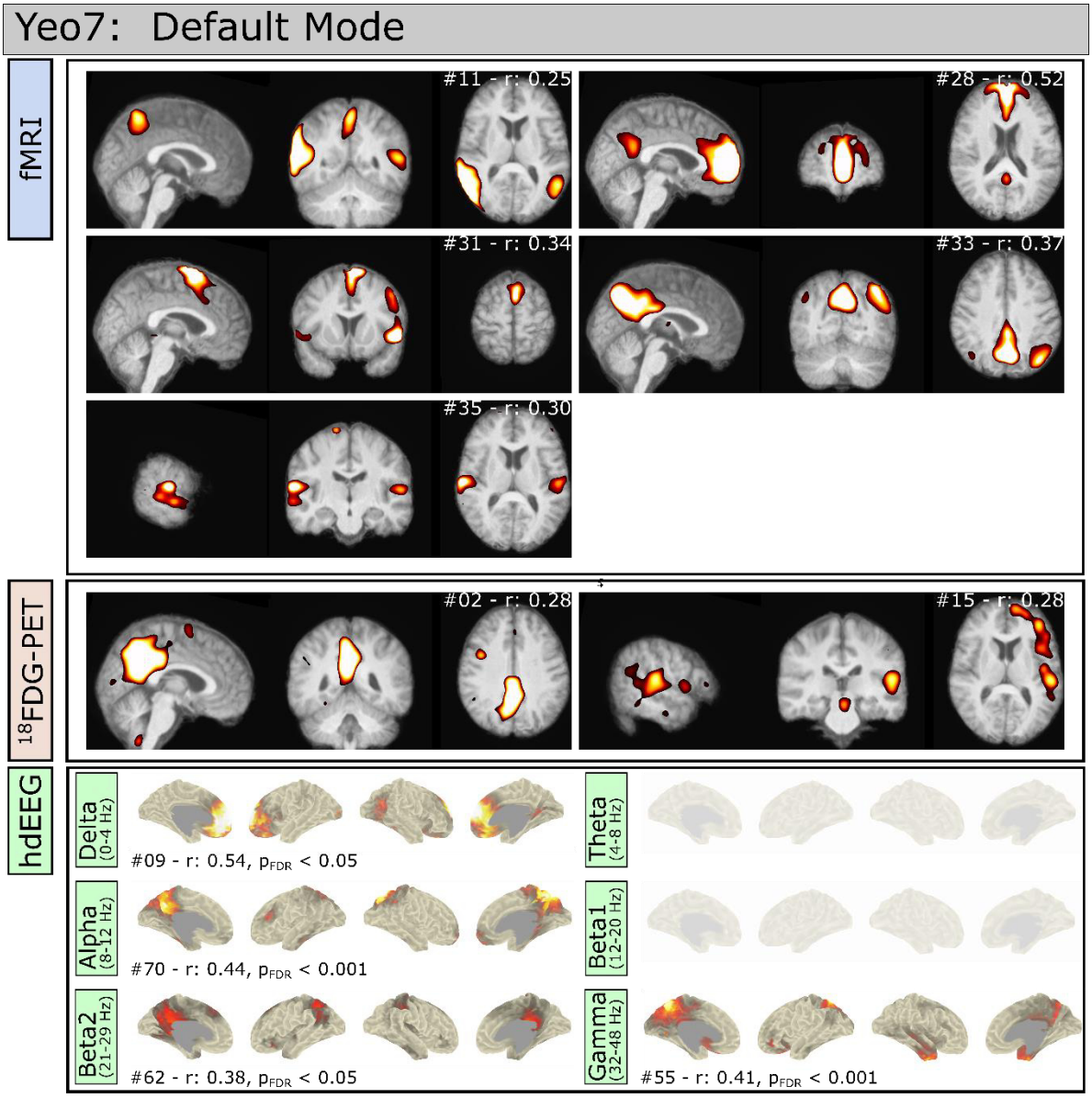

Figure 4.3.7 Default mode network components from fMRI, ^{18}FDG-PET, and hd-EEG.
Five components from fMRI data and two components from ^{18}FDG-PET data were identified via group-ICA that showed high spatial correlation with the default mode network atlas. Four components were identified from hd-EEG data from the delta, alpha, beta2, and gamma frequency bands which showed spatial correlation with the fMRI components of the default mode network. Note that component fMRI$_{\#33}$, ^{18}FDG-PET$_{\#02}$, and the three components from the EEG analysis (Alpha: EEG$_{\#70}$; Beta2: EEG$_{\#62}$, and Gamma: EEG$_{\#55}$) spatially represent the same medial-occipital share of the default mode network.

Discussion

We investigated RSN of three simultaneously measured modalities using a data-driven approach, namely group-level independent component analysis (group-ICA). We showed that, in addition to the established identification of brain networks from fMRI data, it is possible to

detect RSN from the parallel recorded hd-EEG and ^{18}FDG-PET. For most (four of seven) of the typical RSN known from fMRI, we could identify corresponding networks for both hd-EEG and ^{18}FDG-PET from the simultaneous data. However, for the dorsal and ventral attention as well as the limbic network of the Yeo7 atlas no components from hd-EEG data were found that surpassed the surrogate-data threshold.

BOLD/fMRI networks: In this study, all components of the resting-state network derived from fMRI data were comparable to the results of previous studies (Di et al., 2012; Smith et al., 2009; Yeo et al., 2011). Cole et al. identified eight of the most common and consistent RSN (Cole, 2010). With our analysis, we were able to identify these eight RSN, with some RSN (e.g., somatomotor network) consisting of multiple components, i.e., sub-networks. This is probably due to the selected number of components to be identified in the group-ICA. Even though it has already been shown that a higher number of components in the group ICA increases the difficulty to identify and classify the components (Tohka et al., 2008), all non-artifact components derived from fMRI data in this study showed spatial correlations to the networks from the Yeo7 atlas. Despite the reported signal dropout and spatial distortion of BOLD images in the orbitofrontal and anterior temporal cortex (Yeo et al., 2011), we observed components with moderate spatial correlation ($r>0.36$) to the limbic network.

18[F]FDG-PET networks: Our findings for the networks derived from ^{18}FDG-PET data are coherent with previous findings revealing metabolic brain networks in humans (Di et al., 2012; Savio et al., 2017). Similar to our findings, they identified components spatially matching RSN, such as visual, somatomotor, ventral attention (salience network) (Di et al., 2012), dorsal attention (central executive), frontotemporal (central executive network), and DMN (Di et al., 2012; Savio et al., 2017; Trotta et al., 2018). In contrast to those studies, we were not able to extract multiple components spatially describing the visual networks (Di et al., 2012; Savio et al., 2017; Trotta et al., 2018). However, we found the somatomotor, and DMN network to be expressed in multiple (sub-)components. Compared to the fMRI components derived in this study, the number of components was smaller for most of the networks derived from ^{18}FDG-PET (e.g., frontoparietal and DMN networks). This is consistent with the results of a previous study (Di et al., 2012). They hypothesized that the absence of these networks in ^{18}FDG-PET data could be due to: (I) their use of static properties of brain metabolic activities, (II) inter-

regional connectivity beyond the temporal resolution of ^{18}FDG-PET, or (III) differences in measurement environments with respect to noise during measurement (Di et al., 2012). Based on the simultaneous measurement of imaging modalities in our study, we can exclude the difference in acquisition surrounding as cause in our data. The reasons for the absence of these networks in the data are rather, the temporal resolution of the PET modality or its different signal origin (metabolic) compared to BOLD-fMRI. In a previous study, it was found that sufficiently different incoherence of activities in the data causes the group ICA components to split into subnetworks due to the independence thus created (Eichele et al., 2009). Therefore, we can assume, that the fronto-temporal fMRI component spatially correlating the Yeo7 limbic network, identified as two components from the ^{18}FDG-PET data, had a more pronounced difference in activity at the metabolic level than it does at the vascular level.

Neural networks: With this work, we provided evidence for temporal group-ICA to be able to extract independent components in source space from simultaneous hd-EEG/fMRI/^{18}FDG-PET measurements, correlating to an established network atlas derived from fMRI data (Yeo et al., 2011).

Our findings are in line with previous work identifying resting-state components from non-parallel MEG-fMRI, EEG, and one parallel EEG-fMRI data corresponding to: default-mode, (Aoki et al., 2015; M.J. Brookes, Woolrich, et al., 2011; Mantini et al., 2007; Shou et al., 2020; Sockeel et al., 2016; Yuan et al., 2016), visual, sensorimotor, frontoparietal (Aoki et al., 2015; M.J. Brookes, Woolrich, et al., 2011; Mantini et al., 2007; Shou et al., 2020; Sockeel et al., 2016; Yuan et al., 2016). One study also observed left and right frontoparietal networks divided in four components (M.J. Brookes, Woolrich, et al., 2011), which is in line with our findings. We did not find components that are spatially correlated to the dorsal attention network from the Yeo7 atlas with 80 components to be identified via group-ICA. However, with a different number of components to be identified (group-ICA$_{100}$), we found one component in the beta1 frequency band spatially correlated to the dorsal attention network. This is in line with previous findings from a study, which correlated the timecourses of resting-state network components derived from fMRI data via ICA and the power variations in EEG sensor-level during a parallel EEG-fMRI measurement (Mantini et al., 2007). They found that the dorsal attention network had strong relationship to the alpha and beta rhythms of their EEG sensor-

power fluctuations (Mantini et al., 2007) , which fits our identification of the dorsal attention network in the beta1 frequency band. In contrast to a previous study, which identified the right-hemispheric lateral parietal share of the ventral attention network in the alpha band frequency (Aoki et al., 2015), we did not observe a component spatially describing the ventral attention network. Various factors can be responsible for not identifying the ventral attention network in our hd-EEG data, e.g., the size of our cohort, and technical features. The study by Aoki et al. analysed the 19-channel EEG data of 80 subjects without a parallelly measured fMRI, while we investigated the hd-EEG data of 29 subjects of a parallel measurement of hd-EEG/fMRI/[^{18}F]FDG-PET. This difference in measurement conditions alone could be the reason for the difference in our results.

Interestingly, with our analyses of group-ICA$_{60}$ and group-ICA$_{70}$, we found a similar component in both analysis approaches that exceeded the surrogate threshold and appears to represent the limbic functional network from the Yeo7 atlas (see Appendix C Figure 2). To our knowledge, identification of the limbic network is not an established observation in studies examining EEG data with parallel recorded fMRI data. Because the spatial correlations of the hd-EEG components of group-ICA$_{80}$ to the fMRI components are higher compared to other group-ICA approaches, we decided to use 80 components as parameters for the results shown in the main part of this study. Due to the consistent appearance of components (e.g., DMN) and the appearance of other RSN (e.g., limbic, and dorsal attention network) under certain numbers of components to be identified suggests that there is no ideal number of components which serves as parameters for a group-ICA on resting-state hd-EEG data with parallel recorded fMRI/[^{18}F]FDG -PET.

Consistent with our assumption, we observed multiple hd-EEG components distributed in one or more frequency bands that map the same network portion of an fMRI component (e.g., frontal, and occipital DMNs). This could be due to the higher temporal resolution of the EEG, where temporal independence was found and led to a splitting of the components, or to the nature of the group ICA, as the algorithm could have separated the components arbitrarily, e.g., as a result of extracting too many components (Särelä & Vigário, 2003). To control for this, we applied component analyses on EEG data with other numbers of components (see Appendix C table 1), which in most cases identified similar numbers of significant components in comparable localizations with variations in their spatial extent (see Appendix C table 1). This

is in accordance with the experience of the authors who introduced the EEGIFT toolbox (Eichele et al., 2011). Consequently, a spatial correlation was also found between all components identified with 80 ICs to extract and for all other group-ICA approaches with other amounts of ICs to extract (see Appendix C figure 1). Furthermore, for the other group-ICA approaches, some of the components from group-ICA with 80 ICs were found in different frequency bands (see Appendix C figure 2). This is supported by previous findings, that hypothesized that there is no strong relationship between historically EEG frequency bands and resting-state network activity (Mantini et al., 2007). This previous study and our results suggest that RSN in EEG do not occur in specialized frequency bands, but broadband. Thus, our analysis shows that when different components are chosen to be identified using group-ICA in hd-EEG data, spatially coherent network components are found in other frequency bands or are distributed across multiple frequency bands. Regarding the spatial profile of network components identified from hd-EEG/fMRI/[^{18}F]FDG -PET modalities, the differences in spatial patterning and delineation are worth mentioning. Results of fMRI group-ICA showed more centralized pattern structures in the components, which is not surprising, since the group-ICA approach is an established technique yielding robust results applied to fMRI data.

Using our analysis approach for the hd-EEG components, we selected only those components that were spatially correlated with the fMRI components. Therefore, the hd-EEG components have a similar spatial pattern as the fMRI components. However, the existing differences between fMRI and hd-EEG components will most likely be due to the overall data quality of an EEG measurement with a parallel fMRI (Debener et al., 2008; Niazy et al., 2005). Furthermore, differences could also be due to the lower spatial and higher temporal resolutions of EEG, compared to fMRI. However, we found a strong spatial correspondence between EEG and fMRI components, as expectable due to our analysis approach. Since most vascular fMRI networks were also found in neuronal hd-EEG data, this observation provides further evidence of the coupling between vascular and neuronal activity. However, we cannot exclude that there are other EEG RSN that temporally co-operate with RSN derived from other modalities but in different regions.

Metabolic [^{18}F]FDG -PET networks were found to be less spatially defined than their fMRI-derived counterpart, which is most likely due to the spatial smoothness in [^{18}F]FDG -PET images. The components derived from the [^{18}F]FDG -PET data could not always be clearly

spatially separated from each other by the group-ICA and therefore appear clustered in their spatial distribution, which is in line with previous findings (Savio et al., 2017; Trotta et al., 2018). Moreover, it has already been observed that the differences in spatial expression of the networks are strongly influenced by the origin of the fMRI and [^{18}F]FDG-PET signals (Savio et al., 2017). Additionally, the low temporal resolution (change in glucose metabolism in a period, here 60 seconds) of the ^{18}FDG-PET signals results in noisier results, since group-ICA on [^{18}F]FDG-PET data identifies sources of between-subject covariance. Although the spatial correspondence reinforces the linkage of cerebral glucose metabolism to vascular activity, we further observed that metabolic mapping of networks is not as spatially distinct as vascular mapping.

Limitations

Due to the cohort of healthy subjects mixed with patients with focal epilepsy, we cannot exclude patient- / epilepsy-specific effects or detect their influence on the analysis. However, we calculated statistical group differences of various analysis metrics (all modalities: seed-based functional connectivity, functional connectivity on global and vertex/voxel-level; for fMRI and ^{18}FDG-PET: fALFF, regional homogeneity, intrinsic functional connectivity, Local Correlation; for hd-EEG: power on global and vertex-level) and could not observe any statistically significant group difference (healthy subjects vs patients with focal epilepsy).

With respect to the data processing, we applied well-established techniques to remove the gradient and ballistocardiogram artifacts in the hd-EEG data (Niazy et al., 2005). However, we cannot exclude the possibility that other approaches to remove MR environmental artifacts from hd-EEG data may yield different results. For example, instead of using post-processing methods to correct artifacts, the use of carbon wire loops during data acquisition could have improved artifact suppression, resulting in less noisy EEG data. To determine RSN components, we relied on spatial correlation of hd-EEG components to fMRI components. Furthermore, we cannot exclude whether other spatially uncorrelated hd-EEG components would not also be part of an existing (EEG-specific) resting-state network. Lastly, we initially chose the functional network atlas Yeo7 to spatially define resting-state network for fMRI and ^{18}FDG-PET, thus our results must be strictly considered under this constraint.

Conclusion

Overall, we showed that spatially coherent resting-state network can be identified from each modality of a simultaneous trimodal hd-EEG/fMRI/^{18}FDG-PET measurement. Most of vascular fMRI networks, were also found in neuronal hd-EEG data, reinforcing the hypothesized link between vascular signaling and neuronal activity. Each modalities measurement property (metabolic, vascular, neuronal), as well as their spatial and temporal resolution are crucial variables that influence the identification of the RSN in the brain in terms of their spatial profile and the occurrence of networks. Nevertheless, the fact of cross-modal expression of some RSN reinforces further investigation of such analyses of simultaneously measured trimodal (hd-EEG/fMRI/^{18}FDG-PET) datasets, as they hold the potential to identify biomarkers for neuronal disease in multiple spatial and temporal dimensions.

5. General discussion and outlook

This chapter provides the reader with an overview of multimodal brain networks in epilepsy patients, as well as temporal and spatial linkage of brain networks from different imaging modalities in epilepsy patients and healthy controls.

To do this, I will first discuss the multimodal changes in the brain networks in patients with idiopathic generalized epilepsy (IGE) (Chapter 5.1.1), as well as classify the bimodal alterations of the corticothalamic network and discuss about their significance in the context of IGE (Chapter 5.1.2).

Further, I will discuss the impact of methodological choices in source reconstruction in the context of presurgical evaluation (Chapter 5.2.1). Additionally, I will relate these results to the regional decrease in cerebral glucose metabolism from the metabolic neuroimaging modality ^{18}FDG-PET and discuss the significance of their spatial relationship to epileptogenic zones (Chapter 5.2.2).

Finally, building on findings from the previous project (Chapter 4.1), I aim to outline the characteristics and spatial interrelationships of resting-state networks in the human brain derived from a parallel multiple modality measurement, as well as the relevance of these observations to this type of measurement (Chapter 5.3).

5.1. Brain networks in patients with IGE

The results of the first project (Chapter 4.1) of this dissertation can be divided into two partitions. The first partition includes the feasibility of extracting relevant statistical group differences from hd-EEG data measured with a parallel fMRI, after MR artifact rejection methods, at source-level. The second partition builds on the results of the first partition of this project and comprises the detection of thalamocortical network changes in patients with IGE extracted from both modalities measured in parallel (hd-EEG-fMRI).

5.1.1. Parallel EEG-fMRI brain network analysis in patients with IGE

We were able to show that relevant group differences in functional connectivity and power between patients with IGE and healthy controls can also be extracted from the noisier data of an hd-EEG dataset measured with a parallel fMRI (Chapter 4.1). Due to the heterogeneity of epilepsy and its understanding as a brain network disease (Blumenfeld, 2014; Fisher et al., 2005), it is beneficial to study the brain networks in patients with IGE in different temporal and spatial scales, as well as in multiple aspects (e.g., vascular, metabolic etc.) to gain a better insight into the disorder.

Previous studies investigating IGE have used EEG-fMRI imaging, with EEG primarily used to identify the incidence of generalized spike-wave discharges (GSWD). The associated perfusion fluctuations that occur before, during and/or after this event are then analyzed in the fMRI data recorded in parallel. With this approach, the brain networks can be studied in the generation as well as the development of GSWD in fMRI with its high spatial resolution.

Following this analytical approach, one study demonstrated the involvement of basal ganglia and thalamocortical circuits in the development of GSWD in patients with IGE (Li et al., 2009). In another study, changes in functional connectivity between the BOLD fMRI signals of different regions (i.e., the sensorimotor and the occipital default mode networks) were observed in patients with IGE at different time periods: a few minutes before the onset of GSWD, seconds before the onset, during and even several seconds after GSWD (Tangwiriyasakul et al., 2018). In another EEG-fMRI study, it was observed from fMRI signal that deactivations in the default mode network (DMN) and dorsal attention network and activations in the somatomotor network and thalamus occur just before the onset of GSWDs (Klamer et al., 2018). The results of this study suggest that the default-mode network favors

GSWD in patients with IGE. Based on findings that the healthy human cerebral cortex elicits spatiotemporal neuronal activity avalanches (Plenz, 2012), one study demonstrated that epilepsy patients tended to exhibit higher neuronal amplification and larger avalanches - especially during interictal epileptiform activity (Arviv et al., 2016). From these findings, one question can be derived: what is the origin of these affinities of the individual networks in epilepsy patients? Further, what role do changes in the resting-state networks play in relation to these tendencies?

To study the analysis of the resting-state networks by fMRI, an EEG-fMRI measurement uses the EEG to exclude GSWD from fMRI data measured in parallel, to ensure that the data are free of pathological activity and make an unambiguous analysis of the human brain at rest possible. Seed-based analysis of such data revealed a decreased functional connectivity between DMN regions in patients with IGE (Luo et al., 2011; McGill et al., 2012) and functional connectivity alterations in thalamocortical networks (Ji et al., 2015; Wang et al., 2011). These results benefited from the high spatial resolution of the fMRI data being able to well identify the altered areas spatially. However, apart from the fact that these are persistent changes at rest, due to the time resolution of the fMRI one can only make limited statements about the temporal composition of these pathologically altered networks in patients with IGE. Because the complexity of brain networks is due not only to the sheer number of neurons and their connections to 10^3 to 10^4 other neurons, but also to the dynamic features, i.e., the highly nonstationary nature of these networks (Andrzejak et al., 2012), neuroimaging modalities with a high temporal resolution (e.g., EEG and MEG) are necessary.

Recently, comparisons of EEG and MEG data analyses were performed in patients with IGE and healthy controls. These showed an increase in connectivity and power at rest at source level in several widespread cortical and subcortical brain regions in several different frequency bands in patients with IGE (Elshahabi et al., 2015; Li Hegner et al., 2018; Stier et al., 2021). A recently published study also made use of the high temporal resolution of EEG/MEG and showed significant increases in functional connectivity in multiple frequency bands, predominantly at theta and beta frequencies, in patients with IGE that correspond to some degree to DMN areas known from fMRI resting-state studies (Stier et al., 2022). The spatial correspondence to DMN seen in these study (Stier et al., 2022) is supported by previous evidence that resting-state networks delineated using electrophysiology may correspond to

those of resting-state networks from fMRI data in healthy subjects (Brookes et al., 2011; Hipp & Siegel, 2015; Jann et al., 2009; Sadaghiani & Wirsich, 2020).

Even though the results of EEG and MEG studies are inferior to those of fMRI studies in terms of spatial accuracy, they are an essential tool in the study of brain network interaction changes due to their high temporal resolution (Baillet, 2017; Buzsáki et al., 2012; Lopes da Silva, 2013). Previous EEG-fMRI studies have not focused on EEG measurements with parallel fMRI when investigating IGE and have even less conducted analyses at the source level. Their results lack information on temporal aspects, whereas single-modality EEG/MEG studies lack spatial accuracy. One reason for the sparsity of EEG-fMRI studies utilizing EEG data for results is probably the induction of strong EEG artifacts by the fMRI, which require intensive cleaning procedures (Allen et al., 2000; Felblinger et al., 1999). In particular, the removal of the ballistocardiographic (BCG) artifact from EEG data is not a trivial task, due to its temporal non-stationary characteristic (Bonmassar et al., 2002) which has led to the development of various approaches to their removal. These range from techniques for artifact reduction already during measurement using additional hardware components in the EEG cap (van der Meer et al., 2016), to tracking of the subject's head movement during measurement by MR-compatible camera systems for additional information for post measurement processing methods (LeVan et al., 2013), to variations of these post measurement processing approaches. These approaches mostly use data-driven methods such as principal component analysis (Marino et al., 2018; Niazy et al., 2005) or independent component analysis (Joyce et al., 2004), individually or in combination with other techniques such as canonical correlation analysis (Assecondi et al., 2009), empirical mode decomposition (Javed et al., 2017), or spatial-filtering (Rusiniak et al., 2022). All these methods are able to improve the quality of the EEG data acquired during the parallel fMRI measurement. However, it had not been established how the MR artifact cleaning process affects the underlying information content of the EEG data measured with a parallel fMRI at rest.

Subsequently, several studies have investigated the resting-state functional connectivity of the EEG data with a parallel measured fMRI and have provided valuable insights in linking EEG and fMRI on (functional) connectivity level at resting-state, such as the performance of predicting EEG connectomes from fMRI and vice versa, as well as comparisons of fMRI and EEG connectomes (Deligianni et al., 2014). Wirsich et al. demonstrated the feasibility of

extracting joint EEG-fMRI connectomes at 7T field strength and showed that EEG-fMRI connectomes can be reproduced across different MRI acquisition systems (Wirsich et al., 2021). They have also worked on an independent component analysis (ICA) approach to perform a joint ICA of EEG-fMRI connectivity on a cohort of healthy subjects, the results of which suggest that spatial congruent regions of independent functional connectivity state networks are co-expressed in both modalities (Wirsich et al., 2020). Also, the functional connectivity maps from fMRI and EEG were evaluated after pharmacological modulation with ketamine and midazolam (Forsyth et al., 2020). However, it was not established whether EEG metrics applied to inside MR-scanner measured EEG, such as power or functional connectivity, can be used for identification of statistical group differences at source-level.

With our results (Chapter 4.1), we demonstrated that relevant statistical group differences in patients (IGE>HC) in power and functional connectivity in the hd-EEG data from a parallel hd-EEG-fMRI measurement are preserved after cleaning. Our findings of increased phase-based functional connectivity and power in patients with IGE compared to healthy controls are consistent with previous studies (Stier et al., 2021, 2022). Furthermore, we demonstrated that certain group differences in functional connectivity in the theta frequency band EEG were also expressed in vascular changes in the fMRI.

With our analysis approach, we did not combine the high spatial resolution of fMRI and the high temporal resolution of EEG to obtain increased accuracy in both dimensions. This can be done by fusing the brain signals from both modalities, via symmetric approaches (data-driven approaches such as ICA, and principal component analysis (PCA) etc.; model-driven approaches, by including fMRI information in EEG forward models) or asymmetric fusion approaches (e.g., EEG constrained fMRI, or vice versa) (Lei et al., 2012; Tulay et al., 2019; Valdes-Sosa et al., 2009). In future studies, conducting such data fusion before performing statistical group comparisons could lead to better spatial and temporal definition in the group comparison results and provide further insight into network changes in patients with IGE.

In summary, our results (Chapter 4.1) show that despite the removal of MR environment artifacts, the EEG data retained adequate information for extracting relevant group differences in power and functional connectivity on source-level in IGE patients. This evidence may also be of importance beyond the analysis of group differences in patients with IGE, and

may encourage parallel EEG-fMRI studies, in general, for analyzing group comparisons on source-level EEG data as well as fMRI data in other neurological diseases.

5.1.2. Thalamocortical network alterations in patients with IGE

In the second partition of the project (Chapter 4.2) of this dissertation, we showed increased functional networks connectivity between the thalamus and the occipital regions of the default mode network in patients with IGE compared to healthy controls, which was expressed in fMRI and in the theta band of hd-EEG.

Previous EEG-fMRI studies had initially focused on the investigation of the fMRI correlates of GSWD and the involved brain areas, an activated thalamic region and deactivated DMN regions were found in many studies (Aghakhani et al., 2004; Benuzzi et al., 2012; Gotman et al., 2005; Hamandi et al., 2006; Laufs et al., 2006). At the functional level, fMRI network connectivity studies revealed the DMN regions and the thalamus to be altered in the temporal sequence of formation, development, and termination of the GSWD (Klamer et al., 2018; Tangwiriyasakul et al., 2018; Vaudano et al., 2009). The results of these studies clearly establish an involvement in the thalamocortical network in the process of GSWD generation.

Our work, as well as other studies the fMRI data showed alterations in the thalamocortical network in cohorts of patients with IGE at rest and a significant increase in functional connectivity between occipital shares of the DMN network and the thalamus (Ji et al., 2015; Qin et al., 2021, 2022; Weng et al., 2020).

A most recent study applied static and dynamic functional connectivity analysis of the timecourses from independent components derived from resting-state fMRI data of patients with IGE (Qin et al., 2022). In contrast to our results, they found reduced static functional connectivity between the components representing the thalamus and precuneus, these findings of reduced functional connectivity remained statistically uncorrected in this study (Qin et al., 2022). Several fMRI studies in patients with IGE reported either an increase (Ji et al., 2015; Weng et al., 2020) or a decrease (Masterton et al., 2012; Qin et al., 2022) in functional connectivity between thalamus and occipital default mode network regions. Each of these studies, including our own, followed a different analysis procedure in terms of the exact spatial definition of the ROI and the further analysis steps. At this point, one cannot identify the exact reason for the discrepancy between the studies. It has been shown that

variations in the analysis methods among workgroups using the exact same data set has significant implications for the results and, consequently, for the conclusions (Botvinik-Nezer et al., 2020). However, it remains to be noted that whether increasing or decreasing, a change in functional connectivity is present in patients with IGE. More studies are needed to gain clarity on this issue. With our analysis, we have provided evidence that these network changes are not only found at the vascular level but are also expressed in electrophysiological changes. In our IGE cohort the increased functional connectivity in the thalamocortical network was found in the theta frequency band of the EEG. Several previous EEG/MEG studies without an fMRI measured in parallel also found widespread increased theta connectivity in patients with IGE, among others (Clemens et al., 2012, 2021, 2023; Elshahabi et al., 2015; Li Hegner et al., 2018; Stier et al., 2021, 2022). However, the theta band is not commonly reported in the literature as a frequency band of thalamic oscillations associated with cortical communication (Bazhenov & Timofeev, 2006; Buzsáki, 2006; Timofeev & Chauvette, 2011).

Yet, subdural electrocorticographic measurements in two patients with intractable epilepsy in whom depth electrodes were stereotactically implanted in the thalamus provided evidence that the thalamus exerts regulatory control over higher frequency cortical (e.g., beta1) activity via theta rhythms (Malekmohammadi et al., 2015). This type of measurement is highly unusual in humans since the implantation of such electrodes only for study purposes would meet with considerable ethical opposition due to the possible dire consequences. The detection of theta rhythms emanating from the thalamus as a regulatory mechanism over cortical activities remains a most interesting observation. Though, it is not established that these thalamic theta rhythms are related to the default mode network. In this context, we are unable to say whether the origin of our findings of increased thalamocortical connectivity in IGE patients in the theta frequency band has its origin in the thalamus or the cortex.

In another respect, with the increased connectivity in the thalamocortical network which we detected and with the knowledge that the broad and highly complex connections between the thalamus and cortex contribute to the function and dysfunction of the entire brain, and that thalamocortical circuits play a leading role in the organization of cortical excitation and inhibition (Blumenfeld, 2002; Hwang et al., 2017), gives rise to a question: does the increased connectivity of the thalamocortical network promote the occurrence of epileptiform discharges and subsequent seizures?

The nature of our analysis does not allow us to answer this question. However, previous studies observed that the healthy human cerebral cortex elicited spatiotemporal neuronal activity avalanches (Plenz, 2012), whereupon another study demonstrated that epilepsy patients tended to evidence higher neuronal amplification and larger avalanches - especially during interictal epileptiform activity (Arviv et al., 2016). On the other hand, studies provided evidence that epileptiform discharges induce changes in brain networks that which lad to easing (Huberfeld et al., 2011) or hindering (Karoly et al., 2016) seizures, or both (Chang et al., 2018). Yet the question of the consequences of network changes at rest in patients with epilepsy remained open for future studies. It is still an open question which of these occurred first: changes in the network's resting-state or GSWD.

In summary, in this work we have provided evidence of measurable electrophysiological as well as vascular expression of thalamocortical resting-state network changes in patients with IGE. Previous studies on thalamocortical networks in epilepsy support our findings and motivate a more detailed investigation into the spatial and temporal electrophysiological network organization of the thalamocortical network in patients with IGE in the future. The high temporal resolution of EEG/MEG can be used to better understand the role of the thalamus and its connectivity to the default mode network in the context of origin and modulation of epileptiform discharges in patients with IGE. Based on the results of our work, further studies should investigate the thalamocortical network changes in patients with IGE with special attention to the theta frequency band.

5.2. BRAIN NETWORKS IN PATIENTS WITH FOCAL EPILEPSY

The results of the second project (Chapter 4.2) of this dissertation work are, for the sake of the following discussion, divided into two partitions. The first partition addresses the influences of inverse methods on the electric source imaging (ESI) of interictal epileptic discharges (IEDs) in patients with focal epilepsy, as well as the importance of considering the IED time phase to be selected for ESI. The second subsection addresses the spatial relationship of IEDs to the hypometabolism found in focal epilepsy patients' ^{18}FDG-PET data.

5.2.1. INFLUENTIAL PARAMETERS IN THE ESI OF IEDS IN THE PRE-SURGICAL EVALUATION PROCEDURE

In Chapter 4.2 we demonstrated that the choice of inverse method and, even more so, the choice of the IED phase, had an impact on the ESI in terms of its spatial accuracy in defining the irritative zone.

Epilepsy surgery is a final treatment option providing significantly better outcome regarding frequency of seizures and quality of life for patients with focal epilepsy who no longer respond to anti-seizure medication (Engel, 2018; Wiebe et al., 2001). Since this operation procedure is an invasive procedure that ideally involves resection of only the epileptogenic zone tissue without damaging other healthy and functional tissue, a spatial definition of the epileptogenic network is critical. ESI is an important step in the pre-surgical evaluation (Foged et al., 2020). Yet, ESI is only used in nine of 25 epilepsy centers in Europe, and no universally accepted workflow is present (Mouthaan et al., 2016). Considering that epilepsy surgery has a serious impact on the patient's life and given the influence of ESI in the preoperative evaluation (Foged et al., 2020), a gold standard for the use of ESI in preoperative assessment must be established. Therefore, the evaluation of different inverse methods in the setting of IED reconstructions considering the selection of different phases in the temporal course of the IEDs of in the human brain is necessary.

In the past, a variety of methodological studies have compared methods for source estimation in the setting of simulated and/or real data (Baillet, Mosher, et al., 2001; Baillet, Riera, et al., 2001; Friston et al., 2008; Fuchs et al., 1999; Hauk et al., 2011). However, no recommendations or guidelines have yet been established that assist researchers without a methodological

background in source estimation methods in choosing the most appropriate method and the parameter settings best suited for the task at hand (Hauk et al., 2022).

In Chapter 4.2 we show that sLORETA was the source estimation method with the shortest distance to the resection zone in our study. To a certain extent, this agrees with the results of previous studies (Carboni et al., 2022; Plummer et al., 2010). The differences in the methodological choices in the analysis of the ESI, as well as the ongoing analysis to evaluate these results differ. Since the EEG/MEG inverse problem has no unique solution, the source distributions reconstructed from the EEG/MEG data depend to a large extent on the individual parameters assumed for the forward and inverse modeling (Mahjoory et al., 2017), as well as on other a priori information in ESI of IEDs (Mahjoory et al., 2017; Wennberg & Cheyne, 2014). In addition to the methodological factors, the individuality of each patient with focal epilepsy and the resulting influence of the individual on the cohorts also play a sensitive role in the outcome of such studies. More so, it has been shown that there is low reliability in the identification of IEDs by different clinicians in identical patients (Jing et al., 2020). Therefore, the ideal situation for a generally valid evaluation of inverse methods would be, in our case, a constant cohort of patients with focal epilepsy with already identified IEDs. The cohort, with appropriate size, could then be used for any methodological evaluation work on source reconstructions of IEDs in patients with focal epilepsy. The individual epilepsy or research centers each have their own limitations. One study reported considerable differences between epilepsy centers in Europe that use ESI for evaluation before epilepsy surgery (Mouthaan et al., 2016). In the centers, limited resources prevent the availability of the recommended instruments. Furthermore, there is a lack of awareness of recommendations or guidelines regarding protocols for the inclusion of structural MRI, PET, and SPECT in candidates for epilepsy surgery. Further, some centers have limited or no access to functional imaging (Mouthaan et al., 2016).

With our work we showed the influence of the choice of the time phase of the IEDs on the spatial accuracy of the ESI to the resection zone (Chapter 4.2), and that the peak phase of the IED should be considered to achieve the closest distance between ESI and resection zone. Studies have provided evidence on the propagation of interictal epileptiform discharges and its relevance to source localization (Lantz et al., 2003; Schulz et al., 2000; Zumsteg et al., 2006). Recently, one study demonstrated the influence of the choice of time bin during the IED for

the inverse method Local Autoregressive Average (LAURA) as a secondary result, showing that ESI yielded the smallest distances to the resection zone at IED rising phase and IED peak (Vorderwülbecke et al., 2020). Aside from that, the effect of the choice of IED phase on the localization of IED sources has not been further investigated. However, it is already known that time points earlier than the half-rise of the IEDs are less accurate in describing the irritative zone, since the signal-to-noise ratio is low there (Bast et al., 2006; Wennberg & Cheyne, 2014). Nonetheless, it was important to shine a renewed spotlight on the choice of all IED phases in IED's ESI to examine their influence and demonstrate the importance of their choice.

In summary, in this work (Chapter 4.2) we provide evidence for a suitable inverse method in order to obtain the closest distance between ESI maximum amplitude and the resection zone in patients with focal epilepsy. Furthermore, we can recommend utilizing the time point of the IED peak for the smallest distance to the resection zone. In the end, I would like to draw attention once again to the importance of a standardized workflow when evaluating the ESI of IED with respect to various parameters. For such a workflow, the following key points should be considered: among others, a constant cohort (mandatory), common processing procedures from raw IED epochs to before ESI application, standardized settings of the common processing procedures (filtering, artefact rejection etc.), a standardized set of metrics to accurately describe the performance of ESI of IEDs, i.e. distance: Euclidean, or Mahalanobis (Mahalanobis, 1936) etc. from maximum amplitude to center/edge/center of mass of goal region; volumetric: DICE coefficient (Zou et al., 2004), Pearson correlation etc..

5.2.2. ESI AND ^{18}FDG-PET HYPOMETABOLISM CROSS-MODAL RELATIONSHIP IN PATIENTS WITH FOCAL EPILEPSY

In the second part of the project (Chapter 4.2) of this dissertation, we have shown that the smallest spatial distance exists between the ^{18}FDG-PET hypometabolism and the ESI of the afterwaves of IEDs. There is no established explanation for the spatial proximity and its cause in the context of epileptogenic networks in patients with focal epilepsy, but in the following I will attempt to provide an explanation for this finding.

Based on the assumption that interictal epileptic discharges are abnormal bursts that do not evolve into epileptic seizures and that they show spatial proximity to the ^{18}FDG-PET

hypometabolism, one can assume an inhibitory effect in the hypometabolic area. An inhibitory drive ('Surround Inhibition') by a population of neurons surrounding the epileptogenic zone was proposed very early (Prince, 1967), and a relationship between interictal epileptic discharges and hypometabolism was further established (Ackermann et al., 1986; Engel et al., 1990; Witte et al., 1994). The hypometabolism showed proximity to the resection zone, but low volumetric overlap in our cohort. A study utilizing interictal electrocorticography showed that the seizure onset zone and the irritative zone are often found outside but adjacent to the hypometabolic area (Alkonyi et al., 2009; Jeong et al., 2017). In one study, focal penicillin-induced epilepsy was induced in rat models, and there it was shown that hypermetabolic epileptic foci were surrounded by a hypometabolic cortex (Witte et al., 1994). Animal studies utilizing optical imaging for epileptic foci showed a reversed signal associated with decreased blood flow as well as decreased neuronal activity (Schwartz & Bonhoeffer, 2001; Zhao et al., 2009). This supports our hypothesis that the ^{18}FDG-PET hypometabolic area harbors an inhibitory mechanism that may protect cortical areas from rapid seizure involvement, which is, to this point, still not completely proven.

Even though taking ^{18}FDG-PET hypometabolism into consideration is well established in the pre-surgical evaluation of patients with focal epilepsy, its pathological cause, and its relationship to IEDs remain largely unclear and few studies have attempted to fill this gap in knowledge.

In summary, in this work, we were not able to fully elucidate the relationship of ^{18}FDG-PET hypometabolism to IEDs. The findings discussed above and our work, however, provide support for inhibitory mechanisms related to the ^{18}FDG-PET hypometabolism and may stimulate further studies on this topic.

A more detailed investigation of dynamic and causal interrelations of interictal ^{18}FDG-PET hypometabolism and ESI could provide a more nuanced picture of network interactions in patients with focal epilepsy and the role of temporal hierarchies.

5.3. IDENTIFICATION OF RESTING-STATE BRAIN NETWORKS FROM PARALLEL MULTIMODAL IMAGING

The results of the third project (Chapter 4.3) of this dissertation are based on the data of a rarely performed fully simultaneous measurement of hd-EEG, fMRI, and ^{18}FDG-PET. In this project, we showed that it is possible to extract known functional resting-state networks from the individual modalities of such a fully parallel measurement. Furthermore, we provided evidence that resting-state networks are expressed in all three aspects (electrophysiological, vascular, and glucose metabolic).

As already mentioned in the introduction, it must first be made clear that the completely parallel measurement of these three modalities (hd-EEG, fMRI, and ^{18}FDG-PET) is unusual and hardly ever performed. However, this holds great potential, namely the investigation of the human brain in different stages of temporal and spatial resolution without having to deal with confounding factors. Furthermore, trimodal imaging requires only one measurement session, which could be useful in clinical neurology patients when a rapid pharmacological intervention with a minimal waiting time is needed, e.g., in the case of refractory epilepsy. However, this type of imaging is far from having an established place in the clinical setting. Regarding the potential of trimodal imaging, any further findings from studies analyzing these data sets are important. The literature on fully parallel trimodal measurements is sparse. Nevertheless, earlier studies have reported the relationships between simultaneously recorded bimodalities (two modalities): (i) fMRI/PET (Aiello et al., 2015; Riedl et al., 2014, 2016), (ii) fMRI/EEG (Ritter & Villringer, 2006; Ullsperger & Debener, 2010) and (iii) PET/EEG (Hur et al., 2013).

In our work, all Yeo7 resting-state networks (Yeo et al., 2011) were extracted from the fMRI and ^{18}FDG-PET modalities. Although similar results were not extracted from a trimodal dataset, the findings of my project are corroborated by previous studies using one modality or two non-parallel or parallel modalities. The identification of resting-state networks from fMRI data is a common analysis approach and has already led to the creation of established functional network atlases (Doucet et al., 2021; Wang et al., 2021; Yeo et al., 2011); etc.). Therefore, the identification of resting-state networks from fMRI data was expected.

Regarding mapping resting-state networks from ^{18}FDG-PET data, the literature is sparse, but existing study results support the findings in our project. A study utilizing simultaneous fMRI/^{18}FDG-PET identified ten spatially matching resting-state networks from both modalities

(Savio et al., 2017). The first study of this type was performed in 2012 and known resting-state networks were found in the PET data there as well (Di et al., 2012). The sparseness of such PET studies in healthy controls can be explained by ethical concerns. The residual risk of the radiation exposure from the radioactive tracers, which are necessary for PET imaging, is ethically difficult to justify for the measurement in healthy controls, while a clinical indication for diagnostic clarification justifies such measurements. Due to the paucity of studies extracting resting-state networks from ^{18}FDG-PET data, it is important that our results are in line and confirm previous study results (Di et al., 2012; Savio et al., 2017).

We identified EEG resting-state networks at source-level from fully parallel measured hd-EEG/fMRI/^{18}FDG-PET data describing the visual, somatomotor, frontoparietal, and default mode networks in our cohort. Our results are supported by previous studies that have identified such resting-state networks from separately measured EEG/MEG datasets at the source-level (Aoki et al., 2015; Brookes et al., 2011; Shou et al., 2020; Sockeel et al., 2016), or at the sensor-level from EEG data measured with a parallel fMRI (Mantini et al., 2007). We were further able to identify EEG resting-state networks, which are spatially associated with the dorsal attention networks that were observed earlier at sensor-level during a parallel EEG-fMRI measurement (Mantini et al., 2007).

In our work, resting-state network identification was performed based on direct (fMRI and ^{18}FDG-PET) and indirect (hd-EEG) spatial matching to the Yeo7 functional network atlas. This atlas was based on fMRI data using independent component analysis (Yeo et al., 2011). The group-ICA applied to our fMRI data resulted in spatially distinct network components with an optically recognizable underlying pattern. In comparison, the components of the ^{18}FDG-PET data showed clear, but less distinct, network components. That is not surprising, since both modalities capture different aspects of neural brain activity, with ^{18}FDG-PET measuring neural activity depended on glucose metabolism directly, as fMRI captures signals from a composition of cerebral blood flow, volume, and oxygen metabolism (Kim & Ogawa, 2012).

In contrast to the fMRI components, the PET components regularly showed spatial outliers from the main components in the individual components. Previous studies have already shown that since the ^{18}F-FDG-PET data represent an averaged snapshot of tracer uptake over a period of time, group-ICA extracts sources of inter-subject covariance from the available ^{18}FDG-PET data (Calhoun & Allen, 2013; Savio et al., 2017). This results in more noisy results

compared to the results of a group-ICA on fMRI data. Furthermore, the analysis result of a group-ICA on ^{18}FDG-PET data is more dependent on the sample size. Noisier results for ^{18}FDG-PET data were also observed in a study that identified the default mode network in patients with Parkinson's disease using seed-based FC analysis in fMRI and ^{18}FDG-PET (Ruppert et al., 2021). In a further study the application of group-ICA on a cohort size of 40 healthy controls and >100 patients with amyotrophic lateral sclerosis yielded group-ICA components of occipital default mode, and somatomotor network with similar spatial outline as the results of a group-ICA of fMRI data (Pagani et al., 2016). Overall, with our results we showed a coupling of the metabolic activity measured by ^{18}FDG-PET and vascular activity derived from fMRI, like previous studies (Cecchin et al., 2017; Marchitelli et al., 2018; Tahmasian et al., 2015), and, moreover, with evidence of a spatial structure like that of the resting-state functional networks underlying the metabolic ^{18}FDG-PET data.

Spatial comparison of hd-EEG components with fMRI components revealed naturally corresponding component patterns. This is, of course, primarily due to our analysis framework in which we specifically identified hd-EEG components as resting-state network components if they showed a greater spatial correlation with the fMRI data than the hd-EEG surrogate datasets. Nevertheless, our results showed that the resting-state networks known from fMRI could be extracted in a similar spatial structure from hd-EEG, which emphasizes the coupling of the vascular activity underlying the resting-state networks from fMRI with the electrophysiological activity from hd-EEG. Animal studies (anaesthetized cats, and monkeys) provided evidence of temporal coupling between the BOLD signals and several frequency bands of intracranial electrocortical recordings (ECoG) (Niessing et al., 2005; Shmuel & Leopold, 2008). Both studies reported that the strongest correlation between hemodynamic response and neuronal oscillatory amplitude were present in the frequency spectrum >60 Hz. In our work, we observed that components for the resting-state functional networks were found in the hd-EEG data across all analyzed frequency bands. Although this does not demonstrate temporal coupling of signals from both modalities, it nevertheless shows that the spatial patterns of resting state networks in hd-EEG, spatially congruent with fMRI resting state networks, are expressed in multiple frequency bands. This supports previous findings that electrophysiological resting-state networks consist of a combination of different frequency band compounds (Mantini et al., 2007).

In addition, we found a spatial correlation between neuronal oscillations (hd-EEG) and metabolic activity (^{18}FDG-PET), by extracting spatially similar components for functional brain networks (such as visual, and default mode network) from both modalities. Interestingly, a study showed a strong correlation between cortical glucose metabolism patterns (^{18}FDG-PET) and spectral gamma amplitude of intracranial recordings in non-lesional focal epilepsy patients at rest (Nishida et al., 2008). Nishida et al. failed to prove a linear correlation between regional metabolic activities and the other frequency bands (delta, theta, and alpha) of the subdural EEG measurement. In our work, spatially coherent network components (visual, somatomotor, default mode network) in ^{18}FDG-PET and hd-EEG were found in hd-EEG in the spectral bands: alpha, beta, and gamma.

The fully parallel measurement of metabolic, vascular, and electrical brain activity eliminates the bias of study results that establish cross-modal associations between successive measurement sessions. The proof of identification in the modalities of a trimodal (EEG/fMRI/^{18}FDG-PET) measurement is a further step for this type of measurement towards a potential establishment in the field of brain research. As described in the introduction, resting-state networks are an identifiable functional community of regions or networks of sustained spontaneous brain activity in their general resting-state. Disturbances in these networks have already been identified as clear indicators for a number of neurological diseases, i.e., Alzheimer (Engels et al., 2017; Ibrahim et al., 2021), Parkinson (Baggio et al., 2015; Hohenfeld et al., 2018; Tahmasian et al., 2017; Wolters et al., 2019), and epilepsy (Burman & Parrish, 2018; Kramer & Cash, 2012; van Mierlo et al., 2019). Specifically with respect to epilepsy, which is accurately characterized as a neurological network disorder, it is crucial to improve our understanding of the "healthy" network structure of our brain. It follows that further detailed knowledge of brain networks opens up the possibility of improving the diagnosis and treatment of neurological diseases. Characterizing the relationships within and between imaging modalities at different spatial and temporal scales is necessary to better understand brain organization and function (Presigny & De Vico Fallani, 2022).

Although several studies have reported results of analyses examining the functional network between parallel and non-parallel measured bimodal trimodal data, an identification of the electrophysiological (EEG), neurovascular (BOLD fMRI), and glucose metabolic (^{18}FDG-PET)

resting networks in a fully parallel recorded trimodal data set has not yet been published. With our findings, we demonstrate the feasibility of identifying resting-state networks from data of a fully parallel hd-EEG/fMRI/^{18}FDG-PET measurement.

Future studies could apply data fusion approaches prior to further analysis to combine the strengths of each modality (EEG/fMRI/^{18}FDG-PET) to gain a better understanding of brain function. In addition to improved basic understanding of the brain and its functions, a better understanding could further lead to earlier and more specific diagnosis of various brain diseases.

6. Conclusion

This work contributes to a broader understanding of the representation of neuronal networks and their relationships between different modalities in patients with epilepsy, as well as in a mixed cohort of healthy control subjects and patients with focal epilepsy.

This means, on the one hand, that pathological group differences of patients with IGE compared to healthy controls can be identified from interictal hd-EEG data measured with a parallel fMRI. Second, the spatial relations of epileptogenic networks in patients with focal epilepsy extracted from different imaging modalities (hd-EEG, and ^{18}FDG-PET) were provided. Lastly, the identification of known resting-state networks was shown to be possible from each modality of a fully parallel measurement of hd-EEG, fMRI, and ^{18}FDG-PET.

We have shown that hd-EEG resting-state network analysis is suitable for inside MR-scanner measured EEG data. After conventional cleaning of the hd-EEG data from MR-artifacts, hd-EEG power estimates were systematically increased. Yet, the spatial topography and general direction of the group comparisons (IGE>HC) of power and functional connectivity remained similar. Where the group differences for power for the data within the MR-scanner showed no significance for the group difference, phase-shifted coherence (ImCoh) was less affected and provided group difference significances comparable to those of the outside MR scenario. In addition, we showed that there is a spatial correspondence of seed-based functional connectivity group differences (IGE>HC) between the two modalities (hd-EEG, and fMRI) for the thalamus. Moreover, I discussed the significance of our results and that they have the potential to encourage further studies. Future studies are needed to investigate the dynamics of networks in humans in resting-state condition and to take advantage of the high temporal resolution of EEG, possibly with parallel fMRI. Further EEG studies are needed to further investigate the thalamocortical networks in patients with IGE to gain a better understanding of this network disease.

With the work on clinical datasets, we could show that the decision in the choice of the time to reconstruct interictal epileptic discharges (IEDs) for imaging the epileptogenic zone should be made with caution. Likewise, the choice of the inverse method has an influence on the electric source imaging results in the presurgical evaluation procedure. In our work, we showed the shortest distance to the resection zone with the inverse method sLORETA at the peak of interictal epileptic discharge. The other inverse methods in this analysis also showed

the shortest distances to the resection zone in the interictal epileptic discharge peak phase. Furthermore, evidence was provided that the hypometabolism derived from the ^{18}FDG-PET data of patients with focal epilepsy showed proximity to the source reconstructions of the interictal epileptic discharges. Due to the lack of knowledge about this relationship these results may motivate future studies to further investigate this relationship in detail.

In the last project, we have demonstrated the feasibility of extracting known resting-state networks (e.g., visual, somatomotor, frontoparietal, default mode networks) from fully parallel hd-EEG/fMRI/^{18}FDG-PET data using group-ICA. Differences in spatial expression of the resting-state network components among modalities were characterized and on linked to each modalities signal origin, as well as spatial and temporal resolution. This work further indicates the underlying potential of this measurement condition and may encourage for further applications of fully parallel trimodal measurement of hd-EEG/fMRI/^{18}FDG-PET.

7. Other contributions to scientific community

During the period of my doctorate, I was also involved in the preparation of other scientific papers. In the following chapter, my contribution and an insight into this work are provided.

7.1. Feasibility of HD-ESI in the presurgical workflow – Influence of number of spikes recorded and automated spike detection

Feasibility of high-density electric source imaging in the presurgical workflow: Effect of number of spikes and automated spike detection

Authors: Ev-Christin Heide[1,a], **Daniel van de Velden[1,a]**, David Garnica[1], Manuel Hewitt[1], Christian Riedel[2], Niels K. Focke[1]

[a] These authors contributed equally to this work.
[1] Department of Neurology, University Medical Center, Georg-August University, Göttingen, Germany
[2] Institute for Diagnostic and Interventional Neuroradiology, University Medical Center, Georg-August University, Göttingen, Germany

NKF, DvdV, and ECH designed and conceptualized the study; The data were acquired in the course of clinical day-to-day measurements; DvdV and ECH analyzed the data and performed analyses and visualization; DvdV, ECH, and NKF interpreted the results; NKF supervised the project; DvdV and ECH drafted the manuscript; NKF, DG, MH, and CR revised the manuscript for intellectual content.

Published in *Brain Topography*, 2023.

Received: 25 August 2022 | Accepted: 16 March 2023

DOI: 10.1002/epi4.12732

Epilepsia Open™ Open Access

ORIGINAL ARTICLE

Feasibility of high-density electric source imaging in the presurgical workflow: Effect of number of spikes and automated spike detection

Ev-Christin Heide[1] | Daniel van de Velden[1] | David Garnica Agudelo[1] | Manuel Hewitt[1] | Christian Riedel[2] | Niels K. Focke[1]

[1]Department of Neurology, University Medical Center, Georg-August University, Göttingen, Germany

[2]Institute for Diagnostic and Interventional Neuroradiology, University Medical Center, Georg-August University, Göttingen, Germany

Correspondence
Ev-Christin Heide, Robert-Koch-Straße 40, 37075 Göttingen, Germany.
Email: ev-christin-heide@med.uni-goettingen.de

Abstract

Objective: Presurgical high-density electric source imaging (hdESI) of interictal epileptic discharges (IEDs) is only used by few epilepsy centers. One obstacle is the time-consuming workflow both for recording as well as for visual review. Therefore, we analyzed the effect of (a) an automated IED detection and (b) the number of IEDs on the accuracy of hdESI and time-effectiveness.

Methods: In 22 patients with pharmacoresistant focal epilepsy receiving epilepsy surgery (Engel 1) we retrospectively detected IEDs both visually and semi-automatically using the EEG analysis software Persyst in 256-channel EEGs. The amount of IEDs, the Euclidean distance between hdESI maximum and resection zone, and the operator time were compared. Additionally, we evaluated the intra-individual effect of IED quantity on the distance between hdESI maximum of all IEDs and hdESI maximum when only a reduced amount of IEDs were included.

Results: There was no significant difference in the number of IEDs between visually versus semi-automatically marked IEDs (74 ± 56 IEDs/patient vs 116 ± 115 IEDs/patient). The detection method of the IEDs had no significant effect on the mean distances between resection zone and hdESI maximum (visual: 26.07 ± 31.12 mm vs semi-automated: 33.6 ± 34.75 mm). However, the mean time needed to review the full datasets semi-automatically was shorter by 275 ± 46 min (305 ± 72 min vs 30 ± 26 min, $P < 0.001$).

The distance between hdESI of the full versus reduced amount of IEDs of the same patient was smaller than 1 cm when at least a mean of 33 IEDs were analyzed. There was a significantly shorter intraindividual distance between resection zone and hdESI maximum when 30 IEDs were analyzed as compared to the analysis of only 10 IEDs ($P < 0.001$).

Ev-Christin Heide and Daniel van de Velden authors contributed equally to this work.

Significance: Semi-automatized processing and limiting the amount of IEDs analyzed (~30–40 IEDs per cluster) appear to be time-saving clinical tools to increase the practicability of hdESI in the presurgical work-up.

KEYWORDS

amount of IEDs, automation, electric source imaging, focal epilepsy, high-density EEG, Presurgical evaluation

1 | INTRODUCTION

One third of all cases of epilepsy are pharmacoresistant, defined by treatment failure of two tolerated, appropriately chosen and applied anti-seizure medication (ASM).[1] In focal epilepsy patients, surgery is an important treatment option with a significantly better outcome in seizure frequency and quality of life compared to continued ASM treatment.[2,3] The goal of epilepsy surgery is the resection of the epileptogenic zone, to achieve seizure freedom, as well as the sparing of non-epileptic tissue and tissue with important neuropsychological and neurological function.[4] Hence, a detailed presurgical evaluation is required.

The presurgical work-up typically starts with a non-invasive evaluation ("phase one"), which includes high-resolution magnetic resonance imaging (MRI), video scalp electroencephalography (EEG), and neuropsychological assessment. Some epilepsy centers also apply high-density EEG (hdEEG) with electric source imaging (ESI) or, the technically similar, magnetencephalography with magnetic source imaging.[5] ESI is a back-projection of the electric activity recorded at the scalp into the (assumed) sources in the brain. This can be done using the measured EEG activity, a forward model and an inverse method such as weighted Minimum Norm Estimation (wMNE).[6–8]

High-density ESI (hdESI) has proven its usefulness in the presurgical evaluation and provides non-redundant information in a relevant proportion of patients. Compared to low-density ESI, more accurate source localization was achieved by hdESI.[9,10] However, in a meta-analysis including 515 patients by Sharma et al. there was no significant difference in the accuracy of high-density and low-density ESI.[11] These divergent results could be caused by a smooth spatial distribution when a high number of single events in low-density EEG is used. High-density EEG may be beneficial for localizing IED averages with a low signal-to-noise ratio or IED analysis with a low number of single events. In two interrelated studies by Foged et al. and Duez et al.,[12] ESI changed the further diagnostic and therapeutic plan in 34% of the patients. It mainly led to an additional intracranial EEG (icEEG) electrode insertion and had greater agreement with icEEG results than visual review by experienced epileptologists alone.[13]

Key Points

- We evaluated the effect of number of spikes and automated spike detection on the localization of the high-density source maximum.
- A semi-automated spike detection was significantly faster compared to a visual one without affecting source localization results.
- A moderate number of (~30–40) spikes per cluster is advisable to achieve accurate source localization results in our cohort.

Interestingly, the added icEEG electrodes were the ones to localize the irritative and seizure onset zone (SOZ) in 80% of the cases.[14] Furthermore, hdESI is a particularly valuable tool for analyzing patients with normal MRI. In a study with 10 operated patients in whom modern MRI sequences failed to provide evidence of an epileptogenic lesion, ESI localized the focus correctly in eight of them.[15]

However, only nine of the 25 surveyed European epilepsy centers reported using ESI in their presurgical evaluation in 2014.[16] One barrier to a more widespread dissemination of hdESI is its practicability, in particular, the personnel usage for acquisition and review of these datasets. In many centers, only short-term acquisitions lasting 1–2 hours are done. Long-term recordings are possible when special electrode systems are used, but these require even more logistical efforts than short-term recordings (see Section 2.2). Also, physicians should be prepared to invest more time in reviewing long-term recordings. Despite a huge number of studies on the electrode coverage and the time point of the interictal epileptic discharges (IED) used for hdESI, there is a lack of studies analyzing the amount of IEDs needed and, related to this, how long clinical acquisitions need to be.[9,10,17] In a recent study by Cox et al.[13] the authors concluded: "While it is common practice to obtain as many interictal spikes as possible for averaging, there is little data guiding what is an acceptable number of spikes to analyze." Additionally, Vorderwülbecke et al.[18] recently published a study on automated interictal source localization based on hdEEG,

which provided meaningful information in the majority of cases. However, spatial downsampling to low-density ESI did not decrease the accuracy. As the IED detection in big data files such as hdEEG is a very time-consuming process, a semi-automated IED detection could contribute to an improved practicability.

In this study, we have systematically evaluated the effect of semi-automated IED detection by the EEG analysis software Persyst on the accuracy of hdESI and the operator time needed. Moreover, we analyzed the influence of IED quantity on the localization of hdESI. This could help to increase the efficiency of hdESI in the presurgical workflow and guide centers when establishing or optimizing their hdEEG programs.

2 | METHODS

2.1 | Clinical data acquisition

The patients with completed presurgical non-invasive evaluation between September 1, 2017 and February 1, 2021 were selected retrospectively from the "epilepsy surgery database" of the department of Neurology, University Hospital of Göttingen. Inclusion criteria were defined as follows: (1) diagnosis of pharmacoresistant focal epilepsy, (2) presurgical evaluation with 256-channel hdEEG (≥105 min) recording and high-resolution 3 T MRI *with* T1 or MPRAGE sequences, (3) ≥10 IEDs in hdEEG, (4) subsequent first epilepsy surgery with good outcome (Engel 1),[19,20] and (5) postsurgical MRI with T1 sequences. We established the following exclusion criteria: (1) multifocal epilepsy and (2) prior epilepsy surgery. This retrospective study was approved by the local ethics committee at the University Hospital Göttingen (number 3/7/22).

2.2 | Acquisition of hdEEG

HdEEG recordings were performed on the video-EEG monitoring unit using a GES400 system (Electrical Geodesics, Inc., now Magstim EGI, Eugene, USA, at 250 or 1000 Hz sampling rate). In patients with less than 10 IEDs per hour in the preceding low-density EEG a long-term hdEEG (≥03:00 h) was performed, whereas in patients with high more than 10 IEDs per hour in the preceding low-density EEG a short-term hdEEG (≥01:45–03:00 h) was deemed clinically sufficient. The short-term hdEEG was recorded with the HydroCel Geodesic Sensor Net 130 (Electrical Geodesics), where interconnected sponge electrodes are soaked in a saline solution and placed on the patient's head without a paste. In contrast, long-term hdEEG requires a longer application time, as a scalp preparation and placement of a conductive paste under each of the 256 electrodes of the HydroCel Geodesic Sensor Net (130 LT) is needed. Electrode-skin impedances were kept at <15 kΩ.

2.3 | Visual versus semi-automated IED detection in hdEEG

The full-length, filtered hdEEG was displayed by EGI Net Station Review. First, the IEDs were detected purely visually from the beginning to the end by an EEG-experienced clinician (E.-C. Heide, aware of clinical information). All IEDs were marked on the peak using a conventional display (longitudinal bipolar or average montages of the 10–20 electrode array plus extended electrodes in the temporal chain, corresponding to IFCN recommendations[21]) and visually classified into different groups based on their topography, at lobar resolution. The time needed for visual review of the hdEEG was measured and rounded up in 15-minute steps.

Additionally, the full-length, filtered hdEEG was processed by Persyst Spike Detector P14 (Persyst; non-clinical use, version 14, Rev. C). We excluded IEDs with a spike probability measure of less than 0.9, corresponding to the "low sensitivity" settings of the software.[22] The remaining IEDs were grouped automatically into different clusters according to the electrode with the highest amplitude. Each cluster was then sorted by the IED amount and displayed as 2-second event epochs. Semi-automated IED detection includes the review of these epochs by the same clinician (E.-C. Heide) at least 6 months after visual scoring using an extended average reference montage as mentioned above. Automatically detected events that did not meet IED criteria such as artifacts and physiological EEG patterns were excluded. The operator time needed for reviewing all 2-second event epochs was measured and rounded up in 15-minute steps.

In order to compare the visual and semi-automated IED detection, sensitivity, positive predictive value, success rate and Cohen's κ (kappa) were determined. Sensitivity was defined by the amount of visual IEDs detected also by Persyst (sensitivity [%] = (n (IEDs detected visually AND by Persyst)/n (IEDs detected visually)) × 100%), whereas positive predictive value was the amount of IEDs among all detected events. Success rate was described as the probability to detect at least 30 IEDs among all events of one cluster (e.g. success rate of 1st cluster [%] = (n (patients with at least 30 IEDs in the 1st cluster)/n (all patients)) × 100%). In addition, the Cohen's κ for inter-rater agreement analysis was used to observe the agreement reliability between semi-automated or fully-automated IED detection and purely visual detection. It was calculated as

$$\kappa = \frac{\Pr(a) - \Pr(e)}{1 - \Pr(e)}$$

where Pr(a) is the relative observed agreement between selection conditions, and Pr(e) is the hypothetical probability of chance agreement.[23–25]

2.4 | Determination of surgical reference

Postsurgical T1 was co-registered to the presurgical T1 and the resection zone was marked automatically. Details are provided as supplementary information. The extent of the resection was determined clinically including noninvasive and, for some patients, invasive EEG diagnostics and surgical access routes. Given the fact that only patients with Engel 1 postsurgical outcome were included, it can be assumed that the resection zone contains the epileptogenic zone or, at least, clinically relevant propagation areas.

2.5 | Source reconstruction

HdESI was performed with only one cluster of visually as well as semi-automatically detected IEDs per patient. The cluster with the highest number of visually detected IEDs and a comparable cluster of semi-automatically detected IEDs was chosen. For this reason, the semi-automated IEDs clustered automatically by Persyst were grouped visually by hemisphere and lobar resolution to allow comparison with visual hdESI.

Epochs containing the visually or semi-automatically detected IEDs (±2 s) were clipped and exported. They were further processed and analyzed with Fieldtrip (https://www.fieldtriptoolbox.org/, version fieldtrip-20191127) running in Matlab (version 9.0, R2018b, Mathworks Inc.). wMNE as well as the time point at 50% rising phase were chosen for the source reconstruction according to literature.[7,8,26,27] In addition to the measured EEG activity and the inverse method, a forward model is needed. The forward model is based on the head model, the source model and the electrode model. To create the individual head model, the FreeSurfer processed, intensity normalized MRI of each subject was used. A regular 5 mm volumetric grid was constructed in the CAT12 template (CAT12; Christian Gaser 2018, http://www.neuro.uni-jena.de/cat/) in the MNI space. Those standardized volumetric grid points were transformed back to the individual anatomical space by using the inverted DARTEL transformation (DARTEL; SPM12; https://www.fil.ion.ucl.ac.uk/spm/software/spm12/). These volumetric grid points were further used for the source space for each subjects' forward model. An individual boundary element model with three layers of different conductivities (scalp: 0.33S/m, skull: 0.004S/m, and brain: 0.33S/m) was constructed using the "dipoli" method implemented in Fieldtrip. For the sensor model, the sensors were spatially aligned to the anatomical T1 using anatomical landmarks of fiducial positions (left/right preauricular point, nasion). Details on hdESI processing steps are provided as supplementary information. An overview of the processing steps is displayed in Figure 1(A–D).

Source maxima were compared to the sublobe(s) and to the resection itself. The gray matter was divided visually into 19 "sublobes" per hemisphere based on the Lausanne parcellation atlas.[18] In order to evaluate the effect of IED amounts on hdESI accuracy, the shortest Euclidean distance between the resection zone and the maximum amplitude of hdESI was measured for different amounts of IEDs of each patient. Furthermore, the Euclidean distance between the intraindividual hdESI maximum when all IEDs of an individual were included and the hdESI maximum of reduced amounts of IEDs was determined.

2.6 | Statistical analysis

Statistical analysis was performed using GraphPad Prism (version 6, GraphPad Software) and Matlab. Differences were analyzed with Student's *t*-test (or Mann–Whitney U-Test) and shown as means ± standard deviations (SD) (or medians ± interquartile ranges) when data were normally (not normally) distributed. Correlations of nonparametric data were analyzed using the Spearman's rank correlation coefficient (r_s). Cohen's κ was calculated using Matlab, and its interpretation followed the recommended nomenclature.[23,24]

P-values <0.05 were considered statistically significant. They were corrected for multiple comparisons according to Holm–Bonferroni method.

3 | RESULTS

3.1 | Patient cohort and IED frequency

A cohort of 22 patients out of 67 patients was identified retrospectively from the "epilepsy surgery database" between September 2017 and February 2021. All of the identified patients met the inclusion criteria (Figure S1). None of them needed to be excluded. The hdEEG acquisition length was 146 ± 36 min in short-term hdEEG and 914 ± 135 min in long-term hdEEG. Five out of 22 patients

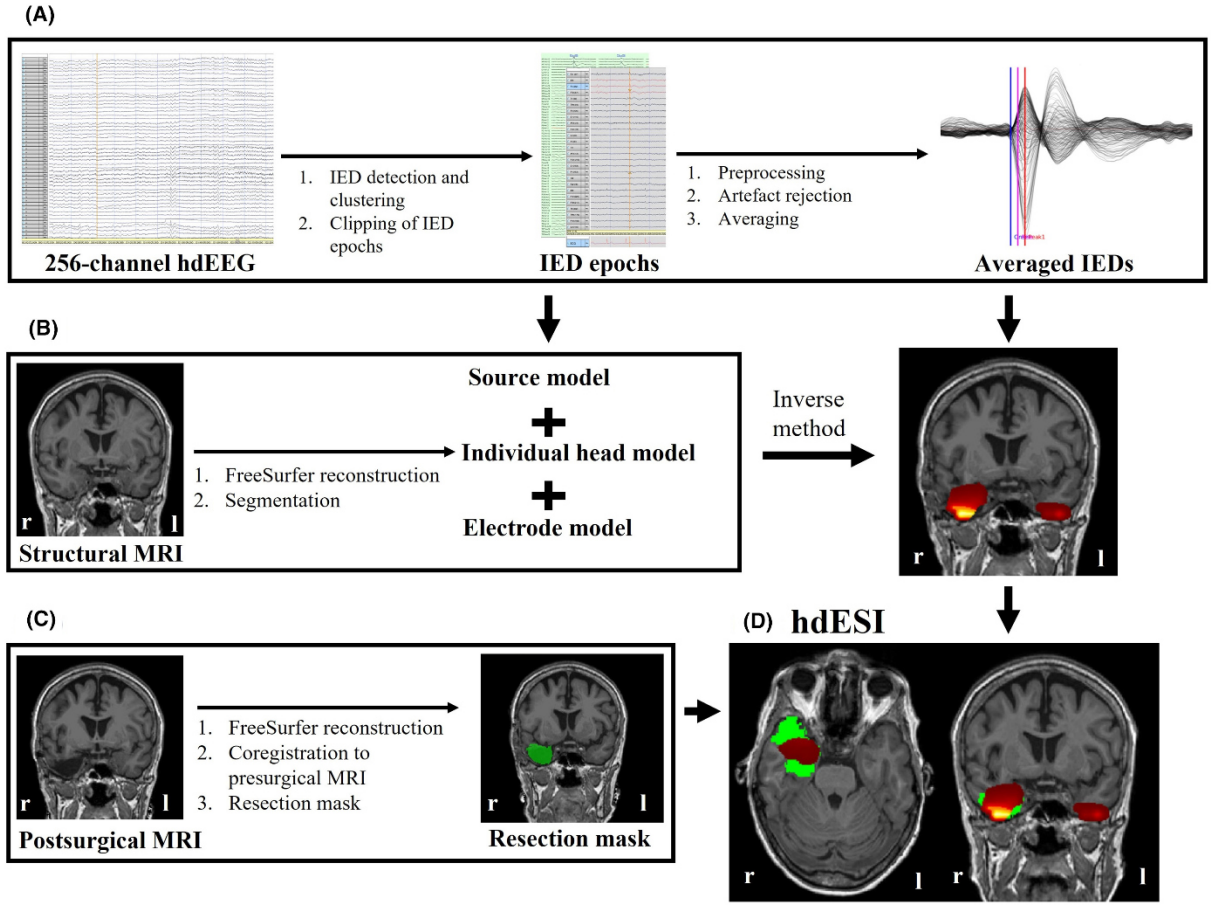

FIGURE 1 Flow-chart of the hdEEG processing steps. Review of the EEG recordings included a visual versus semi-automated marking of IEDs. The 2-s IED epochs were then preprocessed, cleaned of artifacts and averaged within each cluster to improve signal-to-noise ratio (A). Based on the individual structural MRI and the hdEEG a head model, source model and electrode model were created for each patient (B). Furthermore, a resection mask (green) was performed based on the postsurgical MRI (C). HdESI maximum (yellow area within read area) was compared to the resection mask (D).

were diagnosed with extratemporal lobe epilepsy due to low-grade, developmental, epilepsy-associated brain tumors (LEAT), focal cortical dysplasias (FCD) or cavernomas, whereas the remaining 17 patients had temporal lobe epilepsy, mostly with hippocampal sclerosis as the underlying cause. An overview of clinical data and main source imaging results is displayed in Tables 1 and S1.

The detected IED frequency correlated with the seizure frequency before epilepsy surgery (visual detection: $r_s = 0.47$, $P = 0.03$; semi-automated detection: $r_s = 0.59$, $P = 0.008$; $n = 22$), but not with epilepsy duration. Cavernomas and LEATs showed a tendency to a lower IED frequency compared to hippocampal sclerosis regarding visual, but not semi-automatically detected IEDs (2.93 (0.96–4.37 IED/h) versus 5.31 (4.36–22.54 IED/h) (median [IQR]), $P = 0.096$, Mann–Whitney U-Test, $n = 12$). There was no significant difference in IED frequency between extratemporal and temporal lobe epilepsies and no significant correlation between IED frequency and ASM reduction from admission to time of hdEEG.

3.2 | Comparison of visual and semi-automated IED detection

There was no significant difference in the number of IEDs between visually versus semi-automatically marked IEDs (visual detection: 74 ± 56 IEDs/patient versus semi-automated detection: 116 ± 115 IEDs/patient, $P = 0.13$, $n = 22$). However, the difference might become significant with an increasing sample size. The visual IEDs were divided in either one, two or three group(s) ($n = 11$, 7, 4, respectively), according to their lobar topography. The semi-automatically detected IEDs were classified according to the electrode with the highest amplitude into a mean of eight clusters. Overall, Persyst had a mean IED sensitivity of 77.12 ± 21.82%, defined by the ratio of visually detected IEDs also found by Persyst. The mean positive predictive value of Persyst was low with 4.11 ± 2.65%. The other detected events consisted of technical and biological artifacts and physiological EEG patterns such as wicket spikes and sleep patterns. The

TABLE 1 Patient demographics, clinical characteristics and main source imaging results.

		All patients
Group size		22
Sex	Female	8 (36%)
	Male	14 (64%)
Duration epilepsy to surgery (y)		15,45 [14,42]
Age at surgery (y)		40,41 [12.38]
Seizure frequency one y before surgery (seizures per mos)		8.92 [10.83]
Structural MRI	Lesional	15 (68%)
	Non-lesional	7 (32%)
HdEGG length (hh:mm:ss)	Short-term	02:25:34 [00:36:07]
	Long-term	15:14:01 [02:15:13]
HdEEG recording	Short-term	4 (18%)
	Long-term	18 (82%)
SOZ location (TLE; ETLE)	TLE	17 (77%)
	ETLE	5 (23%)
SOZ hemisphere	Left	13 (59%)
	Right	9 (41%)
Surgery	AH + ATR	12 (54.5%)
	AH	2 (9%)
	LiTT	1 (4.5%)
	Other	7 (32%)
Histology	HS	7 (31.8%)
	GG	3 (13.6%)
	FCD	2 (9.1%)
	Cavernoma	3 (13.6%)
	Normal cortex/ Gliosis	6 (27.3%)
Surgical outcome at last follow-up (≥6 mos; Engel classification)	IA	16 (72.73%)
	IB	1 (4.54%)
	ID	5 (22.73%)
Post-op follow-up (mos)		18.27 [9.08]
Spike counts (IEDs/ patient)	Visual	74 [56]
	Semi-automated	116 [115]
Mean Euclidean distance (mm)	Visual	26.07 [31.12]
	Semi-automated	33.64 [34.75]
Sublobar concordance	Visual	13 (61.9)
	Semi-automated	12 (57.14)
Lobar concordance	Visual	14 (66.7)
	Semi-automated	13 (61.9)

Note: All patients had refractory focal epilepsy, all of them with Engel 1 outcome after epilepsy surgery. Data are given as *n* (%) or as mean [standard deviation].

Abbreviations: AH, amygdalohippocampectomy; ATR, anterior temporal lobe resection; ETLE, extratemporal lobe epilepsy; FCD, focal cortical dysplasia; GG, ganglioglioma; hdEEG, high-density EEG; HS, hippocampal sclerosis; LiTT, laser interstitial thermal therapy; mos, months; SOZ, seizure onset zone; TLE, temporal lobe epilepsy; y, year(s).

Cohen's κ for visual versus purely automated IED detection is 0.08, indicating a slight level of agreement. In contrast, the Cohen's κ for visual versus semi-automated IED selection is 0.65, corresponding to a substantial level of agreement.

When analyzing only Persyst detected clusters grouped by the electrode with the highest amplitude, the 10 most prevalent clusters included a mean number of 1951 ± 219 single events and a mean IED sensitivity of $86.64 \pm 15.77\%$, defined by the amount of semi-automated detected IEDs among all Persyst detected events (Figure 2A,B). There was a significantly higher IED sensitivity of the first four clusters compared to the one of the fifth to tenth cluster ($62.75 \pm 35.66\%$ versus $23.88 \pm 24.12\%$, $P < 0.001$, *t*-test). The success rate to detect at least one event cluster with more than 30 IEDs increased from 45.45%, when considering the most prevalent cluster only, to 86.36%, when considering the first 10 clusters (Figure 2C). The mean success rate of a 30 IED-cluster detection was significantly higher in the first four clusters compared to the fifth to tenth cluster (50% vs 4.55%, $P < 0.001$, *t*-test).

The time to select all IEDs in the full-length hdEEG was significantly shorter with the semi-automated compared to the visual marking by 275 ± 46 min (305 ± 72 min vs 30 ± 26 min, $P < 0.001$, *t*-test, $n = 22$; Figure 2).

3.3 | Effect of semi-automated IED detection on hdESI

The mean distance between the resection zone and the hdESI maximum was 26.07 ± 31.12 mm for visual detection and 33.64 ± 34.75 mm for semi-automated detection, without significant difference ($P = 0.46$, Figure 3). Similarly, the sublobar concordance was around 60% in both groups (Table 1). A subgroup analysis of distances

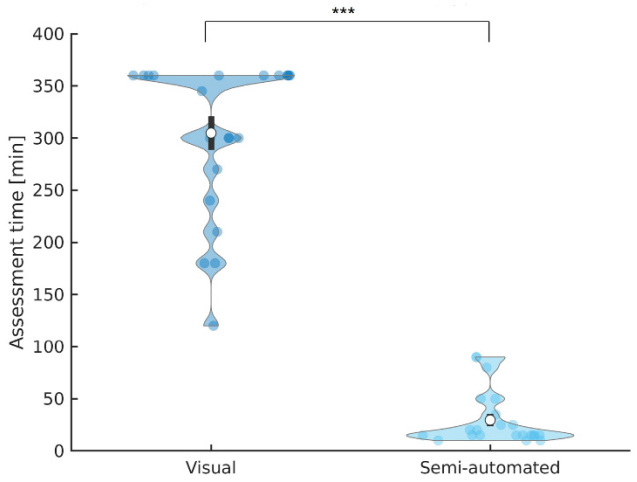

FIGURE 2 Time efficiency of visual IED marking compared to semi-automated IED detection with Persyst. The mean assessment time to score the full length hdEEG was shorter with semi-automated Persyst detection compared to purely visual marking (305 ± 72 min vs 30 ± 26 min, $n = 22$, $P < 0.001$, t-test). Data is shown in mean (white circle) ± standard deviation (black lines) and data density (blue area). Statistically significant group differences are marked with an asterisk (***$P < 0.001$).

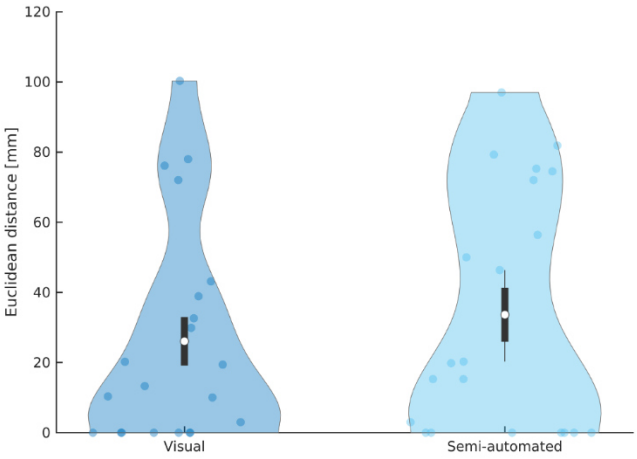

FIGURE 3 Effect of visual versus semi-automated IEDs on hdESI accuracy. There was no significant difference between the mean Euclidean distance of the visual versus semi-automated Persyst detection compared to purely visual marking ($P = 0.87$). Data is shown in mean (white circle) ± standard deviation (black lines) and data density (blue area).

and concordance rates is given in Table S2. In patients with temporal SOZ ($n = 16$) the distance was significantly lower than in patients with extratemporal SOZ ($n = 5$) (visual: 16.07 ± 21.88 mm vs 58.06 ± 37.00 mm and semi-automated: 22.81 ± 28.74 mm vs 68.30 ± 31.15 mm; $P < 0.014$, t-test). There was a significantly higher distance for cavernomas and LEATs compared to hippocampal sclerosis (visual: 47.65 ± 26.00 mm vs 2.22 ± 4.16 mm and semi-automated: 54.15 ± 41.94 mm vs 10.78 ± 18.42 mm [$n = 11$]; $P \leq 0.047$, t-test). Cavernomas and LEATs had an extratemporal SOZ in three out of five patients. There was no significant difference in the distance between the MRI positive and negative group. An example of hdESI results of an MRI positive patient is shown in Figure 4.

3.4 | Effect of IED amount on hdESI

The mean distance between hdESI maximum of the full IED amount and the one of reduced IED amounts of the same patient was lower than 1 cm when a mean number of at least 33 IEDs were included (Figure 5). Similarly, the distance between resection zone and hdESI maximum did not change more than 1 cm above a mean number of 20 ± 26 IEDs.

For intraindividual comparison, all patients with a maximum of 30 or more IEDs ($n = 15$) were selected and mean distance between hdESI maximum of the full amount of IEDs and hdESI maximum of 30 and 10 randomly chosen IEDs of the same individual were compared. In this subgroup analysis, we found a significantly shorter distance when 30 IEDs are included in comparison to 10 IEDs (4.21 ± 18.36 mm vs 35.98 ± 32.55 mm, $P < 0.001$, t-test). Accordingly, we found a significantly shorter distance to the resection zone when 30 IEDs are included compared to 10 IEDs (6.97 ± 31.40 mm vs 31.54 ± 28.85 mm, $P = 0.03$, t-test).

4 | DISCUSSION

In this study we addressed two main issues of practicability of interictal hdESI, namely semi-automated IED detection and minimum amount of IEDs needed. We found that semi-automated IED detection can reduce review time without affecting the localization accuracy of hdESI and that 30–40 IEDs are advisable per cluster.

4.1 | Effect of semi-automated IED detection on hdESI

Most hdESI applications focus on interictal events, hence, the detection of IEDs is an essential part of clinical diagnostics. IED selection can be made purely visually or semi-automatically by different software. Here, Persyst Spike Detector P14 C was able to identify $77.12 \pm 21.82\%$ of the visually detected IEDs. Moreover, sublobar concordance and mean distance between resection zone and hdESI of

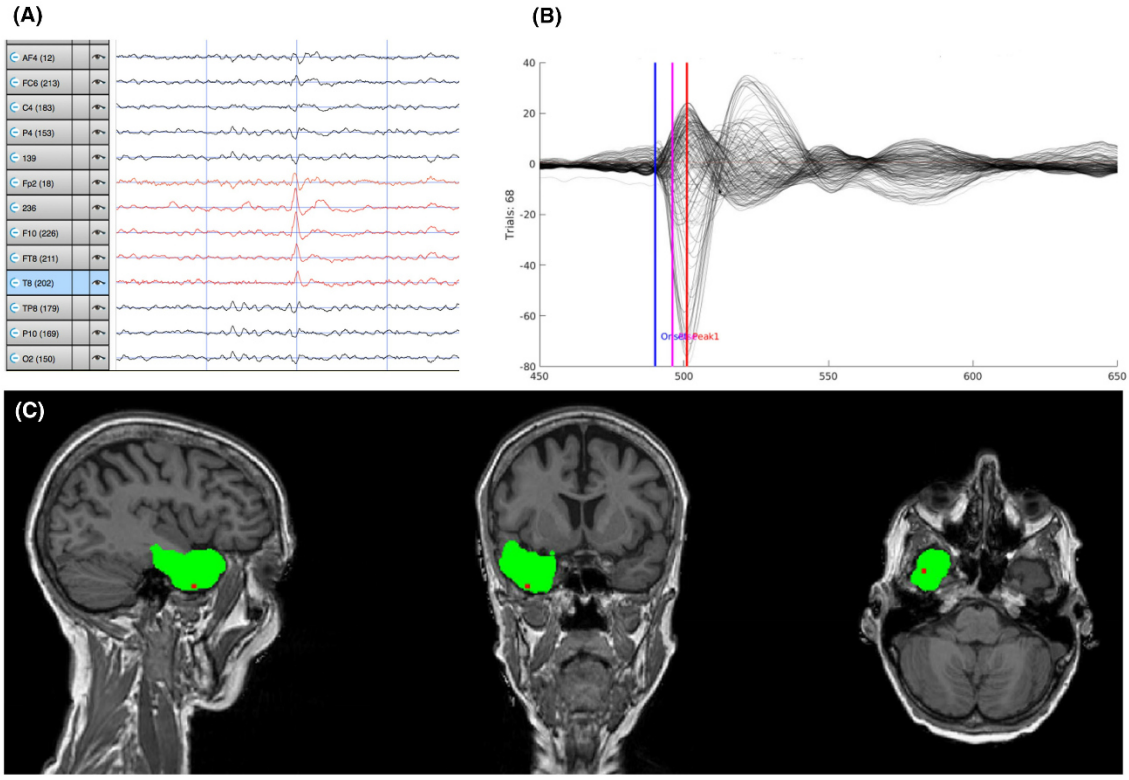

FIGURE 4 ESI results of an MRI positive patient with 256-channel hdEEG. The patient was Engel class 1A at 1-year follow-up after anterior temporal lobectomy. Pathology confirmed hippocampal sclerosis. Single IED on the right temporal electrodes displayed on an extended average montage (A). An average of 68 IEDs (B). HdESI with resected volume (green) and the maximum amplitude of ESI (red point) (C). wMNE sublobar localization was right temporal. Euclidean distance was 0 mm with source maximum being in the resection zone.

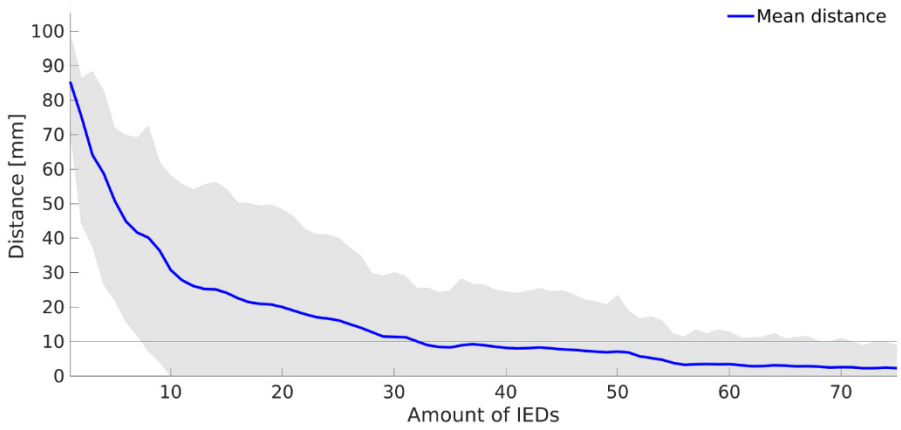

FIGURE 5 Effect of IED amount on localization of hdESI maximum. The mean Euclidean distance between the source reconstruction of the full individual IED amount and the source reconstruction of reduced IED amounts of the same patient was lower than 1 cm above a mean number of 33 IEDs (red line: Euclidean distance of 1 cm; blue line: overall mean distance; gray area: standard deviation).

the visually and semi-automatically detected IEDs was without significant difference.

Concerning the sensitivity of IED detection, a study by Reus et al.[28] compared three commercial automated spike detection software packages (Persyst, Encevis, BESA). IED detection by Persyst was better than the other two software packages concerning sensitivity and similarity to human review. Accordingly, it has been shown, that Persyst was statistically noninferior to the skilled human readers in standard 10–20 system electrode recording sites plus sub-temporal electrodes.[22] The average level of pairwise spike marking sensitivities of three skilled human EEG readers was about 45%, and comparable to a sensitivity of 43.9% of Persyst. Very recently, an artificial intelligence-based computer algorithm had a sensitivity of 89% for identifying EEGs with IEDs recorded from patients with epilepsy, but human expert supervision was still necessary for confirming the clusters of detected IEDs.[29] In previous studies, the reported average pairwise reader spike sensitivities were comparably high with 52%

and 70%, respectively, mostly due to utilizing brief records containing high spike density and largely demonstrative spike types.[30,31]

There are only a few studies addressing the application of automated IED detection in hdEEG, which allows more accurate ESI results than low-density ESI.[9,10,32] Vorderwülbecke et al.[18] recently published a study on the validity of automated hdEEG IED detection by Persyst and hdESI. In contrast to our study, these authors did not compare automated with visual IED detection. Instead, automatically detected clusters were reviewed if they were IEDs or artifacts. A semi-automated spike detection sensitivity of 73% and spike detection rate of 38% was described. Compared to our results, Heers et al. reported a good concordance of the SOZ with the most frequently and visually detected IED types in hdEEG, but not with (semi-) automatically detected IEDs in hdEEG. One reason for the difference could be the newer version of Persyst we used compared to the one used by Heers et al.[33]

The time to score the whole hdEGG was significantly shorter with Persyst. Given the increased number of IEDs available in long-term recordings,[34] this can balance the higher workload needed for reviewing theses datasets. To our knowledge, this is the first study comparing the time between the two different detection methods.

Regarding hdESI results of visually and automatically detected IEDs, the mean sublobar concordance rate of temporal lobe epilepsies was in line with current studies (visual: 75.00% and semi-automated: 68.75%, $n = 16$). However, the concordance rate for extratemporal lobe epilepsies was lower (visual and semi-automated: 20%, $n = 5$). In semi-automated hdESI, a sublobar concordance rate of 75% in a 256-channel setting on half-rise of the averaged IEDs of patients with a favorable postsurgical seizure outcome (ILAE 1 and 2, see Vorderwülbecke et al., table S3) was reported.[18] Visual hdESI studies such as Toscano et al. 2020 and Lascano et al. found a similar sublobar concordance rate of patients with a favorable postsurgical seizure outcome (Engel 1) of 75% and 88%, respectively.[35,36] Interestingly, the sensitivity was lower when fully automatically interictal ESI was performed. For example, Iachim et al.[37] described a sensitivity of 53% based on sublobar concordance between low-density ESI localization and irritative zone in SEEG,[37] whereas van Mierlo et al.[38] reported a sensitivity of 70% based on concordance between low-density ESI localization and resection zone. A comparison of both methods showed a sensitivity of 88% in the semi-automated approach versus 60% in the fully automated method.[39] The mean Euclidean distance between source maximum and resection zone is rarely mentioned in the literature and there is no data on the distance in automated hdESI. Vorderwülbecke et al. 2020 and Carboni et al. 2022 (same cohort) subdivided the Euclidean distance between the source maximum and the resection zone for patients with favorable postsurgical outcome (Engel 1 and 2, $n = 30$) into three groups (<10 mm, <20 mm, >20 mm).[26,40] The proportion of each group in the cohort was given for temporal and extratemporal lobe epilepsies (temporal: 81%, 16%, 5% and extratemporal: 45%, 10%, 45%, see Vorderwülbecke et al. 2020, Figure 3 and Data S2). Our results showed slightly higher distances for temporal lobe epilepsies when subdividing them into the same three groups (visual: 56%, 19%, 25% and semi-automated 50%, 19%, 31%) and much higher distances for extratemporal lobe epilepsies (visual: 20%, 0%, 80% and semi-automated: 0%, 20%, 80%). As the amount of IEDs was lower than in our cohort (median: 29 IEDs/patient and mean: 45 IEDs/patient in Vorderwülbecke et al. 2020, see Data S2, $n = 21$ with 9 of unknown IED amount), this difference is probably not explained by the amount of IEDs. Possible reasons for the higher distances in our cohort, especially in extratemporal lobe epilepsies, include the different inverse method or the different sample composition.[40] Additionally, the extratemporal subgroup was very small. However, in terms of the main question of our work, there was no significant difference in the distance between semi-automated and visual hdESI of extratemporal lobe epilepsies as well as of temporal lobe epilepsies in our cohort. When comparing interictal ESI with the resection zone, the limitations of interictal ESI should be considered. Interictal ESI mainly represents the irritative zone, which may or may not overlap with the epileptogenic zone and SOZ.[9,14]

4.2 | Effect of IED amount on hdESI

Performing hdESI requires expertise and time, especially when a long recording (several hours to several days) is needed to get enough IEDs for ESI. While it is common practice to obtain as many IEDs as possible for averaging, there is little data guiding what is an acceptable number of IEDs to analyze. In our cohort, the difference between 30 and 10 IEDs was more than 30 mm when referenced to hdESI maximum with the full amount of IEDs. However, the difference between 30 IEDs and 10 IEDs was <5 mm when referenced to the resection zone. Depending on the different need of accuracy this could help the clinician to determine the IED amount.

To our knowledge, this has been the first study to analyze this question in hdEEG (256 channels), although many studies expressed the clinical need[13,17] In previous studies, the exact number of IEDs used for hdESI differed widely. Foged et al.,[12] Sohrabpour et al.[10] and Toscano et al.[35] used a minimum of five, 15 or 10 IEDs,

respectively, whereas Plummer et al.[41] and Heers et al.[42] performed hdESI on an average number of 48 and 107 IEDs, respectively. In former low-density EEG studies, the averaging of identical spikes improved source localization accuracy compared to ESI performed on single spikes.[43,44] Considering our results, a number of approximately 30–40 IEDs is sufficient to get accurate hdESI results. However, it should be mentioned, that an IED number higher than 30–40 would decrease localization errors and affect accuracy. The question of similarity concerning localization and morphology of IEDs clustered in one group still remains unclear and needs to be studied in detail.

4.3 | General aspects of hdESI in our cohort

Interestingly, the localization of the SOZ has an impact on hdESI. In our cohort, patients with temporal SOZ had significantly shorter distances between ESI maximum and resection zone than patients with extratemporal SOZ (visual: 16.07 ± 21.88 mm vs 58.06 ± 37.00 mm; semi-automated: 22.81 ± 28.74 mm vs 68.30 ± 31.15 mm). The effect size of the localization of the SOZ on the distance to the resection boundary was higher than the effect of an increasing number of IEDs above a number of 30–40 IEDs. In line with our results, Cox et al.[13] previously found a higher rate of complete concordance of ESI with icEEG on a sublobar level in temporal compared to extratemporal lobe epilepsy.[9,13] The reason for this is not clear, but might be a consequence of different IED topography, different number of IEDs analyzed, the forward model, the inverse method or better scalp EEG accessibility of temporal areas due to thinner bone structures. Another reason could be, that the inclusion of very caudal electrodes as in the 256-channel set-up lead to a shift of the hdESI maximum towards the temporal lobes even in extratemporal epilepsies.[26]

There is little data guiding on how similar spikes should be morphologically in order to be grouped. An additional biasing factor could be etiology of the epilepsy. As extratemporal lobe epilepsies were either LEATs, FCDs or cavernomas, this could have influenced the size of resection and the amount and morphology of IEDs.[45,46] However, the group size in our cohort was too small to study this in detail. Patients with non-lesional and lesional MRI had 86% (6/7) and 57% (8/14) sublobar concordance rates, respectively. This is particular interesting, keeping in mind that hdESI is a very important tool for MRI-negative epilepsies and should be studied in a larger patient sample. In line with our results, a study of Brodbeck et al. reported the correct localization of the epileptogenic focus by ESI in 80% of patients with normal MRI.[15] In a larger study cohort ($n = 74$), the concordance rate of ESI with intracranial EEG was higher in MRI-negative epilepsies compared to MRI-positive epilepsies.[47]

4.4 | Limitations

Our study has limitations given the retrospective nature and logistical constraints. The clinician scoring the hdEEGs is part of the epilepsy team and was not blinded for clinical information. Furthermore, the same hdEEG was scored twice by the same reader, purely visually and semi-automatically, which could have influenced scoring time. By having an interval of at least 6 months in between the two scorings, we argue that the impact of this factor is not strong. An additional limitation is the use of only one inverse method and IED timepoint. However, we chose a common inverse method and timepoint. A previous study by Pellegrino et al. 2020 reported lowest distance between the map maximum and epilepsy focus in MNE.[7] Other studies, found other preferable source reconstruction methods, although differences were often slight.[40] Moreover, although the IED scoring and experimental ESI analysis was not part of the clinical evaluation, all patients received clinically driven ESI (done by other clinicians and using other software), which may have had an influence on indicating surgery especially in non-lesional patients. However, ESI is just one of many modalities used in the (pre-)surgical decision making in our program. As the Matlab toolbox we used may not be suited for all clinical workflows, further studies that compare our results to common clinical software packages are relevant. Prospective and multi-center studies on details of clinical hdEEG use such as the choice of the inverse method or the software package and the effect of IED clusters are needed.

5 | CONCLUSIONS

This study provides evidence for better practicability of hdESI. In particular, we could show that 30–40 IEDs per cluster are advisable. Moreover, semi-automated IED selection dramatically improved the scoring time needed without significantly affecting hdESI results.

Overall, hdESI is a valuable contributory technique in surgical planning. Our results can help to improve the efficiency of hdESI and increase its use in epilepsy centers.

AUTHOR CONTRIBUTIONS

Conception and design of the study: ECH, NF and DvdV; Analysis of data: ECH, DvdV and DG; Drafting of the manuscript: ECH and DvdV; Drafting of the figures: ECH and DvdV; all authors critically revised and approved the final version of the manuscript.

FUNDING INFORMATION

This research did not receive any specific grant from funding agencies in the public, commercial, or not-for-profit sectors.

ACKNOWLEDGMENT

Open Access funding enabled and organized by Projekt DEAL.

CONFLICT OF INTEREST STATEMENT

None of the authors has any conflict of interest to disclose. We confirm that we have read the Journal's position on issues involved in ethical publication and affirm that this report is consistent with those guidelines.

DATA AVAILABILITY STATEMENT

All relevant data are available from the corresponding author upon request. Raw imaging data are not publicly available due to data protection regulations.

ORCID

Ev-Christin Heide https://orcid.org/0000-0003-4511-1022
Daniel van de Velden https://orcid.org/0000-0003-2834-4457
David Garnica Agudelo https://orcid.org/0000-0002-1527-2290
Niels K. Focke https://orcid.org/0000-0001-5486-6289

REFERENCES

1. Kwan P, Arzimanoglou A, Berg AT, Brodie MJ, Allen Hauser W, Mathern G, et al. Definition of drug resistant epilepsy: consensus proposal by the ad hoc task force of the ILAE commission on therapeutic strategies. Epilepsia. 2010;51:1069–77.
2. Engel J. The current place of epilepsy surgery. Curr Opin Neurol. 2018;31:192–7.
3. Wiebe S, Blume WT, Girvin JP, Eliasziw M. A randomized, controlled trial of surgery for temporal-lobe epilepsy. N Engl J Med. 2001;345:311–8.
4. Vakharia VN, Duncan JS, Witt J-A, Elger CE, Staba R, Engel J. Getting the best outcomes from epilepsy surgery. Ann Neurol. 2018;83:676–90.
5. Ryvlin P, Cross JH, Rheims S. Epilepsy surgery in children and adults. Lancet Neurol. 2014;13:1114–26.
6. Hämäläinen MS, Ilmoniemi RJ. Interpreting magnetic fields of the brain: minimum norm estimates. Med Biol Eng Comput. 1994;32:35–42.
7. Pellegrino G, Hedrich T, Porras-Bettancourt M, Lina J-M, Aydin Ü, Hall J, et al. Accuracy and spatial properties of distributed magnetic source imaging techniques in the investigation of focal epilepsy patients. Hum Brain Mapp. 2020;41:3019–33.
8. Sperli F, Spinelli L, Seeck M, Kurian M, Michel CM, Lantz G. EEG source imaging in pediatric epilepsy surgery: a new perspective in presurgical workup. Epilepsia. 2006;47:981–90.
9. Brodbeck V, Spinelli L, Lascano AM, Wissmeier M, Vargas M-I, Vulliemoz S, et al. Electroencephalographic source imaging: a prospective study of 152 operated epileptic patients. Brain. 2011;134:2887–97.
10. Sohrabpour A, Lu Y, Kankirawatana P, Blount J, Kim H, He B. Effect of EEG electrode number on epileptic source localization in pediatric patients. Clin Neurophysiol. 2015;126:472–80.
11. Sharma P, Seeck M, Beniczky S. Accuracy of Interictal and ictal electric and magnetic source imaging: a systematic review and meta-analysis. Front Neurol. 2019;10:1250.
12. Foged MT, Martens T, Pinborg LH, Hamrouni N, Litman M, Rubboli G, et al. Diagnostic added value of electrical source imaging in presurgical evaluation of patients with epilepsy: a prospective study. Clin Neurophysiol. 2020;131:324–9.
13. Cox BC, Danoun OA, Lundstrom BN, Lagerlund TD, Wong-Kisiel LC, Brinkmann BH. EEG source imaging concordance with intracranial EEG and epileptologist review in focal epilepsy. Brain Commun. 2021;3:fcab278.
14. Duez L, Tankisi H, Hansen PO, Sidenius P, Sabers A, Pinborg LH, et al. Electromagnetic source imaging in presurgical workup of patients with epilepsy: a prospective study. Neurology. 2019;92:e576–86.
15. Brodbeck V, Spinelli L, Lascano AM, Pollo C, Schaller K, Vargas MI, et al. Electrical source imaging for presurgical focus localization in epilepsy patients with normal MRI. Epilepsia. 2010;51:583–91.
16. Mouthaan BE, Rados M, Barsi P, Boon P, Carmichael DW, Carrette E, et al. Current use of imaging and electromagnetic source localization procedures in epilepsy surgery centers across Europe. Epilepsia. 2016;57:770–6.
17. Mégevand P, Seeck M. Electric source imaging for presurgical epilepsy evaluation: current status and future prospects. Expert Rev Med Devices. 2020;17:405–12.
18. Vorderwülbecke BJ, Baroumand AG, Spinelli L, Seeck M, van Mierlo P, Vulliémoz S. Automated interictal source localisation based on high-density EEG. Seizure. 2021;92:244–51.
19. Engel J Jr, Van Ness PC, Rasmussen TB, Ojemann LM. Outcome with respect to epileptic seizures. In: Engel J Jr, editor. Surgical treatment of the epilepsies. 2nd ed. New York: Raven Press; 1993. p. 609–21.
20. Wieser HG, Blume WT, Fish D, Goldensohn E, Hufnagel A, King D, et al. ILAE commission report. Proposal for a new classification of outcome with respect to epileptic seizures following epilepsy surgery. Epilepsia. 2001;42:282–6.
21. Seeck M, Koessler L, Bast T, Leijten F, Michel C, Baumgartner C, et al. The standardized EEG electrode array of the IFCN. Clin Neurophysiol. 2017;128:2070–7.
22. Scheuer ML, Bagic A, Wilson SB. Spike detection: inter-reader agreement and a statistical Turing test on a large data set. Clin Neurophysiol. 2017;128:243–50.
23. McHugh ML. Interrater reliability: the kappa statistic. Biochem Med. 2012;22:276–82.

24. Landis JR, Koch GG. The measurement of observer agreement for categorical data. Biometrics. 1977;33:159–74.
25. Cohen J. A coefficient of agreement for nominal scales. Educ Psychol Meas. 1960;20:37–46.
26. Vorderwülbecke BJ, Carboni M, Tourbier S, Brunet D, Seeber M, Spinelli L, et al. High-density electric source imaging of interictal epileptic discharges: how many electrodes and which time point? Clin Neurophysiol. 2020;131:2795–803.
27. Ray A, Tao JX, Hawes-Ebersole SM, Ebersole JS. Localizing value of scalp EEG spikes: a simultaneous scalp and intracranial study. Clin Neurophysiol. 2007;118:69–79.
28. Reus EEM, Cox FME, van Dijk JG, Visser GH. Automated spike detection: which software package? Seizure. 2022;95:33–7.
29. Fürbass F, Kural MA, Gritsch G, Hartmann M, Kluge T, Beniczky S. An artificial intelligence-based EEG algorithm for detection of epileptiform EEG discharges: validation against the diagnostic gold standard. Clin Neurophysiol. 2020;131:1174–9.
30. Webber W, Litt B, Lesser RP, Fisher RS, Bankman I. Automatic EEG spike detection: what should the computer imitate? Electroencephalogr Clin Neurophysiol. 1993;87:364–73.
31. Wilson SB, Harner RN, Duffy FH, Tharp BR, Nuwer MR, Sperling MR, et al. I. Correlation and reliability of human experts. Electroencephalogr Clin Neurophysiol. 1996;98:186–98.
32. Lantz G, Grave de Peralta R, Spinelli L, Seeck M, Michel C. Epileptic source localization with high density EEG: how many electrodes are needed? Clin Neurophysiol. 2003;114:63–9.
33. Heers M, Böttcher S, Kalina A, Katletz S, Altenmüller D-M, Baroumand AG, et al. Detection of interictal epileptiform discharges in an extended scalp EEG array and high-density EEG-A prospective multicenter study. Epilepsia. 2022;63:1619–29.
34. Bach Justesen A, Foged MT, Fabricius M, Skaarup C, Hamrouni N, Martens T, et al. Diagnostic yield of high-density versus low-density EEG: the effect of spatial sampling, timing and duration of recording. Clin Neurophysiol. 2019;130:2060–4.
35. Toscano G, Carboni M, Rubega M, Spinelli L, Pittau F, Bartoli A, et al. Visual analysis of high density EEG: As good as electrical source imaging? Clin Neurophysiol Pract. 2020;5:16–22.
36. Lascano AM, Perneger T, Vulliemoz S, Spinelli L, Garibotto V, Korff CM, et al. Yield of MRI, high-density electric source imaging (HD-ESI), SPECT and PET in epilepsy surgery candidates. Clin Neurophysiol. 2016;127:150–5.
37. Iachim E, Vespa S, Baroumand AG, Danthine V, Vrielynck P, De Tourtchaninoff M, et al. Automated electrical source imaging with scalp EEG to define the insular irritative zone: comparison with simultaneous intracranial EEG. Clin Neurophysiol. 2021;132:2965–78.
38. van Mierlo P, Strobbe G, Keereman V, Birot G, Gadeyne S, Gschwind M, et al. Automated long-term EEG analysis to localize the epileptogenic zone. Epilepsia Open. 2017;2:322–33.
39. Baroumand AG, van Mierlo P, Strobbe G, Pinborg LH, Fabricius M, Rubboli G, et al. Automated EEG source imaging: a retrospective, blinded clinical validation study. Clin Neurophysiol. 2018;129:2403–10.
40. Carboni M, Brunet D, Seeber M, Michel CM, Vulliemoz S, Vorderwülbecke BJ. Linear distributed inverse solutions for interictal EEG source localisation. Clin Neurophysiol. 2022;133:58–67.
41. Plummer C, Vogrin SJ, Woods WP, Murphy MA, Cook MJ, Liley DTJ. Interictal and ictal source localization for epilepsy surgery using high-density EEG with MEG: a prospective long-term study. Brain. 2019;142:932–51.
42. Heers M, Hedrich T, An D, Dubeau F, Gotman J, Grova C, et al. Spatial correlation of hemodynamic changes related to interictal epileptic discharges with electric and magnetic source imaging. Hum Brain Mapp. 2014;35:4396–414.
43. Wennberg R, Cheyne D. EEG source imaging of anterior temporal lobe spikes: validity and reliability. Clin Neurophysiol. 2014;125:886–902.
44. Bast T, Boppel T, Rupp A, Harting I, Hoechstetter K, Fauser S, et al. Noninvasive source localization of interictal EEG spikes: effects of signal-to-noise ratio and averaging. Clin Neurophysiol. 2006;23:487–97.
45. Krsek P, Maton B, Korman B, Pacheco-Jacome E, Jayakar P, Dunoyer C, et al. Different features of histopathological subtypes of pediatric focal cortical dysplasia. Ann Neurol. 2008;63:758–69.
46. Hamer HM, Najm I, Mohamed A, Wyllie E. Interictal epileptiform discharges in temporal lobe epilepsy due to hippocampal sclerosis versus medial temporal lobe tumors. Epilepsia. 1999;40:1261–8.
47. Abdallah C, Maillard LG, Rikir E, Jonas J, Thiriaux A, Gavaret M, et al. Localizing value of electrical source imaging: frontal lobe, malformations of cortical development and negative MRI related epilepsies are the best candidates. NeuroImage Clinical. 2017;16:319–29.

SUPPORTING INFORMATION

Additional supporting information can be found online in the Supporting Information section at the end of this article.

How to cite this article: Heide E-C, van de Velden D, Garnica Agudelo D, Hewitt M, Riedel C, Focke NK. Feasibility of high-density electric source imaging in the presurgical workflow: Effect of number of spikes and automated spike detection. Epilepsia Open. 2023;8:785–796. https://doi.org/10.1002/epi4.12732

8. APPENDIX A

This following chapter contains additional figures and tables related to the project from chapter 4.1.

Appendix A table 1: Percentage differences of global power group mean between conditions for all frequencies.

		Delta	Theta	Alpha	Beta1	Beta2	Gamma
Outside-MR scanner condition	HC	2.1112	2.0046	2.1384	1.6262	1.3325	0.8164
	GGE	2.3866	2.3929	2.5071	1.9374	1.5747	1.0298
Inside-MR scanner condition	HC	2.9626	2.9938	2.9201	2.5125	1.9875	1.4671
	GGE	3.0470	3.1542	3.0965	2.5619	2.1130	1.5739
Group mean change between conditions	HC	40%	49%	37%	55%	49%	80%
	GGE	28%	32%	24%	32%	34%	53%

Appendix A table 2: Percentage difference of global functional connectivity group mean between conditions for all frequencies.

		Delta	Theta	Alpha	Beta1	Beta2	Gamma
Outside-MR scanner condition	HC	0.0199	0.0233	0.0388	0.0268	0.0267	0.0277
	GGE	0.0212	0.0277	0.0420	0.0288	0.0259	0.0254
Inside-MR scanner condition	HC	0.0248	0.0276	0.0357	0.0286	0.0282	0.0275
	GGE	0.0250	0.0339	0.0424	0.0325	0.0304	0.0278
Group mean change between conditions	HC	25%	18%	-8%	7%	6%	-1%
	GGE	18%	22%	1%	13%	17%	10%

Appendix A table 3: 2-way ANOVA analysis of global power and functional connectivity values in each frequency.
The effect of the measurement condition (main effect) was highly statistically significant for global power in all frequency bands. The interaction of the inside-outside factor on the patient-control group was only significant for global power in Beta1 ($p = 0.0447$) and, at trend level, for Delta ($p = 0.0739$). None of these interactions survived FDR correction. For global connectivity, the effect of the measurement condition was highly statistically significant in the delta and theta frequency bands after correcting for multiple comparison via FDR, and, at trend level, for Beta1 and Beta2. No statistically significant for the interaction of the inside-outside factor on the patient-control group was observed.

	Delta	***Theta***	***Alpha***	***Beta1***	***Beta2***	***Gamma***
Global Power						
Main effect of inside/outside MR condition						
p * $p < 0.1$, trend level ** $p < 0.05$, significant	**0.00012	**0.00015	**0.00002	**0.00006	**0.00002	**0.00012
FDR corrected	**< 0.001	**< 0.001	**< 0.001	**< 0.001	**< 0.001	**< 0.001
Interaction of inside/outside MR factor with group difference						
p * $p < 0.1$, trend level ** $p < 0.05$, significant	*0.0739	0.111	0.136	**0.0447	0.148	0.119
FDR corrected	0.148	0.148	0.148	0.148	0.148	0.148
Global functional connectivity						
Main effect of inside/outside MR condition						
p * $p < 0.1$, trend level ** $p < 0.05$, significant	**<0.0001	**0.0002	0.6960	*0.0655	**0.0466	0.2340
FDR corrected	**< 0.0001	**< 0.001	0.696	*0.09825	*0.0932	0.2808
Interaction of inside/outside MR factor with group difference						
p * $p < 0.1$, trend level ** $p < 0.05$, significant	0.351	0.786	0.641	0.7249	0.798	07739
FDR corrected	0.798	0.798	0.798	0.798	0.798	0.798

Appendix A table 4: Spatial Pearson correlation of the cortical maps of group difference maps ($-log_{10}$ p-value maps, GGE>HC) of power and ImCoh in each frequency band.

** $p_{FDR} < 0.001$	Power	ImCoh
Delta	r = 0.8613 **	0.0978 **
Theta	r = 0.8615 **	0.5476 **
Alpha	r = 0.9127 **	0.1664 **
Beta1	r = 0.8916 **	0.2112 **
Beta2	r = 0.9070 **	0.2268 **
Gamma	r = 0.9133 **	0.0831 **

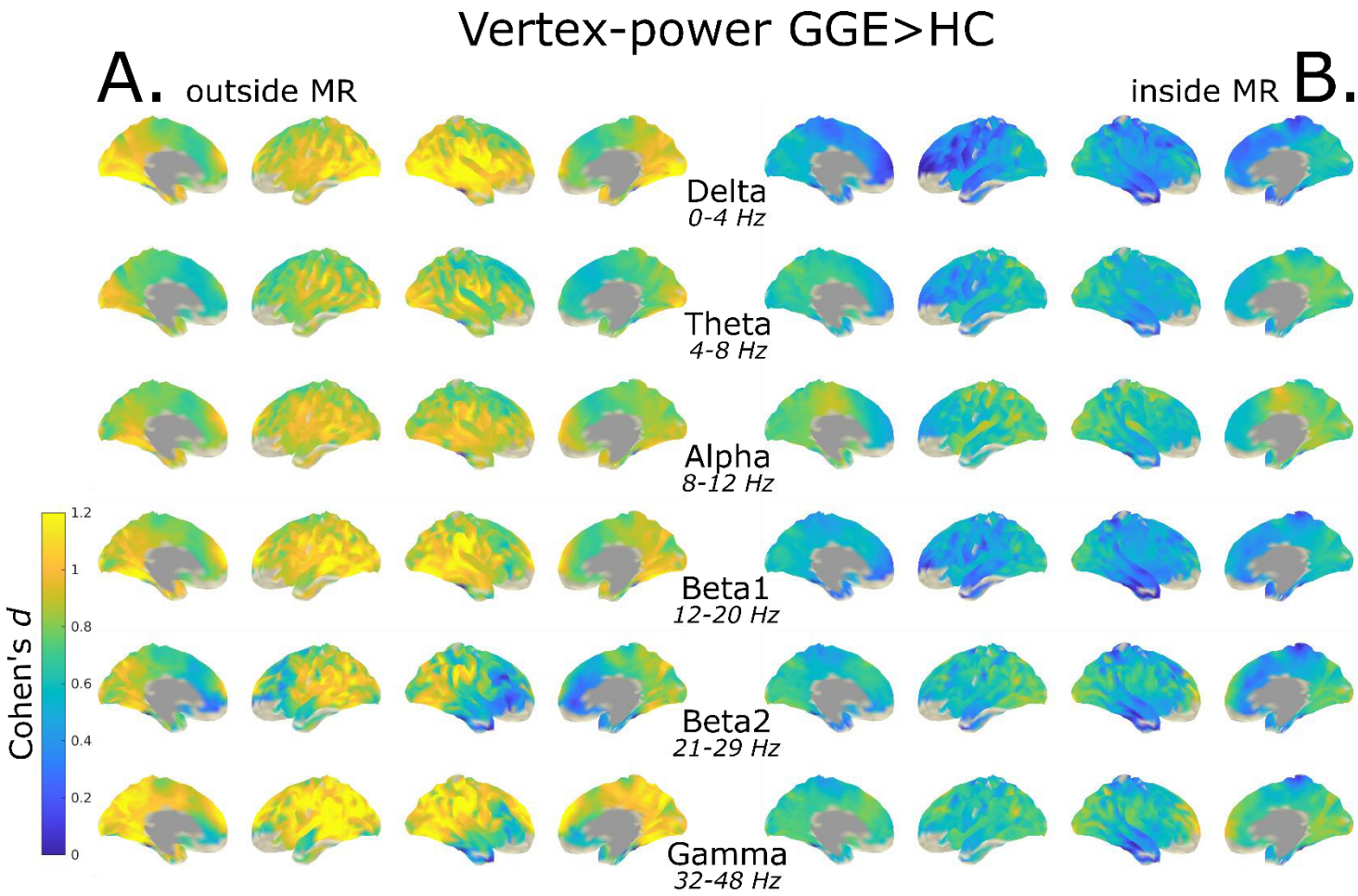

Appendix A figure 1: Vertex-power group analysis results (GGE>HC) of inside- and outside-MR scanner conditions. *Standardized effect sizes (Cohen's d) for group differences (GGE>HC) of vertex-based power for the outside- (A) and inside-MR condition (B). Note the effect size values d in the inside scanner condition are smaller than into the outside condition. They still show strong effect sizes (d > 0.8) in fewer but identical regions.*

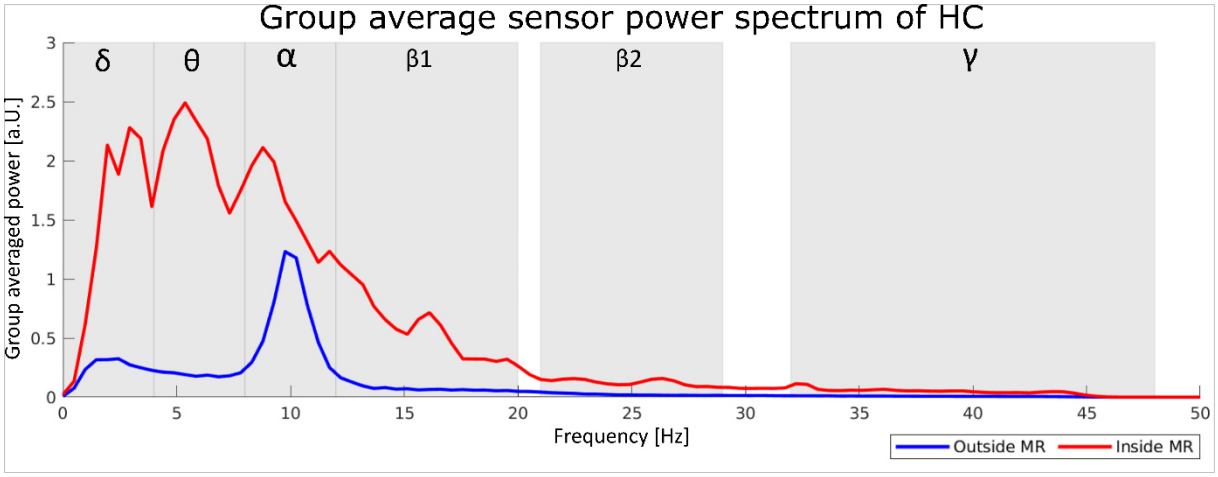

Appendix A figure 2*: Group-averaged sensor power spectrum for inside- and outside-MR scanner condition.*
Note the generally stronger power values in the inside condition compared within the outside condition, and the peaks in the inside-MR scanner condition in the frequency bands: delta (3 Hz), theta (5.5 Hz), alpha (8 Hz, 11.5 Hz) and beta1 (16 Hz).

9. APPENDIX B

This following chapter contains additional figures and tables related to the project from chapter 4.2.

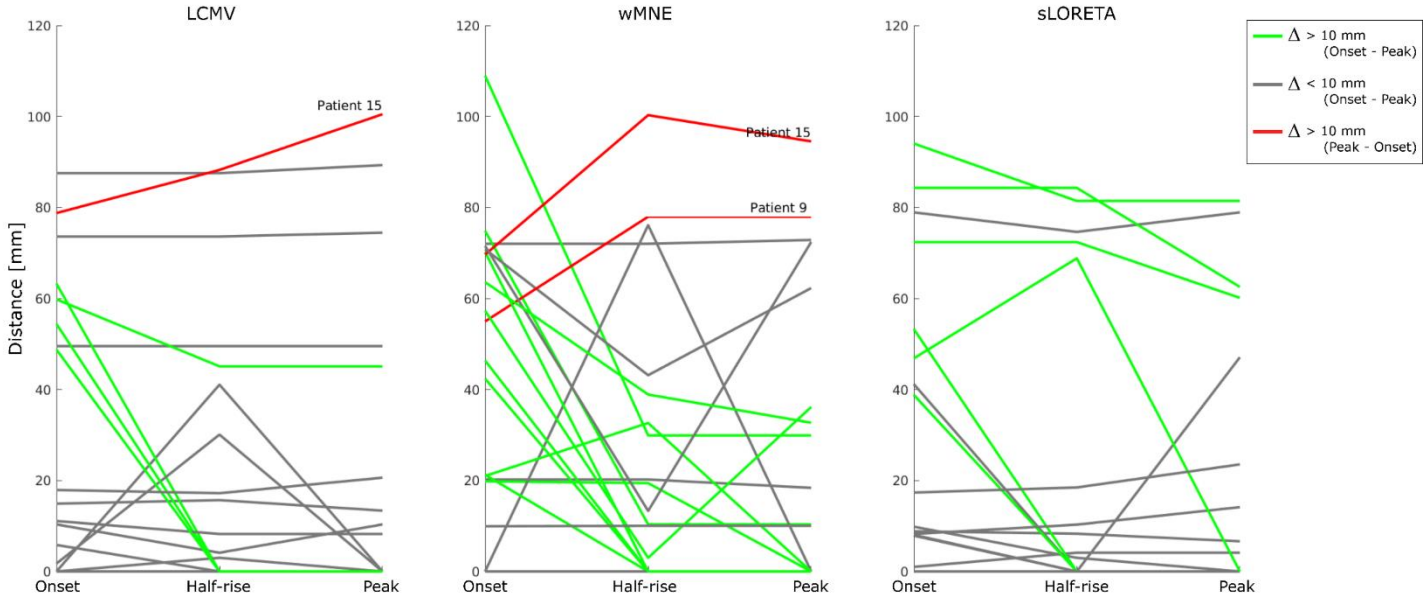

Appendix B figure 1: Individual Euclidean distances of high-density EEG (hd-EEG) source reconstruction to the resection zone (RZ).

Changes in Euclidean distance from maximum amplitude of electric source imaging (ESI) (linearly constrained minimum variance (LCMV); standardized low resolution electromagnetic tomography (sLORETA); weighted minimum-norm estimation (wMNE)) to RZ for each patient. The red lines indicate an increase in Euclidean distance to the RZ of > 10 mm between interictal electric discharge (IED) onset and IED peak, whereas the green lines indicate a decrease in Euclidean distance to the RZ of > 10 mm between IED onset and IED peak. The grey lines indicate either an increase or decrease in Euclidean distance to the RZ of < 10 mm between IED onset and IED peak.

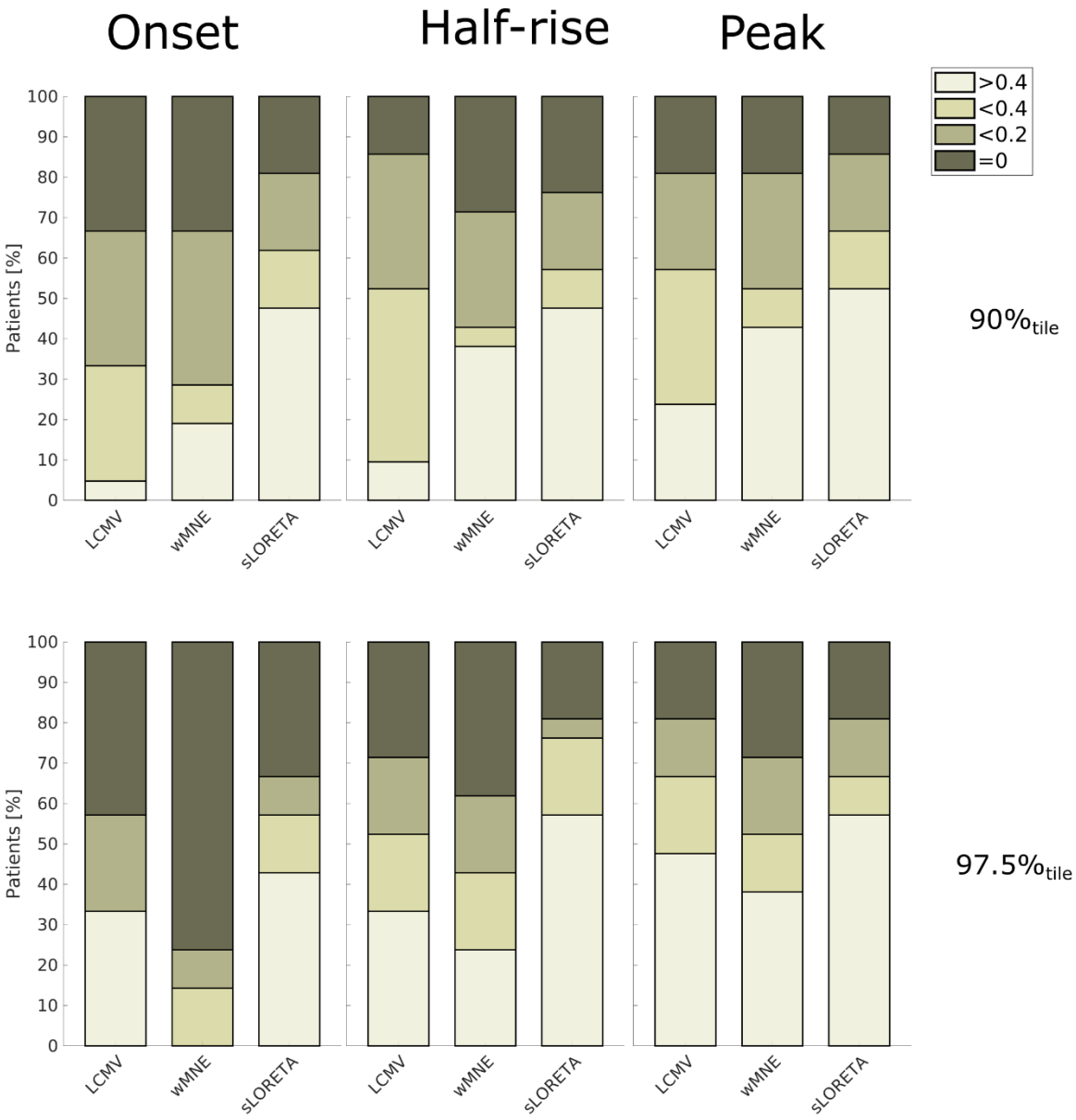

Appendix B figure 2: Volumetric overlap estimated via Dice similarity coefficient (DSC) of resection zone (RZ) high-density EEG (hd-EEG) source reconstruction applying the amplitude thresholds 90%tile and 97.5%tile.
Volumetric overlap of electric source imaging (ESI) (linearly constrained minimum variance (LCMV); standardized low resolution electromagnetic tomography (sLORETA); weighted minimum-norm estimation (wMNE)) to the RZ at each interictal epileptic discharge (IED) timepoint.

10.APPENDIX C

This following chapter contains additional figures and tables related to the project from chapter 4.3.

Appendix C table 1: Overview of amount of EEG components assigned to functional brain networks for different amount of components extracted by group ICA, with spatial correlation (mean, standard deviation) to the fMRI components for each functional brain network.

Amount of ICs	Visual	Somatomotor	Dorsal Attention	Ventral Attention	Limbic	Frontoparietal	Default Mode
50	*2 (r: 0.52 ± 0.06)*	-	-	-	-	-	*3 (r: 0.42 ± 0.06)*
60	-	*1 (r: 0.46 ± 0.00)*	-	-	*1 (r: 0.50 ± 0.00)*	*1 (r: 0.37 ± 0.00)*	-
70	-	-	-	-	*1 (r: 0.48 ± 0.00)*	*1 (r: 0.40 ± 0.00)*	*5 (r: 0.36 ± 0.07)*
80	***1 (r: 0.52 ± 0.00)***	***1 (r: 0.60 ± 0.00)***	-	-	-	***2 (r: 0.41 ± 0.00)***	***4 (r: 0.44 ± 0.07)***
90	-	*3 (r: 0.48 ± 0.04)*	-	-	-	*1 (r: 0.43 ± 0.00)*	*2 (r: 0.42 ± 0.12)*
100	*3 (r: 0.51 ± 0.05)*	*3 (r: 0.47 ± 0.09)*	*1 (r: 0.43 ± 0.00)*	-	-	*3 (r: 0.35 ± 0.04)*	*6 (r: 0.42 ± 0.11)*

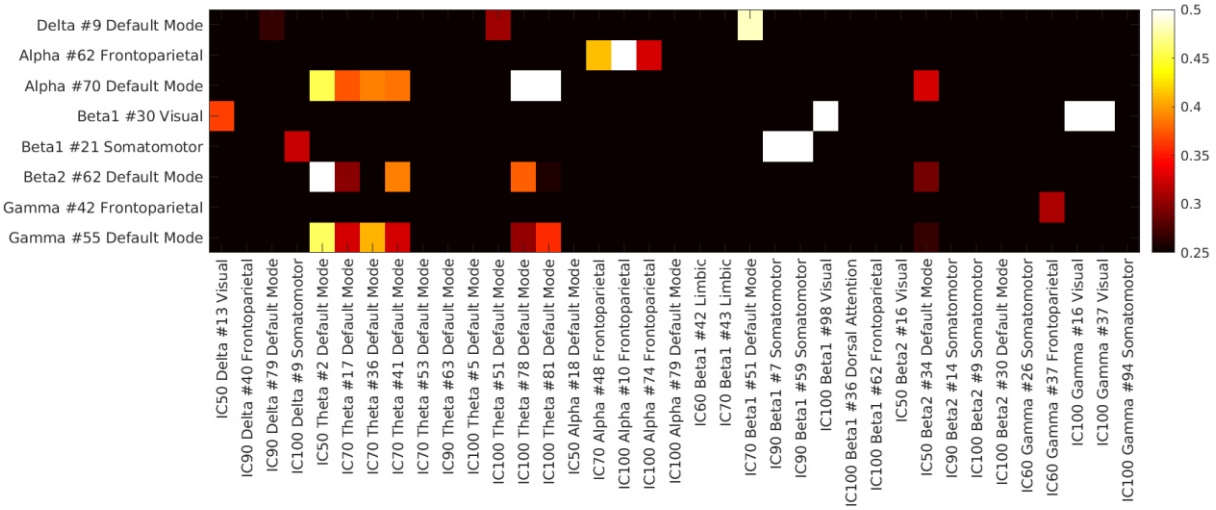

Appendix C figure 1: Spatial cross correlation of all components extracted with all amounts of components to be extracted via group-ICA on hd-EEG data.

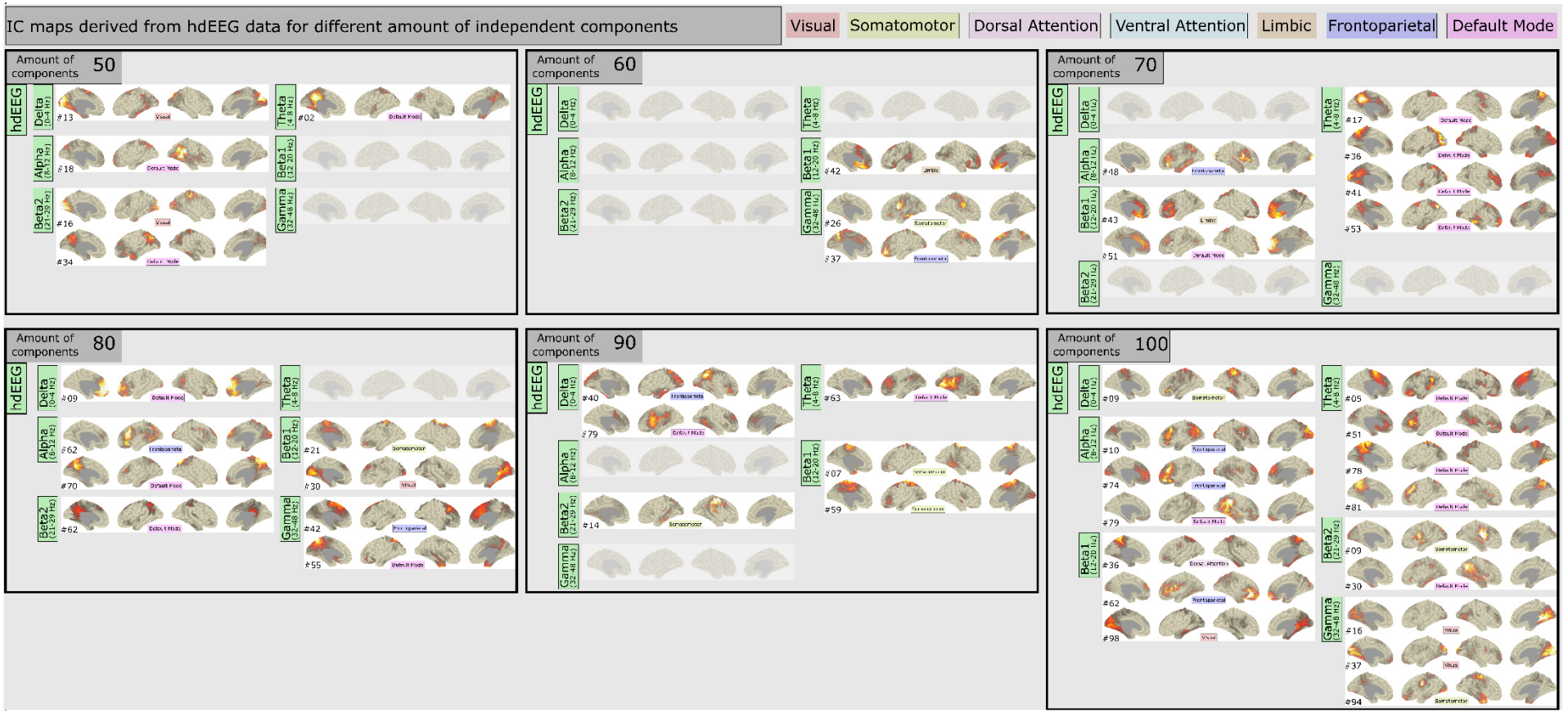

Appendix C figure 2: Network components extracted from hd-EEG data via group-ICA with various amount of independent components to be extracted.

11.BIBLIOGRAPHY

Ackermann, R. F., Engel, J., & Baxter, L. (1986). Positron Emission Tomography and Autoradiographic Studies of Glucose Utilization following Electroconvulsive Seizures in Humans and Rats. *Annals of the New York Academy of Sciences*, *462*(1 Electroconvul), 263–269. https://doi.org/10.1111/j.1749-6632.1986.tb51260.x

Aghakhani, Y., Bagshaw, A. P., Bénar, C. G., Hawco, C., Andermann, F., Dubeau, F., & Gotman, J. (2004). fMRI activation during spike and wave discharges in idiopathic generalized epilepsy. *Brain*, *127*(5), 1127–1144. https://doi.org/10.1093/brain/awh136

Aiello, M., Salvatore, E., Cachia, A., Pappatà, S., Cavaliere, C., Prinster, A., Nicolai, E., Salvatore, M., Baron, J.-C. C., & Quarantelli, M. (2015). Relationship between simultaneously acquired resting-state regional cerebral glucose metabolism and functional MRI: A PET/MR hybrid scanner study. *NeuroImage*, *113*, 111–121. https://doi.org/10.1016/j.neuroimage.2015.03.017

Akaike, H. (1974). A new look at the statistical model identification. *IEEE Transactions on Automatic Control*, *19*(6), 716–723. https://doi.org/10.1109/TAC.1974.1100705

Alavi, A., Yakir, S., & Newberg, A. B. (2011). Positron emission tomography in seizure disorders. *Annals of the New York Academy of Sciences*, *1228*(1), E1–E12. https://doi.org/10.1111/j.1749-6632.2011.06161.x

Aljuaid, M., Booth, S., Hobson, D. E., Borys, A., Williams, K., Katako, A., Ryner, L., Goertzen, A. L., & Ko, J. H. (2019). Blood Flow and Glucose Metabolism Dissociation in the Putamen Is Predictive of Levodopa Induced Dyskinesia in Parkinson's Disease Patients. *Frontiers in Neurology*, *10*(November), 1–10. https://doi.org/10.3389/fneur.2019.01217

Alkonyi, B., Juhász, C., Muzik, O., Asano, E., Saporta, A., Shah, A., & Chugani, H. T. (2009). Quantitative brain surface mapping of an electrophysiologic/metabolic mismatch in human neocortical epilepsy. *Epilepsy Research*, *87*(1), 77–87. https://doi.org/10.1016/j.eplepsyres.2009.08.002

Allen, E. A., Damaraju, E., Eichele, T., Wu, L., & Calhoun, V. D. (2018). EEG Signatures of Dynamic Functional Network Connectivity States. *Brain Topography*, *31*(1), 101–116. https://doi.org/10.1007/s10548-017-0546-2

Allen, P. J., Josephs, O., & Turner, R. (2000). A Method for Removing Imaging Artifact from Continuous EEG Recorded during Functional MRI. *NeuroImage*, *12*(2), 230–239. https://doi.org/10.1006/nimg.2000.0599

Allen, P. J., Polizzi, G., Krakow, K., Fish, D. R., & Lemieux, L. (1998). Identification of EEG Events in the MR Scanner: The Problem of Pulse Artifact and a Method for Its Subtraction. *NeuroImage*, *8*(3), 229–239. https://doi.org/10.1006/nimg.1998.0361

Andermann, F., Kobayashi, E., & Andermann, E. (2005). Genetic Focal Epilepsies: State of the Art and Paths to the Future. *Epilepsia*, *46*(s10), 61–67. https://doi.org/10.1111/j.1528-1167.2005.00361.x

Andersson, J. L. R., Skare, S., & Ashburner, J. (2003). How to correct susceptibility distortions in spin-echo echo-planar images: application to diffusion tensor imaging. *NeuroImage*, *20*(2), 870–888. https://doi.org/10.1016/S1053-8119(03)00336-7

Andrade-Valença, L. P. A., Valença, M. M., Velasco, T. R., Carlotti, C. G., Assirati, J. A., Galvis-Alonso, O. Y., Neder, L., Cendes, F., & Leite, J. P. (2008). Mesial temporal lobe epilepsy: Clinical and neuropathologic findings of familial and sporadic forms. *Epilepsia*, *49*(6), 1046–1054. https://doi.org/10.1111/j.1528-1167.2008.01551.x

Andrzejak, R. G., Schindler, K., & Rummel, C. (2012). Nonrandomness, nonlinear dependence, and nonstationarity of electroencephalographic recordings from epilepsy patients. *Physical Review E*, *86*(4), 046206. https://doi.org/10.1103/PhysRevE.86.046206

Angelicheva, D., Tournev, I., Guergueltcheva, V., Mihaylova, V., Azmanov, D. N., Morar, B., Radionova, M., Smith, S. J., Zlatareva, D., Stevens, J. M., Kaneva, R., Bojinova, V., Carter, K., Brown, M., Jablensky, A., Kalaydjieva, L., & Sander, J. W. (2009). Partial epilepsy syndrome in a Gypsy family linked to 5q31.3-q32. *Epilepsia*, *50*(7), 1679–1688. https://doi.org/10.1111/j.1528-1167.2009.02066.x

Aoki, Y., Ishii, R., Pascual-Marqui, R. D., Canuet, L., Ikeda, S., Hata, M., Imajo, K., Matsuzaki, H., Musha, T., Asada, T., Iwase, M., & Takeda, M. (2015). Detection of EEG-resting state independent networks by eLORETA-ICA method. *Frontiers in Human Neuroscience*, *9*. https://doi.org/10.3389/fnhum.2015.00031

Arviv, O., Medvedovsky, M., Sheintuch, L., Goldstein, A., & Shriki, O. (2016). Deviations from critical dynamics in interictal epileptiform activity. *Journal of Neuroscience*, *36*(48), 12276–12292. https://doi.org/10.1523/JNEUROSCI.0809-16.2016

Assecondi, S., Hallez, H., Staelens, S., Bianchi, A. M., Huiskamp, G. M., & Lemahieu, I. (2009). Removal of the ballistocardiographic artifact from EEG-fMRI data: A canonical correlation approach. *Physics in Medicine and Biology*, *54*(6), 1673–1689. https://doi.org/10.1088/0031-9155/54/6/018

Attwell, D., & Iadecola, C. (2002). The neural basis of functional brain imaging signals. *Trends in Neurosciences*, *25*(12), 621–625. https://doi.org/10.1016/S0166-2236(02)02264-6

Avila, E. K., & Graber, J. (2010). Seizures and Epilepsy in Cancer Patients. *Current Neurology and Neuroscience Reports*, *10*(1), 60–67. https://doi.org/10.1007/s11910-009-0080-z

Baggio, H. C., Segura, B., & Junque, C. (2015). Resting-State Functional Brain Networks in Parkinson's Disease. *CNS Neuroscience & Therapeutics*, *21*(10), 793–801. https://doi.org/10.1111/cns.12417

Baillet, S. (2017). Magnetoencephalography for brain electrophysiology and imaging. *Nature Neuroscience*, *20*(3), 327–339. https://doi.org/10.1038/nn.4504

Baillet, S., Mosher, J. C., & Leahy, R. M. (2001). Electromagnetic brain mapping. *IEEE Signal Processing Magazine*, *18*(6), 14–30. https://doi.org/10.1109/79.962275

Baillet, S., Riera, J. J., Marin, G., Mangin, J. F., Aubert, J., & Garnero, L. (2001). Evaluation of inverse methods and head models for EEG source localization using a human skull phantom. *Physics in Medicine and Biology*, *46*(1), 77–96. https://doi.org/10.1088/0031-9155/46/1/306

Bartolomei, F., Lagarde, S., Wendling, F., McGonigal, A., Jirsa, V., Guye, M., & Bénar, C. (2017). Defining epileptogenic networks: Contribution of SEEG and signal analysis. *Epilepsia*, *58*(7), 1131–1147. https://doi.org/10.1111/epi.13791

Bassett, D. S., & Sporns, O. (2017). Network neuroscience. *Nature Neuroscience*, *20*(3), 353–364. https://doi.org/10.1038/nn.4502

Bast, T., Boppel, T., Rupp, A., Harting, I., Hoechstetter, K., Fauser, S., Schulze-Bonhage, A., Rating, D., & Scherg, M. (2006). Noninvasive source localization of interictal EEG spikes: Effects of signal-to-noise ratio and averaging. *Journal of Clinical Neurophysiology*, *23*(6), 487–497. https://doi.org/10.1097/01.wnp.0000232208.14060.c7

Baumgartner, C., Koren, J. P., Britto-Arias, M., Zoche, L., & Pirker, S. (2019). Presurgical epilepsy evaluation and epilepsy surgery. *F1000Research*, *8*, 1818. https://doi.org/10.12688/f1000research.17714.1

Bazhenov, M., & Timofeev, I. (2006). Thalamocortical oscillations. *Scholarpedia*, *1*(6), 1319. https://doi.org/10.4249/scholarpedia.1319

Beckmann, C. F., & Smith, S. M. (2005). Tensorial extensions of independent component analysis for multisubject FMRI analysis. *NeuroImage*, *25*(1), 294–311. https://doi.org/10.1016/j.neuroimage.2004.10.043

Beghi, E., Giussani, G., Nichols, E., Abd-Allah, F., Abdela, J., Abdelalim, A., Abraha, H. N., Adib, M. G., Agrawal, S., Alahdab, F., Awasthi, A., Ayele, Y., Barboza, M. A., Belachew, A. B., Biadgo, B., Bijani, A., Bitew, H., Carvalho, F., Chaiah, Y., … Murray, C. J. L. (2019). Global, regional, and national burden of epilepsy, 1990–2016: a systematic analysis for the Global Burden of Disease Study 2016. *The Lancet Neurology*, *18*(4), 357–375. https://doi.org/10.1016/S1474-4422(18)30454-X

Belliveau, J. W., Kennedy, D. N., McKinstry, R. C., Buchbinder, B. R., Weisskoff, R. M., Cohen, M. S., Vevea, J. M., Brady, T. J., & Rosen, B. R. (1991). Functional Mapping of the Human Visual Cortex by Magnetic Resonance Imaging. *Science*, *254*(5032), 716–719. https://doi.org/10.1126/science.1948051

Bénar, C.-G., Aghakhani, Y., Wang, Y., Izenberg, A., Al-Asmi, A., Dubeau, F., & Gotman, J. (2003). Quality of EEG in simultaneous EEG-fMRI for epilepsy. *Clinical Neurophysiology*, *114*(3), 569–580. https://doi.org/10.1016/S1388-2457(02)00383-8

Benjamini, Y., & Hochberg, Y. (1995). Controlling the False Discovery Rate: A Practical and Powerful Approach to Multiple Testing. *Journal of the Royal Statistical Society. Series B (Methodological)*, *57*(1), 289–300.

Benuzzi, F., Mirandola, L., Pugnaghi, M., Farinelli, V., Tassinari, C. A., Capovilla, G., Cantalupo, G., Beccaria, F., Nichelli, P., & Meletti, S. (2012). Increased cortical BOLD signal anticipates generalized spike and wave discharges in adolescents and adults with idiopathic generalized epilepsies. *Epilepsia*, *53*(4), 622–630. https://doi.org/10.1111/j.1528-1167.2011.03385.x

Bernhardt, B. C., Rozen, D. A., Worsley, K. J., Evans, A. C., Bernasconi, N., & Bernasconi, A. (2009). Thalamo-cortical network pathology in idiopathic generalized epilepsy: Insights from MRI-based morphometric correlation analysis. *NeuroImage*, *46*(2), 373–381. https://doi.org/10.1016/j.neuroimage.2009.01.055

Beyer, T., Townsend, D. W., Brun, T., Kinahan, P. E., Charron, M., Roddy, R., Jerin, J., Young, J., Byars, L., & Nutt, R. (2000). A combined PET/CT scanner for clinical oncology. *Journal of Nuclear Medicine : Official Publication, Society of Nuclear Medicine*, *41*(8), 1369–1379.

Biswal, B., Yetkin, F. Z., Haughton, V. M., & Hyde, J. S. (1995). *Functional Connectivity in the Motor Cortex of Resting Human Brain Using Echo-Planar MRI*.

Blümcke, I. (2009). Neuropathology of focal epilepsies: A critical review. *Epilepsy & Behavior*, *15*(1), 34–39. https://doi.org/10.1016/j.yebeh.2009.02.033

Blümcke, I., Thom, M., Aronica, E., Armstrong, D. D., Bartolomei, F., Bernasconi, A., Bernasconi, N., Bien, C. G., Cendes, F., Coras, R., Cross, J. H., Jacques, T. S., Kahane, P., Mathern, G. W., Miyata, H., Moshé, S. L., Oz, B., Özkara, Ç., Perucca, E., … Spreafico, R. (2013). International consensus classification of hippocampal sclerosis in temporal lobe epilepsy: A Task Force report from the ILAE Commission on Diagnostic Methods. *Epilepsia*, *54*(7), 1315–1329. https://doi.org/10.1111/epi.12220

Blumenfeld, H. (2002). The Thalamus and Seizures. *Archives of Neurology*, *59*(1), 135. https://doi.org/10.1001/archneur.59.1.135

Blumenfeld, H. (2014). What is a seizure network? Long-range network consequences of focal seizures. *Advances in Experimental Medicine and Biology*, *813*, 63–70. https://doi.org/10.1007/978-94-17-8914-1_5

Blumenfeld, H., Westerveld, M., Ostroff, R. B., Vanderhill, S. D., Freeman, J., Necochea, A., Uranga, P., Tanhehco, T., Smith, A., & Seibyl, J. P. (2003). Selective frontal, parietal, and temporal networks in generalized seizures. *NeuroImage*, *19*(4), 1556–1566. https://doi.org/10.1016/S1053-8119(03)00204-0

Bonmassar, G., Purdon, P. L., Jääskeläinen, I. P., Chiappa, K., Solo, V., Brown, E. N., & Belliveau, J. W. (2002). Motion and ballistocardiogram artifact removal for interleaved recording of EEG and EPs during MRI. *NeuroImage*, *16*(4), 1127–1141. https://doi.org/10.1006/nimg.2002.1125

Botvinik-Nezer, R., Holzmeister, F., Camerer, C. F., Dreber, A., Huber, J., Johannesson, M., Kirchler, M., Iwanir, R., Mumford, J. A., Adcock, R. A., Avesani, P., Baczkowski, B. M., Bajracharya, A., Bakst, L., Ball, S., Barilari, M., Bault, N., Beaton, D., Beitner, J., … Schonberg, T. (2020). Variability in the analysis of a single neuroimaging dataset by many teams. *Nature*, *582*(7810), 84–88. https://doi.org/10.1038/s41586-020-2314-9

Bridwell, D. A., Wu, L., Eichele, T., & Calhoun, V. D. (2013). The spatiospectral characterization of brain networks: Fusing concurrent EEG spectra and fMRI maps. *NeuroImage*, *69*, 101–111. https://doi.org/10.1016/j.neuroimage.2012.12.024

Britz, J., Van De Ville, D., & Michel, C. M. (2010). BOLD correlates of EEG topography reveal rapid resting-state network dynamics. *NeuroImage*, *52*(4), 1162–1170. https://doi.org/10.1016/j.neuroimage.2010.02.052

Brookes, M. J., Liddle, E. B., Hale, J. R., Woolrich, M. W., Luckhoo, H., Liddle, P. F., & Morris, P. G. (2012). Task induced modulation of neural oscillations in electrophysiological brain networks. *NeuroImage*, *63*(4), 1918–1930. https://doi.org/10.1016/j.neuroimage.2012.08.012

Brookes, M. J., Mullinger, K. J., Stevenson, C. M., Morris, P. G., & Bowtell, R. (2008). Simultaneous EEG source localisation and artifact rejection during concurrent fMRI by means of spatial filtering. *NeuroImage*, *40*(3), 1090–1104. https://doi.org/10.1016/j.neuroimage.2007.12.030

Brookes, M. J., Stevenson, C. M., Barnes, G. R., Hillebrand, A., Simpson, M. I. G., Francis, S. T., & Morris, P. G. (2007). Beamformer reconstruction of correlated sources using a modified source model. *NeuroImage*, *34*(4), 1454–1465. https://doi.org/10.1016/j.neuroimage.2006.11.012

Brookes, M. J., Woolrich, M., Luckhoo, H., Price, D., Hale, J. R., Stephenson, M. C., Barnes, G. R., Smith, S. M., & Morris, P. G. (2011). Investigating the electrophysiological basis of resting state networks using magnetoencephalography. *Proceedings of the National Academy of Sciences*, *108*(40), 16783–16788. https://doi.org/10.1073/pnas.1112685108

Burman, R. J., & Parrish, R. R. (2018). The Widespread Network Effects of Focal Epilepsy. *The Journal of Neuroscience*, *38*(38), 8107–8109. https://doi.org/10.1523/JNEUROSCI.1471-18.2018

Buzsáki, G. (2006). Rhythms of the Brain. In *Rhythms of the Brain*. Oxford University Press. https://doi.org/10.1093/acprof:oso/9780195301069.001.0001

Buzsáki, G., Anastassiou, C. A., & Koch, C. (2012). The origin of extracellular fields and currents — EEG, ECoG, LFP and spikes. *Nature Reviews Neuroscience*, *13*(6), 407–420. https://doi.org/10.1038/nrn3241

Calhoun, V. D., Adali, T., Pearlson, G. D., & Pekar, J. J. (2001). *A Method for Making Group Inferences from Functional MRI Data Using Independent Component Analysis*. https://doi.org/10.1002/hbm

Calhoun, V. D., & Allen, E. A. (2013). Extracting Intrinsic Functional Networks with Feature-Based Group Independent Component Analysis. *Psychometrika*, *78*(2), 243–259. https://doi.org/10.1007/s11336-012-9291-3

Carboni, M., Brunet, D., Seeber, M., Michel, C. M., Vulliemoz, S., & Vorderwülbecke, B. J. (2022). Linear distributed inverse solutions for interictal EEG source localisation. *Clinical Neurophysiology*, *133*, 58–67. https://doi.org/10.1016/j.clinph.2021.10.008

Cecchin, D., Palombit, A., Castellaro, M., Silvestri, E., Bui, F., Barthel, H., Sabri, O., Corbetta, M., & Bertoldo, A. (2017). Brain PET and functional MRI: why simultaneously using hybrid PET/MR systems? *The Quarterly Journal of Nuclear Medicine and Molecular Imaging*, *61*(4), 345–359. https://doi.org/10.23736/S1824-4785.17.03008-4

Cendes, F., Theodore, W. H., Brinkmann, B. H., Sulc, V., & Cascino, G. D. (2016). *Neuroimaging of epilepsy* (pp. 985–1014). https://doi.org/10.1016/B978-0-444-53486-6.00051-X

Cerulli Irelli, E., Morano, A., Barone, F. A., Fisco, G., Fanella, M., Orlando, B., Fattouch, J., Manfredi, M., Giallonardo, A. T., & Di Bonaventura, C. (2020). Persistent treatment resistance in genetic generalized epilepsy: A long-term outcome study in a tertiary epilepsy center. *Epilepsia*, *61*(11), 2452–2460. https://doi.org/10.1111/epi.16708

Chang, W.-C., Kudlacek, J., Hlinka, J., Chvojka, J., Hadrava, M., Kumpost, V., Powell, A. D., Janca, R., Maturana, M. I., Karoly, P. J., Freestone, D. R., Cook, M. J., Palus, M., Otahal, J., Jefferys, J. G. R., & Jiruska, P. (2018). Loss of neuronal network resilience precedes seizures and determines the ictogenic nature of interictal synaptic perturbations. *Nature Neuroscience*, *21*(12), 1742–1752. https://doi.org/10.1038/s41593-018-0278-y

Chassoux, F. (2004). Metabolic changes and electro-clinical patterns in mesio-temporal lobe epilepsy: a correlative study. *Brain*, *127*(1), 164–174. https://doi.org/10.1093/brain/awh014

Chavez, M., Valencia, M., Navarro, V., Latora, V., & Martinerie, J. (2010). Functional modularity of background activities in normal and epileptic brain networks. *Physical Review Letters*, *104*(11), 1–4. https://doi.org/10.1103/PhysRevLett.104.118701

Cho, Y. W., Yi, S. D., Lim, J. G., Kim, D. K., & Motamedi, G. K. (2008). Autosomal dominant nocturnal frontal lobe epilepsy and mild memory impairment associated with CHRNB2 mutation I312M in the neuronal nicotinic acetylcholine receptor. *Epilepsy and Behavior*, *13*(2), 361–365. https://doi.org/10.1016/j.yebeh.2008.04.017

Chowdhury, F. A., Woldman, W., FitzGerald, T. H. B., Elwes, R. D. C., Nashef, L., Terry, J. R., & Richardson, M. P. (2014). Revealing a Brain Network Endophenotype in Families with Idiopathic Generalised Epilepsy. *PLoS ONE*, *9*(10), e110136. https://doi.org/10.1371/journal.pone.0110136

Clemens, B., Emri, M., Csaba Aranyi, S., Fekete, I., & Fekete, K. (2021). Resting-state EEG theta activity reflects degree of genetic determination of the major epilepsy syndromes. *Clinical Neurophysiology*, *132*(9), 2232–2239. https://doi.org/10.1016/j.clinph.2021.06.012

Clemens, B., Emri, M., Fekete, I., & Fekete, K. (2023). Epileptic diathesis: An EEG-LORETA study. *Clinical Neurophysiology*, *145*, 54–61. https://doi.org/10.1016/j.clinph.2022.11.004

Clemens, B., Puskás, S., Besenyei, M., Emri, M., Opposits, G., Kis, S. A., Hollódy, K., Fogarasi, A., Kondákor, I., Füle, K., Bense, K., & Fekete, I. (2012). EEG-LORETA endophenotypes of the common idiopathic generalized epilepsy syndromes. *Epilepsy Research*, *99*(3), 281–292. https://doi.org/10.1016/j.eplepsyres.2011.12.008

Cole. (2010). Advances and pitfalls in the analysis and interpretation of resting-state FMRI data. *Frontiers in Systems Neuroscience*, *4*(April), 8. https://doi.org/10.3389/fnsys.2010.00008

Commission on Classification and Terminology of the International League Against Epilepsy. (1981). Proposal for Revised Clinical and Electroencephalographic Classification of Epileptic Seizures. *Epilepsia*, *22*(4), 489–501. https://doi.org/10.1111/j.1528-1157.1981.tb06159.x

Commission on Classification and Terminology of the International League Against Epilepsy, 1989. (1989). Proposal for Revised Classification of Epilepsies and Epileptic Syndromes. *Epilepsia*, *30*(4), 389–399. https://doi.org/10.1111/j.1528-1157.1989.tb05316.x

Custo, A., Van De Ville, D., Wells, W. M., Tomescu, M. I., Brunet, D., & Michel, C. M. (2017). Electroencephalographic Resting-State Networks: Source Localization of Microstates. *Brain Connectivity*, *7*(10), 671–682. https://doi.org/10.1089/brain.2016.0476

Dalal, S. S., Zumer, J. M., Guggisberg, A. G., Trumpis, M., Wong, D. D. E., Sekihara, K., & Nagarajan, S. S. (2011). MEG/EEG Source Reconstruction, Statistical Evaluation, and Visualization with NUTMEG. *Computational Intelligence and Neuroscience*, *2011*, 17. https://doi.org/10.1155/2011/758973

Dale, A. M., & Sereno, M. I. (1993). Improved Localizadon of Cortical Activity by Combining EEG and MEG with MRI Cortical Surface Reconstruction: A Linear Approach. *Journal of Cognitive Neuroscience*, *5*(2), 162–176. https://doi.org/10.1162/jocn.1993.5.2.162

Dammers, J., & Ioannides, A. A. (2000). Neuromagnetic localization of CMV generators using incomplete and full- head biomagnetometer. *NeuroImage*, *11*(3), 167–178. https://doi.org/10.1006/nimg.1999.0524

Damoiseaux, J. S., Rombouts, S. A. R. B., Barkhof, F., Scheltens, P., Stam, C. J., Smith, S. M., & Beckmann, C. F. (2006). Consistent resting-state networks across healthy subjects. *Proceedings of the National Academy of Sciences*, *103*(37), 13848–13853. https://doi.org/10.1073/pnas.0601417103

Dazzo, E., Rehberg, K., Michelucci, R., Passarelli, D., Boniver, C., Vianello Dri, V., Striano, P., Striano, S., Pasterkamp, R. J., & Nobile, C. (2018). Mutations in MICAL-1 cause autosomal-dominant lateral temporal epilepsy. *Annals of Neurology*, *83*(3), 483–493. https://doi.org/10.1002/ana.25167

De Luca, M., Beckmann, C. F., De Stefano, N., Matthews, P. M., & Smith, S. M. (2006). fMRI resting state networks define distinct modes of long-distance interactions in the human brain. *NeuroImage*, *29*(4), 1359–1367. https://doi.org/10.1016/j.neuroimage.2005.08.035

De Marco, E. V., Gambardella, A., Annesi, F., Labate, A., Carrideo, S., Forabosco, P., Civitelli, D., Candiano, I. C. C., Tarantino, P., Annesi, G., & Quattrone, A. (2007). Further evidence of genetic heterogeneity in families with autosomal dominant nocturnal frontal lobe epilepsy. *Epilepsy Research*, *74*(1), 70–73. https://doi.org/10.1016/j.eplepsyres.2006.12.006

Debener, S., Mullinger, K. J., Niazy, R. K., & Bowtell, R. W. (2008). Properties of the ballistocardiogram artefact as revealed by EEG recordings at 1.5, 3 and 7 T static

magnetic field strength. *International Journal of Psychophysiology*, *67*(3), 189–199. https://doi.org/10.1016/j.ijpsycho.2007.05.015

Del Guerra, A., Ahmad, S., Avram, M., Belcari, N., Berneking, A., Biagi, L., Bisogni, M. G., Brandl, F., Cabello, J., Camarlinghi, N., Cerello, P., Choi, C.-H., Coli, S., Colpo, S., Fleury, J., Gagliardi, V., Giraudo, G., Heekeren, K., Kawohl, W., … Ziegler, S. (2018). TRIMAGE: A dedicated trimodality (PET/MR/EEG) imaging tool for schizophrenia. *European Psychiatry*, *50*, 7–20. https://doi.org/10.1016/j.eurpsy.2017.11.007

Deligianni, F., Centeno, M., Carmichael, D. W., & Clayden, J. D. (2014). Relating resting-state fMRI and EEG whole-brain connectomes across frequency bands. *Frontiers in Neuroscience*, *8*(August), 1–16. https://doi.org/10.3389/fnins.2014.00258

Desikan, R. S., Ségonne, F., Fischl, B., Quinn, B. T., Dickerson, B. C., Blacker, D., Buckner, R. L., Dale, A. M., Maguire, R. P., Hyman, B. T., Albert, M. S., & Killiany, R. J. (2006). An automated labeling system for subdividing the human cerebral cortex on MRI scans into gyral based regions of interest. *NeuroImage*, *31*(3), 968–980. https://doi.org/10.1016/j.neuroimage.2006.01.021

Destrieux, C., Fischl, B., Dale, A., & Halgren, E. (2010). Automatic parcellation of human cortical gyri and sulci using standard anatomical nomenclature. *NeuroImage*, *53*(1), 1–15. https://doi.org/10.1016/j.neuroimage.2010.06.010

Detre, J. A. (2006). Clinical applicability of functional MRI. In *Journal of Magnetic Resonance Imaging* (Vol. 23, Issue 6, pp. 808–815). https://doi.org/10.1002/jmri.20585

Devinsky, O., Spruill, T., Thurman, D., & Friedman, D. (2015). Recognizing and preventing epilepsy-related mortality A call for action. *American Academy of Neurology*, *86*, 779–786.

Devinsky, O., Vezzani, A., O'Brien, T. J., Jette, N., Scheffer, I. E., de Curtis, M., & Perucca, P. (2018). Epilepsy. *Nature Reviews Disease Primers*, *4*(1), 18024. https://doi.org/10.1038/nrdp.2018.24

Di, X., Biswal, B. B., & Alzheimer's Disease Neuroimaging Initiative. (2012). Metabolic Brain Covariant Networks as Revealed by FDG-PET with Reference to Resting-State fMRI Networks. *Brain Connectivity*, *2*(5), 275–283. https://doi.org/10.1089/brain.2012.0086

Doucet, G. E., Labache, L., Thompson, P. M., Joliot, M., & Frangou, S. (2021). Atlas55+: Brain Functional Atlas of Resting-State Networks for Late Adulthood. *Cerebral Cortex*, *31*(3), 1719–1731. https://doi.org/10.1093/cercor/bhaa321

Drew, P. J. (2019). Vascular and neural basis of the BOLD signal. *Current Opinion in Neurobiology*, *58*, 61–69. https://doi.org/10.1016/j.conb.2019.06.004

Duvernoy, H. M., Cattin, F., Naidich, T. P., Raybaud, C., Risold, P. Y., Salvolini, U., & Scarabine, U. (2005). The Human Hippocampus: Functional Anatomy, Vascularization and Serial Sections with MRI. In *Springer-Verlag* (3rd Editio, Vol. 62, Issue 1). Springer-Verlag.

Eichele, T., Calhoun, V. D., & Debener, S. (2009). Mining EEG-fMRI using independent component analysis. *International Journal of Psychophysiology*, *73*(1), 53–61. https://doi.org/10.1016/j.ijpsycho.2008.12.018

Eichele, T., Rachakonda, S., Brakedal, B., Eikeland, R., & Calhoun, V. D. (2011). EEGIFT: Group independent component analysis for event-related EEG data. *Computational Intelligence and Neuroscience*, *2011*. https://doi.org/10.1155/2011/129365

Eickhoff, S. B., & Grefkes, C. (2020). Modeling Connectivity in Health and Disease: Examples from the Motor System. In *fMRI* (pp. 321–334). Springer International Publishing. https://doi.org/10.1007/978-3-030-41874-8_22

Elshahabi, A., Klamer, S., Sahib, A. K., Lerche, H., Braun, C., & Focke, N. K. (2015). Magnetoencephalography reveals a widespread increase in network connectivity in idiopathic/genetic generalized epilepsy. *PLoS ONE*, *10*(9), 1–16. https://doi.org/10.1371/journal.pone.0138119

Emanuelson, I., & Uvebrant, P. (2009). Occurrence of epilepsy during the first 10 years after traumatic brain injury acquired in childhood up to the age of 18 years in the south western Swedish population-based series. *Brain Injury*, *23*(7–8), 612–616. https://doi.org/10.1080/02699050902973913

Engel. (1993). Outcome with respect to epileptic seizures. In *Surgical treatment of the epilepsies*. New York: Raven Press.

Engel, J. (1984). A Practical Guide for Routine EEG Studies in Epilepsy. *Journal of Clinical Neurophysiology*, *1*(2), 109–142. https://doi.org/10.1097/00004691-198404000-00001

Engel, J. (2018). The current place of epilepsy surgery. *Current Opinion in Neurology*, *31*(2), 192–197. https://doi.org/10.1097/WCO.0000000000000528

Engel, J., Henry, T. R., Risinger, M. W., Mazziotta, J. C., Sutherling, W. W., Levesque, M. F., & Phelps, M. E. (1990). Presurgical evaluation for partial epilepsy. *Neurology*, *40*(11), 1670–1670. https://doi.org/10.1212/WNL.40.11.1670

Engels, M. M. A., van der Flier, W. M., Stam, C. J., Hillebrand, A., Scheltens, P., & van Straaten, E. C. W. (2017). Alzheimer's disease: The state of the art in resting-state magnetoencephalography. *Clinical Neurophysiology*, *128*(8), 1426–1437. https://doi.org/10.1016/j.clinph.2017.05.012

Fanciulli, M., Santulli, L., Errichiello, L., Barozzi, C., Tomasi, L., Rigon, L., Cubeddu, T., de Falco, A., Rampazzo, A., Michelucci, R., Uzzau, S., Striano, S., de Falco, F. A., Striano, P., & Nobile, C. (2012). LGI1 microdeletion in autosomal dominant lateral temporal epilepsy. *Neurology*, *78*(17), 1299–1303. https://doi.org/10.1212/WNL.0b013e3182518328

Felblinger, J., Slotboom, J., Kreis, R., Jung, B., & Boesch, C. (1999). Restoration of electrophysiological signals distorted by inductive effects of magnetic field gradients during MR sequences. *Magnetic Resonance in Medicine*, *41*(4), 715–721. https://doi.org/10.1002/(SICI)1522-2594(199904)41:4<715::AID-MRM9>3.0.CO;2-7

Fiest, K. M., Sauro, K. M., Wiebe, S., Patten, S. B., Kwon, C.-S., Dykeman, J., Pringsheim, T., Lorenzetti, D. L., & Jetté, N. (2017). Prevalence and incidence of epilepsy. *Neurology*, *88*(3), 296–303. https://doi.org/10.1212/WNL.0000000000003509

Fischl, B., Salat, D. H., Busa, E., Albert, M., Dieterich, M., Haselgrove, C., Van Der Kouwe, A., Killiany, R., Kennedy, D., Klaveness, S., Montillo, A., Makris, N., Rosen, B., & Dale, A. M. (2002). Whole brain segmentation: Automated labeling of neuroanatomical structures in the human brain. *Neuron*, *33*(3), 341–355. https://doi.org/10.1016/S0896-6273(02)00569-X

Fisher, R. S., Acevedo, C., Arzimanoglou, A., Bogacz, A., Cross, J. H., Elger, C. E., Engel, J., Forsgren, L., French, J. A., Glynn, M., Hesdorffer, D. C., Lee, B. I., Mathern, G. W., Moshé, S. L., Perucca, E., Scheffer, I. E., Tomson, T., Watanabe, M., & Wiebe, S. (2014). ILAE Official Report: A practical clinical definition of epilepsy. *Epilepsia*, *55*(4), 475–482. https://doi.org/10.1111/epi.12550

Fisher, R. S., Cross, J. H., French, J. A., Higurashi, N., Hirsch, E., Jansen, F. E., Lagae, L., Moshé, S. L., Peltola, J., Roulet Perez, E., Scheffer, I. E., & Zuberi, S. M. (2017). Operational classification of seizure types by the International League Against Epilepsy: Position

Paper of the ILAE Commission for Classification and Terminology. *Epilepsia*, *58*(4), 522–530. https://doi.org/10.1111/epi.13670

Fisher, R. S., van Emde Boas, W., Blume, W., Elger, C., Genton, P., Lee, P., & Engel, J. (2005). Response: Definitions Proposed by the International League Against Epilepsy (ILAE) and the International Bureau for Epilepsy (IBE). *Epilepsia*, *46*(10), 1701–1702. https://doi.org/10.1111/j.1528-1167.2005.00273_4.x

Foged, M. T., Martens, T., Pinborg, L. H., Hamrouni, N., Litman, M., Rubboli, G., Leffers, A. M., Ryvlin, P., Jespersen, B., Paulson, O. B., Fabricius, M., & Beniczky, S. (2020). Diagnostic added value of electrical source imaging in presurgical evaluation of patients with epilepsy: A prospective study. *Clinical Neurophysiology*, *131*(1), 324–329. https://doi.org/10.1016/j.clinph.2019.07.031

Forsyth, A., McMillan, R., Campbell, D., Malpas, G., Maxwell, E., Sleigh, J., Dukart, J., Hipp, J., & Muthukumaraswamy, S. D. (2020). Modulation of simultaneously collected hemodynamic and electrophysiological functional connectivity by ketamine and midazolam. *Human Brain Mapping*, *41*(6), 1472–1494. https://doi.org/10.1002/hbm.24889

Fox, M. D., & Raichle, M. E. (2007). Spontaneous fluctuations in brain activity observed with functional magnetic resonance imaging. *Nature Reviews Neuroscience*, *8*(9), 700–711. https://doi.org/10.1038/nrn2201

Fox, M. D., Snyder, A. Z., Vincent, J. L., Corbetta, M., Van Essen, D. C., & Raichle, M. E. (2005). The human brain is intrinsically organized into dynamic, anticorrelated functional networks. *Proceedings of the National Academy of Sciences*, *102*(27), 9673–9678. https://doi.org/10.1073/pnas.0504136102

Freitag, C. M., May, T. W., Pfäfflin, M., König, S., & Rating, D. (2001). Incidence of Epilepsies and Epileptic Syndromes in Children and Adolescents: A Population-Based Prospective Study in Germany. *Epilepsia*, *42*(8), 979–985. https://doi.org/10.1046/j.1528-1157.2001.042008979.x

Friston, K., Harrison, L., Daunizeau, J., Kiebel, S., Phillips, C., Trujillo-Barreto, N., Henson, R., Flandin, G., & Mattout, J. (2008). Multiple sparse priors for the M/EEG inverse problem. *NeuroImage*, *39*(3), 1104–1120. https://doi.org/10.1016/j.neuroimage.2007.09.048

Friston, K. J., Frith, C. D., Liddle, P. F., & Frackowiak, R. S. J. (1993). Functional Connectivity: The Principal-Component Analysis of Large (PET) Data Sets. *Journal of Cerebral Blood Flow & Metabolism*, *13*(1), 5–14. https://doi.org/10.1038/jcbfm.1993.4

Fuchs, M., Wagner, M., Köhler, T., & Wischmann, H.-A. (1999). Linear and Nonlinear Current Density Reconstructions. *Journal of Clinical Neurophysiology*, *16*(3), 267–295.

Fukuchi, T., Okauchi, T., Shigeta, M., Yamamoto, S., Watanabe, Y., & Enomoto, S. (2017). Positron emission tomography with additional γ -ray detectors for multiple-tracer imaging. *Medical Physics*, *44*(6), 2257–2266. https://doi.org/10.1002/mp.12149

Gesche, J., Hjalgrim, H., Rubboli, G., & Beier, C. P. (2020). Patterns and prognostic markers for treatment response in generalized epilepsies. *Neurology*, *95*(18), e2519–e2528. https://doi.org/10.1212/WNL.0000000000010644

Gesche, J., Khanevski, M., Solberg, C., & Beier, C. P. (2017). Resistance to valproic acid as predictor of treatment resistance in genetic generalized epilepsies. *Epilepsia*, *58*(4), e64–e69. https://doi.org/10.1111/epi.13702

Ghinda, D. C., Wu, J. S., Duncan, N. W., & Northoff, G. (2018). How much is enough—Can resting state fMRI provide a demarcation for neurosurgical resection in glioma?

Neuroscience and Biobehavioral Reviews, *84*, 245–261. https://doi.org/10.1016/j.neubiorev.2017.11.019

Glauser, T., Ben-Menachem, E., Bourgeois, B., Cnaan, A., Guerreiro, C., Kälviäinen, R., Mattson, R., French, J. A., Perucca, E., & Tomson, T. (2013). Updated ILAE evidence review of antiepileptic drug efficacy and effectiveness as initial monotherapy for epileptic seizures and syndromes. *Epilepsia*, *54*(3), 551–563. https://doi.org/10.1111/epi.12074

Golkowski, D., Merz, K., Mlynarcik, C., Kiel, T., Schorr, B., Lopez-Rolon, A., Lukas, M., Jordan, D., Bender, A., & Ilg, R. (2017). Simultaneous EEG–PET–fMRI measurements in disorders of consciousness: an exploratory study on diagnosis and prognosis. *Journal of Neurology*, *264*(9), 1986–1995. https://doi.org/10.1007/s00415-017-8591-z

Gotman, J., Grova, C., Bagshaw, A., Kobayashi, E., Aghakhani, Y., & Dubeau, F. (2005). Generalized epileptic discharges show thalamocortical activation and suspension of the default state of the brain. *Proceedings of the National Academy of Sciences*, *102*(42), 15236–15240. https://doi.org/10.1073/pnas.0504935102

Grech, R., Cassar, T., Muscat, J., Camilleri, K. P., Fabri, S. G., Zervakis, M., Xanthopoulos, P., Sakkalis, V., & Vanrumste, B. (2008). Review on solving the inverse problem in EEG source analysis. *Journal of NeuroEngineering and Rehabilitation*, *5*(1), 25. https://doi.org/10.1186/1743-0003-5-25

Greenblatt, R. E., Pflieger, M. E., & Ossadtchi, A. E. (2012). Connectivity measures applied to human brain electrophysiological data. *Journal of Neuroscience Methods*, *207*(1), 1–16. https://doi.org/10.1016/j.jneumeth.2012.02.025

Gross, J., Kujala, J., Hämäläinen, M., Timmermann, L., Schnitzler, A., & Salmelin, R. (2001). Dynamic imaging of coherent sources: Studying neural interactions in the human brain. *Proceedings of the National Academy of Sciences*, *98*(2), 694–699. https://doi.org/10.1073/PNAS.98.2.694

Hämäläinen, M., Hari, R., Ilmoniemi, R. J., Knuutila, J., & Lounasmaa, O. V. (1993). Magnetoencephalography—theory, instrumentation, and applications to noninvasive studies of the working human brain. *Reviews of Modern Physics*, *65*(2), 413–497. https://doi.org/10.1103/RevModPhys.65.413

Hämäläinen, M. S., & Ilmoniemi, R. J. (1994). Interpreting magnetic fields of the brain: minimum norm estimates. *Medical & Biological Engineering & Computing*, *32*(1), 35–42. https://doi.org/10.1007/BF02512476

Hamandi, K., Salek-Haddadi, A., Laufs, H., Liston, A., Friston, K., Fish, D. R., Duncan, J. S., & Lemieux, L. (2006). EEG–fMRI of idiopathic and secondarily generalized epilepsies. *NeuroImage*, *31*(4), 1700–1710. https://doi.org/10.1016/j.neuroimage.2006.02.016

Hampson, M., Olson, I. R., Leung, H.-C., Skudlarski, P., & Gore, J. C. (2004). Changes in functional connectivity of human MT/V5 with visual motion input. *NeuroReport*, *15*(8), 1315–1319. https://doi.org/10.1097/01.wnr.0000129997.95055.15

Hansen, P., Kringelbach, M., & Salmelin, R. (2010). MEG: An introduction to methods. In P. Hansen, M. Kringelbach, & R. Salmelin (Eds.), *MEG: An Introduction to Methods* (Vol. 58, Issue 12). Oxford University Press. https://doi.org/10.1093/acprof:oso/9780195307238.001.0001

Hauk, O., Stenroos, M., & Treder, M. S. (2022). Towards an objective evaluation of EEG/MEG source estimation methods – The linear approach. *NeuroImage*, *255*(August 2021), 119177. https://doi.org/10.1016/j.neuroimage.2022.119177

Hauk, O., Wakeman, D. G., & Henson, R. (2011). Comparison of noise-normalized minimum norm estimates for MEG analysis using multiple resolution metrics. *NeuroImage*, *54*(3), 1966–1974. https://doi.org/10.1016/j.neuroimage.2010.09.053

Hauser, W. A., Annegers, J. F., & Kurland, L. T. (1993). Incidence of Epilepsy and Unprovoked Seizures in Rochester, Minnesota: 1935-1984. *Epilepsia*, *34*(3), 453–458. https://doi.org/10.1111/j.1528-1157.1993.tb02586.x

Hayman, M., Scheffer, I. E., Chinvarun, Y., Berlangieri, S. U., & Berkovic, S. F. (1997). Autosomal dominant nocturnal frontal lobe epilepsy: Demonstration of focal frontal onset and intrafamilial variation. *Neurology*, *49*(4), 969–975. https://doi.org/10.1212/WNL.49.4.969

Hill, R. A., Chiappa, K. H., Huang-Hellinger, F., & Jenkins, B. G. (1995). EEG during MR imaging: Differentiation of movement artifact from paroxysmal cortical activity. *Neurology*, *45*(10), 1942–1943. https://doi.org/10.1212/WNL.45.10.1942-a

Hiltunen, T., Kantola, J., Abou Elseoud, A., Lepola, P., Suominen, K., Starck, T., Nikkinen, J., Remes, J., Tervonen, O., Palva, S., Kiviniemi, V., & Palva, J. M. (2014). Infra-Slow EEG Fluctuations Are Correlated with Resting-State Network Dynamics in fMRI. *Journal of Neuroscience*, *34*(2), 356–362. https://doi.org/10.1523/JNEUROSCI.0276-13.2014

Himberg, J., Hyvärinen, A., & Esposito, F. (2004). Validating the independent components of neuroimaging time series via clustering and visualization. *NeuroImage*, *22*(3), 1214–1222. https://doi.org/10.1016/j.neuroimage.2004.03.027

Hipp, J. F., & Siegel, M. (2015). BOLD fMRI Correlation Reflects Frequency-Specific Neuronal Correlation. *Current Biology*, *25*(10), 1368–1374. https://doi.org/10.1016/j.cub.2015.03.049

Hirsch, E., French, J., Scheffer, I. E., Bogacz, A., Alsaadi, T., Sperling, M. R., Abdulla, F., Zuberi, S. M., Trinka, E., Specchio, N., Somerville, E., Samia, P., Riney, K., Nabbout, R., Jain, S., Wilmshurst, J. M., Auvin, S., Wiebe, S., Perucca, E., … Zhou., D. (2022). ILAE definition of the Idiopathic Generalized Epilepsy Syndromes: Position statement by the ILAE Task Force on Nosology and Definitions. *Epilepsia*, *63*(6), 1475–1499. https://doi.org/10.1111/epi.17236

Hohenfeld, C., Werner, C. J., & Reetz, K. (2018). Resting-state connectivity in neurodegenerative disorders: Is there potential for an imaging biomarker? *NeuroImage: Clinical*, *18*(November 2017), 849–870. https://doi.org/10.1016/j.nicl.2018.03.013

Holmes, M. D., Brown, M., & Tucker, D. M. (2004). Are "Generalized" Seizures Truly Generalized? Evidence of Localized Mesial Frontal and Frontopolar Discharges in Absence. *Epilepsia*, *45*(12), 1568–1579. https://doi.org/10.1111/j.0013-9580.2004.23204.x

Huberfeld, G., Menendez de la Prida, L., Pallud, J., Cohen, I., Le Van Quyen, M., Adam, C., Clemenceau, S., Baulac, M., & Miles, R. (2011). Glutamatergic pre-ictal discharges emerge at the transition to seizure in human epilepsy. *Nature Publishing Group*. https://doi.org/10.1038/nn.2790

Huettel, S. A., Song, A. W., & McCarthy, G. (2004). *Functional Magnetic Resonance Imaging*. Sinauer Associates, Inc.

Humm, J. L., Rosenfeld, A., & Del Guerra, A. (2003). From PET detectors to PET scanners. *European Journal of Nuclear Medicine and Molecular Imaging*, *30*(11), 1574–1597. https://doi.org/10.1007/s00259-003-1266-2

Hunyadi, B., Woolrich, M. W., Quinn, A. J., Vidaurre, D., & De Vos, M. (2019). A dynamic system of brain networks revealed by fast transient EEG fluctuations and their fMRI

correlates. *NeuroImage*, *185*, 72–82. https://doi.org/10.1016/j.neuroimage.2018.09.082

Hur, Y. J., Lee, J. S., Lee, J. D., Yun, M. J., & Kim, H. D. (2013). Quantitative analysis of simultaneous EEG features during PET studies for childhood partial epilepsy. *Yonsei Medical Journal*, *54*(3), 572–577. https://doi.org/10.3349/ymj.2013.54.3.572

Huster, R. J., Plis, S. M., & Calhoun, V. D. (2015). Group-level component analyses of EEG: Validation and evaluation. *Frontiers in Neuroscience*, *9*(JUL), 254. https://doi.org/10.3389/fnins.2015.00254

Hwang, K., Bertolero, M. A., Liu, W. B., & D'Esposito, M. (2017). The Human Thalamus Is an Integrative Hub for Functional Brain Networks. *The Journal of Neuroscience*, *37*(23), 5594–5607. https://doi.org/10.1523/JNEUROSCI.0067-17.2017

Hytti, H., Takalo, R., & Ihalainen, H. (2006). Tutorial on multivariate autoregressive modelling. *Journal of Clinical Monitoring and Computing*, *20*(2), 101–108. https://doi.org/10.1007/s10877-006-9013-4

Hyvärinen, A., & Oja, E. (1997). A Fast Fixed-Point Algorithm for Independent Component Analysis. *Neural Computation*, *9*(7), 1483–1492. https://doi.org/10.1162/neco.1997.9.7.1483

Ibrahim, B., Suppiah, S., Ibrahim, N., Mohamad, M., Hassan, H. A., Nasser, N. S., & Saripan, M. I. (2021). Diagnostic power of resting-state fMRI for detection of network connectivity in Alzheimer's disease and mild cognitive impairment: A systematic review. *Human Brain Mapping*, *42*(9), 2941–2968. https://doi.org/10.1002/hbm.25369

International League Against Epilepsy Consortium on Complex Epilepsies. (2018). Genome-wide mega-analysis identifies 16 loci and highlights diverse biological mechanisms in the common epilepsies. *Nature Communications*, *9*(1), 5269. https://doi.org/10.1038/s41467-018-07524-z

Ionescu, T. M., Amend, M., Hafiz, R., Biswal, B. B., Wehrl, H. F., Herfert, K., & Pichler, B. J. (2021). Elucidating the complementarity of resting-state networks derived from dynamic [18F]FDG and hemodynamic fluctuations using simultaneous small-animal PET/MRI. *NeuroImage*, *236*(March), 118045. https://doi.org/10.1016/j.neuroimage.2021.118045

Ives, J. R., Warach, S., Schmitt, F., Edelman, R. R., & Schomer, D. L. (1993). Monitoring the patient's EEG during echo planar MRI. *Electroencephalography and Clinical Neurophysiology*, *87*(6), 417–420. https://doi.org/10.1016/0013-4694(93)90156-P

Izquierdo-Garcia, D., & Catana, C. (2016). MR Imaging-Guided Attenuation Correction of PET Data in PET/MR Imaging. In *PET Clinics* (Vol. 11, Issue 2, pp. 129–149). https://doi.org/10.1016/j.cpet.2015.10.002

Jaisani, Z., Miletich, R. S., Ramanathan, M., & Weinstock, A. L. (2020). Clinical FDG-PET Findings in Patients with Temporal Lobe Epilepsy: Concordance with EEG and MRI. *Journal of Neuroimaging*, *30*(1), 119–125. https://doi.org/10.1111/jon.12671

Jallon, P., & Latour, P. (2005). Epidemiology of Idiopathic Generalized Epilepsies. *Epilepsia*, *46*(s9), 10–14. https://doi.org/10.1111/j.1528-1167.2005.00309.x

Jamadar, S. D., Ward, P. G. D., Close, T. G., Fornito, A., Premaratne, M., O'Brien, K., Stäb, D., Chen, Z., Shah, N. J., & Egan, G. F. (2020). Simultaneous BOLD-fMRI and constant infusion FDG-PET data of the resting human brain. *Scientific Data*, *7*(1), 363. https://doi.org/10.1038/s41597-020-00699-5

Jann, K., Dierks, T., Boesch, C., Kottlow, M., Strik, W., & Koenig, T. (2009). BOLD correlates of EEG alpha phase-locking and the fMRI default mode network. *NeuroImage*, *45*(3), 903–916. https://doi.org/10.1016/J.NEUROIMAGE.2009.01.001

Javed, E., Faye, I., Malik, A. S., & Abdullah, J. M. (2017). Removal of BCG artefact from concurrent fMRI-EEG recordings based on EMD and PCA. *Journal of Neuroscience Methods*, *291*, 150–165. https://doi.org/10.1016/j.jneumeth.2017.08.020

Jehi, L. (2018). The Epileptogenic Zone: Concept and Definition. *Epilepsy Currents*, *18*(1), 12–16. https://doi.org/10.5698/1535-7597.18.1.12

Jenkinson, M. (2002). Improved Optimization for the Robust and Accurate Linear Registration and Motion Correction of Brain Images. *NeuroImage*, *17*(2), 825–841. https://doi.org/10.1016/S1053-8119(02)91132-8

Jeong, J.-W., Asano, E., Pilli, V. K., Nakai, Y., Chugani, H. T., Juh Asz, C., & Library, W. O. (2017). Objective 3D Surface Evaluation of Intracranial Electrophysiologic Correlates of Cerebral Glucose Metabolic Abnormalities in Children with Focal Epilepsy. *Human Brain Mapping*, *38*, 3098–3112. https://doi.org/10.1002/hbm.23577

Ji, G.-J., Zhang, Z., Xu, Q., Wang, Z., Wang, J., Jiao, Q., Yang, F., Tan, Q., Chen, G., Zang, Y.-F., Liao, W., & Lu, G. (2015). Identifying Corticothalamic Network Epicenters in Patients with Idiopathic Generalized Epilepsy. *American Journal of Neuroradiology*, *36*(8), 1494–1500. https://doi.org/10.3174/ajnr.A4308

Jiménez-Bonilla, J. F., & Banzo, I. (2018). Non-oncological applications of PET/CT. *Medicina Clínica (English Edition)*, *150*(10), 387–389. https://doi.org/10.1016/j.medcle.2017.10.044

Jing, J., Herlopian, A., Karakis, I., Ng, M., Halford, J. J., Lam, A., Maus, D., Chan, F., Dolatshahi, M., Muniz, C. F., Chu, C., Sacca, V., Pathmanathan, J., Ge, W., Sun, H., Dauwels, J., Cole, A. J., Hoch, D. B., Cash, S. S., & Westover, M. B. (2020). Interrater Reliability of Experts in Identifying Interictal Epileptiform Discharges in Electroencephalograms. *JAMA Neurology*, *77*(1), 49–57. https://doi.org/10.1001/jamaneurol.2019.3531

Jobst, B. C., Siegel, A. M., Thadani, V. M., Roberts, D. W., Rhodes, H. C., & Williamson, P. D. (2000). Intractable Seizures of Frontal Lobe Origin: Clinical Characteristics, Localizing Signs, and Results of Surgery. *Epilepsia*, *41*(9), 1139–1152. https://doi.org/10.1111/j.1528-1157.2000.tb00319.x

Joyce, C. A., Gorodnitsky, I. F., & Kutas, M. (2004). Automatic removal of eye movement and blink artifacts from EEG data using blind component separation. *Psychophysiology*, *41*(2), 313–325. https://doi.org/10.1111/j.1469-8986.2003.00141.x

Judenhofer, M. S., Wehrl, H. F., Newport, D. F., Catana, C., Siegel, S. B., Becker, M., Thielscher, A., Kneilling, M., Lichy, M. P., Eichner, M., Klingel, K., Reischl, G., Widmaier, S., Röcken, M., Nutt, R. E., Machulla, H.-J., Uludag, K., Cherry, S. R., Claussen, C. D., & Pichler, B. J. (2008). Simultaneous PET-MRI: a new approach for functional and morphological imaging. *Nature Medicine*, *14*(4), 459–465. https://doi.org/10.1038/nm1700

Jutten, C., & Herault, J. (1991). Blind separation of sources, part I: An adaptive algorithm based on neuromimetic architecture. *Signal Processing*, *24*(1), 1–10. https://doi.org/10.1016/0165-1684(91)90079-X

Kalachikov, S., Evgrafov, O., Ross, B., Winawer, M., Barker-Cummings, C., Boneschi, F. M., Choi, C., Morozov, P., Das, K., Teplitskaya, E., Yu, A., Cayanis, E., Penchaszadeh, G., Kottmann, A. H., Pedley, T. A., Hauser, W. A., Ottman, R., & Gilliam, T. C. (2002).

Mutations in LGI1 cause autosomal-dominant partial epilepsy with auditory features. *Nature Genetics*, *30*(3), 335–341. https://doi.org/10.1038/ng832

Kane, N., Acharya, J., Beniczky, S., Caboclo, L., Finnigan, S., Kaplan, P. W., Shibasaki, H., Pressler, R., & van Putten, M. J. A. M. (2017). A revised glossary of terms most commonly used by clinical electroencephalographers and updated proposal for the report format of the EEG findings. Revision 2017. *Clinical Neurophysiology Practice*, *2*, 170–185. https://doi.org/10.1016/j.cnp.2017.07.002

Karoly, P. J., Freestone, D. R., Boston, R., Grayden, D. B., Himes, D., Leyde, K., Seneviratne, U., Berkovic, S., O'Brien, T., & Cook, M. J. (2016). Interictal spikes and epileptic seizures: their relationship and underlying rhythmicity. *Brain*, *139*(4), 1066–1078. https://doi.org/10.1093/brain/aww019

Kawamata, J., Ikeda, A., Fujita, Y., Usui, K., Shimohama, S., & Takahashi, R. (2010). Mutations in LGI1 gene in Japanese families with autosomal dominant lateral temporal lobe epilepsy: The first report from Asian families. *Epilepsia*, *51*(4), 690–693. https://doi.org/10.1111/j.1528-1167.2009.02309.x

Kay, B. P., Holland, S. K., Privitera, M. D., & Szaflarski, J. P. (2014). Differences in paracingulate connectivity associated with epileptiform discharges and uncontrolled seizures in genetic generalized epilepsy. *Epilepsia*, *55*(2), 256–263. https://doi.org/10.1111/epi.12486

Kerezoudis, P., McCutcheon, B., Murphy, M. E., Rajjoub, K. R., Ubl, D., Habermann, E. B., Worrell, G., Bydon, M., & Van Gompel, J. J. (2018). Thirty-day postoperative morbidity and mortality after temporal lobectomy for medically refractory epilepsy. *Journal of Neurosurgery*, *128*(4), 1158–1164. https://doi.org/10.3171/2016.12.JNS162096

Kim, S.-G., & Ogawa, S. (2012). Biophysical and Physiological Origins of Blood Oxygenation Level-Dependent fMRI Signals. *Journal of Cerebral Blood Flow & Metabolism*, *32*(7), 1188–1206. https://doi.org/10.1038/jcbfm.2012.23

Klamer, S., Ethofer, T., Torner, F., Sahib, A. K., Elshahabi, A., Marquetand, J., Martin, P., Lerche, H., Erb, M., & Focke, N. K. (2018). Unravelling the brain networks driving spike-wave discharges in genetic generalized epilepsy-common patterns and individual differences. *Epilepsia Open*, *3*(4), 485–494. https://doi.org/10.1002/epi4.12252

Knowlton, R. C., Laxer, K. D., Klein, G., Sawrie, S., Ende, G., Hawkins, R. A., Aassar, O. S., Soohoo, K., Wong, S., & Barbaro, N. (2001). In vivo hippocampal glucose metabolism in mesial temporal lobe epilepsy. *Neurology*, *57*(7), 1184–1190. https://doi.org/10.1212/WNL.57.7.1184

Koutroumanidis, M., Hennessy, M. J., Seed, P. T., Elwes, R. D. C., Jarosz, J., Morris, R. G., Maisey, M. N., Binnie, C. D., & Polkey, C. E. (2000). Significance of interictal bilateral temporal hypometabolism in temporal lobe epilepsy. *Neurology*, *54*(9), 1811–1821. https://doi.org/10.1212/WNL.54.9.1811

Krakow, K., Messina, D., Lemieux, L., Duncan, J. S., & Fish, D. R. (2001). Functional MRI Activation of Individual Interictal Epileptiform Spikes. *NeuroImage*, *13*(3), 502–505. https://doi.org/10.1006/nimg.2000.0708

Kramer, M. A., & Cash, S. S. (2012). Epilepsy as a Disorder of Cortical Network Organization. *The Neuroscientist*, *18*(4), 360–372. https://doi.org/10.1177/1073858411422754

Kwan, P., & Brodie, M. J. (2000). Early Identification of Refractory Epilepsy. *New England Journal of Medicine*, *342*(5), 314–319. https://doi.org/10.1056/NEJM200002033420503

Kwong, K. K., Belliveau, J. W., Chesler, D. A., Goldberg, I. E., Weisskoff, R. M., Poncelet, B. P., Kennedy, D. N., Hoppel, B. E., Cohen, M. S., & Turner, R. (1992). Dynamic magnetic

resonance imaging of human brain activity during primary sensory stimulation. *Proceedings of the National Academy of Sciences*, *89*(12), 5675–5679. https://doi.org/10.1073/pnas.89.12.5675

la Fougère, C., Rominger, A., Förster, S., Geisler, J., & Bartenstein, P. (2009). PET and SPECT in epilepsy: A critical review. *Epilepsy & Behavior*, *15*(1), 50–55. https://doi.org/10.1016/j.yebeh.2009.02.025

Labounek, R., Bridwell, D. A., Mareček, R., Lamoš, M., Mikl, M., Bednařík, P., Baštinec, J., Slavíček, T., Hluštík, P., Brázdil, M., & Jan, J. (2019). EEG spatiospectral patterns and their link to fMRI BOLD signal via variable hemodynamic response functions. *Journal of Neuroscience Methods*, *318*, 34–46. https://doi.org/10.1016/j.jneumeth.2019.02.012

Lagarde, S., Boucekine, M., McGonigal, A., Carron, R., Scavarda, D., Trebuchon, A., Milh, M., Boyer, L., Bartolomei, F., & Guedj, E. (2020). Relationship between PET metabolism and SEEG epileptogenicity in focal lesional epilepsy. *European Journal of Nuclear Medicine and Molecular Imaging*, *47*(13), 3130–3142. https://doi.org/10.1007/s00259-020-04791-1

Lai, M., Demuru, M., Hillebrand, A., & Fraschini, M. (2018). A comparison between scalp- and source-reconstructed EEG networks. *Scientific Reports*, *8*(1), 12269. https://doi.org/10.1038/s41598-018-30869-w

Lamarche, F., Job, A. S., Deman, P., Bhattacharjee, M., Hoffmann, D., Gallazzini-Crépin, C., Bouvard, S., Minotti, L., Kahane, P., & David, O. (2016). Correlation of FDG-PET hypometabolism and SEEG epileptogenicity mapping in patients with drug-resistant focal epilepsy. *Epilepsia*, *57*(12), 2045–2055. https://doi.org/10.1111/epi.13592

Lantz, G., Spinelli, L., Seeck, M., de Peralta Menendez, R. G., Sottas, C. C., & Michel, C. M. (2003). Propagation of Interictal Epileptiform Activity Can Lead to Erroneous Source Localizations: A 128-Channel EEG Mapping Study. *Journal of Clinical Neurophysiology*, *20*(5), 311–319. https://doi.org/10.1097/00004691-200309000-00003

Larivière, S., Rodríguez-Cruces, R., Royer, J., Caligiuri, M. E., Gambardella, A., Concha, L., Keller, S. S., Cendes, F., Yasuda, C., Bonilha, L., Gleichgerrcht, E., Focke, N. K., Domin, M., von Podewills, F., Langner, S., Rummel, C., Wiest, R., Martin, P., Kotikalapudi, R., … Bernhardt, B. C. (2020). Network-based atrophy modeling in the common epilepsies: A worldwide ENIGMA study. *Science Advances*, *6*(47), 1–14. https://doi.org/10.1126/sciadv.abc6457

Laufs, H., Holt, J. L., Elfont, R., Krams, M., Paul, J. S., Krakow, K., & Kleinschmidt, A. (2006). Where the BOLD signal goes when alpha EEG leaves. *NeuroImage*, *31*(4), 1408–1418. https://doi.org/10.1016/j.neuroimage.2006.02.002

Laufs, H., Kleinschmidt, A., Beyerle, A., Eger, E., Salek-Haddadi, A., Preibisch, C., & Krakow, K. (2003). EEG-correlated fMRI of human alpha activity. *NeuroImage*, *19*(4), 1463–1476. https://doi.org/10.1016/S1053-8119(03)00286-6

Laufs, H., Lengler, U., Hamandi, K., Kleinschmidt, A., & Krakow, K. (2006). Linking generalized spike-and-wave discharges and resting state brain activity by using EEG/fMRI in a patient with absence seizures. *Epilepsia*, *47*(2), 444–448. https://doi.org/10.1111/j.1528-1167.2006.00443.x

League, I., & Epilepsy, A. (1985). Proposal for classification of epilepsies and epileptic syndromes. Commission on Classification and Terminology of the International League Against Epilepsy. *Epilepsia*, *26*(3), 268–278.

Lee, M. H., Smyser, C. D., & Shimony, J. S. (2013). Resting-State fMRI: A Review of Methods and Clinical Applications. *American Journal of Neuroradiology*, *34*(10), 1866–1872. https://doi.org/10.3174/ajnr.A3263

Lei, X., Valdes-Sosa, P. A., & Yao, D. (2012). EEG/fMRI fusion based on independent component analysis: Integration of data-driven and model-driven methods. *Journal of Integrative Neuroscience*, *11*(03), 313–337. https://doi.org/10.1142/S0219635212500203

Lemieux, L., Allen, P. J., Franconi, F., Symms, M. R., & Fish, D. K. (1997). Recording of EEG during fMRI experiments: Patient safety. *Magnetic Resonance in Medicine*, *38*(6), 943–952. https://doi.org/10.1002/mrm.1910380614

Lemieux, L., Salek-Haddadi, A., Josephs, O., Allen, P., Toms, N., Scott, C., Krakow, K., Turner, R., & Fish, D. R. (2001). Event-Related fMRI with Simultaneous and Continuous EEG: Description of the Method and Initial Case Report. *NeuroImage*, *14*(3), 780–787. https://doi.org/10.1006/nimg.2001.0853

Leutmezer, F., Lurger, S., & Baumgartner, C. (2002). Focal features in patients with idiopathic generalized epilepsy. *Epilepsy Research*, *50*(3), 293–300. https://doi.org/10.1016/S0920-1211(02)00084-0

LeVan, P., Maclaren, J., Herbst, M., Sostheim, R., Zaitsev, M., & Hennig, J. (2013). Ballistocardiographic artifact removal from simultaneous EEG-fMRI using an optical motion-tracking system. *NeuroImage*, *75*, 1–11. https://doi.org/10.1016/j.neuroimage.2013.02.039

Levira, F., Thurman, D. J., Sander, J. W., Hauser, W. A., Hesdorffer, D. C., Masanja, H., Odermatt, P., Logroscino, G., & Newton, C. R. (2017). Premature mortality of epilepsy in low- and middle-income countries: A systematic review from the Mortality Task Force of the International League Against Epilepsy. *Epilepsia*, *58*(1), 6–16. https://doi.org/10.1111/epi.13603

Li Hegner, Y., Marquetand, J., Elshahabi, A., Klamer, S., Lerche, H., Braun, C., & Focke, N. K. (2018). Increased Functional MEG Connectivity as a Hallmark of MRI-Negative Focal and Generalized Epilepsy. *Brain Topography*, *31*(5), 863–874. https://doi.org/10.1007/s10548-018-0649-4

Li, Q., Luo, C., Yang, T., Yao, Z., He, L., Liu, L., Xu, H., Gong, Q., Yao, D., & Zhou, D. (2009). EEG-fMRI study on the interictal and ictal generalized spike-wave discharges in patients with childhood absence epilepsy. *Epilepsy Research*, *87*(2–3), 160–168. https://doi.org/10.1016/j.eplepsyres.2009.08.018

Lin, F. H., Witzel, T., Ahlfors, S. P., Stufflebeam, S. M., Belliveau, J. W., & Hämäläinen, M. S. (2006). Assessing and improving the spatial accuracy in MEG source localization by depth-weighted minimum-norm estimates. *NeuroImage*, *31*(1), 160–171. https://doi.org/10.1016/j.neuroimage.2005.11.054

Logothetis, N. K., Pauls, J., Augath, M., Trinath, T., & Oeltermann, A. (2001). Neurophysiological investigation of the basis of the fMRI signal. *Nature*, *412*(6843), 150–157. https://doi.org/10.1038/35084005

Lopci, E., & Fanti, S. (2020). Non-FDG PET/CT. In O. Schober, F. Kiessling, & J. Debus (Eds.), *Molecular Imaging in Oncology* (pp. 669–718). Springer International Publishing. https://doi.org/10.1007/978-3-030-42618-7_20

Lopes da Silva, F. (2013). EEG and MEG: Relevance to Neuroscience. *Neuron*, *80*(5), 1112–1128. https://doi.org/10.1016/j.neuron.2013.10.017

Lozano, A. M., Gildenberg, P. L., & Tasker, R. R. (2009). *Textbook of Stereotactic and Functional Neurosurgery: Impedance Recording in Functional Neurosurgery.* 1325–1330.
Luo, C., Li, Q., Lai, Y., Xia, Y., Qin, Y., Liao, W., Li, S., Zhou, D., Yao, D., & Gong, Q. (2011). Altered functional connectivity in default mode network in absence epilepsy: A resting-state fMRI study. *Human Brain Mapping*, *32*(3), 438–449. https://doi.org/10.1002/hbm.21034
Mahalanobis, P. C. (1936). On the generalized distance in statistics. *Proceedings of the National Institute of Sciences of India*.
Mahjoory, K., Nikulin, V. V., Botrel, L., Linkenkaer-Hansen, K., Fato, M. M., & Haufe, S. (2017). Consistency of EEG source localization and connectivity estimates. *NeuroImage*, *152*, 590–601. https://doi.org/10.1016/j.neuroimage.2017.02.076
Malekmohammadi, M., Elias, W. J., & Pouratian, N. (2015). Human thalamus regulates cortical activity via spatially specific and structurally constrained phase-amplitude coupling. *Cerebral Cortex*, *25*(6), 1618–1628. https://doi.org/10.1093/cercor/bht358
Mantini, D., Perrucci, M. G., Cugini, S., Ferretti, A., Romani, G. L., & Del Gratta, C. (2007). Complete artifact removal for EEG recorded during continuous fMRI using independent component analysis. *NeuroImage*, *34*(2), 598–607. https://doi.org/10.1016/j.neuroimage.2006.09.037
Mantini, D., Perrucci, M. G., Del Gratta, C., Romani, G. L., & Corbetta, M. (2007). Electrophysiological signatures of resting state networks in the human brain. *Proceedings of the National Academy of Sciences*, *104*(32), 13170–13175. https://doi.org/10.1073/pnas.0700668104
Marchitelli, R., Aiello, M., Cachia, A., Quarantelli, M., Cavaliere, C., Postiglione, A., Tedeschi, G., Montella, P., Milan, G., Salvatore, M., Salvatore, E., Baron, J. C., & Pappatà, S. (2018). Simultaneous resting-state FDG-PET/fMRI in Alzheimer Disease: Relationship between glucose metabolism and intrinsic activity. *NeuroImage*, *176*, 246–258. https://doi.org/10.1016/j.neuroimage.2018.04.048
Marino, M., Liu, Q., Koudelka, V., Porcaro, C., Hlinka, J., Wenderoth, N., & Mantini, D. (2018). Adaptive optimal basis set for BCG artifact removal in simultaneous EEG-fMRI. *Scientific Reports*, *8*(1), 8902. https://doi.org/10.1038/s41598-018-27187-6
Masterton, R. A., Carney, P. W., & Jackson, G. D. (2012). Cortical and thalamic resting-state functional connectivity is altered in childhood absence epilepsy. *Epilepsy Research*, *99*(3), 327–334. https://doi.org/10.1016/j.eplepsyres.2011.12.014
Masterton, R. A. J., Abbott, D. F., Fleming, S. W., & Jackson, G. D. (2007). Measurement and reduction of motion and ballistocardiogram artefacts from simultaneous EEG and fMRI recordings. *NeuroImage*, *37*(1), 202–211. https://doi.org/10.1016/j.neuroimage.2007.02.060
Matthews, P. M., Honey, G. D., & Bullmore, E. T. (2006). Applications of fMRI in translational medicine and clinical practice. In *Nature Reviews Neuroscience* (Vol. 7, Issue 9, pp. 732–744). https://doi.org/10.1038/nrn1929
Mauguière, F., & Ryvlin, P. (2004). The role of PET in presurgical assessment of partial epilepsies. *Epileptic Disorders*, *6*(3), 193–215.
McGill, M. L., Devinsky, O., Kelly, C., Milham, M., Castellanos, F. X., Quinn, B. T., DuBois, J., Young, J. R., Carlson, C., French, J., Kuzniecky, R., Halgren, E., & Thesen, T. (2012). Default mode network abnormalities in idiopathic generalized epilepsy. *Epilepsy & Behavior*, *23*(3), 353–359. https://doi.org/10.1016/j.yebeh.2012.01.013

Meyer, M. C., van Oort, E. S. B., & Barth, M. (2013). Electrophysiological Correlation Patterns of Resting State Networks in Single Subjects: A Combined EEG–fMRI Study. *Brain Topography*, *26*(1), 98–109. https://doi.org/10.1007/s10548-012-0235-0

Michel, C. M., Murray, M. M., Lantz, G., Gonzalez, S., Spinelli, L., & Grave De Peralta, R. (2004). EEG source imaging. *Clinical Neurophysiology*, *115*(10), 2195–2222. https://doi.org/10.1016/j.clinph.2004.06.001

Michelucci, R., Passarelli, D., Pitzalis, S., Dal Corso, T. G., Tassinari, C. A., & Nobile, C. (2000). *Autosomal Dominant Partial Epilepsy with Auditory Features: Description of a New Family* (Vol. 41, Issue 8). Lippincott Williams & Wilkins, Inc.

Middlebrooks, E. H., Ver Hoef, L., & Szaflarski, J. P. (2017). Neuroimaging in Epilepsy. *Current Neurology and Neuroscience Reports*, *17*(4), 32. https://doi.org/10.1007/s11910-017-0746-x

Moeller, F., Siebner, H. R., Wolff, S., Muhle, H., Boor, R., Granert, O., Jansen, O., Stephani, U., & Siniatchkin, M. (2008). Changes in activity of striato–thalamo–cortical network precede generalized spike wave discharges. *NeuroImage*, *39*(4), 1839–1849. https://doi.org/10.1016/j.neuroimage.2007.10.058

Mosher, J. C., Lewis, P. S., & Leahy, R. M. (1992). Multiple Dipole Modeling and Localization from Spatio-Temporal MEG Data. *IEEE Transactions on Biomedical Engineering*, *39*(6), 541–557. https://doi.org/10.1109/10.141192

Mouthaan, B. E., Rados, M., Barsi, P., Boon, P., Carmichael, D. W., Carrette, E., Craiu, D., Cross, J. H., Diehl, B., Dimova, P., Fabo, D., Francione, S., Gaskin, V., Gil-Nagel, A., Grigoreva, E., Guekht, A., Hirsch, E., Hecimovic, H., Helmstaedter, C., … Braun, K. P. J. (2016). Current use of imaging and electromagnetic source localization procedures in epilepsy surgery centers across Europe. *Epilepsia*, *57*(5), 770–776. https://doi.org/10.1111/epi.13347

Musso, F., Brinkmeyer, J., Mobascher, A., Warbrick, T., & Winterer, G. (2010). Spontaneous brain activity and EEG microstates. A novel EEG/fMRI analysis approach to explore resting-state networks. *NeuroImage*, *52*(4), 1149–1161. https://doi.org/10.1016/j.neuroimage.2010.01.093

Ngugi, A. K., Bottomley, C., Kleinschmidt, I., Sander, J. W., & Newton, C. R. (2010). Estimation of the burden of active and life-time epilepsy: A meta-analytic approach. *Epilepsia*, *51*(5), 883–890. https://doi.org/10.1111/j.1528-1167.2009.02481.x

Niazy, R. K., Beckmann, C. F., Iannetti, G. D., Brady, J. M., & Smith, S. M. (2005). Removal of FMRI environment artifacts from EEG data using optimal basis sets. *NeuroImage*, *28*(3), 720–737. https://doi.org/10.1016/j.neuroimage.2005.06.067

Niessing, J., Ebisch, B., Schmidt, K. E., Niessing, M., Singer, W., & Galuske, R. A. W. (2005). Hemodynamic Signals Correlate Tightly with Synchronized Gamma Oscillations. *Science*, *309*(5736), 948–951. https://doi.org/10.1126/science.1110948

Nishida, M., Juhász, C., Sood, S., Chugani, H. T., & Asano, E. (2008). Cortical glucose metabolism positively correlates with gamma-oscillations in nonlesional focal epilepsy. *NeuroImage*, *42*(4), 1275–1284. https://doi.org/10.1016/j.neuroimage.2008.06.027

Nolte, T., Gross-Weege, N., & Schulz, V. (2020). Molecular Imaging in Oncology. In O. Schober, F. Kiessling, & J. Debus (Eds.), *Recent Results in Cancer Research* (Vol. 216). Springer International Publishing. https://doi.org/10.1007/978-3-030-42618-7

Nugent, A. C., Luber, B., Carver, F. W., Robinson, S. E., Coppola, R., & Zarate, C. A. (2017). Deriving frequency-dependent spatial patterns in MEG-derived resting state

sensorimotor network: A novel multiband ICA technique. *Human Brain Mapping*, *38*(2), 779–791. https://doi.org/10.1002/hbm.23417

Nugent, A. C., Martinez, A., D'Alfonso, A., Zarate, C. A., & Theodore, W. H. (2015). The Relationship between Glucose Metabolism, Resting-State fMRI BOLD Signal, and GABA A -Binding Potential: A Preliminary Study in Healthy Subjects and Those with Temporal Lobe Epilepsy. *Journal of Cerebral Blood Flow & Metabolism*, *35*(4), 583–591. https://doi.org/10.1038/jcbfm.2014.228

Nugent, A. C., Robinson, S. E., Coppola, R., Furey, M. L., & Zarate, C. A. (2015). Group differences in MEG-ICA derived resting state networks: Application to major depressive disorder. *NeuroImage*, *118*, 1–12. https://doi.org/10.1016/j.neuroimage.2015.05.051

O'Brien, T. J., Newton, M. R., Cook, M. J., Berlangieri, S. U., Kilpatrick, C., Morris, K., & Berkovic, S. F. (1997). Hippocampal Atrophy Is Not a Major Determinant of Regional Hypometabolism in Temporal Lobe Epilepsy. In *Epilepsia* (Vol. 38, Issue 1).

Ogawa, S., Lee, T.-M., Nayak, A. S., & Glynn, P. (1990). Oxygenation-sensitive contrast in magnetic resonance image of rodent brain at high magnetic fields. *Magnetic Resonance in Medicine*, *14*(1), 68–78. https://doi.org/10.1002/mrm.1910140108

Pagani, M., Öberg, J., De Carli, F., Calvo, A., Moglia, C., Canosa, A., Nobili, F., Morbelli, S., Fania, P., Cistaro, A., & Chiò, A. (2016). Metabolic spatial connectivity in amyotrophic lateral sclerosis as revealed by independent component analysis. *Human Brain Mapping*, *37*(3), 942–953. https://doi.org/10.1002/hbm.23078

Panebianco, M., Zavanone, C., Dupont, S., Restivo, D. A., & Pavone, A. (2016). Vagus nerve stimulation therapy in partial epilepsy: a review. *Acta Neurologica Belgica*, *116*(3), 241–248. https://doi.org/10.1007/s13760-016-0616-3

Parrino, L., De Paolis, F., Milioli, G., Gioi, G., Grassi, A., Riccardi, S., Colizzi, E., & Terzano, M. G. (2012). Distinctive polysomnographic traits in nocturnal frontal lobe epilepsy. *Epilepsia*, *53*(7), 1178–1184. https://doi.org/10.1111/j.1528-1167.2012.03502.x

Parsons, N., Bowden, S. C., Vogrin, S., & D'Souza, W. J. (2020). Default mode network dysfunction in idiopathic generalised epilepsy. *Epilepsy Research*, *159*, 106254. https://doi.org/10.1016/j.eplepsyres.2019.106254

Pascarella, A., & Sorrentino, A. (2011). Statistical Approaches to the Inverse Problem. In *Magnetoencephalography* (pp. 1–21). InTech. https://doi.org/10.5772/27932

Pascual-Marqui, R. D. (2002). Standardized low-resolution brain electromagnetic tomography (sLORETA): technical details. *Methods and Findings in Experimental and Clinical Pharmacology*, *24 Suppl D*(1), 5–12.

Pascual-Marqui, R. D., Michel, C. M., & Lehmann, D. (1994). Low resolution electromagnetic tomography: a new method for localizing electrical activity in the brain. *International Journal of Psychophysiology*, *18*(1), 49–65. https://doi.org/10.1016/0167-8760(84)90014-X

Pillai, J., & Sperling, M. R. (2006). Interictal EEG and the Diagnosis of Epilepsy. *Epilepsia*, *47*(s1), 14–22. https://doi.org/10.1111/j.1528-1167.2006.00654.x

Plenz, D. (2012). Neuronal avalanches and coherence potentials. *The European Physical Journal Special Topics*, *205*(1), 259–301. https://doi.org/10.1140/epjst/e2012-01575-5

Plummer, C., Wagner, M., Fuchs, M., Harvey, A. S., & Cook, M. J. (2010). Dipole versus distributed EEG source localization for single versus averaged spikes in focal epilepsy. *Journal of Clinical Neurophysiology*, *27*(3), 141–162. https://doi.org/10.1097/WNP.0b013e3181dd5004

Pond, D. A. (2019). Clinical Electroencephalography. In O. Mecarelli (Ed.), *British Journal of Psychiatry* (Vol. 122, Issue 569). Springer International Publishing. https://doi.org/10.1007/978-3-030-04573-9

Presigny, C., & De Vico Fallani, F. (2022). Colloquium: Multiscale modeling of brain network organization. *Reviews of Modern Physics*, *94*(3), 31002. https://doi.org/10.1103/RevModPhys.94.031002

Prince, D. A. (1967). Control Mechanisms in Cortical Epileptogenic Foci*. *Archives of Neurology*, *16*(2), 194. https://doi.org/10.1001/archneur.1967.00470200082007

Qin, Y., Li, S., Yao, D., & Luo, C. (2022). Causality Analysis to the Abnormal Subcortical–Cortical Connections in Idiopathic-Generalized Epilepsy. *Frontiers in Neuroscience*, *16*. https://doi.org/10.3389/fnins.2022.925968

Qin, Y., Zhang, N., Chen, Y., Tan, Y., Dong, L., Xu, P., Guo, D., Zhang, T., Yao, D., & Luo, C. (2021). How Alpha Rhythm Spatiotemporally Acts Upon the Thalamus-Default Mode Circuit in Idiopathic Generalized Epilepsy. *IEEE Transactions on Biomedical Engineering*, *68*(4), 1282–1292. https://doi.org/10.1109/TBME.2020.3026055

Raichle, M. E., MacLeod, A. M., Snyder, A. Z., Powers, W. J., Gusnard, D. A., & Shulman, G. L. (2001). A default mode of brain function. *Proceedings of the National Academy of Sciences*, *98*(2), 676–682. https://doi.org/10.1073/pnas.98.2.676

Rajkumar, R., Régio Brambilla, C., Veselinović, T., Bierbrier, J., Wyss, C., Ramkiran, S., Orth, L., Lang, M., Rota Kops, E., Mauler, J., Scheins, J., Neumaier, B., Ermert, J., Herzog, H., Langen, K.-J., Binkofski, F. C., Lerche, C., Shah, N. J., & Neuner, I. (2021). Excitatory–inhibitory balance within EEG microstates and resting-state fMRI networks: assessed via simultaneous trimodal PET–MR–EEG imaging. *Translational Psychiatry*, *11*(1), 60. https://doi.org/10.1038/s41398-020-01160-2

Rajkumar, R., Rota Kops, E., Mauler, J., Tellmann, L., Lerche, C., Herzog, H., Shah, N. J., & Neuner, I. (2017). Simultaneous trimodal PET-MR-EEG imaging: Do EEG caps generate artefacts in PET images? *PLOS ONE*, *12*(9), e0184743. https://doi.org/10.1371/journal.pone.0184743

Ramkumar, P., Parkkonen, L., & Hyvärinen, A. (2014). Group-level spatial independent component analysis of Fourier envelopes of resting-state MEG data. *NeuroImage*, *86*, 480–491. https://doi.org/10.1016/j.neuroimage.2013.10.032

Ramos-Perdigués, S., Baillés, E., Mané, A., Carreño, M., Donaire, A., Rumia, J., Bargalló, N., Boget, T., Setoain, X., Valdes, M., & Pintor, L. (2016). A prospective study contrasting the psychiatric outcome in drug-resistant epilepsy between patients who underwent surgery and a control group. *Epilepsia*, *57*(10), 1680–1690. https://doi.org/10.1111/epi.13497

Riedl, V., Bienkowska, K., Strobel, C., Tahmasian, M., Grimmer, T., Förster, S., Friston, K. J., Sorg, C., & Drzezga, A. (2014). Local activity determines functional connectivity in the resting human brain: A simultaneous FDG-PET/fMRI study. *Journal of Neuroscience*, *34*(18), 6260–6266. https://doi.org/10.1523/JNEUROSCI.0492-14.2014

Riedl, V., Utz, L., Castrillón, G., Grimmer, T., Rauschecker, J. P., Ploner, M., Friston, K. J., Drzezga, A., & Sorg, C. (2016). Metabolic connectivity mapping reveals effective connectivity in the resting human brain. *Proceedings of the National Academy of Sciences*, *113*(2), 428–433. https://doi.org/10.1073/pnas.1513752113

Ritter, P., & Villringer, A. (2006). Simultaneous EEG-fMRI. *Neuroscience and Biobehavioral Reviews*, *30*(6), 823–838. https://doi.org/10.1016/j.neubiorev.2006.06.008

Rosenow, F. (2001). Presurgical evaluation of epilepsy. *Brain*, *124*(9), 1683–1700. https://doi.org/10.1093/brain/124.9.1683

Ruppert, M. C., Greuel, A., Freigang, J., Tahmasian, M., Maier, F., Hammes, J., van Eimeren, T., Timmermann, L., Tittgemeyer, M., Drzezga, A., Eggers, C., Eimeren, T., Timmermann, L., Tittgemeyer, M., Drzezga, A., & Eggers, C. (2021). The default mode network and cognition in Parkinson's disease: A multimodal resting-state network approach. *Human Brain Mapping*, *42*(8), 2623–2641. https://doi.org/10.1002/hbm.25393

Rusiniak, M., Bornfleth, H., Cho, J. H., Wolak, T., Ille, N., Berg, P., & Scherg, M. (2022). EEG-fMRI: Ballistocardiogram Artifact Reduction by Surrogate Method for Improved Source Localization. *Frontiers in Neuroscience*, *16*. https://doi.org/10.3389/fnins.2022.842420

Ryvlin, P., Cross, J. H., & Rheims, S. (2014). Epilepsy surgery in children and adults. *The Lancet Neurology*, *13*(11), 1114–1126. https://doi.org/10.1016/S1474-4422(14)70156-5

Sadaghiani, S., & Wirsich, J. (2020). Intrinsic connectome organization across temporal scales: New insights from cross-modal approaches. *Network Neuroscience*, *4*(1), 1–29. https://doi.org/10.1162/netn_a_00114

Sadler, R. M. (2006). The syndrome of mesial temporal lobe epilepsy with hippocampal sclerosis: clinical features and differential diagnosis. *Advances in Neurology*, *97*, 27–37.

Särelä, J., & Vigário, R. (2003). Overlearning in Marginal Distribution-Based ICA: Analysis and Solutions. *Journal of Machine Learning Research*, *1*(4), 1447–1469.

Sarikaya, I. (2015). PET studies in epilepsy. *American Journal of Nuclear Medicine and Molecular Imaging*, *5*(5), 416–430.

Savio, A., Fünger, S., Tahmasian, M., Rachakonda, S., Manoliu, A., Sorg, C., Grimmer, T., Calhoun, V., Drzezga, A., Riedl, V., & Yakushev, I. (2017). Resting-state networks as simultaneously measured with functional MRI and PET. *Journal of Nuclear Medicine*, *58*(8), 1314–1317. https://doi.org/10.2967/jnumed.116.185835

Sazgar, M., & Young, M. G. (2019). Overview of EEG, Electrode Placement, and Montages. In *Absolute Epilepsy and EEG Rotation Review* (pp. 117–125). Springer International Publishing. https://doi.org/10.1007/978-3-030-03511-2_5

Scheffer, I. E. (2000). Autosomal Dominant Nocturnal Frontal Lobe Epilepsy. *Epilepsia*, *41*(8), 1059–1060. https://doi.org/10.1111/j.1528-1157.2000.tb00298.x

Scheffer, I. E., Berkovic, S., Capovilla, G., Connolly, M. B., French, J., Guilhoto, L., Hirsch, E., Jain, S., Mathern, G. W., Moshé, S. L., Nordli, D. R., Perucca, E., Tomson, T., Wiebe, S., Zhang, Y. H., & Zuberi, S. M. (2017). ILAE classification of the epilepsies: Position paper of the ILAE Commission for Classification and Terminology. *Epilepsia*, *58*(4), 512–521. https://doi.org/10.1111/epi.13709

Schimpf, P. H., Ramon, C., & Haueisen, J. (2002). Dipole models for the EEG and MEG. *IEEE Transactions on Biomedical Engineering*, *49*(5), 409–418. https://doi.org/10.1109/10.995679

Schlemmer, H. P. W., Pichler, B. J., Schmand, M., Burbar, Z., Michel, C., Ladebeck, R., Jattke, K., Townsend, D., Nahmias, C., Jacob, P. K., Heiss, W. D., & Claussen, C. D. (2008). Simultaneous MR/PET imaging of the human brain: Feasibility study. *Radiology*, *248*(3), 1028–1035. https://doi.org/10.1148/radiol.2483071927

Schnakers, C., Demertzi, A., Cavaliere, C., Kandeepan, S., Aiello, M., Ribeiro de Paula, D., Marchitelli, R., Fiorenza, S., Orsini, M., Trojano, L., Masotta, O., St Lawrence, K., Loreto, V., Alexander Chronik, B., Nicolai, E., Soddu, A., Estraneo, A., & Vanvitelli, L. (2018). Multimodal Neuroimaging Approach to Variability of Functional Connectivity in

Disorders of Consciousness: A PET/MRI Pilot Study. *Frontiers in Neurology | Www.Frontiersin.Org*, *9*, 861. https://doi.org/10.3389/fneur.2018.00861

Schulz, R., Luders, H. O., Hoppe, M., Tuxhorn, I., May, T., & Ebner, A. (2000). Interictal EEG and Ictal Scalp EEG Propagation Are Highly Predictive of Surgical Outcome in Mesial Temporal Lobe Epilepsy. *Epilepsia*, *41*(5), 564–570. https://doi.org/10.1111/j.1528-1157.2000.tb00210.x

Schwartz, T. H., & Bonhoeffer, T. (2001). In vivo optical mapping of epileptic foci and surround inhibition in ferret cerebral cortex. *Nature Medicine*, *7*(9), 1063–1067. https://doi.org/10.1038/nm0901-1063

Semah, F., Picot, M.-C., Adam, C., Broglin, D., Arzimanoglou, A., Bazin, B., Cavalcanti, D., & Baulac, M. (1998). Is the underlying cause of epilepsy a major prognostic factor for recurrence? *Neurology*, *51*(5), 1256–1262. https://doi.org/10.1212/WNL.51.5.1256

Shah, N. J. (2015). Multimodal neuroimaging in humans at 9.4 T: a technological breakthrough towards an advanced metabolic imaging scanner. *Brain Structure and Function*, *220*(4), 1867–1884. https://doi.org/10.1007/s00429-014-0843-4

Shah, N. J., Arrubla, J., Rajkumar, R., Farrher, E., Mauler, J., Kops, E. R., Tellmann, L., Scheins, J., Boers, F., Dammers, J., Sripad, P., Lerche, C., Langen, K. J., Herzog, H., & Neuner, I. (2017). Multimodal Fingerprints of Resting State Networks as assessed by Simultaneous Trimodal MR-PET-EEG Imaging. *Scientific Reports*, *7*(1), 6452. https://doi.org/10.1038/s41598-017-05484-w

Shah, N. J., Oros-Peusquens, A.-M., Arrubla, J., Zhang, K., Warbrick, T., Mauler, J., Vahedipour, K., Romanzetti, S., Felder, J., Celik, A., Rota-Kops, E., Iida, H., Langen, K.-J., Herzog, H., & Neuner, I. (2013). Advances in multimodal neuroimaging: Hybrid MR–PET and MR–PET–EEG at 3T and 9.4T. *Journal of Magnetic Resonance*, *229*, 101–115. https://doi.org/10.1016/j.jmr.2012.11.027

Shmuel, A., & Leopold, D. A. (2008). Neuronal correlates of spontaneous fluctuations in fMRI signals in monkey visual cortex: Implications for functional connectivity at rest. *Human Brain Mapping*, *29*(7), 751–761. https://doi.org/10.1002/hbm.20580

Shou, G., Yuan, H., Li, C., Chen, Y., Chen, Y., & Ding, L. (2020). Whole-brain electrophysiological functional connectivity dynamics in resting-state EEG. *Journal of Neural Engineering*, *17*(2), 026016. https://doi.org/10.1088/1741-2552/ab7ad3

Singh, A., & Trevick, S. (2016). The Epidemiology of Global Epilepsy. *Neurologic Clinics*, *34*(4), 837–847. https://doi.org/10.1016/j.ncl.2016.06.015

Sisodiya, S. M., Fauser, S., Cross, J. H., & Thom, M. (2009). Focal cortical dysplasia type II: biological features and clinical perspectives. *The Lancet Neurology*, *8*(9), 830–843. https://doi.org/10.1016/S1474-4422(09)70201-7

Sloviter, R. S. (1994). The functional organization of the hippocampal dentate gyrus and its relevance to the pathogenesis of temporal lobe epilepsy. *Annals of Neurology*, *35*(6), 640–654. https://doi.org/10.1002/ana.410350604

Smith, S. M., Fox, P. T., Miller, K. L., Glahn, D. C., Fox, P. M., Mackay, C. E., Filippini, N., Watkins, K. E., Toro, R., Laird, A. R., & Beckmann, C. F. (2009). Correspondence of the brain's functional architecture during activation and rest. *Proceedings of the National Academy of Sciences*, *106*(31), 13040–13045. https://doi.org/10.1073/pnas.0905267106

Sockeel, S., Schwartz, D., Pélégrini-Issac, M., & Benali, H. (2016). Large-Scale Functional Networks Identified from Resting-State EEG Using Spatial ICA. *PLOS ONE*, *11*(1), e0146845. https://doi.org/10.1371/journal.pone.0146845

Sokoloff, L. (2008). The physiological and biochemical bases of functional brain imaging. *Cognitive Neurodynamics*, *2*(1), 1–5. https://doi.org/10.1007/s11571-007-9033-x

Sperling, M. R., Barshow, S., Nei, M., & Asadi-Pooya, A. A. (2016). A reappraisal of mortality after epilepsy surgery. *Neurology*, *86*(21), 1938–1944. https://doi.org/10.1212/WNL.0000000000002700

Stern. (2002). Simultaneous EEG and fMRI of the alpha rhythm. *NeuroReport*, *13*(18), 2487–2492. https://doi.org/10.1097/01.wnr.0000047685.08940.d0

Stier, C., Elshahabi, A., Li Hegner, Y., Kotikalapudi, R., Marquetand, J., Braun, C., Lerche, H., & Focke, N. K. (2021). Heritability of Magnetoencephalography Phenotypes Among Patients With Genetic Generalized Epilepsy and Their Siblings. *Neurology*, *97*(2), e166–e177. https://doi.org/10.1212/WNL.0000000000012144

Stier, C., Loose, M., Kotikalapudi, R., Elshahabi, A., Li Hegner, Y., Marquetand, J., Braun, C., Lerche, H., & Focke, N. K. (2022). Combined electrophysiological and morphological phenotypes in patients with genetic generalized epilepsy and their healthy siblings. *Epilepsia*, *63*(7), 1643–1657. https://doi.org/10.1111/epi.17258

Striano, P., Busolin, G., Santulli, L., Leonardi, E., Coppola, A., Vitiello, L., Rigon, L., Michelucci, R., Tosatto, S. C. E., Striano, S., & Nobile, C. (2011). Familial temporal lobe epilepsy with psychic auras associated with a novel LGI1 mutation. *Neurology*, *76*(13), 1173–1176. https://doi.org/10.1212/WNL.0b013e318212ab2e

Striano, P., de Falco, A., Diani, E., Bovo, G., Furlan, S., Vitiello, L., Pinardi, F., Striano, S., Michelucci, R., de Falco, F. A., & Nobile, C. (2008). A Novel Loss-of-Function LGI1 Mutation Linked to Autosomal Dominant Lateral Temporal Epilepsy. *Archives of Neurology*, *65*(7). https://doi.org/10.1001/archneur.65.7.939

Su, H., Zuo, C., Zhang, H., Jiao, F., Zhang, B., Tang, W., Geng, D., Guan, Y., & Shi, S. (2018). Regional cerebral metabolism alterations affect resting-state functional connectivity in major depressive disorder. *Quantitative Imaging in Medicine and Surgery*, *8*(9), 910–924. https://doi.org/10.21037/qims.2018.10.05

Sun, W., Zhang, M., Zhang, Y., Li, B., & Li, Y. (2021). Brain Intrinsic Functional Activity in Relation to Metabolic Changes in Alzheimer's Disease: A Simultaneous PET/fMRI study. *Proceedings of the Annual International Conference of the IEEE Engineering in Medicine and Biology Society, EMBS*, *81871083*, 3467–3470. https://doi.org/10.1109/EMBC46164.2021.9630966

Sveinsson, O., Andersson, T., Carlsson, S., & Tomson, T. (2017). The incidence of SUDEP. *Neurology*, *89*(2), 170–177. https://doi.org/10.1212/WNL.0000000000004094

Szaflarski, J. P., Kay, B., Gotman, J., Privitera, M. D., & Holland, S. K. (2013). The relationship between the localization of the generalized spike and wave discharge generators and the response to valproate. *Epilepsia*, *54*(3), 471–480. https://doi.org/10.1111/epi.12062

Tahmasian, M., Eggers, C., Riedl, V., Sorg, C., & Drzezga, A. (2015). Editorial: Utilization of hybrid PET/MR in neuroimaging. *Basic and Clinical Neuroscience*, *6*(3), 143–145.

Tahmasian, M., Eickhoff, S. B., Giehl, K., Schwartz, F., Herz, D. M., Drzezga, A., van Eimeren, T., Laird, A. R., Fox, P. T., Khazaie, H., Zarei, M., Eggers, C., & Eickhoff, C. R. (2017). Resting-state functional reorganization in Parkinson's disease: An activation likelihood estimation meta-analysis. *Cortex*, *92*, 119–138. https://doi.org/10.1016/j.cortex.2017.03.016

Takamura, T., & Hanakawa, T. (2017). Clinical utility of resting-state functional connectivity magnetic resonance imaging for mood and cognitive disorders. In *Journal of Neural*

Transmission (Vol. 124, Issue 7, pp. 821–839). Springer-Verlag Wien. https://doi.org/10.1007/s00702-017-1710-2

Tangwiriyasakul, C., Perani, S., Centeno, M., Yaakub, S. N., Abela, E., Carmichael, D. W., & Richardson, M. P. (2018). Dynamic brain network states in human generalized spike-wave discharges. *Brain*, *141*(10), 2981–2994. https://doi.org/10.1093/brain/awy223

Tassi, L. (2002). Focal cortical dysplasia: neuropathological subtypes, EEG, neuroimaging and surgical outcome. *Brain*, *125*(8), 1719–1732. https://doi.org/10.1093/brain/awf175

Tatum, W. O., Rubboli, G., Kaplan, P. W., Mirsatari, S. M., Radhakrishnan, K., Gloss, D., Caboclo, L. O., Drislane, F. W., Koutroumanidis, M., Schomer, D. L., Kasteleijn-Nolst Trenite, D., Cook, M., & Beniczky, S. (2018). Clinical utility of EEG in diagnosing and monitoring epilepsy in adults. *Clinical Neurophysiology*, *129*(5), 1056–1082. https://doi.org/10.1016/j.clinph.2018.01.019

Taussig, D., Petrescu, A. M., Aghakhani, N., Herbrecht, A., Dorfmüller, G., Ferrand-Sorbets, S., Chipaux, M., Fohlen, M., Rodrigo, S., & Bouilleret, V. (2021). 18 F-FDG-PET hypometabolic pattern reveals multifocal epileptic foci despite limited unique stereotyped seizures. *Epilepsy Research*, *172*(January), 106589. https://doi.org/10.1016/j.eplepsyres.2021.106589

Téllez-Zenteno, J. F., & Hernández-Ronquillo, L. (2012). A Review of the Epidemiology of Temporal Lobe Epilepsy. *Epilepsy Research and Treatment*, *2012*, 1–5. https://doi.org/10.1155/2012/630853

Tessa, C., Michelucci, R., Nobile, C., Giannelli, M., Nave, R. D., Testoni, S., Bianucci, D., Tinuper, P., Bisulli, F., Sofia, V., De Feo, M. R., Giallonardo, A. T., Tassinari, C. A., & Mascalchi, M. (2007). STRUCTURAL ANOMALY OF LEFT LATERAL TEMPORAL LOBE IN EPILEPSY DUE TO MUTATED LGI1. *Neurology*, *69*(12), 1298–1300. https://doi.org/10.1212/01.wnl.0000277045.16688.b6

Thurman, D. J., Logroscino, G., Beghi, E., Hauser, W. A., Hesdorffer, D. C., Newton, C. R., Scorza, F. A., Sander, J. W., & Tomson, T. (2017). The burden of premature mortality of epilepsy in high-income countries: A systematic review from the Mortality Task Force of the International League Against Epilepsy. *Epilepsia*, *58*(1), 17–26. https://doi.org/10.1111/epi.13604

Timofeev, I., & Chauvette, S. (2011). Thalamocortical Oscillations: Local Control of EEG Slow Waves. *Current Topics in Medicinal Chemistry*, *11*(19), 2457–2471. https://doi.org/10.2174/156802611797470376

Tohka, J., Foerde, K., Aron, A. R., Tom, S. M., Toga, A. W., & Poldrack, R. A. (2008). Automatic independent component labeling for artifact removal in fMRI. *NeuroImage*, *39*(3), 1227–1245. https://doi.org/10.1016/j.neuroimage.2007.10.013

Tomasi, D., Wang, G. J., & Volkow, N. D. (2013). Energetic cost of brain functional connectivity. *Proceedings of the National Academy of Sciences of the United States of America*, *110*(33), 13642–13647. https://doi.org/10.1073/pnas.1303346110

Tong, S., Alessio, A. M., & Kinahan, P. E. (2010). Image reconstruction for PET/CT scanners: Past achievements and future challenges. *Imaging in Medicine*, *2*(5), 529–545. https://doi.org/10.2217/iim.10.49

Townsend, D. W., Beyer, T., & Blodgett, T. M. (2003). PET/CT scanners: A hardware approach to image fusion. *Seminars in Nuclear Medicine*, *33*(3), 193–204. https://doi.org/10.1053/snuc.2003.127314

Townsend, D. W., Carney, J. P. J., Yap, J. T., & Hall, N. C. (2004). PET/CT today and tomorrow. *Journal of Nuclear Medicine : Official Publication, Society of Nuclear Medicine*, *45 Suppl 1*(9999), 4S-14S.

Trotta, N., Baete, K., Laere, K. Van, Goldman, S., Tiège, X. De, & Wens, V. (2018). Neurometabolic Resting-State Networks Derived from Seed-Based Functional Connectivity Analysis. *Journal of Nuclear Medicine*, *59*(10), 1642–1643. https://doi.org/10.2967/jnumed.118.212878

Tulay, E. E., Metin, B., Tarhan, N., & Arıkan, M. K. (2019). Multimodal Neuroimaging: Basic Concepts and Classification of Neuropsychiatric Diseases. *Clinical EEG and Neuroscience*, *50*(1), 20–33. https://doi.org/10.1177/1550059418782093

Uji, M., Cross, N., Pomares, F. B., Perrault, A. A., Jegou, A., Nguyen, A., Aydin, U., Lina, J. M., Dang-Vu, T. T., & Grova, C. (2021). Data-driven beamforming technique to attenuate ballistocardiogram artefacts in electroencephalography–functional magnetic resonance imaging without detecting cardiac pulses in electrocardiography recordings. *Human Brain Mapping*, *42*(12), 3993–4021. https://doi.org/10.1002/hbm.25535

Ullsperger, M., & Debener, S. (2010). *Simultaneous EEG and fMRI* (M. Ullsperger & S. Debener, Eds.; 1st Editio). Oxford University Press.

Vaishnavi, S. N., Vlassenko, A. G., Rundle, M. M., Snyder, A. Z., Mintun, M. A., & Raichle, M. E. (2010). Regional aerobic glycolysis in the human brain. *Proceedings of the National Academy of Sciences*, *107*(41), 17757–17762. https://doi.org/10.1073/pnas.1010459107

Vakharia, V. N., Duncan, J. S., Witt, J.-A., Elger, C. E., Staba, R., & Engel, J. (2018). Getting the best outcomes from epilepsy surgery. *Annals of Neurology*, *83*(4), 676–690. https://doi.org/10.1002/ana.25205

Valdes-Sosa, P. A., Sanchez-Bornot, J. M., Sotero, R. C., Iturria-Medina, Y., Aleman-Gomez, Y., Bosch-Bayard, J., Carbonell, F., & Ozaki, T. (2009). Model driven EEG/fMRI fusion of brain oscillations. *Human Brain Mapping*, *30*(9), 2701–2721. https://doi.org/10.1002/hbm.20704

van der Meer, J. N., Pampel, A., Van Someren, E. J. W., Ramautar, J. R., van der Werf, Y. D., Gomez-Herrero, G., Lepsien, J., Hellrung, L., Hinrichs, H., Möller, H. E., & Walter, M. (2016). Carbon-wire loop based artifact correction outperforms post-processing EEG/fMRI corrections—A validation of a real-time simultaneous EEG/fMRI correction method. *NeuroImage*, *125*, 880–894. https://doi.org/10.1016/j.neuroimage.2015.10.064

van Mierlo, P., Höller, Y., Focke, N. K., & Vulliemoz, S. (2019). Network Perspectives on Epilepsy Using EEG/MEG Source Connectivity. *Frontiers in Neurology*, *10*. https://doi.org/10.3389/fneur.2019.00721

Van Veen, B. D., Van Drongelen, W., Yuchtman, M., & Suzuki, A. (1997). Localization of brain electrical activity via linearly constrained minimum variance spatial filtering. *IEEE Transactions on Biomedical Engineering*, *44*(9), 867–880. https://doi.org/10.1109/10.623056

Vasios, C. E., Angelone, L. M., Purdon, P. L., Ahveninen, J., Belliveau, J. W., & Bonmassar, G. (2006). EEG/(f)MRI measurements at 7 Tesla using a new EEG cap ("InkCap"). *NeuroImage*, *33*(4), 1082–1092. https://doi.org/10.1016/j.neuroimage.2006.07.038

Vaudano, A. E., Laufs, H., Kiebel, S. J., Carmichael, D. W., Hamandi, K., Guye, M., Thornton, R., Rodionov, R., Friston, K. J., Duncan, J. S., & Lemieux, L. (2009). Causal Hierarchy

within the Thalamo-Cortical Network in Spike and Wave Discharges. *PLoS ONE*, *4*(8), e6475. https://doi.org/10.1371/journal.pone.0006475

Von Helmholtz, H. L. F. (1853). Ueber einige Gesetze der Verteilung elektrischer Str¨ome in k¨orperlichen Leitern mit Anwendung auf die tierisch elektrischen Versuche. In *Ann. Physik und Chemie* (Vol. 89, Issue 6, pp. 211–233, 354–377).

Vorderwülbecke, B. J., Carboni, M., Tourbier, S., Brunet, D., Seeber, M., Spinelli, L., Seeck, M., & Vulliemoz, S. (2020). High-density Electric Source Imaging of interictal epileptic discharges: How many electrodes and which time point? *Clinical Neurophysiology*, *131*(12), 2795–2803. https://doi.org/10.1016/j.clinph.2020.09.018

Vos, T., Allen, C., Arora, M., Barber, R. M., Bhutta, Z. A., Brown, A., Carter, A., Casey, D. C., Charlson, F. J., Chen, A. Z., Coggeshall, M., Cornaby, L., Dandona, L., Dicker, D. J., Dilegge, T., Erskine, H. E., Ferrari, A. J., Fitzmaurice, C., Fleming, T., … Murray, C. J. L. (2016). Global, regional, and national incidence, prevalence, and years lived with disability for 310 diseases and injuries, 1990–2015: a systematic analysis for the Global Burden of Disease Study 2015. *The Lancet*, *388*(10053), 1545–1602. https://doi.org/10.1016/S0140-6736(16)31678-6

Wang, H. E., Scholly, J., Triebkorn, P., Sip, V., Medina Villalon, S., Woodman, M. M., Le Troter, A., Guye, M., Bartolomei, F., & Jirsa, V. (2021). VEP atlas: An anatomic and functional human brain atlas dedicated to epilepsy patients. *Journal of Neuroscience Methods*, *348*, 108983. https://doi.org/10.1016/j.jneumeth.2020.108983

Wang, J., Shan, Y., Dai, J., Cui, B., Shang, K., Yang, H., Chen, Z., Shan, B., Zhao, G., & Lu, J. (2020). Altered coupling between resting-state glucose metabolism and functional activity in epilepsy. *Annals of Clinical and Translational Neurology*, *7*(10), 1831–1842. https://doi.org/10.1002/acn3.51168

Wang, Z., Lu, G., Zhang, Z., Zhong, Y., Jiao, Q., Zhang, Z., Tan, Q., Tian, L., Chen, G., Liao, W., Li, K., & Liu, Y. (2011). Altered resting state networks in epileptic patients with generalized tonic–clonic seizures. *Brain Research*, *1374*, 134–141. https://doi.org/10.1016/j.brainres.2010.12.034

Warach, S., Ives, J. R., Schlaug, G., Patel, M. R., Darby, D. G., Thangaraj, V., Edelman, R. R., & Schomer, D. L. (1996). EEG-triggered echo-planar functional MRI in epilepsy. *Neurology*, *47*(1), 89–93. https://doi.org/10.1212/WNL.47.1.89

Warbrick, T. (2022). Simultaneous EEG-fMRI: What Have We Learned and What Does the Future Hold? *Sensors*, *22*(6), 2262. https://doi.org/10.3390/s22062262

Warbrick, T., Reske, M., & Shah, N. J. (2013). Do EEG paradigms work in fMRI? Varying task demands in the visual oddball paradigm: Implications for task design and results interpretation. *NeuroImage*, *77*, 177–185. https://doi.org/10.1016/j.neuroimage.2013.03.026

Wehrl, H. F., Hossain, M., Lankes, K., Liu, C.-C., Bezrukov, I., Martirosian, P., Schick, F., Reischl, G., & Pichler, B. J. (2013). Simultaneous PET-MRI reveals brain function in activated and resting state on metabolic, hemodynamic and multiple temporal scales. *Nature Medicine*, *19*(9), 1184–1189. https://doi.org/10.1038/nm.3290

Weng, Y., Larivière, S., Caciagli, L., Vos de Wael, R., Rodríguez-Cruces, R., Royer, J., Xu, Q., Bernasconi, N., Bernasconi, A., Thomas Yeo, B. T., Lu, G., Zhang, Z., & Bernhardt, B. C. (2020). Macroscale and microcircuit dissociation of focal and generalized human epilepsies. *Communications Biology*, *3*(1), 1–11. https://doi.org/10.1038/s42003-020-0958-5

Wennberg, R., & Cheyne, D. (2014). EEG source imaging of anterior temporal lobe spikes: Validity and reliability. *Clinical Neurophysiology*, *125*(5), 886–902. https://doi.org/10.1016/j.clinph.2013.09.042

Westmijse, I., Ossenblok, P., Gunning, B., & van Luijtelaar, G. (2009). Onset and propagation of spike and slow wave discharges in human absence epilepsy: A MEG study. *Epilepsia*, *50*(12), 2538–2548. https://doi.org/10.1111/j.1528-1167.2009.02162.x

Whitfield-Gabrieli, S., & Nieto-Castanon, A. (2012). Conn: A Functional Connectivity Toolbox for Correlated and Anticorrelated Brain Networks. *Brain Connectivity*, *2*(3), 125–141. https://doi.org/10.1089/brain.2012.0073

Whiting, S., & Duchowny, M. (1999). Topical Review: Clinical Spectrum of Cortical Dysplasia in Childhood: Diagnosis and Treatment Issues. *Journal of Child Neurology*, *14*(12), 759–771. https://doi.org/10.1177/088307389901401201

WHO. (2019). *Epilepsy: a public health imperative. Summary.*

Wiebe, S., Blume, W. T., Girvin, J. P., & Eliasziw, M. (2001). A Randomized, Controlled Trial of Surgery for Temporal-Lobe Epilepsy. *New England Journal of Medicine*, *345*(5), 311–318. https://doi.org/10.1056/NEJM200108023450501

Wieser, H. G., Blume, W. T., Fish, D., Goldensohn, E., Hufnagel, A., King, D., Sperling, M. R., Lüders, H., Pedley, T. A., & Commission on Neurosurgery of the International League Against Epilepsy (ILAE). (2001). ILAE Commission Report. Proposal for a new classification of outcome with respect to epileptic seizures following epilepsy surgery. *Epilepsia*, *42*(2), 282–286.

Winawer, MelodieR., Boneschi, F., Barker-Cummings, C., Lee, JosephH., Liu, J., Mekios, C., Gilliam, T. C., Pedley, TimothyA., Hauser, W. A., & Ottman, R. (2002). Four New Families with Autosomal Dominant Partial Epilepsy with Auditory Features: Clinical Description and Linkage to Chromosome 10q24. *Epilepsia*, *43*(1), 60–67. https://doi.org/10.1046/j.1528-1157.2002.45001.x

Wirsich, J., Amico, E., Giraud, A.-L., Goñi, J., & Sadaghiani, S. (2020). Multi-timescale hybrid components of the functional brain connectome: A bimodal EEG-fMRI decomposition. *Network Neuroscience*, *4*(3), 658–677. https://doi.org/10.1162/netn_a_00135

Wirsich, J., Jorge, J., Iannotti, G. R., Shamshiri, E. A., Grouiller, F., Abreu, R., Lazeyras, F., Giraud, A. L., Gruetter, R., Sadaghiani, S., & Vulliémoz, S. (2021). The relationship between EEG and fMRI connectomes is reproducible across simultaneous EEG-fMRI studies from 1.5T to 7T. *NeuroImage*, *231*(February), 117864. https://doi.org/10.1016/j.neuroimage.2021.117864

Witte, O. W., Bruehl, C., Schlaug, G., Tuxhorn, I., Lahl, R., Villagran, R., & Seitz, R. J. (1994). Dynamic changes of focal hypometabolism in relation to epileptic activity. *Journal of the Neurological Sciences*, *124*(2), 188–197. https://doi.org/10.1016/0022-510X(94)90325-5

Wolters, A. F., van de Weijer, S. C. F., Leentjens, A. F. G., Duits, A. A., Jacobs, H. I. L., & Kuijf, M. L. (2019). Resting-state fMRI in Parkinson's disease patients with cognitive impairment: A meta-analysis. *Parkinsonism & Related Disorders*, *62*(December), 16–27. https://doi.org/10.1016/j.parkreldis.2018.12.016

Womelsdorf, T., Schoffelen, J.-M., Oostenveld, R., Singer, W., Desimone, R., Engel, A. K., & Fries, P. (2007). Modulation of Neuronal Interactions Through Neuronal Synchronization. *Science*, *316*(5831), 1609–1612. https://doi.org/10.1126/science.1139597

Woolrich, M. W., Baker, A., Luckhoo, H., Mohseni, H., Barnes, G., Brookes, M., & Rezek, L. (2013). Dynamic state allocation for MEG source reconstruction. *NeuroImage*, *77*, 77–92. https://doi.org/10.1016/j.neuroimage.2013.03.036

Wu, L., Eichele, T., & Calhoun, V. D. (2010). Reactivity of hemodynamic responses and functional connectivity to different states of alpha synchrony: A concurrent EEG-fMRI study. *NeuroImage*, *52*(4), 1252–1260. https://doi.org/10.1016/j.neuroimage.2010.05.053

Xiong, J., Parsons, L. M., Gao, J.-H., & Fox, P. T. (1999). Interregional connectivity to primary motor cortex revealed using MRI resting state images. *Human Brain Mapping*, *8*(2–3), 151–156. https://doi.org/10.1002/(SICI)1097-0193(1999)8:2/3<151::AID-HBM13>3.0.CO;2-5

Yao, Z., Hu, B., Xie, Y., Moore, P., & Zheng, J. (2015). A review of structural and functional brain networks: small world and atlas. *Brain Informatics*, *2*(1), 45–52. https://doi.org/10.1007/s40708-015-0009-z

Yeo, B. T. T., Krienen, F. M., Sepulcre, J., Sabuncu, M. R., Lashkari, D., Hollinshead, M., Roffman, J. L., Smoller, J. W., Zöllei, L., Polimeni, J. R., Fischl, B., Liu, H., & Buckner, R. L. (2011). The organization of the human cerebral cortex estimated by intrinsic functional connectivity. *Journal of Neurophysiology*, *106*(3), 1125–1165. https://doi.org/10.1152/jn.00338.2011

Yuan, H., Ding, L., Zhu, M., Zotev, V., Phillips, R., & Bodurka, J. (2016). Reconstructing Large-Scale Brain Resting-State Networks from High-Resolution EEG: Spatial and Temporal Comparisons with fMRI. *Brain Connectivity*, *6*(2), 122–135. https://doi.org/10.1089/brain.2014.0336

Yuen, A. W. C., Keezer, M. R., & Sander, J. W. (2018). Epilepsy is a neurological and a systemic disorder. *Epilepsy & Behavior*, *78*, 57–61. https://doi.org/10.1016/j.yebeh.2017.10.010

Zang, Z., Song, T., Li, J., Nie, B., Mei, S., Zhang, C., Wu, T., Zhang, Y., & Lu, J. (2022). Simultaneous PET/fMRI revealed increased motor area input to subthalamic nucleus in Parkinson's disease. *Cerebral Cortex*, 1–9. https://doi.org/10.1093/cercor/bhac059

Zhang, D., & Raichle, M. E. (2010). Disease and the brain's dark energy. *Nature Reviews Neurology*, *6*(1), 15–28. https://doi.org/10.1038/nrneurol.2009.198

Zhang, M., Guan, Z., Zhang, Y., Sun, W., Li, W., Hu, J., Li, B., Ye, G., Meng, H., Huang, X., Lin, X., Wang, J., Liu, J., Li, B., & Li, Y. (2022). Disrupted coupling between salience network segregation and glucose metabolism is associated with cognitive decline in Alzheimer's disease – A simultaneous resting-state FDG-PET/fMRI study. *NeuroImage: Clinical*, *34*(September 2021), 102977. https://doi.org/10.1016/j.nicl.2022.102977

Zhao, M., Ma, H., Suh, M., & Schwartz, T. H. (2009). Spatiotemporal Dynamics of Perfusion and Oximetry during Ictal Discharges in the Rat Neocortex. *Journal of Neuroscience*, *29*(9), 2814–2823. https://doi.org/10.1523/JNEUROSCI.4667-08.2009

Zou, K. H., Warfield, S. K., Bharatha, A., Tempany, C. M. C., Kaus, M. R., Haker, S. J., Wells, W. M., Jolesz, F. A., & Kikinis, R. (2004). Statistical Validation of Image Segmentation Quality Based on a Spatial Overlap Index. *Academic Radiology*, *11*(2), 178–189. https://doi.org/10.1016/S1076-6332(03)00671-8

Zumsteg, D., Friedman, A., Wieser, H., & Wennberg, R. (2006). Propagation of interictal discharges in temporal lobe epilepsy: Correlation of spatiotemporal mapping with intracranial foramen ovale electrode recordings. *Clinical Neurophysiology*, *117*(12), 2615–2626. https://doi.org/10.1016/j.clinph.2006.07.319

12.DECLARATION

I hereby certify that the work presented in this thesis entitled ”Neural network integration from multimodal imaging in epilepsy and healthy controls” is my own. When information from other sources has been used, it has been properly cited in the paper.

_____

Daniel van de Velden, Göttingen, 22nd December 2022